Spring 2023

Spin Mediated Topological Black Hole in Acoustic Metamaterials Near Dirac-Like Cone Frequencies.

Mustahseen Mobashwer Indaleeb

SPIN MEDIATED TOPOLOGICAL BLACK HOLE IN ACOUSTIC METAMATERIALS NEAR DIRAC-LIKE CONE FREQUENCIES.

by

Mustahseen Mobashwer Indaleeb

Bachelor of Science
Military Institute of Science & Technology, 2013

Master of Science
University of South Carolina, 2019

Submitted in Partial Fulfillment of the Requirements

For the Degree of Doctor of Philosophy in

Mechanical Engineering

College of Engineering and Computing

University of South Carolina

2023

Accepted by:

Sourav Banerjee, Major Professor

Jafer Gürdal, Committee Member

Tanvir I. Farouk, Committee Member

Sumanta Tewari, Committee Member

Cheryl L. Addy, Interim Vice Provost and Dean of the Graduate School

DEDICATION

This dissertation is dedicated to my parents Mr. Mobashwer Ali Khandaker and Mrs. Flora Nasrin. I would also like to dedicate this work to my lovely wife Faequa Uniza Rahman (Eashna) for her constant support, love and affection to fulfill my dream.

ACKNOWLEDGEMENTS

I would like to express my deep gratitude and thanks to my advisor Dr. Sourav Banerjee, Associate Professor, University of South Carolina for his guidance, invaluable suggestions, constructive criticisms and sharing his knowledge throughout this work. It has been a great privilege and honor for me to work with him. I would also like to thank Dr. Jafer Gürdal and Dr. Tanvir I. Farouk for their precious concern in this research and kindly agreeing to officially serve as the reader. I would also like extend my gratitude to Dr. Sumanta Tewari for wholeheartedly accepting my request to be part of my committee too. I would also like to thank all the members of iMAPS (Integrated Material Assessment and Predictive Simulation) for their guidance in my progress, especially Hossain Ahmed and Sadegh Saadatzi for their kind support. Finally, special thanks go to my wife, Faequa Uniza Rahman (Eashna) and my family for their support and encouragements to achieve this goal.

ABSTRACT

A unique bulk-boundary distinction and acoustic topological phenomena is discovered and explained in this dissertation. The overall objective was to discover the hidden physics, dynamic and mechanics of acoustic wave behavior that causes the formation of extremely rare 'Topologically protected Black Hole' (TBH) in acoustic microarchitecture metamaterials. This behavior is immensely valuable for numerous mechanical and civil engineering applications where acoustic insulators are required to create sound-free or vibration-free exterior surfaces. On the other hand, to contain the energy within the structure, for impact mitigation and energy absorption in vehicles, space crafts, aircrafts, and civil infrastructures such materials will be immensely valuable. Unlike other unit cell acoustic black holes, TBH has unique bulk-boundary distinction creating an acoustic energy sink during wave propagation inside the bulk metamaterial, while keeping the boundaries insulated. This is exactly opposite to the behavior of a topological acoustic insulator (TAI).

Traditionally, mechanical vibration, acoustic waves and elastic waves are widely studied using Newtonian mechanics. Surprisingly since the beginning of the twenty first century for some cases of acoustic and elastic waves in periodic media were observed to demonstrate properties that are analogous to the quantum behavior prevalent in solid state physics. Suddenly the quantum mechanical understanding of acoustic and elastic waves become imperative. Thus, in this dissertation many such quantum mechanical terms are used to explain the phenomena discovered. Primary understanding starts from the physics

of Dirac cones and Dirac-like cones at the boundary and at the center of the Brillouin zone in a periodic metastructure. The study of this periodic acoustic or mechanical metastructures consists of Phononic Crystals (PnCs), has now matured into an exciting research field. Over the past two decades, complementary to the photonics, phononics in periodic architecture with PnCs and periodic metamaterials have dominated the acoustic and elastic wave research field.

This dissertation first presents the understanding of accidental degeneracies in periodic media at the center of the Brillouin zone. It is shown that simplest geometric microarchitecture of PnCs in a periodic structure can be modulated to obtain the accidental triple degeneracies that make a Dirac-like cone at the Γ point ($\vec{k} = 0$) by breaking the time reversal symmetry. A non-trivial nondispersive "deaf" band is demonstrated and obtained from any arbitrary periodic structure made of similar PnCs which remains unaltered. Further this deaf band-based tuning is demonstrated to achieve orthogonal wave guiding at selected frequencies and the phenomena is exploited to demonstrate the possibility of acoustic computing for engineering applications. While doing so, at a specific doubly degenerated frequency near Dirac-like cone the TBH phenomena emerged. It was found that TBH is microarchitecture independent phenomenon and does not require any breaking of the time reversal symmetry or the space inversion symmetry if the ‘Deaf band’ dominates the local dispersion.

This phenomenon is not like the previously reported topological trio phenomena namely Quantum Halle Effect (QHE), Quantum Spin Hall Effect (QSHE) and Quantum Valley Hall Effect (QVHE), where the media boundary is conductive i.e., the acoustic wave energy is confined to the boundary while keeping the bulk media insulated. It was found

that TBH will only happen when the polarization of two doubly degenerate mode for all possible wave direction is orthogonal to each other. This scenario results continuously changing up spin and down spin of the wave energy in the media and remain trapped without specific preferential direction of wave transport. The spin here as it is described in this dissertation was found to generate the positive orbital angular momentum and cause the change in geometric phase from $0 - 2\pi$ for the up spin, and then generate the negative orbital angular momentum and cause the change in geometric phase from $2\pi - 0$, leaving no resultant geometric phase, while the energy is trapped in the media. This trapped wave was found to be topologically protected, means irrespective of media configuration, wave is always trapped within the entire bulk. Owing to the clockwise and anti-clockwise spin that eventually causing the topologically contained wave, the term blackhole is used herein.

TABLE OF CONTENTS

LIST OF FIGURES

CHAPTER 1

INTRODUCTION

The unique dispersion behavior of acoustic ultrasonic waves at the Dirac frequencies have recently been shown to create opportunities that can be used to exploit extraordinary wave transport [1-5], which would not be possible otherwise. In a periodic medium, in a reduced wave vector space (k), the Dirac points are found either at the Brillouin boundary [1] or at the center of the Brillouin zone (BZ) [6]. In photonics, the Dirac cone at the Brillouin boundary exhibits phenomena such as Zitterbewegung oscillation [7], Klein tunneling [8, 9], anti-localization [10, 11] and the integer quantum Hall effect [12]. These phenomena arise due to the breaking of the time reversal symmetry in a zero refractive index material [13] at certain frequencies. In photonics, researchers have experimentally proved the existence of these phenomena in the presence of an external magnetic field. However, limited activity in this regard can be found in phononics, where an alternative field to replace the magnetic field does not exist.

Acoustic periodic system has been designed to demonstrate a wide variety of extraordinary waveguiding capabilities using their unique wave dispersion properties. These acoustic systems are realized for potential applications, including acoustic super-tunneling [14], cloaking[16, 17], designing acoustic lenses [18], imaging with subwavelength resolutions [19, 20], etc. Over the past few decades, competing with photonics, periodic architecture of phononic crystals (PnCs) has guided the research on acoustic waves in a whole new direction [21-24]. Likewise, capabilities of extraordinary wave transport and possibilities of engineered energy control for periodic architectures

(PnCs) at Dirac cone frequencies, created a new direction in the metamaterial research [25, 26]. In photonics, this phenomenon occurs at the Fermi level. As the Dirac equation describes the relativistic spin ½ particles, the band structure near Fermi level at the hexagonal corners of Graphene exhibits Dirac dispersion and is explained by massless Dirac equation. This dispersion band at the fermi level is linear at the *K* and *K'* points where the dispersion close to the fermi energy level forms a conical shape [27]. This Dirac point and the conical shaped Dirac cone lead to many novel phenomena in electronic transport such as Zitterbewegung oscillation, Klein tunneling, antilocalization and integer quantum Hall effect [1, 8, 12, 28]. Researchers have realized and experimentally proved these behaviors in photonic crystals while the material was interacting with the electromagnetic waves in the presence of magnetic field. However, lack of such synonymous magnetic field challenges phononics to achieve ubiquitous photonics behavior and leads to accidental degeneracies at the Dirac-like points [29]. Dirac cones, with their inimitable linear dispersion features, have attracted significant attention since its first successful extraction by the classical wave system. It occurs at the intersection of two bands at the corners of the Brillouin Zone in a triangular and in a hexagonal honeycomb metamaterial which led to some interesting wave transport properties in phononics. Few researchers reported that the Dirac cones also yield phenomena like object cloaking [6] and super-anisotropy [3].

Despite this fact, Dirac cones are found at the intersection of two bands at the corners of the BZ (the K point), when the PnCs are periodically arranged in a triangular or hexagonal pattern [1]. Few other researchers have reported that the Dirac cones can also yield phenomena such as object cloaking [6] and super-anisotropy [2, 3]. The transmission of acoustic waves with frequencies near the Dirac point through two-dimensional PnCs,

pseudo-diffusion behavior and the Zitterbewegung effect, all of which have equivalent counterparts in photonics, have been demonstrated [2, 3]. The phenomena in photonics and phononics are equivalent in many respects. Hence, it is understood that the photonics [6] counterpart of accidental degeneracies at the center of the BZ (i.e., at $\vec{k} = 0$) should also exist in phononics. These works have recently shown that at $\vec{k} = 0$, accidental degeneracy may result in a triple degenerate eigenstate, having two linear bands that form a cone and a nearly flat band that passes through the tip of the cone. This result a conical singularity at the center of the BZ [6]. Despite having linear bands for both Dirac points at the Brillouin boundary (the K point) and at the center of the BZ (the Γ point), they apparently do not reflect the same physics. In photonics, the Dirac point at the center of the BZ occurs due to accidental degeneracy, which is why the point at the BZ boundary is called the Dirac point, and the linear dispersion is called the Dirac cone. In contrast, in phononics, the point at the center of the BZ is called the 'Dirac-like point' and the dispersion cone is called the 'Dirac-like cone' [2, 4].

To simulate the quantum Hall effect (topological insulator) equivalent to the spinning electrons inside the material and the propagating waves around the boundary of the material block, a recent study proposed circular air duct PnCs in which air flow can be rotated by injecting a forced air flow, which is a counterpart to the magnetic field in phononics [30]. This study was a successful attempt to create a Dirac-like cone, albeit through a complicated approach. It is argued that by using the simplest baseline PnCs (which have already been established for band gap studies), it would be possible to passively generate the Dirac-like cones without the use of an active forced air flow, which

consumes additional energy. This article demonstrates that by pivoting on the 'deaf' band, this prediction can be realized even within the simplest PnC-based system.

In this report, a simple arrangement of cylindrical polyvinyl chloride (PVC) rods as PnCs immersed in an air matrix is considered. This arrangement was previously studied for band gaps and wave bifurcation [31]. With a C_{4v} symmetry, the lattice constant of the unit cell was considered, *a = 1 inch*. The initial arbitrary radius of the resonator was set to *r = 0.193a (11.7% volume fraction)*. The density, Young's modulus and Poisson's ratio of the PVC solid rods were 1760 kg/m^3, 2.9 GPa and 0.4, respectively. Here, we report two Dirac-like cones at the center of the BZ using the same lattice structure by modulating the geometric parameters of the resonator, changing the volume fraction of the PVC in the air matrix. The numerical results indicate that these Dirac-like cones are formed due to a triple degeneracy, which simultaneously contains double and single degenerate states when these degenerated bands show linear dispersions at $\vec{k} = 0$. Notably, a flat branch passes through each of these degenerate points with zero or approximately zero group velocity. Due to the breaking of symmetry [32], we have shown that this flat branch does not transport any acoustic energy in the direction of propagation and, instead, exhibits spatial localization. Due to this non-transporting acoustical deafness behavior, this central flat band has been termed the 'deaf' band [32-34]. When a plane wave is incident on the PnCs, this flat band shows an antisymmetric acoustic mode shape with respect to the direction of incidence. The deaf band is a consequence of the zero-effective density of the system and is only excited with the incidence of nonzero k-parallel components [32]. In this work, we present a predictive nature of accidental degeneracy yielding Dirac-like dispersions that exploit the properties of the 'deaf' band. Here, we present the design of generation, modulation and

control over Dirac-like cones. In addition, the acoustic pressure field distributions are demonstrated over a range of Dirac frequencies [35-37]. Despite a similar band structure presenting at different Dirac-like points, we demonstrate dissimilar behaviors at two Dirac frequencies. Using the first Dirac frequency, we show that the incident wave on the proposed PnCs is transported at an orthogonal direction, as predicted by the dispersion mode shapes. Furthermore, two 45° symmetric bent lines are observed to leave a non-propagating zone that is insulated from the defects in the PnCs. However, at the second Dirac frequency, a spiral wave is observed that repeats the convergence and divergence of the acoustic pressure fields in the orthogonal directions with respect to the incident plane wave. Following the numerical simulations, an experimental setup was realized to verify the acoustic properties of the proposed structure. A good agreement was found between the numerical and experimental outcomes. Experimental verification confirms the existence of Dirac-like cones at the predicted frequencies.

Doubly degenerated Dirac cones were found at the intersection of two bands at the corners of the Brillouin zone [1], i.e. at the *M* and *K* points, in triangular and hexagonal honeycomb metamaterials. However, the occurrence of degeneracies at the Γ-point is purely accidental and there was no guideline where it would occur along with the frequency band. Hence, a challenge in phononics remains to find a Dirac cone at the center of the Brillouin Zone which happens only due to accidental degeneracy. A common feature was found to have a triple degenerate eigenstate with a flat band and a conical singularity. Since the physics of Dirac cone is largely influenced by its location at BZ, Dirac cone at Γ-point is referred as ‘Dirac-like cone”[2]. In photonics, regardless of the type of degeneracy [38], a non-zero mode coupling integral between the degenerate Bloch states guarantees the

Dirac-like point. In phononics, a recent study [30] on tunable topological PnCs has demonstrated the quantum Hall effect in acoustics. A Dirac-like cone was generated by rotating the airflow, mimicking the magnetic field counterpart in phononics. This method needs additional energy to create a Dirac-like cone at the center of the Brillouin zone. However, without this requirement, with the simplest baseline PnCs, recently it is shown that a 'deaf-band' based predictive model can help generate the Dirac-like cones. The philosophy of pivoting 'deaf-band' based workflow along with the features of a Dirac-like cone generated at one of the frequency regions called 'Region A' is presented by us in ref [39].

To control the width of the tunable phononic band gaps numerous approaches are described in the literature by placing inclusions at well-defined places. It was previously reported that complete acoustic band gaps can be artificially increases by removing band degeneracies. It was achieved by manipulating doubly or triply degenerated bands and maneuvering spectral responses. However, using the same process achieving Dirac like cones is not only rare but is extremely difficult. Although the quest for Dirac-like cones proliferated in past few years [40], periodic composite materials are demonstrated to obtain complete acoustic band gaps in air media. Apart from rigid cylinders in fluid [41, 42], various geometrical unit shapes with different lattice structures were studied [43, 44]. Such studies demonstrated the correlations between the lattice symmetry and complete acoustic band gaps. The tuning process was adopted to lift/move certain bands to enhance the band gaps. Investigations on square inclusion in air medium were reported with a prime focus on complete acoustic band gaps. Tuning techniques are reported multiple times, especially to widen complete acoustic band gaps by decoupling degenerated states. Goffaux et al. [45]

reported the progressive widening of complete acoustic band gaps by tuning a hard square rod immersed in an air matrix by rotating the rod with respect to the initial lattice orientation. Other studies reported square inclusion in air with an intention of breaking degeneracies to yield band gaps [46-49]. In this study, we report that exploiting similar square geometric tuning, researchers missed the opportunity to observe more than one triply degenerated point, the Dirac-like cones reported herein. Predicting Dirac phenomena is challenging. Triple degeneration due to accidental degeneracies makes them difficult to predict. However, defying the convenient methods, deaf band-based tuning is demonstrated in this article to obtain multiple Dirac-like points at two different energy states. A deaf band-based predictive model was recently proposed to control Dirac cones [50, 51], which is further understood and enhanced in this article.

Traditionally occurrence of Dirac-cone is linked with quantum Hall effect. In this section, we discuss different quantum Hall phenomena that require Dirac cones. The traditional quantum Hall effect (QHE) requires active control of the metamaterial [52] through external fields that help break the time reversal symmetry. In phononics, breaking the time reversal symmetry is difficult due to the inherent nature of acoustic waves and can be achieved only through artificial control [53]. Alternatively, the quantum spin Hall effect (QSHE) preserves the time reversal symmetry and does not require any active external fields [54]. These states are generated through quadruple degeneracies forming double Dirac cones. To date, the QSHE is restricted to only one energy state and/or one unique frequency. The manipulation of wave guiding was further achieved by symmetry reduction of the crystals, removing the band degeneracies and allowing directional band gaps [41, 55]. Continuous time modulation of stiffness is responsible for these states. Alternatively,

as evident from the QSHE, wave guiding in a specific direction at specific frequencies can be one of the major applications of Dirac cones without breaking the symmetry. Any accidental threefold degenerate Bloch mode generating any high symmetry point yields Dirac cones [40]. Multifold degeneracy occurs due to periodic symmetry of hard inclusions hosted in a matrix. This phenomenon has been meticulously reported at the edge of the Brillouin zone (BZ) at the K and K' points. This is commonly known as the topological edge effect concurrent with the quantum valley Hall effect (QVHE). The QVHE is demonstrated using many structures [10, 56] with C_3 symmetry. Although time reversal symmetry is preserved to achieve the QVHE, space invariant symmetry must be broken to create an edge state around the domain wall. None of these phenomenon (QSHE or QVHE) are demonstrated at the center of the BZ or at the Γ point except C6 symmetry based QSHE in photonics [57]. Moreover, structural designs to obtain edge states are permanent and cannot be tuned to generate other bulk states. Bulk-boundary distinctions are permanent per the design. Using active QHE modalities, it is possible to regain the original state when active perturbation is lifted. Topological optimization has also recently been studied where genetic algorithm has been exploited to obtain acoustic Dirac cones and topological insulators as well [58]. However, these situations are not possible at simultaneous multiple acoustic frequencies. Using these two different scenarios, researchers are seeking an alternative approach in which Dirac phenomena can be achieved at multiple frequencies neither by permanent breaking of the space invariant symmetry nor by breaking the time reversal symmetry via active energy, such as rotating spinning rotors or fluids. Dirac cones at the center of the BZ create such an opportunity; however, generating these phenomena at the center of the BZ is challenging. This because the periodic insertions reshape the

spectral responses, especially when their elastic density is very high compared to other constituents. This often happens for solid inclusions in fluid matrices.

Dirac-like cones that occur at the center of the BZ (Γ point) contain a doubly degenerate state containing two intersecting linear dispersion bands and an additional single flat band, forming a three-fold degeneracy that has a linear dispersion at $\vec{k} = 0$. Among three degenerated bands, there is a flat band which passes through the degenerated point. The band has inherently an antisymmetric mode shape and zero or minimal group velocity. Because it is nearly flat and has no group velocity with antisymmetric mode shape, it exhibits spatial localization allowing minimum acoustic energy to transport through PnCs along the direction of incidence. Bands exhibiting this non-transporting acoustical deafness behavior are called deaf bands. Deaf bands play a major role in increasing and reducing the band gap above or below the respective band. It also help degeneration from non-degenerate modes [51]. Due to an anti-symmetric acoustic mode shape with respect to the direction of the incident plane wave, it can only be excited by the incident non-zero k-parallel components [34, 59]. The tuning techniques previously proposed by researchers required total replacement of the PnCs due to the required changes in their geometrical dimensions. In this article, we propose a deaf band-based predictive modeling and tuning technique avoiding the shape optimization process, in which replacement of the inclusions is not necessary. Instead of cylindrical inclusions, square-section rods hosted in air matrix distributed in a square lattice arrangement is proposed. *As it needs no additional insertions, the tuning technique proposed herein is based on a predictive static rotating mechanism of PnCs that is neither permanent (like it is for QSHE and QVHE) nor requires any continuous energy consumption (as required for the QHE),*

providing enormous possibilities for acoustic wave guiding on demand, acoustic computing, pseudo-diffusion, need-based acoustic cloaking, or ballistic wave transmission. These phenomena will be valuable for engineering and biomedical applications.

Moreover, a spin modulated topological state has been reported and discussed thoroughly, capable of unique wave propagation behavior. Deaf band based modeling of such system is generated and analyzed to obtain the physics behind the phenomenon. Acting almost like the counterpart of the widely discussed Topological insulator, our setup, named as Topological Blackhole (TBH) allows wave to travel through the periodic metastructures with zero edge state perturbance. Changing the waveguide shape and size preserves the topology of the system, turning it as a robust topological system. Alike acoustic blackhole researched widely for past few years, this topological blackhole will open a new sector to the field of acoustics wave propagation.

In this thesis, we present a comprehensive study on the behavior of Dirac-like cone in PnCs in acoustic media for another frequency region. We proposed an arrangement of Polyvinyl Chloride (PVC) cylindrical rods as PnCs with variable physical parameters, immersed in the air that was previously studied for band gaps and wave bifurcation. Here two Dirac-like cones have been reported for the same lattice at the center of the Brillouin Zone by modulating the physical parameter of the resonator of which, one of them is emphasized in this article as the rest has been explained and reported earlier in ref [39]. A predictive nature of accidental degeneracy yielding Dirac – like dispersion depending on a flat dipolar band, named as deaf band, has been presented. Acoustic pressure field distribution has also been demonstrated over a range of different Dirac frequencies. Despite similar band structure at multiple Dirac-like points, we observed different behaviors at

different Dirac-like points. Orthogonal wave transportation has been observed for one of the Dirac-like points. However, at the second Dirac-like cone a spiral wave-guiding phenomenon, having repeated convergence and divergence in the orthogonal direction, has been generated. Two 45° symmetric bent lines during the orthogonal transport, leaving an undisturbed zone that is insulated from PnCs defects are shown. Although not demonstrated, the undisturbed zone or the 'No Zone' is realized for the potential application of acoustic cloaking. We also have guided this research in obtaining a new phenomenon, named as TBH, acquiring bulk propagation through periodic materials, acting as a waveguide. Initial theory behind the principle of this system has been discussed in detail.

The organization of the study is given below:

Chapter 1: Describes the target and the necessities of this work. This chapter also describes the corresponding background and the state-of-the-art technologies

Chapter 2: This chapter has four primary sections. In the first section, analytical derivation to find the dispersion curves for the periodic media mentioned above is presented. Also, a deaf band-band based predictive Dirac-like point modeling of resonator has been proposed to predict the occurrence of triple degeneracy and dedicated to two Regions of Dirac-like cones in the dispersion curve. We present and explain the orthogonal wave transport phenomena at the Dirac-like frequencies in the PnCs, which are predictively identified. Here we have showed multiple Dirac-like point behavior under plane wave actuation condition. Numerical and experimental validation and study has been portrayed also.

Chapter 3: The third chapter is regarding generation of dual-Dirac points by using angle orientation tuning. This chapter has 3 primary sections. In Section I, we have discussed the analytical approach for the dispersion relationship of a circular resonator, In Section II, numerical study along with waveguiding phenomena at Dirac-like frequency of region B has been addressed. In Section III, the transmission properties are validated using experimental analysis.

Chapter 4: This chapter describes the tunable dependency between acoustic deaf band modes and rotation of a solid square rod with respect to the lattice orientation. To confirm the emergence of Dirac cones at the center of the BZ at multiple frequencies, we observe the orthogonal guidance of elastic waves through PnCs near Dirac frequencies. To explore if the design, such as length width of the megastructure and placement of PnCs have any role on the wave behavior at the Dirac cone, different modes of orthogonal and longitudinal transports are investigated. The method of finding the band structure for composite media and numerical models are briefly reported in Section II. The numerical results are discussed in Section III. Experimental validation is presented in Section IV.

Chapter 5: In this chapter, Hermitian Dirac-like cones are proposed for creating acoustic logic gates herein. The predictive phenomenon of creating Dirac-like cones near a bipolar antisymmetric deaf band was found to be useful for acoustic computing of Boolean algebra. Unlike previous approaches Dirac-like cone creates exclusive opportunity to perform all possible Boolean algebra computation with valid inputs. The phenomenon is demonstrated in two-dimensional Phononic Crystals (PnCs) consisting of tunable square columns in air media. By predictive tuning of the deaf bands, we report to form a triply to doubly degenerated Dirac-like cone, particularly useful for acoustic

computing. It is only possible when a bottom band has a negative curvature. But that is lifted from a nearby doubly degenerated band with positive curvature, which is again degenerated with a deaf band. On the contrary similar computing possibilities are difficult when the bottom band degenerates with the deaf band, and the top band is lifted. Utilizing these phenomena, acoustic logic gates are designed to perform Boolean algebra through AND, NAND, OR and NOR gate operations. A simple one degree of freedom and a complex six degrees of freedom systems are proposed and demonstrated, where simple rotation of the PnCs activates a specific gate.

Chapter 6: In this chapter, development of a unique and intriguing wave propagation feature has been described, termed as "Topological Acoustic Black-holes (TBH)". Deaf band modulated unique bulk propagation mode is observed and discussed in detail. TBH, a counterpart of topological insulator, permits energy transportation through the bulk of periodic metastructures, without interrupting the edge states. Moderately higher robustness with preserved topology makes the system very unique and a completely new technique. Spin dependent topology protection explains the principle behind the phenomenon and is tailorable to attain multiple benefits out of the system. In addition to the proposed numerical models for novel topologically protected mechanism, few innovative applications of the proposed models are also presented.

Chapter 7: Summarizes the contributions of this work and finally conclude the dissertation with future prospects and development of this research.

CHAPTER 2

DEAF BAND-BASED ENGINEERED DIRAC CONE – I

In this study, the principal aim is to demonstrate the feasibility of designing a phononic crystal based periodic metamaterials, comprising of the capability of generating multiple Dirac-like cones to exploit extra-ordinary wave dispersion behaviors due to Dirac point properties. Here, we report two Dirac-like cones at the center of the BZ using the same lattice structure by modulating the geometric parameters of the resonator, changing the volume fraction of the PVC in the air matrix. The numerical results indicate that these Dirac-like cones are formed due to a triple degeneracy, which simultaneously contains double and single degenerate states when these degenerated bands show linear dispersions at $\vec{k} = 0$. Notably, a flat branch passes through each of these degenerate points with zero or approximately zero group velocity.

2.1 ANALYTICAL THEORY

It is reported that the plane wave expansion method in a 3D periodic structure in a solid-fluid medium with spherical PnCs is not convenient [60-63] due to convergence issues with a smaller number of expansions. However, with increasing computing facility and by using a larger number of expansions, one could obtain convergence with careful sorting of the eigenmodes and proper definition of the structural factor [64]. In this study, long cylindrical PVC rods arranged in an air matrix are considered, in which the wave modes propagating in the x-y plane orthogonal to the axis of the cylinders (i.e., the z-axis) are decoupled from the waves in the z-direction and the analysis remains 2D. Such

conditions were solved with the plane wave expansion method and were proved to be accurate in Al/air [65] and PVC/air [66, 67] systems, by incorporating a sufficiently large number of reciprocal space vectors. The study reported in Ref [66] utilized the plane wave expansion method and was thoroughly verified [16] using finite element method simulation. The analytical solution of wave dispersion in a periodic structure formed by solid circular PnCs in an air medium was previously studied using the plane wave expansion method and is briefly reviewed herein.

The governing differential equation of wave motion in any medium can be written as

$$\sigma_{nl,l} + f_n = \rho \ddot{u_n} \qquad (1)$$

Utilizing standard index notations, we define $\sigma_{nl,l}$ as the derivative of the stresses with respect to the l^{th} direction, f_n as the body force in the n^{th} directions, ρ as the density of the material and $\ddot{u_n}$ as the acceleration in the n^{th} direction. In a PVC-air setup, this results in two governing differential equations.

Applying the Bloch-Floquet condition [68] in reciprocal wave number space and adding $G_1 = \frac{2\pi j}{D_1}$ and $G_2 = \frac{2\pi m}{D_2}$ with the eigenvalue wave number, we obtain the Bloch-Floquet displacement function as follows:

$$u_1(\mathbf{x}, t) = \sum_j \sum_m A_{jm} e^{i\mathbf{k}.\mathbf{x}} e^{i\mathbf{G}.\mathbf{x}} e^{-i\omega t} \qquad (2)$$

$$u_2(\mathbf{x}, t) = \sum_j \sum_m B_{jm} e^{i\mathbf{k}.\mathbf{x}} e^{i\mathbf{G}.\mathbf{x}} e^{-i\omega t} \qquad (3)$$

where j and m are integers, $\mathbf{G} = G_i \hat{e}_i$ and $\hat{e}_i$ are the Cartesian basis vectors. Similarly, differentiating the displacement function twice with respect to time, the acceleration can be found as follows:

$$\ddot{u_1}(\mathbf{x}, t) = -\omega^2 \sum_j \sum_m A_{jm} e^{i(\mathbf{k}+\mathbf{G}).\mathbf{x}} e^{-i\omega t} \qquad (4)$$

$$\ddot{u_2}(\mathbf{x},t) = -\omega^2 \sum_j \sum_m B_{jm} e^{i(\mathbf{k}+\mathbf{G}).\mathbf{x}} e^{-i\omega t} \qquad (5)$$

where j and m take numbers from -h to +h, where h is also an integer, and D_i = a = lattice constant of the unit cell. The expression in Eq. (2) to Eq. (5) signifies summations over a range of values of j and m.

The stress function in Eq. (1) is the multiplication of the constitutive properties of the medium and the strain function, which can be further derived from the derivative of the displacement functions in Eqs. (2) and (3). Here, the constitutive properties are assumed to be the function of space and are expressed using Fourier coefficients in the periodic medium. Hence, applying the Fourier transform on the constitutive function and writing $C_{ts}(x)$ in terms of C_{ts}^{pq}, we obtain

$$C_{ts}(x) = \sum_{p=-h}^{h} \sum_{q=-h}^{h} C_{ts}^{pq} e^{i\left({}^{2\pi p}/_{D_1} x_1 + {}^{2\pi q}/_{D_2} x_2\right)} = \sum\sum C_{ts}^{pq} e^{i\mathbf{G_{pq}}.\mathbf{x}} \qquad (6)$$

Similarly, the derivative of the constitutive function with respect to space x_l can be written as follows:

$$\frac{\partial C_{ts}(x)}{\partial x_l} = (-1)^{l+1} \sum\sum i C_{ts}^{pq} \, 2\pi[p(2-l) + q(1-l)] \Big/ D_l \, e^{i\mathbf{G_{pq}}.\mathbf{x}} \qquad (7)$$

where $C_{ts}^{pq} = \frac{1}{A_c} \int C_{ts}(x) \; e^{-i\mathbf{G_{pq}}.\mathbf{x}}$

and can be expressed as

$$C_{ts}^{pq} = \zeta_{air} \delta_{G_{pq}0} + (\zeta_{PVC} - \zeta_{air}) F(G_{pq}) \qquad (8)$$

where, ζ is the volume fraction of the respective constituent medium, δ is the Kronecker delta symbol, $F(G_{pq})$ is the structure factor of PVC in air and can be expressed as [64] $2fJ_1(G_{pq}r)/G_{pq}r$, where J_1 is the Bessel function of the first kind, and r is the radius of the PVC rods.

Substituting Eqs. (2) to (7) into Eq. (1), we obtain two equations as follows:

$$\sum_j \sum_m \sum_p \sum_q \Bigg[A_{jm} C_{11}^{pq} e^{i(\mathbf{k}+\mathbf{G_{pq}}+\mathbf{G_{jm}}).\mathbf{x}} \left(k_1 + \frac{2\pi j}{D_1}\right)\left[-k_1 - \frac{2\pi j}{D_1} - \frac{2\pi p}{D_1}\right] +$$

$$\frac{1}{2} A_{jm} C_{66}^{pq} e^{i(\mathbf{k}+\mathbf{G_{pq}}+\mathbf{G_{jm}}).\mathbf{x}} \left(k_2 + \frac{2\pi m}{D_2}\right)\left[-k_2 - \frac{2\pi m}{D_2} - \frac{2\pi q}{D_2}\right] + B_{jm} C_{12}^{pq} e^{i(\mathbf{k}+\mathbf{G_{pq}}+\mathbf{G_{jm}}).\mathbf{x}} \left(k_2 +$$

$$\frac{2\pi m}{D_2}\right)\left[-k_1 - \frac{2\pi j}{D_1} - \frac{2\pi p}{D_1}\right] + + \frac{1}{2} B_{jm} C_{66}^{pq} e^{i(\mathbf{k}+\mathbf{G_{pq}}+\mathbf{G_{jm}}).\mathbf{x}} \left(k_1 + \frac{2\pi j}{D_1}\right)\left[-k_2 - \frac{2\pi m}{D_2} - \frac{2\pi q}{D_2}\right] \Bigg] =$$

$$-\rho\omega^2 \sum_j \sum_m A_{jm} e^{i(\mathbf{k}+\mathbf{G}).\mathbf{x}} e^{-i\omega t} \qquad \ldots\ldots (9)$$

$$\sum_j \sum_m \sum_p \sum_q \; A_{jm} C_{21}^{pq} e^{i(\mathbf{k}+\mathbf{G_{pq}}+\mathbf{G_{jm}}).\mathbf{x}} \left(k_1 + \frac{2\pi j}{D_1}\right)\left[-k_2 - \frac{2\pi m}{D_2} - \frac{2\pi q}{D_2}\right] +$$

$$+ \frac{1}{2} A_{jm} C_{66}^{pq} e^{i(\mathbf{k}+\mathbf{G_{pq}}+\mathbf{G_{jm}}).\mathbf{x}} \left(k_2 + \frac{2\pi m}{D_2}\right)\left[-k_1 - \frac{2\pi j}{D_1} - \frac{2\pi p}{D_1}\right] +$$

$$+ B_{jm} C_{22}^{pq} e^{i(\mathbf{k}+\mathbf{G_{pq}}+\mathbf{G_{jm}}).\mathbf{x}} \left(k_2 + \frac{2\pi m}{D_2}\right)\left[-k_2 - \frac{2\pi m}{D_2} - \frac{2\pi q}{D_2}\right] +$$

$$+ \frac{1}{2} B_{jm} C_{66}^{pq} e^{i(\mathbf{k}+\mathbf{G_{pq}}+\mathbf{G_{jm}}).\mathbf{x}} \left(k_1 + \frac{2\pi j}{D_1}\right)\left[-k_1 - \frac{2\pi j}{D_1} - \frac{2\pi p}{D_1}\right] =$$

$$-\rho\omega^2 \sum_j \sum_m A_{jm} e^{i(\mathbf{k}+\mathbf{G}).\mathbf{x}} e^{-i\omega t}$$

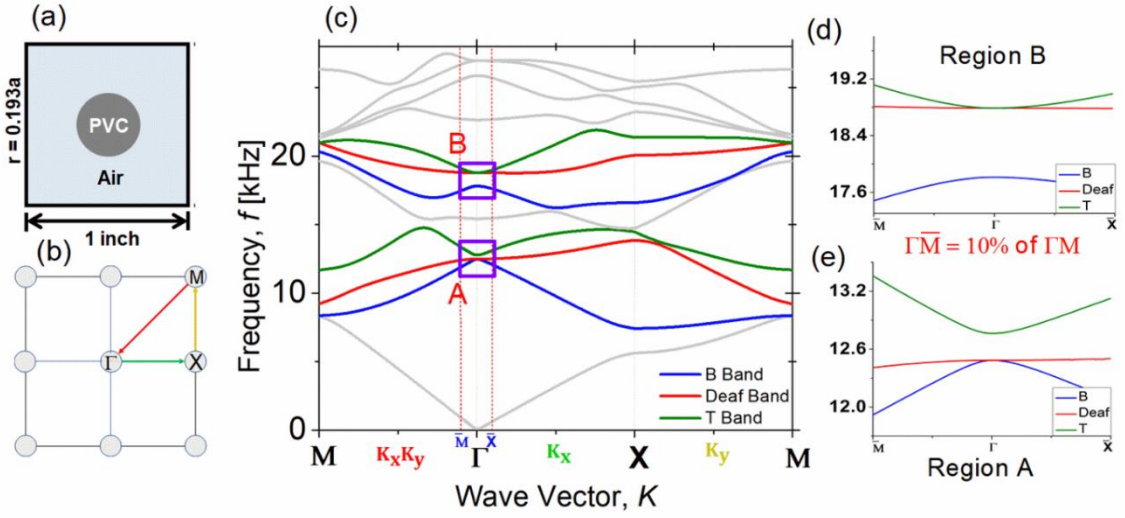

Figure 2.1: (a) A single lattice of a = 1 inch and r=0.193a, (b) BZ depicting reduced wave vector direction, (c) Band structure for the unit cell, (d) Band structure of the unit cell, showing 'Region A' and 'Region B', with two possible Dirac-like degenerated point, (b) and (c) Zoomed in view of 'Region A' and 'Region B'.

.(10)

Mathematical simplification of Eq. (9) and Eq. (10) results in an eigenvalue problem, and the size of the matrix depends on the number of reciprocal space vectors used in the expansion. In this study, 532 reciprocal space vectors were used in the plane wave expansion, and the dispersion curves were verified with the results using the finite element method obtained from a COMSOL Multiphysics 4.3 simulation to ensure convergence.

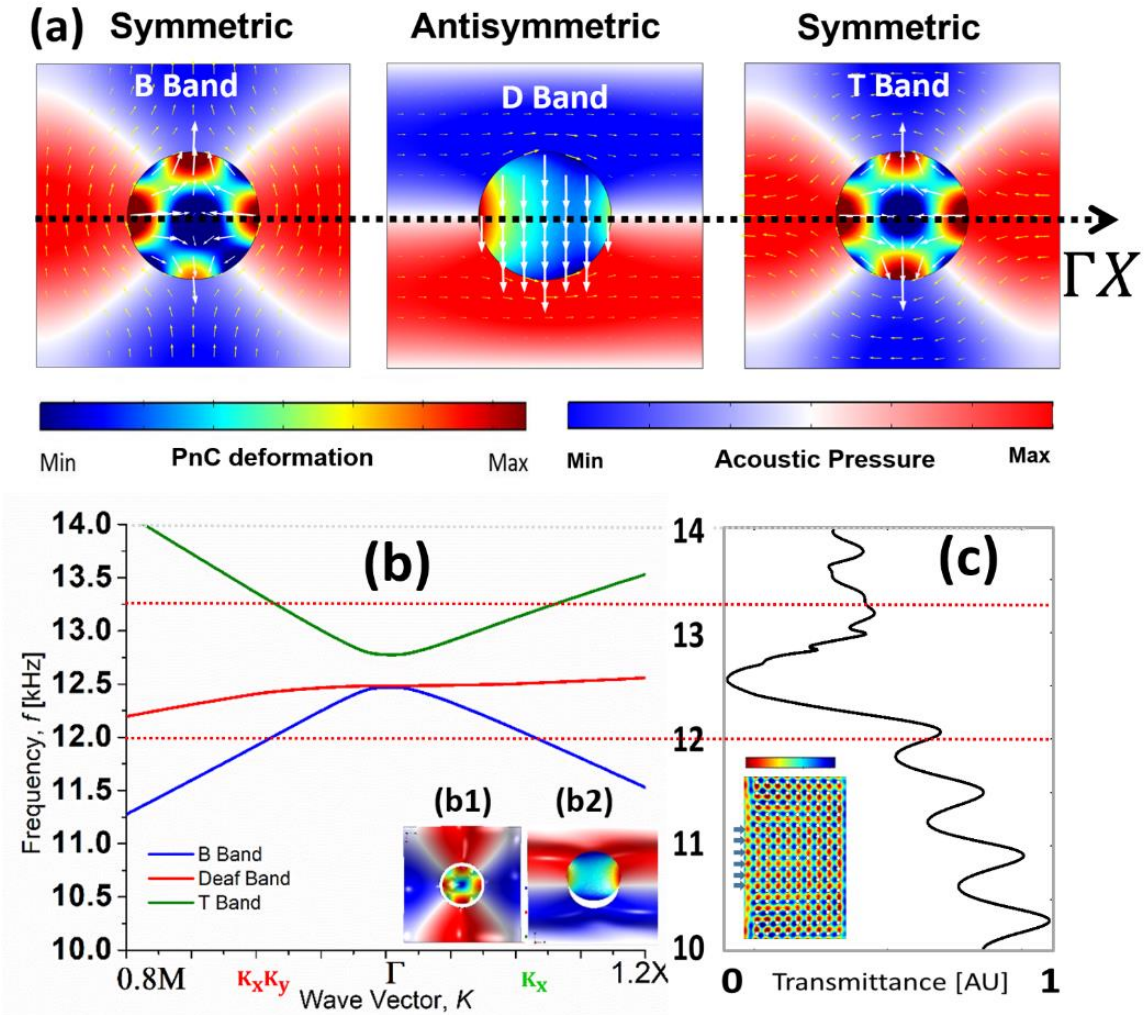

Figure 2.2: a) The 'B', deaf' and 'T' band mode shapes of the PVC cylinder surrounded by the air pressure mode shapes with arrows, b) Band structure before tunning, identified near Region A. b1) Deformation of the air matrix and the PVC cylinders for the 'B' band, b2) deformation of the air matrix and the PVC cylinders for the 'deaf' band, c) numerical calculation of the transmittance through a 15x9 cell of PVC/air matrix, showing almost zero transmission near the 'deaf' band.

The dispersion behavior in the PVC/air matrix is shown in Figure 2. **1,** where the frequency bands of the possible Dirac-like cones are identified at 'Region A' and 'Region B'.

2.2 DEAF BAND-BASED PREDICTIVE MODULATION OF PNCS

Unlike systematic essential degeneracies, accidental degeneracy depends on the geometric parameters of the system. The term 'accidental' indicates two eigenfunctions belonging to the bases of two different irreducible representations that correspond to the same level of energy. Although geometrically symmetric, in the case of accidental degeneracy, the obvious equivalent configuration of the irreducible representations is not always guaranteed. Hence, accidental degeneracy and the generation of the double or triple degeneracy occurs at certain specific configurations that remain unknown. In this article, a 'deaf' band-based nearly predictive nature of the accidental degeneracies at the Dirac-like points is proposed for the case in which the 'deaf' bands are identified from the dispersion behavior utilizing an arbitrary geometric structure.

First, the possible frequency regions at the Γ (where the wave vector $\vec{k} = 0$) point are identified based on the 'deaf' bands. From the frequency-wavenumber plot for PnCs (*r = 0.193a, 11.7% volume fraction)*, the trends necessary to generate probable Dirac-like points at different frequencies are determined. In this study, we identified two probable points near ~12.5 kHz and ~18.5 kHz where the possibility of obtaining a Dirac-like phenomenon was obvious because of the existence of two double degenerate states. We named these regions 'Region A' and 'Region B'. More specifically, 'Region A' was within the band of ~11.7 – 13.5 kHz, and 'Region B' was within ~17.5 – 19.7 kHz, as shown in Figure 2.**1**. The top and bottom bands in 'Region A' and 'Region B' are named 'T' and 'B', respectively, with respect to the 'deaf' band. The acoustic pressure mode shapes with

the deformation of the PVC rods are presented in Figure 2.**2a** for the ‘T’, ‘B’ and ‘deaf’ bands. Investigating the air pressure wave modes of ‘T’, ‘B’ and the ‘deaf’ band, it can clearly be seen that ‘T’ and ‘B’ (two orthogonal quadrupole mode) has proper symmetry that can be excited by an incident plane wave along the ΓX [100] and XM [010] directions, whereas the ‘deaf’ band mode (dipolar) is antisymmetric, with almost zero group velocity along the incident wave direction. The deformation pattern of the PVC rods from the height expression (Figure **2.2b1** and **2.2b2**) for the ‘deaf’ band is actually dominated by the deformation of the rods along the incident direction with a very small translation (Figure **2.2b2**) along the XM direction, which is orthogonal to the ΓX. In contrast, for the ‘T’ and ‘B’ bands, the PVC rods exhibit quadrupole deformation with a reduced radius but without translation along any direction (Figure **2.2b1**). Thus, the ‘deaf’ band cannot be excited by the normal-incident plane wave due to asymmetry. Moreover, superposition of the air pressure of the ‘T’ and ‘B’ bands near the possible Dirac frequency may overlap to cause reduced transmission of the incident wave. A sample domain of 15 x 9 block of PnCs before tuning (i.e., with *r = 0.193a, 11.7% volume fraction*) is investigated numerically within the band 10 kHz – 14 kHz. Although the zero group velocity band starts at ~12.55 kHz, the transmission begins to decrease to less than 50% at frequencies close to ~12.0 kHz. The transmission further decreases to almost zero due to the asymmetric ‘deaf’ band, although there is no band gap along the ΓX [100] direction. Here, we call the nearly zero group velocity band the ‘deaf’ band as previously identified in Ref [32-34].

2.3 GEOMETRIC TUNING

From Figure 2. 1, it is intuitive that if band ‘T’ in ‘Region A’ is moved downward and band ‘B’ in ‘Region B’ is moved upward, triple degeneracies are possible. Hence, optimizing or tuning the geometric parameter could lead to the dispersion modes aiming to generate an accidental triple degeneracy. Although it was shown that this antisymmetric mode cannot be excited [32, 62] in the incident direction, we found that after tuning at the Dirac-like cone frequency, due to the triple degenerate state, waves begin to propagate along the orthogonal direction, maintaining the antisymmetric pattern along the incident

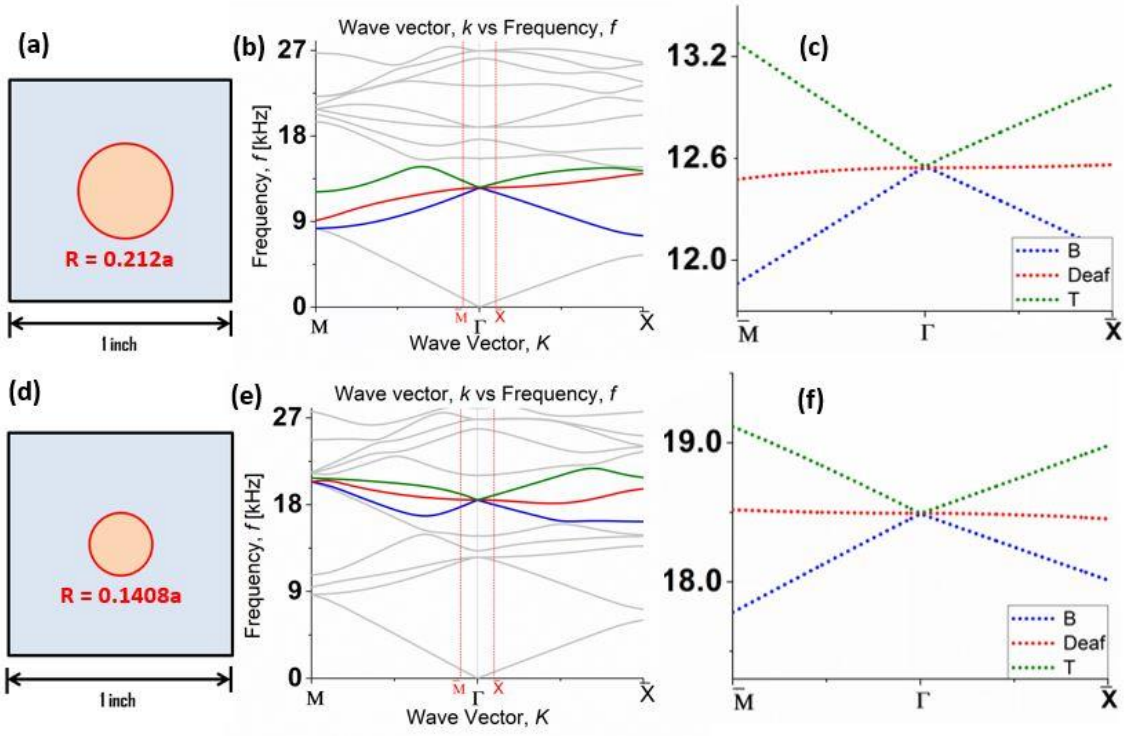

Figure 2.3: Accidental degeneracy at ‘Region A’ and ‘Region B’. (a) A unit cell for region ‘A’ with PnCs of radius r = 0.212a in air matrix, (b) dispersion relation for region ‘A’ after increasing the radius r = 0.193a to r = 0.212a where the ‘T’ band is lowered with respect to the ‘deaf’ band and having an accidental degeneracy for the frequency f = 12.551 kHz, c) magnified view of the ‘Region A’ Dirac-like point, d) a unit cell for region ‘B’ with PnCs of radius r = 0.1408a in air matrix, (e) dispersion relation after decreasing the radius r = 0.193a to r = ~0.1408a where the ‘B’ band moves upward with respect to the ‘deaf’ band and having an accidental degeneracy for the frequency ω = 18.512 kHz, and f) magnified view of the ‘Region B’ Dirac-like point.

direction, a sharp 45° bent line to the incident wave and the Berry-phase equal to zero [68] at the Dirac frequency.

Close observation of 'Region A' reveals that band 'B' and the 'deaf' band are already merged; however, band 'T' maintains an apparent band gap with the 'deaf' band, as shown in Figure 2.1e. An apparent solution could be lowering band 'T' with respect to the frequency without altering the position of the 'deaf' band, which would result in a Dirac-like point. The geometric parameter, radii in this case, has been optimized and increased from $r = 0.193a$ to $r = 0.212a$ (11.7% to 14.1% volume fraction) of the

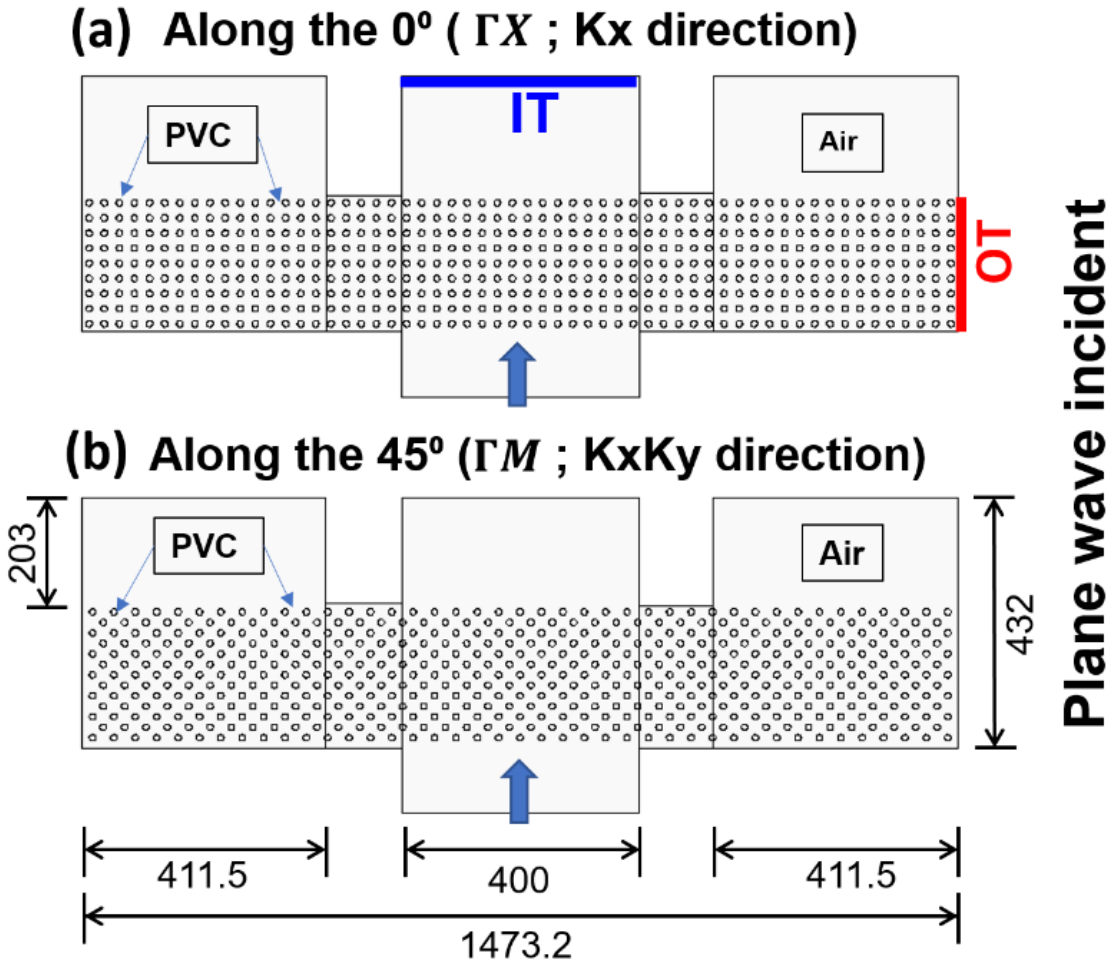

Figure 2.4: Arrangement of PnCs in air matrix for the numerical experiment performed in this article. a) Wave incidence along the ΓX direction, where IT and OT are marked to find the output wave energy at two different locations, and b) wave incidence along the ΓM direction.

resonators. Significant alteration of band 'T' is evident, whereas the positions of the frequencies of the 'deaf' band' and band 'B' remained approximately (~+0.08%) fixed at the Γ point. The dispersion of band 'T' is altered to a local linear dispersion. Two branches of linear dispersion intersect at a triply degenerate point at $\vec{k} = 0$, forming a Dirac-like cone at *f = ~12.551 kHz*. The triply degenerate Dirac-like point in 'Region A' is shown in Figure 2.3a-c.

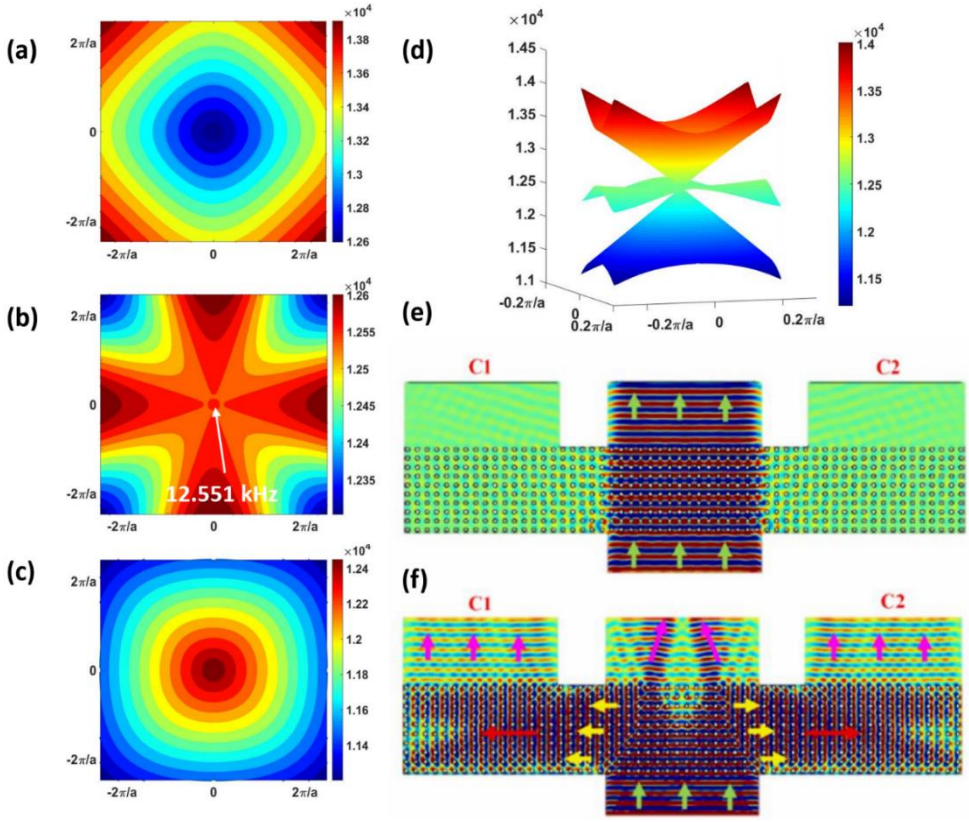

Figure 2.5: (a), (b) and (c) depict the equifrequency surface (EFS) for the 'T' band, 'deaf' band and 'B' band, respectively, for region A. Here, the frequency contour of the Dirac-like frequency appears circular (in (b)), by proving the isometric behavior of the acoustic wave at the Dirac frequency; in contrast, at all other frequencies, the contours are not fully circular anisotropic). (d) An equifrequency contour (EFC) of region A, (E) the absolute acoustic pressure field for a plane wave generated in the ΓX direction for frequencies of f = 10 kHz and f = 12.551 kHz, respectively. Here, it can be seen that while the plane wave was propagating through the PnCs at f = ~10 kHz without changing in direction, the wave has been transported orthogonally in a converging – diverging pattern when propagated at the Dirac-like frequency of f = ~12.551 kHz. After reaching the end of the tunnel, the wave has again turned orthogonally, keeping the plane wave pattern undisturbed along the C1 and C2 channels.

A similar approach was adopted for ‘Region B’ (Figure 2.1d), in which band ‘T’ and the ‘deaf’ band intersect at the Γ point, forming a local band gap with band ‘B’. Unlike in ‘Region A’, because the gap was between band ‘B’ and the doubly degenerate state, through optimization, the radius of the PVC rods was decreased from *r = 0.193a to r = 0.1408a* (11.7% to 6.22% volume fraction). This decrease resulted in a significant alteration of the dispersion of band ‘B’ in terms of frequency position and formed a local linear dispersion that intersected the ‘deaf’ band. While the frequency position of band ‘B’ has changed, the frequencies of the ‘deaf’ band and band ‘T’ remain very close to the frequencies at which the Γ point was originally detected, within ~1% error; this creates another Dirac-like point at a frequency of *f = ~18.512 kHz*. The triply degenerate Dirac-like point at ‘Region B’ is shown in Figure 2. 3d-f. Notably, in both cases, it is evident that the ‘deaf’ band plays an important role in pivoting the triple degeneracy. Thus, if the radii of the resonators are increased, the Γ point frequency of the ‘T’ band is decreased, whereas if the radii of the resonators are decreased, the Γ point frequency of the ‘B’ band is increased.

2.4 NUMERICAL SIMULATIONS

To prove whether the triply degenerate Dirac-like points are actually achieved through ‘deaf’ band-based geometric tuning, we simulated PnCs made of PVC rods (57 × 10 solid PVC cylinders in an air medium) in two configurations, one with r = 0.212a and the other with r = 0.1408a, using the commercially available COMSOL Multiphysics simulation software, as shown in Figure 2. 4. The actuation of the PnC arrangement was performed by a guided plane wave source located at a distance of 112 mm from the air-PVC interface. As shown in Figure 2.s 4(a) and 4(b), two incidences along (a) 0° (ΓX

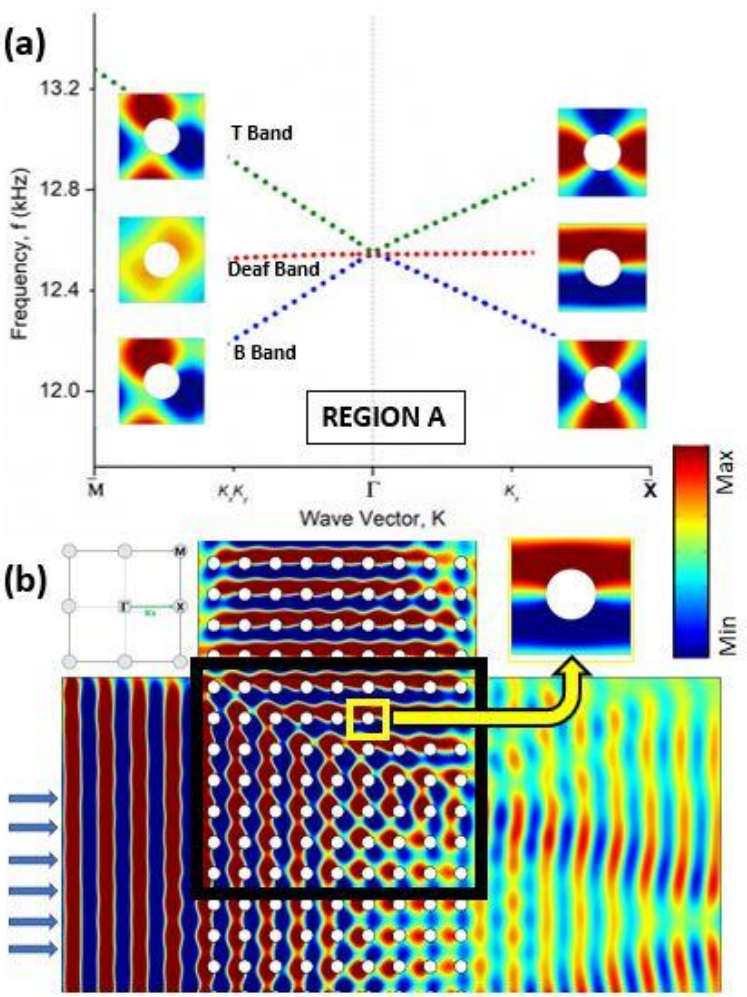

Figure 2.6: (a) Band structure with mode shapes of the 'T', 'deaf' and 'B' bands in the ΓX direction, (b) depicting the resemblance of the acoustic pressure distribution during orthogonal transportation with the ΓX deaf band mode shape, with the direction of excitation being ΓX (given in the inset).

direction) and (b) 45° (MΓ direction), respectively, are studied. A plane wave radiation boundary condition was assumed at all of the boundaries. To demonstrate behaviors such as orthogonal wave transportation and negative refraction at Dirac-like frequency points, two channels, namely, C1 and C2, are created at a distance of ~533 mm from the central line of the central channel, as shown in Figure 2. 4. Although both 'Region A' and 'Region B' demonstrate orthogonal wave transport, each region has its own unique features that are explained through the respective wave dispersion behavior in subsequent sections.

2.5 REGION A: PROOF AND FEATURES OF DIRAC-LIKE CONE

2.5.1 Orthogonal Wave Transportation – Wave incidence along $\boldsymbol{\Gamma X}$

Orthogonal wave transport near the Dirac-like frequencies due to the occurrence of triple degeneracy at the Γ point (wave vector, $\vec{k} = 0$) was achieved. Wave guiding and propagation pattern were studied inside and outside the PnC arrangement (Figure 2. 5) near

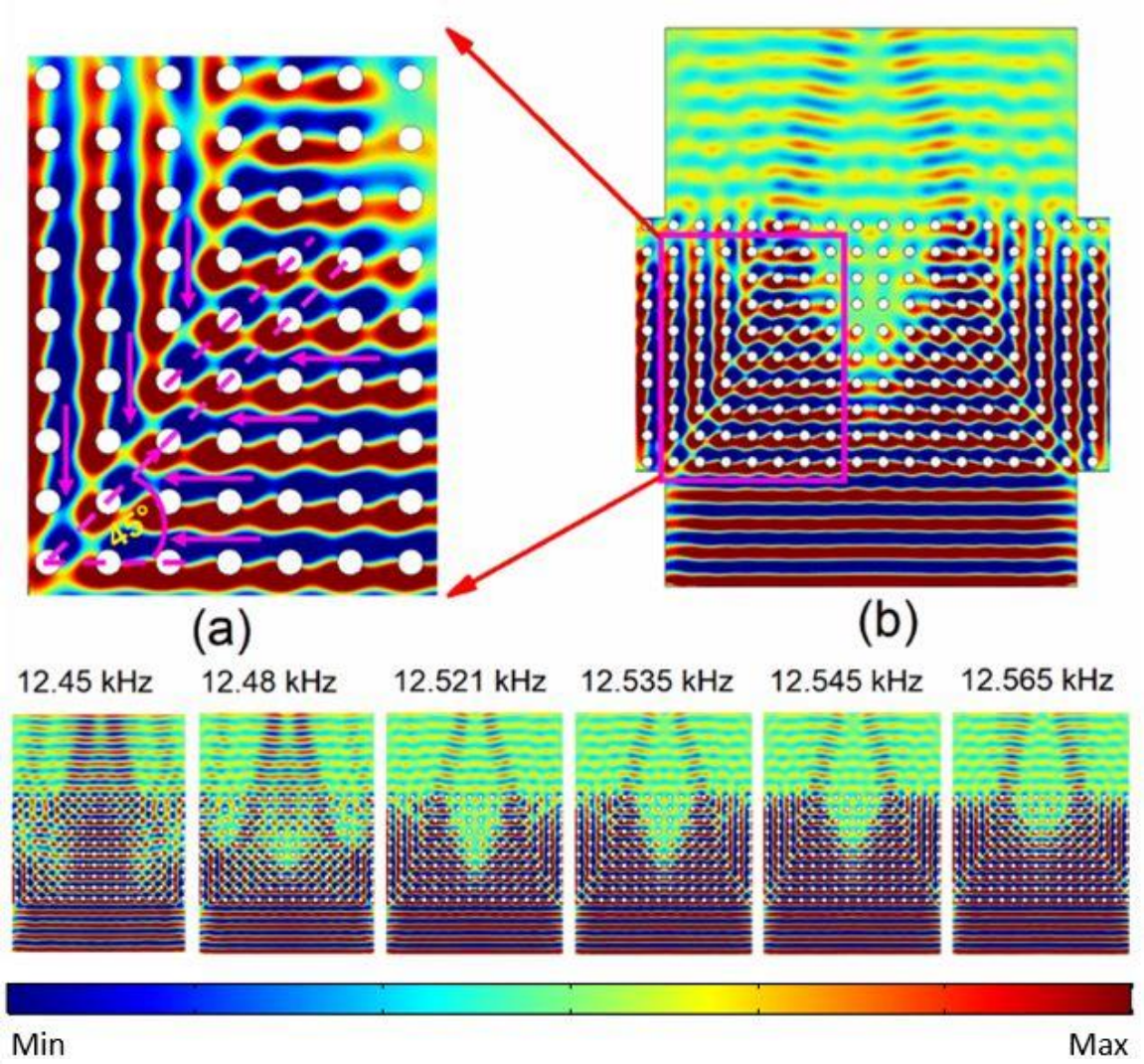

Figure 2.7: (a) The bent line where the plane wave deviates orthogonally maintaining a 45° bent line (marked by pink dotted lines), (b) the same region at lower magnification, showing a 'No Zone' at the convergence point of two bent lines, creating a small region that remains untouched by the plane waves, (c) the gradual formation of the 'No Zone' with increasing frequency toward the Dirac-like frequency in Region A. It should be noted that the largest 'No Zone' was identified at the actuated frequency of f =~12.521 kHz.

the estimated Dirac frequency. Figure 2. 5a-c shows the equifrequency surfaces of the ‘T’, ‘deaf’ and ‘B’ bands, respectively. Figure 2. 5d shows the 3D representation of the Dirac-cone. Figure 2. 5e shows the acoustic pressure field distribution at a frequency 10 kHz, which is slightly below the Dirac frequency. A similar pattern was observed above the Dirac frequency (not shown). This observation is consistent with the phenomena reported in Ref. [3, 6].

Although at frequencies slightly less than or greater than the Dirac frequency, the incident plane wave propagates in the direction of actuation without any distortion, a

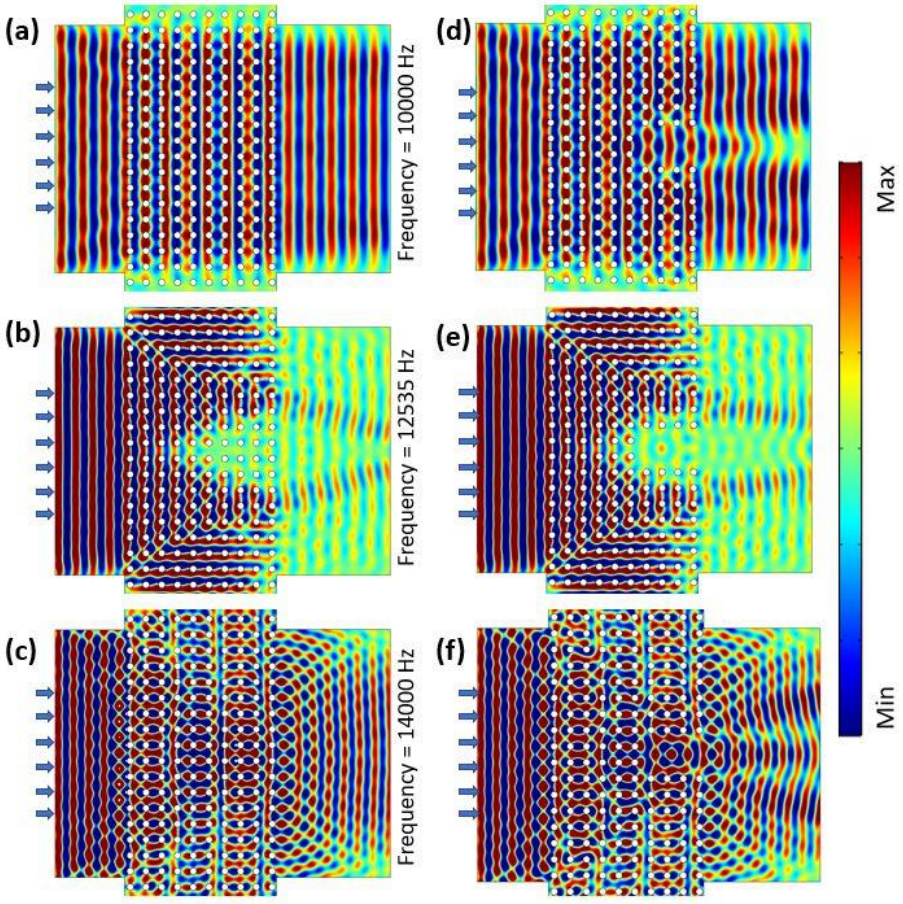

Figure 2.8: The acoustic cloaking phenomenon was observed in (a), (b) and (c), depicting the acoustic pressure field and wave transportation at frequencies of ~10, ~12.535 and ~14 kHz, respectively, showing that the 'No Zone' is evident at f=~12.535 kHz. Now, after removing the PVC PnCs in this particular ‘No Zone’ field, we achieved a similar phenomenon to that shown in Fig. 8c.

drastic orthogonal bent nonetheless can be observed at the Dirac frequency, as shown in Figure 2. 5f. At the Dirac frequency, minimal acoustic energy propagates in the direction of actuation creating a partial band gap-like situation. As the wave propagates inside the

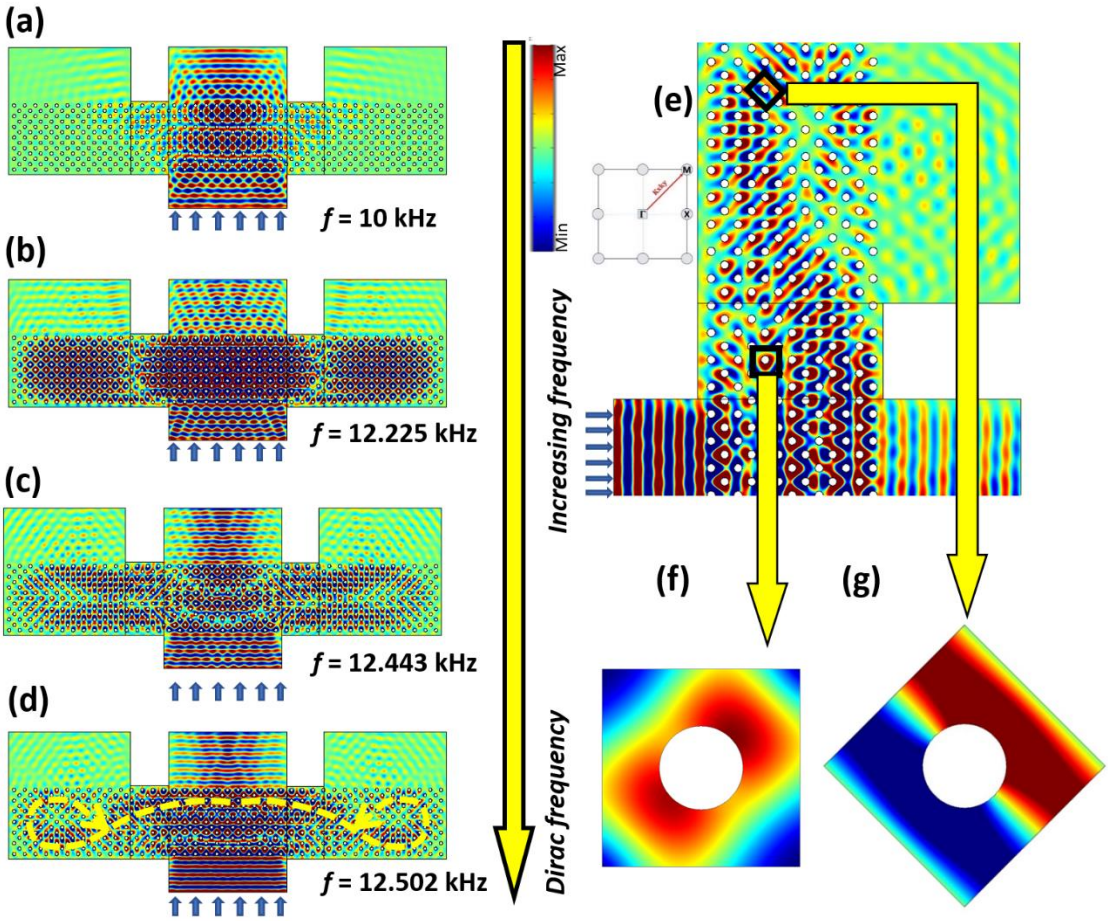

Figure 2.9: Plane wave transportation actuated in the MΓ direction with respect to the PnCs arrangement at different frequencies. Orthogonal wave transport was observed at the frequencies around and at the Dirac-like point. Here, we show the acoustic pressure field of the wave actuated at (a) 10 kHz, (b) 12.225 kHz, (c) 12.443 kHz and (d) 12.502 kHz, e) a close view of the wave field inside the tunnel, f) the weaker 'deaf' band mode along the MΓ direction, g) the strong 'deaf' band mode along the local ΓX direction.

material, the orthogonal transport becomes prominent, leaving a 45° bifurcation, as shown in Figure 2. 5f. In addition, the wave again takes a 90° bend toward the original direction of wave propagation into the C1 and C2 channels, which results from the negative refraction of the wave, creating a negative refractive material at the Dirac frequency.

In general, the ‘deaf’ bands due to the antisymmetric acoustic modes exhibit strong spatial localization and cannot be excited; however, due to the tuned triple degeneracy at the Dirac-like cone frequency, the bands actually maintain their antisymmetric shape to propagate orthogonally.

The reason for this behavior is explained using the local dispersion of the degenerated total absolute acoustic pressure mode shapes at the Γ point (Figure 2. 6a). The ‘T’ band and ‘B’ band mode shapes are quadrupolar modes, orthogonal to each other; in contrast, the ‘deaf’ band mode is a dipolar mode. Hence, at the Dirac frequency, the ‘T’ band and the ‘B’ band nullify each other, keeping the ‘deaf’ band dipolar mode to dominate the propagation of waves in the material. Now, if we look at the wave transmission behavior from the acoustic pressure field at the Dirac-like cone (Figure 2. 6b), to keep the dominant dipolar mode alive, a 45° bent line must develop to carry over the plane wave orthogonally.

2.5.2 Formation of a ‘No Zone’ of Propagation along $\boldsymbol{\Gamma X}$

Figure 2.s 7a and 7b show a magnified view of the acoustic wave field, in which the incident plane waves are transported orthogonally inside the PnCs, leaving two 45° bent lines. As the acoustic energy diverts along these 45° bent lines, some of the unit cells along the direction of propagation remain unaffected by the incoming waves. The region of the PnCs in which no acoustic energy is available is referred to as the ‘No Zone’ in this article. The formation of a ‘No Zone’ begins at ~12.48 kHz, as shown in Figure 2. 7, and the area of the ‘No Zone’ continues to increase as the frequency increases. At ~12.52 kHz, which is close to the Dirac frequency, the largest number of unit cells is unaffected, and hence, the largest area of the ‘No Zone’ is reported.

2.5.3 Acoustic Cloaking - Propagation along $\boldsymbol{\Gamma X}$

Because the 'No Zone' is entirely unaffected by the influence of the incoming or outgoing acoustic energy, the presence or absence of any object placed in this area can hardly be identified. To support this claim, eight PVC cylinders located in a rectangular fashion at the center of the 'No Zone' were removed, and plane waves were excited at 10 kHz, 12.535 kHz and 14 kHz. Figure 2. 8 shows that the wave field is significantly affected at frequencies below or above the Dirac frequency, whereas at the Dirac frequency, the absence of the PnCs at the center of the 'No Zone' has no effect (Figure 2. 8e) on the wave field. This phenomenon has the potential for application in acoustic clocking.

2.5.4 Orthogonal Wave Transportation - Propagation along $\boldsymbol{M\Gamma}$

Next, the incident wave was actuated in the MΓ direction, i.e., along the 45° (numerical setup shown in Figure 2. 4b) with respect to the orientation of the PnCs, by sweeping the frequency between 10 kHz and 13 kHz. Actuating the bottom boundary as shown in Figure 2. 9, it can be seen that the plane wave travels along the direction of actuation below the Dirac-like frequency, f = 10 kHz (Figure 2. 9a). With increasing frequency from the 'Region A', a Dirac-like point emerges, and the wave begins to propagate orthogonally. The orthogonal wave again is transported orthogonally toward the C1 and C2 channels, leaving the leaky plane waves at f = ~12.225 kHz (Figure 2. 10b). However, at f = ~12.443 kHz (Figure 2. 10c) and ~12.50 kHz (Figure 2. 10d), the orthogonally transported waves have different behaviors compared to the incident wave along the ΓX direction. Here, the waves are divided into two tracks, forming a hollow lobe that facilitates acoustic cloaking and creates a wave vortex (or acoustic self-looping) with imaginary sources in the C1 and C2 channels.

Such behavior can be explained using the local dispersion of the degenerated mode shapes at the Dirac frequency along the MΓ and ΓX directions. As discussed in section 3.1.1 with Figure 2. 6a, the 'deaf' band mode is the dominant mode shape at the Dirac frequency along the ΓX direction that causes the orthogonal bend. However, along either the 45° or MΓ direction, the 'deaf' band mode is weaker in magnitude (Figure 2. 6b) compared to the 'T' and 'B' band mode shapes. This unique combination helps the wave to undergo a 135° bend (Figure 2. 9f), which is a local orthogonal direction along the ΓX. However, due to the further weakening of the 'deaf' bands along the MΓ direction, the wave takes another local 45° bend to maintain the dominant 'deaf' band mode shape along the ΓX direction (Figure 2. 9g), thereby leaving the weaker MΓ 'deaf' band mode shape at the boundaries. This hindrance continues, and the traveling wave rotates back to the entry point, creating a wave vortex. We call this phenomenon self-looping at the Dirac frequency, and it leaves a small 'No Zone' in which the divergence of the acoustic displacement field is zero.

2.6 EXPERIMENTAL VALIDATION

To illustrate the Dirac-like features by modulating the radii of the PVC resonators, an experimental setup was created. Moreover, to validate the numerical results, incident wave transport (along IT in Figure 2. 4a) and orthogonal wave transport (along OT in Figure 2. 4a) were investigated experimentally over a range of frequencies from 10 kHz – 14.5 kHz, which includes the 'Region A' Dirac-like frequency at 12.551 kHz. The coefficients of transmissibility along IT and OT were obtained from numerical experiments over the same frequency range.

First, 140 commercially available extruded PVC cylinders of r = 0.212a = 5.4 mm (the lattice constant a = 25.4 mm) were arranged in a 10 × 14 matrix as shown in Figure 2. 10a. The PVC cylinders were cut to 4" length elements and machined to have a smooth surface to minimize the experimental error. Acoustic pressure was created from one side (Figure 2.s 10a and 10b) using a speaker (Pyle Gear (PLG 3.2) 3.5" 2-way coaxial, 120-watt, 4-ohm impedance) capable of generating frequencies as great as 18 kHz. To absorb the acoustic energy at the boundaries in order to avoid reflection, acoustic dampers (0.5-inch-thick foam sheets) were used along the boundary of the experimental setup (Figure 2. 10a). Similar to the numerical study setup with absorbing boundary conditions, a channel made of foam was designed to guide the incident acoustic wave. The desired frequency ranges for validating orthogonal wave transport at the Dirac-like frequency is 12.5 – 12.7 kHz. A condenser pressure microphone (Sterling S30 Class-A FET 30 Hz –18 kHz) was used to detect the acoustic transmission (Figure 2. 10a and 10b), placed at orthogonal (for OT) and incident (for IT) directions. The signal was collected, conditioned and processed

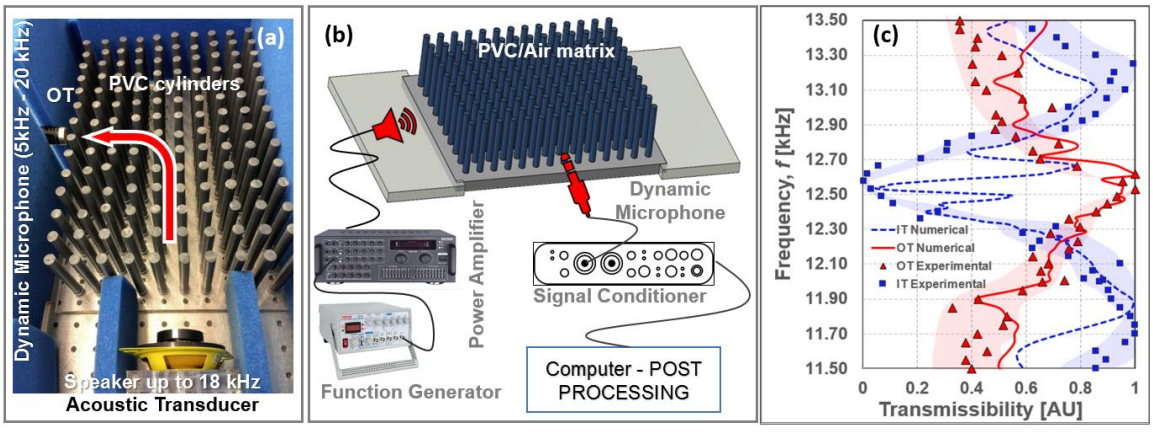

Figure 2.10: (a) Experimental setup, (b) schematic diagram of the experimental setup, and (c) a comparison of the numerical and experimental results of acoustic transmission (normalized) excited along the ΓX direction with 'Region A' frequencies. The peak transmission is seen at the Dirac-like frequency for both the numerical and experimental analyses along the orthogonal direction.

using an acoustic signal conditioner. Finally, the spectral analyses were performed to obtain the transmissibility at the IT and the OT locations.

Figure 2. 10c shows the normalized transmissibility along IT and OT from the

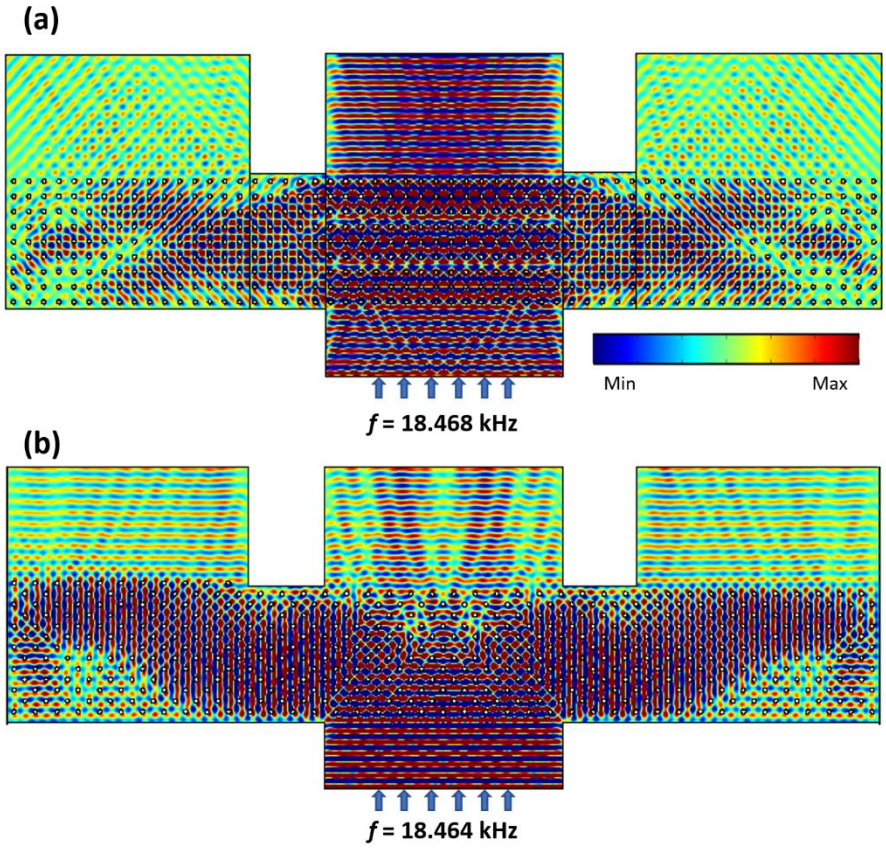

Figure 2.11: (a) Plane wave transportation at the Dirac-like frequency of 'Region B', for ΓX and MΓ incidence, respectively, in (a) and (b). An intriguing way of orthogonal wave tailoring is observed here.

numerical and experimental studies. It is clearly evident that the wave transmission along OT is quite high compared to IT at or around the Dirac cone frequency. The complete experiment was repeated more than 10 times, and the normalized spectral data presented are within the 98% confidence interval (shaded red and blue bands) observed during the experiment. Hence, this evidence conclusively demonstrates that the 'deaf' band-based

engineered Dirac cone was achieved and that orthogonal transport at the Dirac frequency was eminent.

2.7 REGION B: PROOF AND FEATURES OF THE DIRAC-LIKE CONE

A similar phenomenon was observed in 'Region B'. The most interesting phenomenon starts to emerge at the frequency of ~18.46 kHz, which is very close (0.44%) to the Dirac-like frequency. Here, the orthogonally transported wave fronts form a converging-diverging pattern inside the periodic crystals. After increasing the column number of the PnCs, we confirmed that the convergent-divergent pattern remains unchanged throughout the periodic materials. Figure 2. 11a shows that the incident wave converges at a focal point and simultaneously travels in a spiral pattern inside the PnCs. Interestingly, the plane wave that was actuated in the Kx direction continues to propagate through the PnCs, and after leaving the last row of PnCs, the travelling wave maintains the forward direction of the plain wave-front. Figure 2. 11b shows that the plane wave-front excited in the MΓ direction depicts a similar phenomenon.

2.8 CHAPTER SUMMARY

In this chapter, we have analytically solved the dispersion behavior of PVC PnCs in an air medium, with multiple probable triple degeneracies at the Dirac-like point at $\vec{k} = 0$. We designed our study around two 'deaf' bands that are identified as the probable governor of the Dirac–like cones. Then, we selected two frequency regions to explore whether the accidental degeneracies occur by modulating the physical parameters of the resonators. The predictive optimization process discussed in this article leads us to find the region of the Dirac-like cone based on the zero-group velocity flat bands, or the 'deaf' bands. With this unique phenomenon depending on the 'deaf' band, we fabricated two

numerical experiments to determine the behaviors of the Dirac-like points in order to test whether the regions identified were actually the Dirac-like points. After the test, we demonstrated that the orthogonal wave guidance at the Dirac points was evident in ‘Region A’ and ‘Region B’. In this article, however, only the ‘Region A’ Dirac point behaviors were discussed in detail, with several other phenomena possible, such as orthogonal wave transport, channeling plane waves along the offset axes, the acoustic ‘No Zone’, acoustic cloaking, an acoustic vortex or self-looping leaving imaginary acoustic sources at offset locations. Mode identification, the relation between the mode shapes and their role in the above-mentioned unique wave propagation behavior were analyzed logically and discussed in depth. Furthermore, the creation of the Dirac-like cone in the proposed setup was experimentally proved. Thus, in the future, the results of this study will help us to further identify the intriguing wave guiding properties of the Dirac cone in acoustic metamaterials.

CHAPTER 3

DEAF BAND-BASED ENGINEERED DIRAC CONE – II

In this chapter, we present a comprehensive study on the behavior of Dirac-like cone in PnCs in acoustic media for another frequency region, named as 'Region B'. We proposed an arrangement of Polyvinyl Chloride (PVC) cylindrical rods as PnCs with variable physical parameters, immersed in the air that was previously studied for band gaps and wave bifurcation. Here two Dirac-like cones have been reported for the same lattice at the center of the Brillouin Zone by modulating the physical parameter of the resonator of which, one of them is emphasized in this article as the rest has been explained and reported earlier in ref [39].

3.1 ANALYTICAL THEORY:

Previously, the detailed analytical approach of a 3D periodic structure in a solid-fluid media with cylindrical PnCs is reported using plane-wave expansion (PWE) method [64]. Due to infrequent convergence issues [60-62], improved PWE for a solid-fluid mixed-media is used to obtain the desired convergence with careful sorting of eigenmodes and appropriate definition of structural factors with a larger number of expansions [64]. Here, wave modes in x-y planes were decoupled from z-axis modes and the analyses were kept simpler. Upon employing a sufficiently large number of reciprocal space vectors, the study was verified by finite element (FE) simulations [16]. Analytical solution of wave dispersion

in a periodic structure formed by solid circular PnCs in fluid media was previously studied using the PWE method [69].

As such, the governing equation of wave motion takes the following form:

$$\sigma_{nl,l} + f_n = \rho \ddot{u_n} \qquad (1)$$

Where, $\sigma_{nl,l}$ is the derivative of the stresses with respect to the l^{th} direction, f_n is the body force in the n^{th} directions, ρ is the density of the material and $\ddot{u_n}$ is the acceleration in the n^{th} direction. In the PVC-air setup, this will result in two governing differential

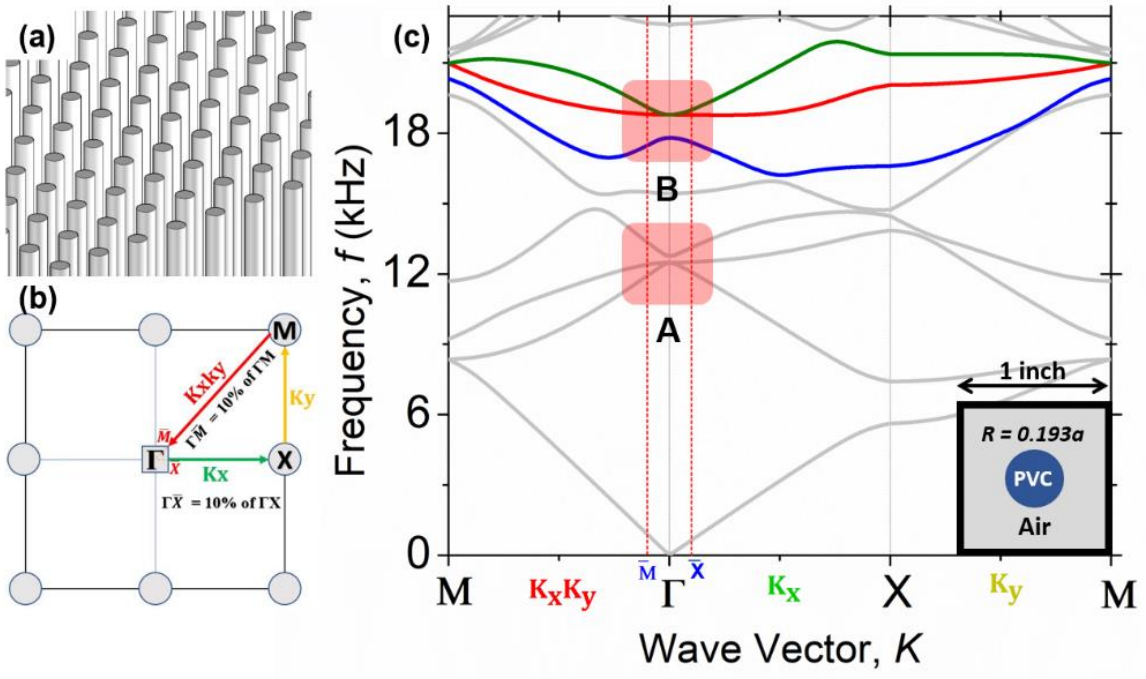

Figure 3.1: (a) PVC cylinders PnCs immersed in air, (b) BZ depicting reduced wave vector direction, (c) Full dispersion band structure for PVC in air (MΓ-ΓX - XM) representing region A and B, unit cell lattice of a = 1 inch and r=0.193a in inset.

equations. Now, Applying Bloch-Floquet condition [70] in reciprocal wave number space and adding $\mathbf{G} = G_i \hat{e}_i$ where $G_1 = \frac{2\pi j}{D_1}$ and $G_2 = \frac{2\pi m}{D_2}$ with the Eigen value wave number, we obtain Bloch-Floquet displacement functions. The derivative of displacement functions can be derived as the strain function while stress function can be obtained from the

constitutive properties of the media. Constitutive functions can be surmised to be functions of space and derived by Fourier coefficients, once derived with respect to space x_l, then

$$\frac{\partial C_{ts}(x)}{\partial x_l} = (-1)^{l+1} \sum\sum iC_{ts}^{pq} \frac{2\pi(p(2-l)+q(1-l))}{D_l} e^{i\mathbf{G_{pq}}.\mathbf{x}} \quad (2)$$

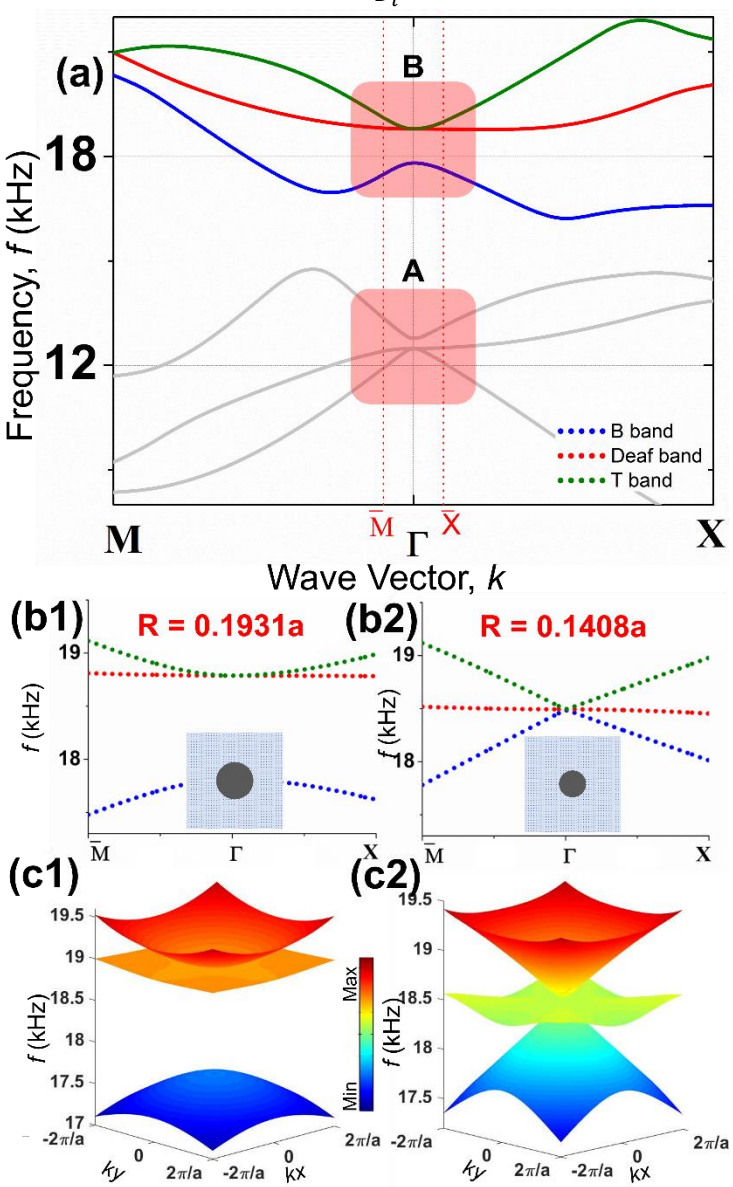

Figure 3.2: Dispersion band structure for PVC in air (MΓ-ΓX) representing region A and B, BZ and unit cell in inset, (b1) and (b2) Close dispersion ($\bar{M}\Gamma$-$\Gamma\bar{X}$) for region B at r=0.1931a and r=00.1408a respectively, (c1) and (c2) Equi-frequency contours before and at Dirac-like frequency respectively

Where,

$$C_{ts}^{pq} = \frac{1}{A_c} \int C_{ts}(x)\ e^{-i\mathbf{G_{pq}}.\mathbf{x}}$$

And can be written as

$$C_{ts}^{pq} = \zeta_{air}\delta_{\mathbf{G_{pq}}0} + (\zeta_{PVC} - \zeta_{air})F(G_{pq}) \qquad (3)$$

where, ζ_{air} or ζ_{PVC} is the volume fraction of the respective constituent media, δ is Kronecker delta symbol, $F(G_{pq})$ is called the structural factor of the PVC in air, can be expressed as $2fJ_1(G_{pq}r)/\mathrm{G_{pq}r}$, Where, J_1 is the Bessel function of the first kind, r is the radius of the PVC rods [64]. Substituting the Eq. (2) through Eq. (7) in to Eq. (1) we get

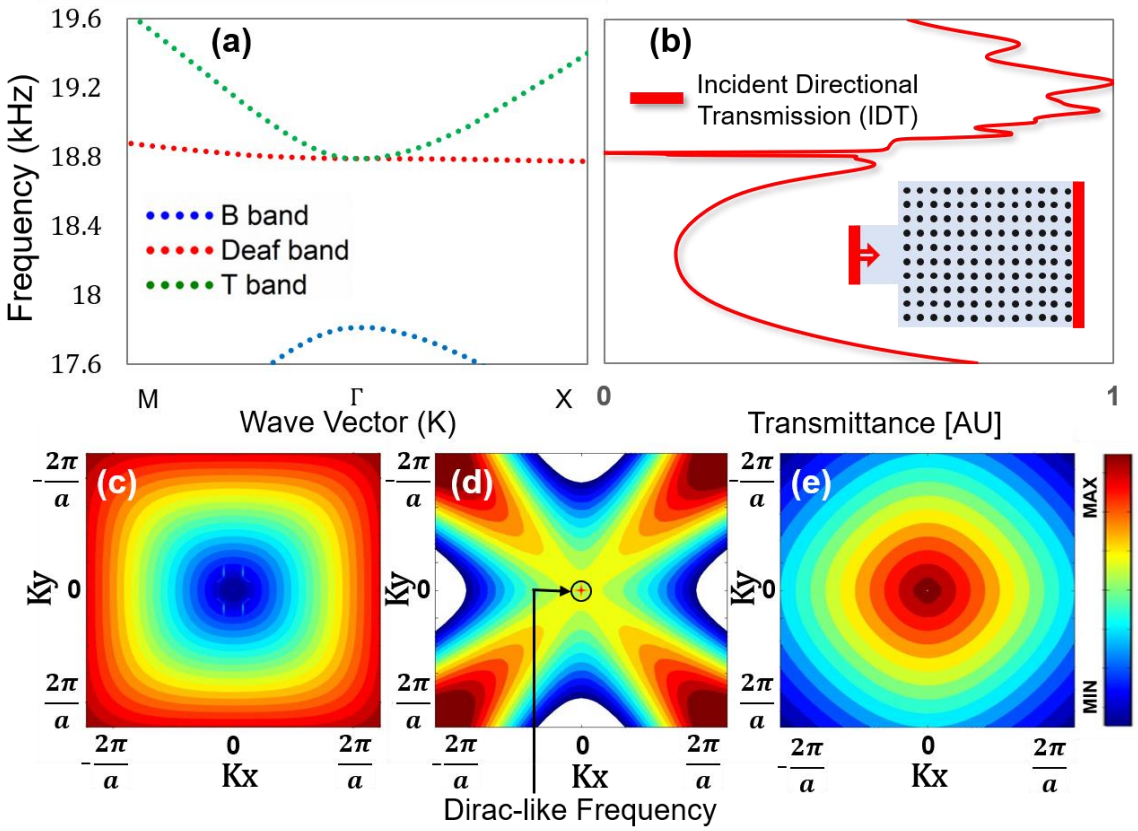

Figure 3.3: (a) Dispersion curve showing region B for r = 0.193a, where the deaf band and the B band has a directional frequency band gap along ΓX, (b) The transmission spectrum for the band strcuture showing zero transmission due to band gap and presence of deaf band, (c), (d) and (e) shows the equifrequency surfaces (EFS) for the 'T' band, 'deaf' band and 'B' band, respectively, for region B. Here, the frequency contour of the Dirac-like frequency appears circular (in (b)), demonstrating isometric behavior of the acoustic wave at the Dirac frequency; in contrast, at other frequencies, the contours are not fully circular i.e. anisotropic).

two equations as follows,

$$\sum_j \sum_m \sum_p \sum_q \Bigg[\; A_{jm} C_{11}^{pq} e^{i(\mathbf{k}+\mathbf{G_{pq}}+\mathbf{G_{jm}}).\mathbf{x}} \left(k_1 + \frac{2\pi j}{D_1}\right)\left[-k_1 - \frac{2\pi j}{D_1} - \frac{2\pi p}{D_1}\right]$$

$$+ \frac{1}{2} A_{jm} C_{66}^{pq} e^{i(\mathbf{k}+\mathbf{G_{pq}}+\mathbf{G_{jm}}).\mathbf{x}} \left(k_2 + \frac{2\pi m}{D_2}\right)\left[-k_2 - \frac{2\pi m}{D_2} - \frac{2\pi q}{D_2}\right]$$

$$+ B_{jm} C_{12}^{pq} e^{i(\mathbf{k}+\mathbf{G_{pq}}+\mathbf{G_{jm}}).\mathbf{x}} \left(k_2 + \frac{2\pi m}{D_2}\right)\left[-k_1 - \frac{2\pi j}{D_1} - \frac{2\pi p}{D_1}\right]$$

$$+ + \frac{1}{2} B_{jm} C_{66}^{pq} e^{i(\mathbf{k}+\mathbf{G_{pq}}+\mathbf{G_{jm}}).\mathbf{x}} \left(k_1 + \frac{2\pi j}{D_1}\right)\left[-k_2 - \frac{2\pi m}{D_2} - \frac{2\pi q}{D_2}\right]\Bigg]$$

$$= \; -\rho\omega^2 \sum_j \sum_m A_{jm} e^{i(\mathbf{k}+\mathbf{G}).\mathbf{x}} e^{-i\omega t} \qquad (4)$$

$$\sum_j \sum_m \sum_p \sum_q \Bigg[A_{jm} C_{21}^{pq} e^{i(\mathbf{k}+\mathbf{G_{pq}}+\mathbf{G_{jm}}).\mathbf{x}} \left(k_1 + \frac{2\pi j}{D_1}\right)\left[-k_2 - \frac{2\pi m}{D_2} - \frac{2\pi q}{D_2}\right]$$

$$+ \frac{1}{2} A_{jm} C_{66}^{pq} e^{i(\mathbf{k}+\mathbf{G_{pq}}+\mathbf{G_{jm}}).\mathbf{x}} \left(k_2 + \frac{2\pi m}{D_2}\right)\left[-k_1 - \frac{2\pi j}{D_1} - \frac{2\pi p}{D_1}\right]$$

$$+ \; B_{jm} C_{22}^{pq} e^{i(\mathbf{k}+\mathbf{G_{pq}}+\mathbf{G_{jm}}).\mathbf{x}} \left(k_2 + \frac{2\pi m}{D_2}\right)\left[-k_2 - \frac{2\pi m}{D_2} - \frac{2\pi q}{D_2}\right]$$

$$+ \frac{1}{2} B_{jm} C_{66}^{pq} e^{i(\mathbf{k}+\mathbf{G_{pq}}+\mathbf{G_{jm}}).\mathbf{x}} \left(k_1 + \frac{2\pi j}{D_1}\right)\left[-k_1 - \frac{2\pi j}{D_1} - \frac{2\pi p}{D_1}\right]\Bigg]$$

$$= \; -\rho\omega^2 \sum_j \sum_m A_{jm} e^{i(\mathbf{k}+\mathbf{G}).\mathbf{x}} e^{-i\omega t} \qquad (5)$$

The matrix sizes of the expressions (1) and (2) are directly dependent on the number of reciprocal space vectors used in the expansion. Here 532 reciprocal space vectors are used for PWE. Dispersion band structures are verified by matching the results from FE analysis using commercial package COMSOL to ensure convergence. The probable accidental degeneracies identified in the band structure of Figure 3. 1a is termed ‘Region

A' and 'Region B'. The behavior and features of the Dirac-like point of region A are reported in ref [39]. In this article, the discussion is limited to 'Region B' only.

3.2 SETUP AND NUMERICAL APPROACH

A PnCs arrangement of cylindrical rods immersed in the air was proposed previously to study the band gaps and wave bifurcation [71-76] extensively. Here, we report similar Polyvinyl Chloride (PVC) rods with a square lattice structure in the air to generate Dirac-like cones (Fig 1a). With a C_{4v} symmetry, the lattice constant of the unit cell was considered, *a = 1 inch = 0.0254 m,* given in the inset of Fig 1c. The initial arbitrary radius of the resonator was set to *r = 0.1931a (11.7% volume fraction)*. The density, Young's modulus and Poisson's ratio of the PVC solid rods were 1760 kg/m^3, 2.9 GPa and 0.4, respectively. Firstly, the possible frequency regions at the Γ (where the wave vector $\vec{k} = 0$) point are acknowledged based on the 'deaf' bands, in Fig 1c. From the frequency-wavenumber plot for PnCs, the trends essential to produce probable Dirac-like cones at different frequencies are determined. Numerical results indicate that these Dirac-like cones are formed due to a triple degeneracy, consisting of a double degenerate state and a single degenerate state showing linear dispersion at $\vec{k} = 0$. Here, initially, we report two Dirac-like cones at the center of the Brillouin Zone (BZ) (Fig 1b) using the same lattice structure by modulating the geometric parameters (*r = 0.1931a, 11.7% volume fraction)* of the resonator, changing the volume fraction of the PVC in the air matrix. Their probable regions were identified near ~12.5 kHz and ~18.5 kHz where the possibility of obtaining a Dirac-like phenomenon was obvious because of the existence of two double degenerate states with a deaf band each. We named these regions 'Region A' and 'Region B'. More specifically, 'Region A' was within the band of ~11.7 – 13.5 kHz and 'Region B' was

within ~17.5 – 19.7 kHz, as shown in Figure 3. 2a. Dirac-like cone of 'Region A' has been discussed and reported in detail in ref [39], where only the 'Region A' Dirac point behaviors were discussed in detail, with several phenomena possible, such as orthogonal wave transport, channeling plane waves along the offset axes, the acoustic 'No Zone', acoustic cloaking, and acoustic vortex or self-looping leaving imaginary acoustic sources at offset locations. Mode identification, the relation between the mode shapes and their role in the above-mentioned unique wave propagation behavior were also analyzed logically

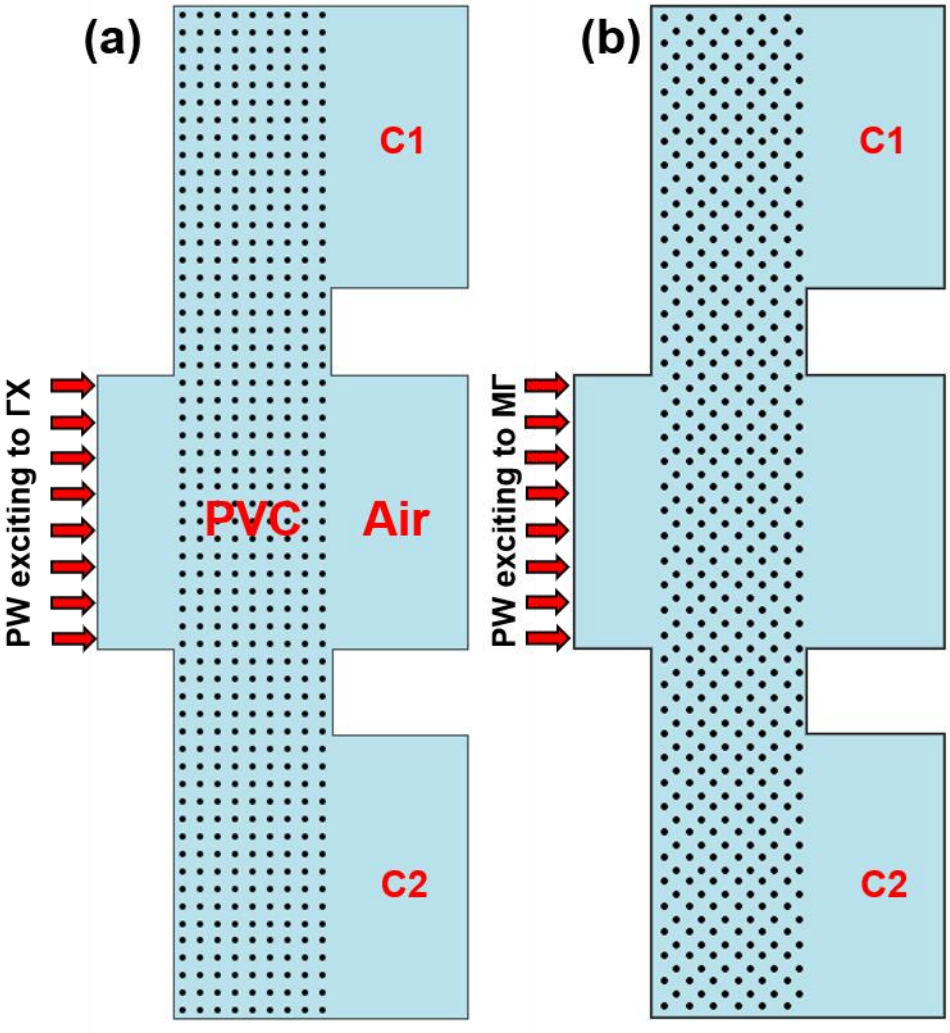

Figure 3.4: Model for the numerical experiments, and analysis for plane wave propagation through PVC PnCs having incident at 0 Degree and 45 Degree angle, respectively (ΓX and MΓ direction, respectively)

and discussed in depth. Hence in this article, the physics associated with the formation of the second Dirac-like point (Region B) in an acoustic media is reviewed along with the comprehensive study on its behavior. Among 3 of the bands of 'Region B', the top (green) and bottom (blue) bands are named 'T' and 'B', respectively, with respect to the red flat band, as 'deaf' band (Fig 2a). In literature, a predictive nature of accidental degeneracy is presented yielding Dirac – like dispersion depending on a flat 'deaf band'[39]. Despite the presence of a similar band structure at multiple Dirac-like points, each Dirac-like point can be distinguished by its unique characteristics.

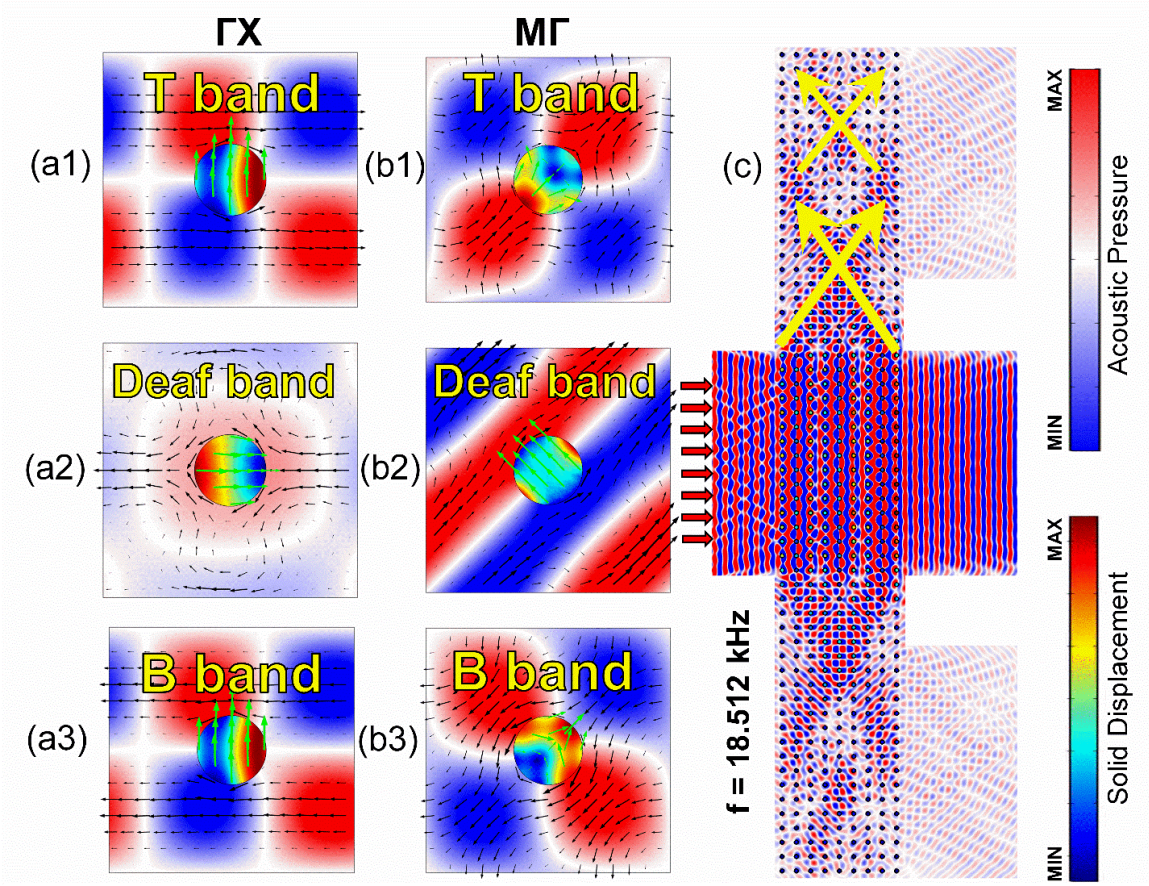

Figure 3.5: (a) and (b) Absolute acoustic pressure field and solid displacement field mode shapes for air and PVC of unit cell for ΓX and MΓ respectively, (c) Acoustic beams swirling inside PnCs at Dirac-like frequency orthogonally.

3.3 VALIDATION OF DIRAC-LIKE CONE

Using deaf band based predictive modulation, dispersion modes of the PVC inclusion in air matrix (lattice constant, $a = 0.0254\ m$) are altered by modulating the physical parameter (radius in this case) of the PnCs'. The radius is optimized from $r = 0.193a$ to $r = 0.1408a$ as shown in Figure 3. 2b1 – 2b2 with a reduction of volume fraction from 11.7% to 6.22%. This optimization resulted in the bottom band to move up in frequency. A significant alteration of the dispersion of the 'B' band, in terms of frequency fluctuation, keeping 'T' and 'deaf band' relatively unaltered (within ~1% error) forming a local linear dispersion intersecting the 'deaf' band (Figure 3. 2b2). This degenerated point is the 'Dirac-like point' as it forms a triply degenerated conical mode region at $f \cong 18.512\ kHz$. Equifrequency contours for both the physical conditions are given in Fig 2c1 – 2c2. A sample domain of 10 x 13 block of PVC PnCs in the air before tuning (i.e., with $r = 0.193a$, *11.7% volume fraction*) is investigated numerically within the band 17.6 kHz – 19.6 kHz (Fig 3a – 3b). Although the zero-group velocity band starts at ~18.8 kHz, the transmission begins to decrease to less than 50% at frequencies close to ~18.0 kHz. Along the ΓX [100] direction, the transmission further decreases to almost zero due to the asymmetric 'deaf' band, although there is no bandgap. Hence, the zero-transmissivity at the flat band frequency proves its deafness which is evident in the acoustic transmission spectrum and hence deaf band-based modulation is valid in our case, similar to ref [32-34]. Furthermore, a periodic media made of different densities is generally anisotropic in nature, however, the triple degeneracy at Γ point confirms the isotropic behavior at Dirac-like frequency [68] which creates almost circular equifrequency contours. In this study, the equifrequency surfaces for all the three modes at Dirac-like point are shown in Figure 3.

3c – 3f, where circular equifrequency contour at 18.512 kHz is depicted in Fig 3d. Thus, the existence of a Dirac-like cone is verified.

3.4 REGION B: PROOF AND FEATURES OF DIRAC-LIKE CONE

At Dirac-like frequency ($f \cong 18.512\ kHz$), acoustic pressure field distribution is demonstrated over a given range of frequencies pivoting the Dirac-like point. Orthogonal wave transportation was observed. However, in addition to the orthogonal transport, a spiral waveguiding due to repeated total internal refraction caused convergence-divergence phenomena at the Region B Dirac-like point (18.512 kHz). Two 45° bent lines were generated leaving an undisturbed zone or a 'No Zone' which is unaffected by any PnCs defect. Although not demonstrated here, this undisturbed zone can be realized for a potential application of acoustic cloaking. To identify the wave transmission properties, a frequency domain study setup is designed to obtain the acoustic pressure field. A

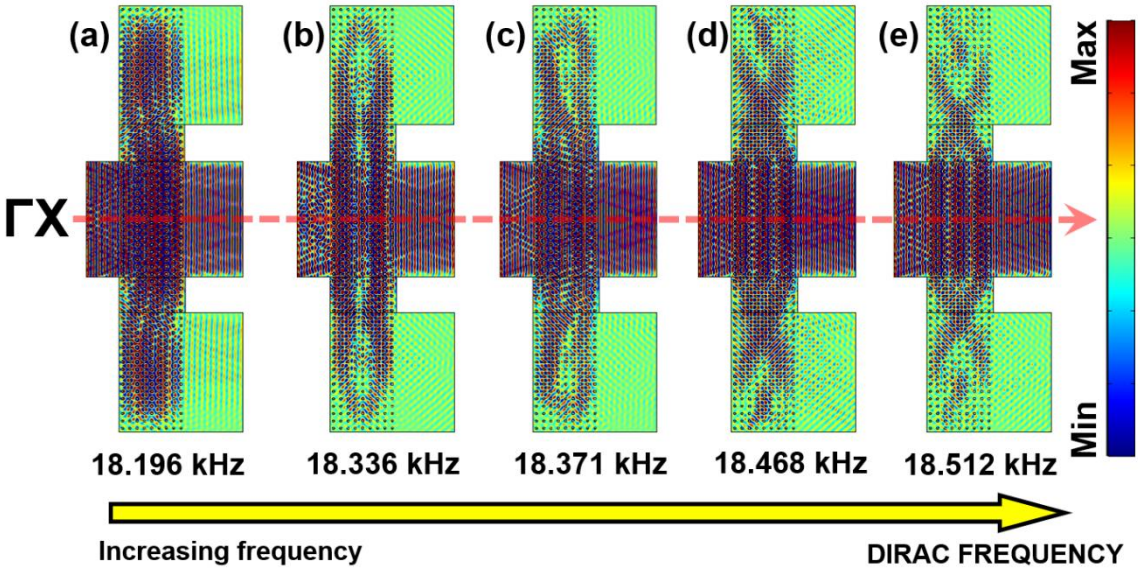

Figure 3.6: Plane wave excited in ΓX direction for PnCs by frequencies, (a) 18.196 kHz, (b) 18.336 kHz, (c) 18.371 kHz, (d) 18.468 kHz and (e) 18.512 kHz, which is the Dirac-like frequency for region B, demonstrating orthogonal spiral wave transportation.

metamaterial model of rectangular arrangement consisting of 57 x 10 solid PVC cylinders in air media is considered for the numerical simulations (Fig 4). This PnCs arrangement is

actuated by a plane wave source located at ~0.1143 m (to generate fully matured wave with five wavelengths) away from the PVC-air interface. Two angles of incidence are considered, along 0^O (ΓX direction, Fig 4a) and along 45^O (MΓ direction, Fig 4b). In addition to the central channel, two channels, C1 and C2, are constructed, located at ~1.07 m away from each other along the direction of actuation. These two channels are required to demonstrate the properties of the Dirac-like points that helped understand the wave routes as well as the behavior of the transmitted wave field.

Waveguiding and propagation pattern is studied inside and outside of the PnC arrangement. The local dispersion of the degenerated total absolute acoustic pressure mode shapes and solid displacement mode shapes at *~18.512 kHz* are shown in Fig 5. Clearly, the contribution of MΓ directional deaf band is dominated over the ΓX directional deaf band, as the total acoustic pressure field magnitude of ΓX mode shape is negligible compared to the MΓ mode shape (Fig 5a-2 & 5b-2). In the case of 'T' and 'B' band, the acoustic pressure mode shapes are quadrupolar and orthogonal to each other in MΓ direction, eventually getting nullified. Moreover, pressure field vectors of the mode shapes of these two bands are in stark contrast to each other especially in ΓX direction resulting in an insignificant dominance at degenerated Dirac-like point. On the other hand, the deaf band shows dipolar acoustic mode shapes, antisymmetric with respect to the actuation direction, exhibiting special localization (Fig 5a-2 & 5b-2). It can only be excited about the incidence of nonzero k-parallel components [59, 77]. Therefore, MΓ directional mode shapes of the Deaf band dominates the propagation of incident plane waves and the orthogonal transmission of the wave at the Dirac-like frequency.

3.5 ORTHOGONAL WAVE TRANSPORTATION: PROPAGATION ALONG ΓX

Figure 3. 5c shows the acoustic pressure field distribution of the wave transmission at *18.512 kHz*. Plane-wave, actuated by the wave source with a normal displacement in ΓX direction, travels through the waveguide and transported inside the PnCs, following the MΓ deaf band mode shape. While the dispersed guided wave maintains the direction of MΓ mode shape locally, the global direction of propagation is observed orthogonal with respect to the direction of excitation. Herein, an orthogonal wave transportation at the Dirac-like frequency with convergence – divergence spiral wave phenomena are reported due to sequential total internal refraction. Figure 3. 6 shows the acoustic pressure field distribution for a range of frequencies around the Dirac-like frequency of 'Region B'. At frequencies before and after the Dirac-like point, a negligible plane wave leakage is observed in the directions orthogonal to the direction of excitation. Close to Dirac-like frequency, a convergence – divergence spiral wave transportation phenomenon is prominent. In Figure 3. 6b, plane wave, getting converged at a focal point and traveling

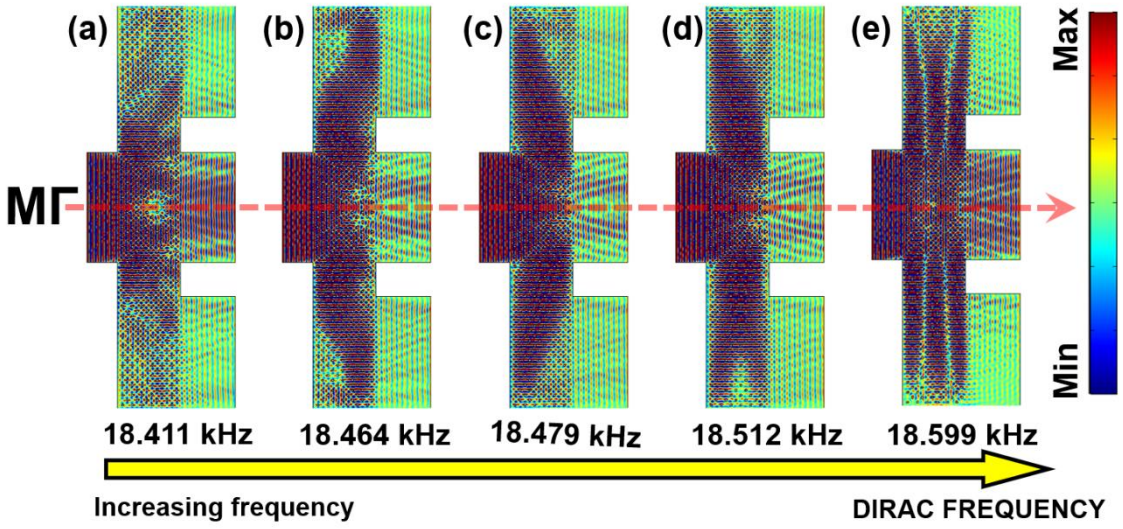

Figure 3.7: Plane wave excited in MΓ direction for PnCs by frequencies, (a) 18.411 kHz, (b) 18.464 kHz, (c) 18.479 kHz, (d) 18.512 kHz and (e) 18.599 kHz, which is the Dirac-like frequency for region B, demonstrating orthogonal spiral wave transportation.

spirally, inside the PnCs is realized. However, with the increase of the frequency towards the Dirac-like point, the converging focal length inside the PnCs keeps reducing and the wave beams that are being converged get narrowed. As the focal point of orthogonally converging wave beams changes with frequency, it can be tuned and modulated to achieve phenomena such as acoustic imaging [78]. After increasing the column number of the matrix, it has been confirmed (not reported herein) that the convergent-divergent phenomenon remains unaltered. Notably, wave propagation along actuation direction occurs due to the local dispersion of the ΓX deaf band's solid displacement mode shape and this keeps the plane wavefront unperturbed with zero phase change (Fig 6a). After increasing the actuation frequency towards Dirac-like frequency, at $f \cong 18.336\, kHz$, the wave gets split into two beams, creating a non-affected PnC region at the center, shown in Fig 6b. The wave tends to reflect at the boundary after bouncing back towards the center of the PnC set, which is similar to a feedback phenomenon of 'Region A' [39]. The most interesting phenomenon starts emerging at the frequency of $f \cong 18.468\, kHz$, when the orthogonally transported wave fronts form a converging-diverging phenomenon inside the periodic crystals (Fig 6d). Finally, at the Dirac-like frequency ($f \cong 18.512\, kHz$) the orthogonal spiral propagation is distinct and dominant (Figure 3. 6e). Clearly, plane wave-front does not alter its phase during its propagation from the excitation source until it passes through C1 and C2 (labeled in Fig 4). Hence, channelized wave transport is realized herein, suitable for designing tailored wave propagation at and around Dirac-like frequency.

3.6 ORTHOGONAL WAVE TRANSPORTATION: PROPAGATION ALONG MΓ

To reinforce this claim, the Dirac-like features are investigated by actuating the guided wave source in MΓ direction. In this case, the PnCs are oriented at 45^{O} angle with the actuation direction (Fig 4b) and actuated from 18.411 to 18.599 kHz. As the frequency increases towards the Dirac-like point, initialization of orthogonal wave transportation is

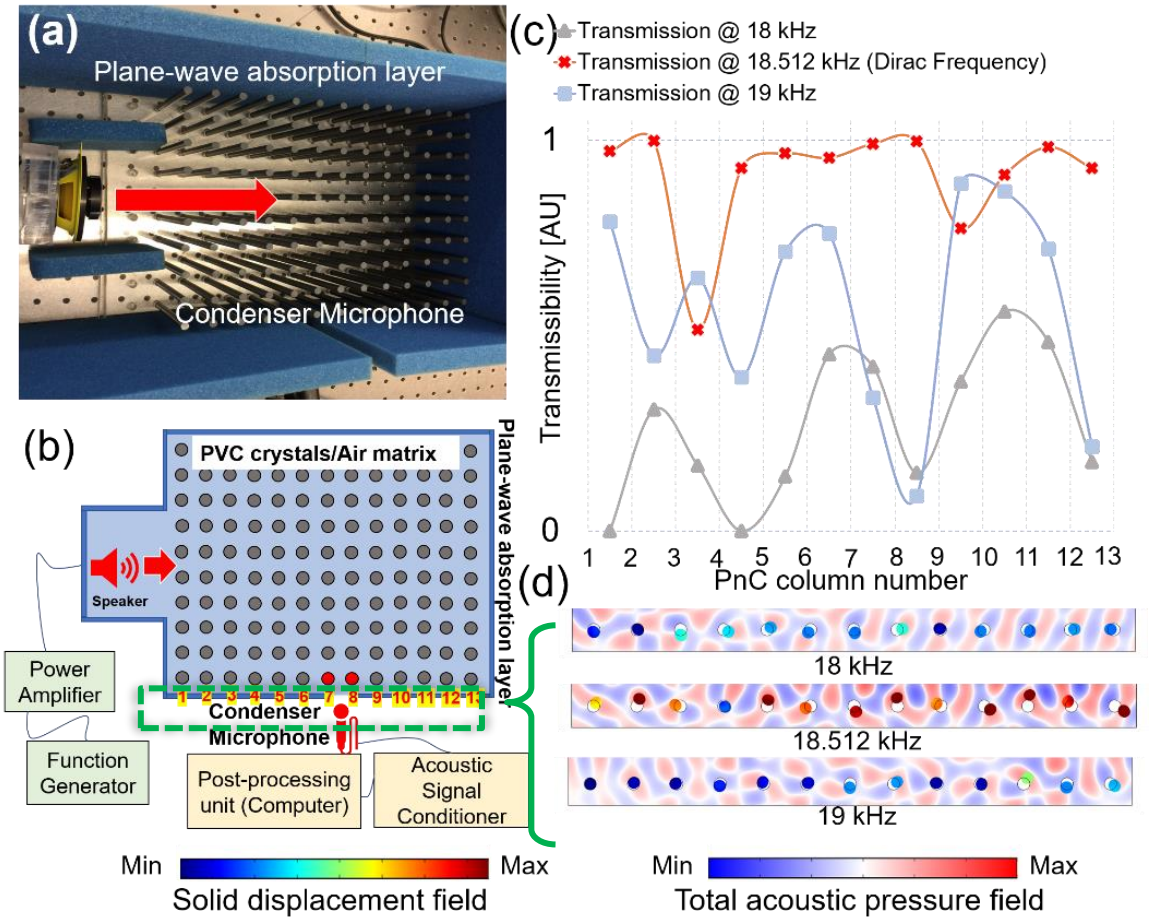

Figure 3.8: (a) Experimental setup, with 13 x 10 PnC matrix, (b) Schematic of the experimental setup labeled with boundary cylinder numbers, (c) Normalized transmission @Dirac-like frequency for each of the 13 columned PVC of last row numbered, showing maximum transmission between PnC 7-8, (d) Spatial solid displacement of PnCs showing perturbation maximum for PnC 7-8

observed inside the PnCs forming two inclined conical-shaped distribution of acoustic pressure. Eventually, the wave beams at orthogonal waveguides experience an obvious

convergent-divergence phenomenon at Dirac-like frequency (Figure 3. 7b). Moreover, a plane wave propagating along excitation direction (ΓX) leaks at lesser rates as compared to the case described in the last paragraph. No phase change of the wavefront is observed

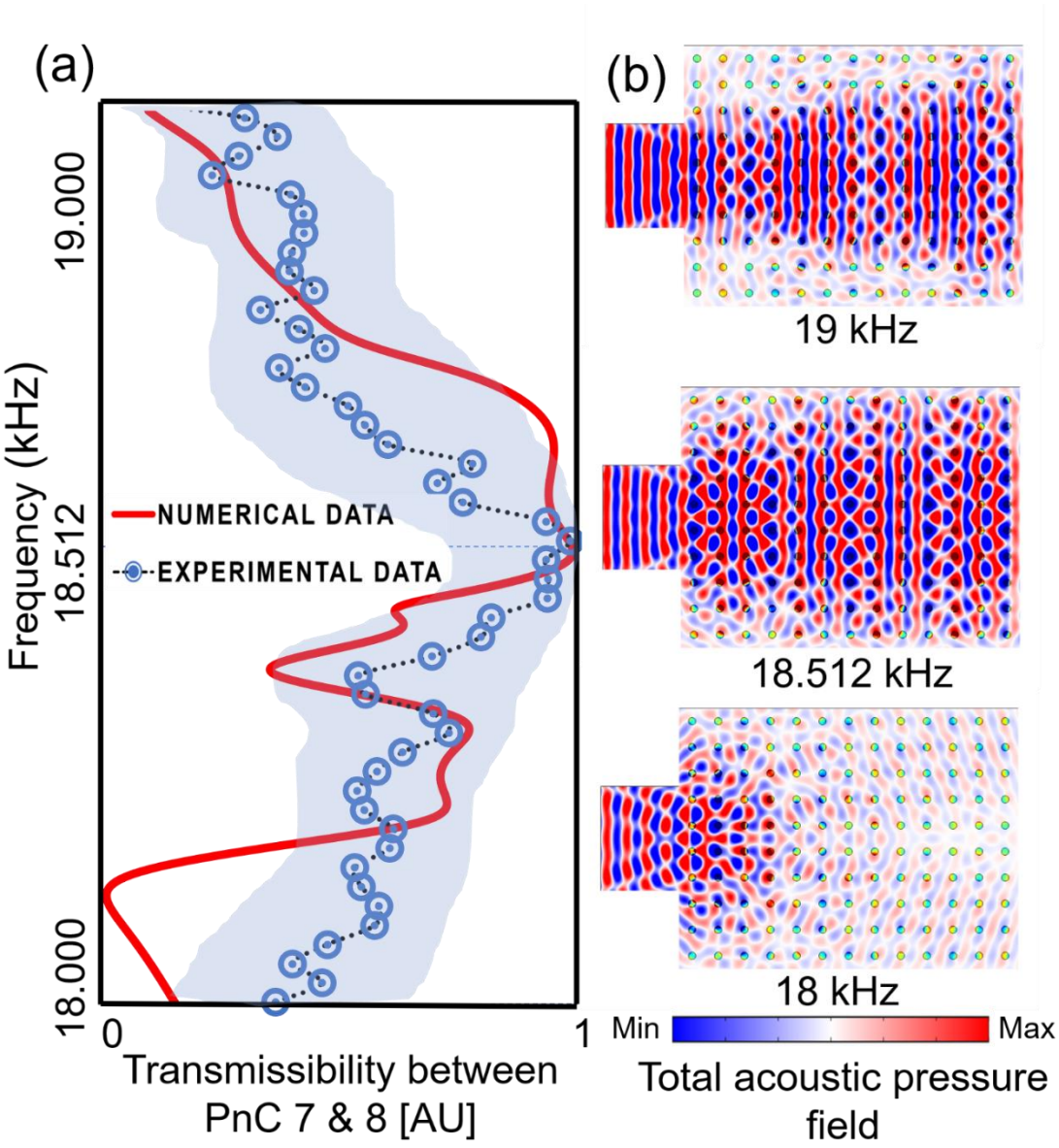

Figure 3.9: (a) Numerical and experimental normalized transmission shows maximum transmissibility at Dirac-like frequency, 18.512 kHz, (b) Numerical study of total acoustic pressure field distribution matching experimental setup.

until pivoting towards C1 and C2. The orthogonal wave beam shifts its inclination direction from one side to another from 18.464 kHz to 18.479 kHz (Figure 3. 7c). Eventually, the

wave beams at orthogonal PnC waveguides realize a convergence-divergence phenomenon at Dirac-like frequency (Figure 3. 7d). Interestingly, beyond the Dirac-like frequency, the orthogonal wave beam gets split into 3 spikes leaving undisturbed zones between them (Figure 3. 7e). Nevertheless, at Dirac-like frequency, the orthogonal spiral wave transportation through PnCs exhibits consistent behavior if excited along ΓX and MΓ.

3.7 EXPERIMENTAL APPROACH

Experimental validation of the numerical results is presented using a carefully designed experimental setup. Firstly, 130 commercially available extruded PVC cylinders having physical parameter, $r = 0.1408a = 3.58\ mm$ ($a = 25.4\ mm$), are arranged in a 10 × 13 matrix as shown in Fig 8a – 8b. The height of these cylinders is 100 mm and both ends are machined to have smooth surfaces. An acoustic speaker (Pyle Gear (PLG 3.2) 3.5" 2-way coaxial, 300-watt, 4-ohm impedance) is used as the guided wave source (Fig 8a – 8b) capable of generating pressure frequencies up to 20 kHz. To justify plane-wave radiation boundary condition used in the numerical study, acoustic dampers (13 mm-thick foam sheets) are placed along the boundaries to help prevent unwanted acoustic reflections and noise. A condenser pressure microphone (Sterling S30 Class-A FET 30 Hz –20 kHz) is used to detect the acoustic transmission, placed at desired orthogonal locations. The acquired signals are conditioned and processed using an acoustic signal conditioner. Based on numerical results, orthogonal wave transportation is measured at selected locations of the PnCs. Wave propagation transmissibility at 18 kHz, 18.512 kHz, and 19 kHz are numerically calculated (Figure 3. 8c) at each of the 13 orthogonal boundary cylinders labeled in Fig 8b. From Fig 8c, the normalized transmissibility along orthogonal cylinders are shown, where clearly, acoustic transmissibility at Dirac-like frequency is higher than

that of its adjacent frequencies (18 and 19 kHz). Additionally, at 18.512 kHz, wave transmission between cylinders 1&2, 7&8 and 11&12 is higher compared to other locations. Furthermore, solid displacement amplitudes at these frequencies are measured at each cylinder and displayed in Fig 8d. Perturbations are higher in magnitude at Dirac-like frequency, 18.512 kHz than 18 and 19 kHz. Convincingly, that perturbations at Dirac-like frequency show the highest at cylinders 2, 7 and 11. Comparing these two results from Fig 8c and 8d, it is reasonable to measure acoustic pressure between cylinders 7 and 8 rather than the cylinders at corner edges. Figure 3. 9a exhibits the superimposition of normalized transmissibility measure by numerical and experimental methods between cylinders 7 & 8. We demonstrated the calculated transmission spectrum for a range around the Dirac-like frequency. Evidently, the maximum transmission is observed at Dirac-like frequency in both numerical and experimental analyses. The complete experiment was repeated more than 10 times, and the average experimental data closely follow the numerical data with an average error of ~ 2%. Therefore, it can be inferred orthogonal waveguiding can be achieved by modulating the 'Deaf band' based engineered Dirac-like cone.

3.8 CHAPTER SUMMARY

In this article, we have numerically solved the dispersion behavior and relation of 2D PVC PnCs in acoustic media, having multiple probable triple degeneracy regions. One of the many regions was selected and investigated further to generate accidental degeneracy by the deaf band based predictive modeling. Our numerical and experimental results hold equally well for the deaf-band modulated Dirac-like cones at $\vec{k} = 0$. A numerical study of determining the band structure for this PnC setup is postulated and

orthogonal wave guidance using Dirac frequency is also demonstrated. Dipolar antisymmetric Deaf-band pressure distribution completely dictates PnC assisted wave transport discarding/avoiding/diminishing quadrupolar modes. Acoustically conversed wave beams inside PnCs yielding tunable focus points has been materialized. Experimentally obtained wave transmissibility confirmed the orthogonal wave transport phenomenon at degenerated Dirac-like point, including converging wave beams inside PnCs. Finally, a new way of relativistic wave guiding phenomenon exploiting properties of a Dirac-like cone has been proposed.

CHAPTER 4

MULTIFREQUENCY DIRAC CONES WITHOUT BREAKING SYMMETRY

4.1 ANALYTICAL MODEL

Periodic inhomogeneities characterized by different elastic properties cause varied spectral responses and play a vital role in band degeneracies. Slopes of linear branches from the center of the BZ inherit different sound velocities. Opening and closing partial or complete band gaps depends on adjusting the physical parameters such as the mass densities or acoustic speed. In solid/fluid mixed media, due to inhomogeneous elastic constants, coupling of transverse and longitudinal modes is inevitable. Nevertheless, partial decoupling can occur in 2D PnCs, demonstrating that the incidental wave is normal with respect to the normal direction to the periodic plane. Hence, pure transverse modes prevail along this axis (the Z axis) and are completely independent of the coupled modes (longitudinal) propagating through PnCs along the periodic plane [79]. In this solid/fluid mixed media system, plane wave expansion (PWE) is fully approximated [65, 80]. The governing wave motion equation in solid-fluid media is expressed as:

$$\sigma_{ij,j}(x_k) + f_i = \rho(x_k)\ddot{u}_i \qquad (1)$$

where $i, j,$ and k are the index notation with values 1 and 2 considering the 2D cross-sectional plane of PnCs, $\sigma_{ij,j}(x_k)$ is the derivative of the stresses at location x_k with respect

to the jth direction, f_i is the body force in the ith direction, $\rho(x_k)$ is the density at location x_k in the material, and $\ddot{u}_i$ is the acceleration in the ith direction.

The Bloch-Floquet periodic boundary conditions [68] in the reciprocal wave number space are then applied. $G_1 = 2\pi m/D_1$ and $G_2 = 2\pi n/D_2$ are real values of the periodic wave numbers or Bloch wave numbers (where $m = -\infty\ to + \infty$ and $n = -\infty\ to + \infty$ using only integers) added with the eigen wave number to obtain the Bloch-Floquet displacement function. D_i is the periodicity of the media in the ith direction. If at a certain frequency ω the wave number $\mathbf{k}$ in Eqs. (2) and (3) is a solution of the system, then $\mathbf{k} + \mathbf{G}$ is also a solution of the system at the same frequency. The Bloch-Floquet displacement function is expressed as

$$u_1(x_k, t) = \sum_m \sum_n A_{mn} e^{i\mathbf{k}.\mathbf{x}} e^{i\mathbf{G}.\mathbf{x}} e^{-i\omega t} \qquad (2)$$

$$u_2(x_k, t) = \sum_m \sum_n B_{mn} e^{i\mathbf{k}.\mathbf{x}} e^{i\mathbf{G}.\mathbf{x}} e^{-i\omega t}, \qquad (3)$$

where $\mathbf{G} = G_i \hat{e}_i$ and $\hat{e}_i$ are the Cartesian basis vectors and $\mathbf{G}.\mathbf{x} = G_k x_k$ is the dot product between the reciprocal Bloch wave number and position vector. Similarly, differentiating the displacement function twice with respect to time, the acceleration is

$$\ddot{u}_1(x_k, t) = -\omega^2 \sum_m \sum_n A_{mn} e^{i(\mathbf{k}+\mathbf{G}).\mathbf{x}} e^{-i\omega t} \qquad (4)$$

$$\ddot{u}_2(x_k, t) = -\omega^2 \sum_m \sum_n B_{mn} e^{i(\mathbf{k}+\mathbf{G}).\mathbf{x}} e^{-i\omega t} \qquad (5)$$

The expressions in Eqs. (2) to (5) signify the summations over a range of integer values of m and n. In continuum mechanics, the stresses in Eq. (1) are further expressed as a product of the constitutive properties of the medium and strain functions. The strain functions can be further derived from the derivative of the displacement functions in Eqs. (2) and (3) with respect to the spatial domain x_k. Within an array of PnCs, the constitutive matrix can be assumed to be the periodic function of space and is expressed using Fourier coefficients in the periodic medium. Hence, applying the Fourier transform constitutive function $C_{ij}(x)$ in terms of the Fourier coefficients C_{ij}^{pq} is expressed as

$$C_{ij}(x_k) = \sum_{p=-\infty}^{\infty} \sum_{q=-\infty}^{\infty} C_{ij}^{mn} e^{i\left({}^{2\pi p}/_{D_1} x_1 + {}^{2\pi q}/_{D_2} x_2\right)} = \sum\sum C_{ij}^{pq} e^{i\mathbf{G}.\mathbf{x}} \qquad (6)$$

where similar to m and n, $p = -\infty\ to + \infty$ and $q = -\infty\ to + \infty$ also use only integers. The derivative of the constitutive function with respect to space x_l is expressed as

$$\frac{\partial C_{ij}(x_k)}{\partial x_l} = (-1)^{l+1} \sum\sum i C_{ij}^{pq} \frac{2\pi(p(2-l)+q(1-l))}{D_l} e^{i\mathbf{G}.\mathbf{x}} \qquad (7)$$

where l is also an index with values 1 and 2 and

$$C_{ij}^{pq} = \frac{1}{A_c} \int C_{ij}(x_k)\ e^{-i\mathbf{G}.\mathbf{x}} d\mathbf{x} \qquad (8)$$

Similarly, the density $\rho(x_k)$ is also expressed with respect to the Fourier coefficients and is expressed as

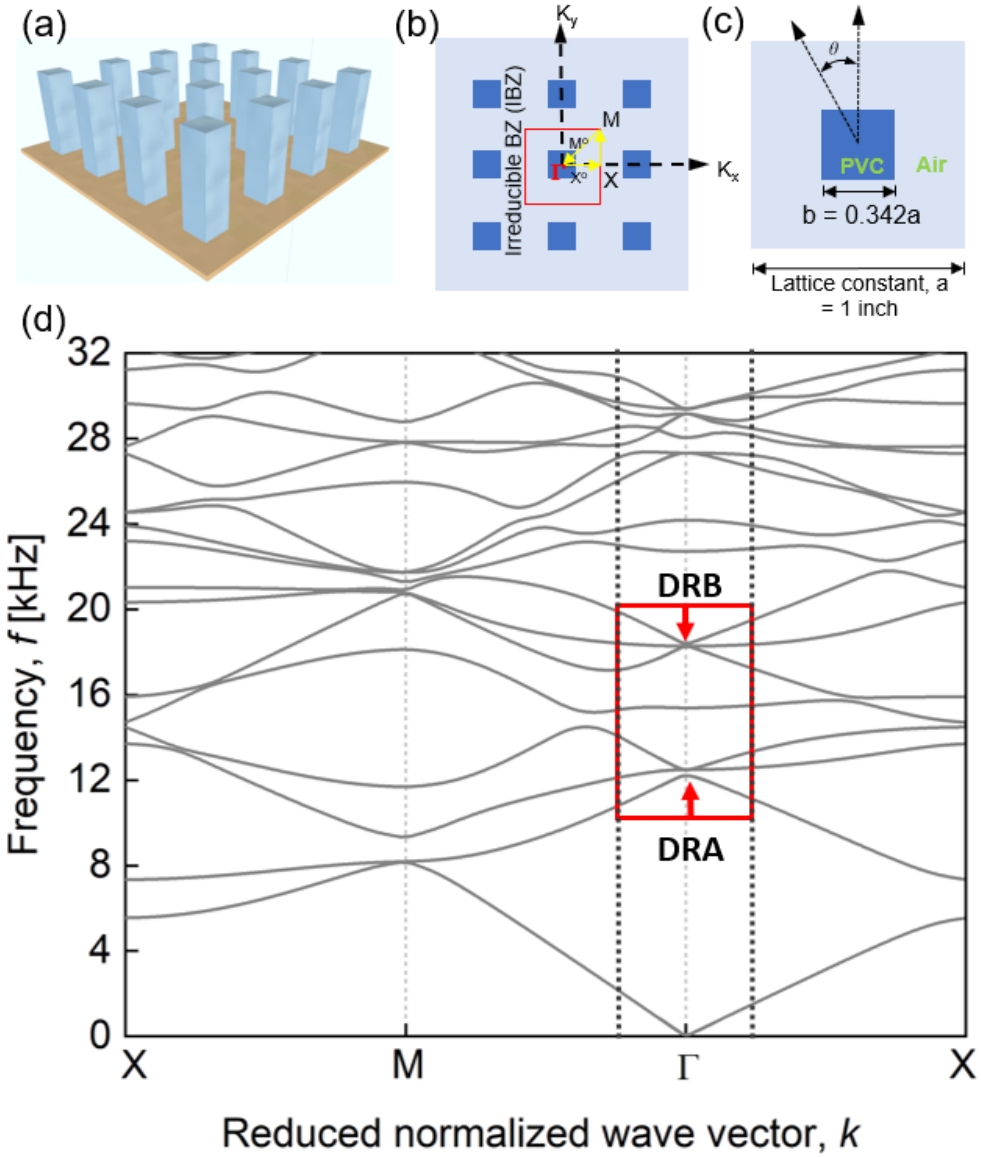

Figure 4.1: (a) Schematic representation of the 2-dimensional periodic systems of hard square rods in a square lattice. The filling fraction is 0.1169 and the square array has the same orientation as the lattice. (b) Transverse cross-section of 2D square lattice in a 3 x 3 supercell with 9 squares of b=0.342a (where a=lattice constant) hosted in air media, depicting the irreducible BZ with wave-vector directions (ΓX-XM-MΓ). (c) Schematic view of a single PnC inside irreducible BZ composed of PVC, where the two constituents are denoted by white and blue as air and PVC rods, respectively. (d) Acoustic band structure of PVC square rods with filling fractions F = 0.1169 embedded in an air host. The rotational angle is Θ = 0°. The colored blocked regions around the Γ point denote probable Dirac region A (bottom) and Dirac region B (top)

$$\rho^{pq} = \frac{1}{A_c} \int \rho(x_k)\ e^{-i\mathbf{G}.\mathbf{x}} d\mathbf{x} \qquad (9)$$

A generalized expression for the modulus or density is thus expressed as

$$\alpha^{pq} = \frac{1}{A_c} \int \alpha(x_k)\ e^{-i\mathbf{G}.\mathbf{x}} d\mathbf{x} \qquad (10)$$

where $\alpha(x_k)$ is equivalent to $C_{ij}(x_k)$ or $\rho(x_k)$

Substituting Eq. (8) into Eq. (7) and then modifying Eqs. (7) and (8) into Eq. (1) obtains two governing equations in a generalized form as follows

$$\begin{aligned}\sum_m \sum_n \sum_p \sum_q \Bigg[& A_{mn} C_{11}^{pq} e^{i(\mathbf{k}+\mathbf{G_{pq}}+\mathbf{G_{mn}}).\mathbf{x}} \left(k_1 + \frac{2\pi m}{D_1}\right)\left[-k_1 - \frac{2\pi m}{D_1} - \frac{2\pi p}{D_1}\right] \\ & + \frac{1}{2} A_{mn} C_{66}^{pq} e^{i(\mathbf{k}+\mathbf{G_{pq}}+\mathbf{G_{mn}}).\mathbf{x}} \left(k_2 + \frac{2\pi n}{D_2}\right)\left[-k_2 - \frac{2\pi n}{D_2} - \frac{2\pi q}{D_2}\right] \\ & + B_{mn} C_{12}^{pq} e^{i(\mathbf{k}+\mathbf{G_{pq}}+\mathbf{G_{mn}}).\mathbf{x}} \left(k_2 + \frac{2\pi n}{D_2}\right)\left[-k_1 - \frac{2\pi m}{D_1} - \frac{2\pi p}{D_1}\right] \\ & + \frac{1}{2} B_{mn} C_{66}^{pq} e^{i(\mathbf{k}+\mathbf{G_{pq}}+\mathbf{G_{mn}}).\mathbf{x}} \left(k_1 + \frac{2\pi m}{D_1}\right)\left[-k_2 - \frac{2\pi n}{D_2} - \frac{2\pi q}{D_2}\right]\Bigg] \\ = & -\omega^2 \sum_m \sum_n \sum_p \sum_q A_{mn} \rho^{pq} e^{i(\mathbf{k}+\mathbf{G_{pq}}+\mathbf{G_{mn}}).\mathbf{x}} \qquad (11)\end{aligned}$$

$$\begin{aligned}\sum_m \sum_n \sum_p \sum_q \Bigg[& A_{mn} C_{21}^{pq} e^{i(\mathbf{k}+\mathbf{G_{pq}}+\mathbf{G_{mn}}).\mathbf{x}} \left(k_1 + \frac{2\pi m}{D_1}\right)\left[-k_2 - \frac{2\pi n}{D_2} - \frac{2\pi q}{D_2}\right] \\ & + \frac{1}{2} A_{mn} C_{66}^{pq} e^{i(\mathbf{k}+\mathbf{G_{pq}}+\mathbf{G_{mn}}).\mathbf{x}} \left(k_2 + \frac{2\pi n}{D_2}\right)\left[-k_1 - \frac{2\pi m}{D_1} - \frac{2\pi p}{D_1}\right] \\ & + B_{mn} C_{22}^{pq} e^{i(\mathbf{k}+\mathbf{G_{pq}}+\mathbf{G_{mn}}).\mathbf{x}} \left(k_2 + \frac{2\pi n}{D_2}\right)\left[-k_2 - \frac{2\pi n}{D_2} - \frac{2\pi q}{D_2}\right] \\ & + \frac{1}{2} B_{mn} C_{66}^{pq} e^{i(\mathbf{k}+\mathbf{G_{pq}}+\mathbf{G_{mn}}).\mathbf{x}} \left(k_1 + \frac{2\pi m}{D_1}\right)\left[-k_1 - \frac{2\pi m}{D_1} - \frac{2\pi p}{D_1}\right]\Bigg] \\ = & -\omega^2 \sum_m \sum_n \sum_p \sum_q B_{mn} \rho^{pq} e^{i(\mathbf{k}+\mathbf{G_{pq}}+\mathbf{G_{mn}}).\mathbf{x}}, \qquad (12)\end{aligned}$$

where $\mathbf{k} = k_1\hat{e}_1 + k_2\hat{e}_2$, $\mathbf{x} = x_1\hat{e}_1 + x_2\hat{e}_2$ $\mathbf{G_{pq}} = \frac{2\pi p}{D_1}\hat{e}_1 + \frac{2\pi q}{D_2}\hat{e}_2$, and $\mathbf{G_{mn}} = \frac{2\pi m}{D_1}\hat{e}_1 + \frac{2\pi n}{D_2}\hat{e}_2$.

For square PnCs with dimension b in an air matrix with equal periodicity $D_1 = D_2 = a$ in both directions, the Fourier coefficients are expressed as

$$\alpha^{mn} = \frac{4\alpha_{sq}}{a^2 G_1 G_2}\sin\left(\frac{G_1 b}{2}\right)\sin\left(\frac{G_2 b}{2}\right), \qquad (13)$$

where α_{sq} is the numerical value of the respective property of a square PnC. Eq. (13) is obtained from a generalized equation derived in Appendix A. It is proposed to tune the Bloch modes to obtain dual Dirac cones at the Γ point in the Brillouin zone. Hence, by rotating the square rod at an angle θ (see the Appendix A), the reciprocal lattice vectors following Eq. (A.14) $G_{1'}$ and $G_{2'}$ in transformed system can be written as

$$G_{1'} = \frac{2\pi}{a}(mcos\theta + nsin\theta) \qquad G_{2'} = \frac{2\pi}{a}(-msin\theta + ncos\theta), \qquad (14)$$

where m and n are the integers defined earlier and a is the lattice constant defined in the Appendix. Hence, both $\mathbf{G_{pq}}'$ and $\mathbf{G_{mn}}'$ are transformed due to the rotation of the square PnCs with their respective integers and are substituted in Eqs. (11) and (12). Eqs. (11) and (12) together create an eigen value problem and at given frequency ω, $\mathbf{k}$ will solve the system of equations. The solution in the $k - \omega$ domain is the dispersion solution. To obtain the converged dispersion relationship using the PWE on the periodic media, the eigen analysis was conducted with 625 reciprocal vectors, which was adequate when m and n were -12 to 12 [23].

4.2 NUMERICAL MODEL:

Apart from the analytical model, a numerical model is also formed for the proposed PnC. An Eigenfrequency analysis has been performed to analyze the dispersion behavior for the proposed PnC. A commercial finite element analysis-based COMSOL Multiphysics software package is used to simulate the wave propagation in the composite metamedia of square PnCs at specific frequencies to visualize the wave fields.

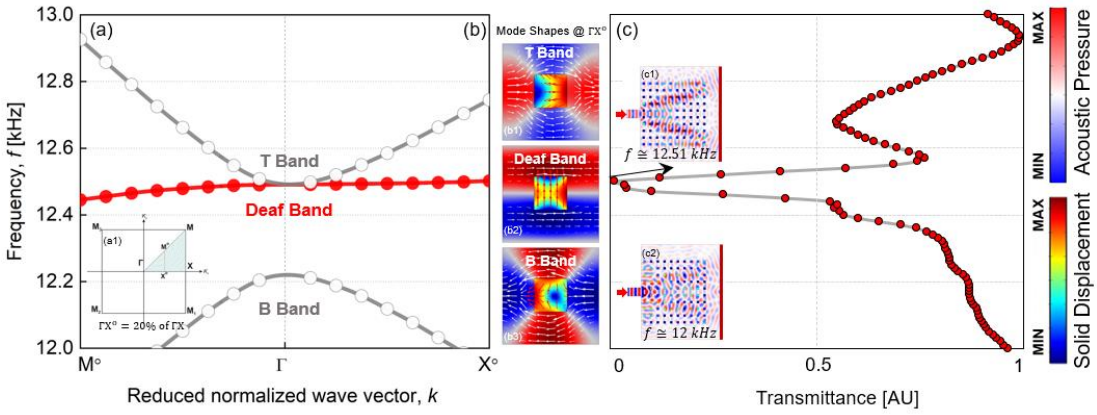

Figure 4.2: (a) Dispersion diagram for the DRA location, showing a small band gap between doubly degenerated 'T band' and 'Deaf band' and a 'B band', the irreducible BZ is demonstrated on the inset as (a1), (b) Respective mode shapes of a unit lattice of 'T band', 'Deaf band' and 'B band' along ΓX normalized wave vector direction. Both the absolute acoustic pressure distribution field and the solid displacement field are shown in two different colormaps, with their respective displacement vectors (white arrowed vectors depicts absolute acoustic pressure and red arrows inside the square PnC depicts solid displacement, c) The wave transmission decreases to zero near the deaf band if transmitted along ΓX [100] (top). The numerically calculated acoustic pressure field and solid displacement fields are shown for a 10×10 PnC matrix, excited at 'Deaf band' frequency and another arbitrary frequency for B band.

4.3 RESULTS AND DISCUSSION

First, tunable periodic square PVC rods (Figure 4.1) in air media with dimension b = 0.342a and filling fraction = 0.1169, where a = lattice constant ≈ 25.4 mm, shown in

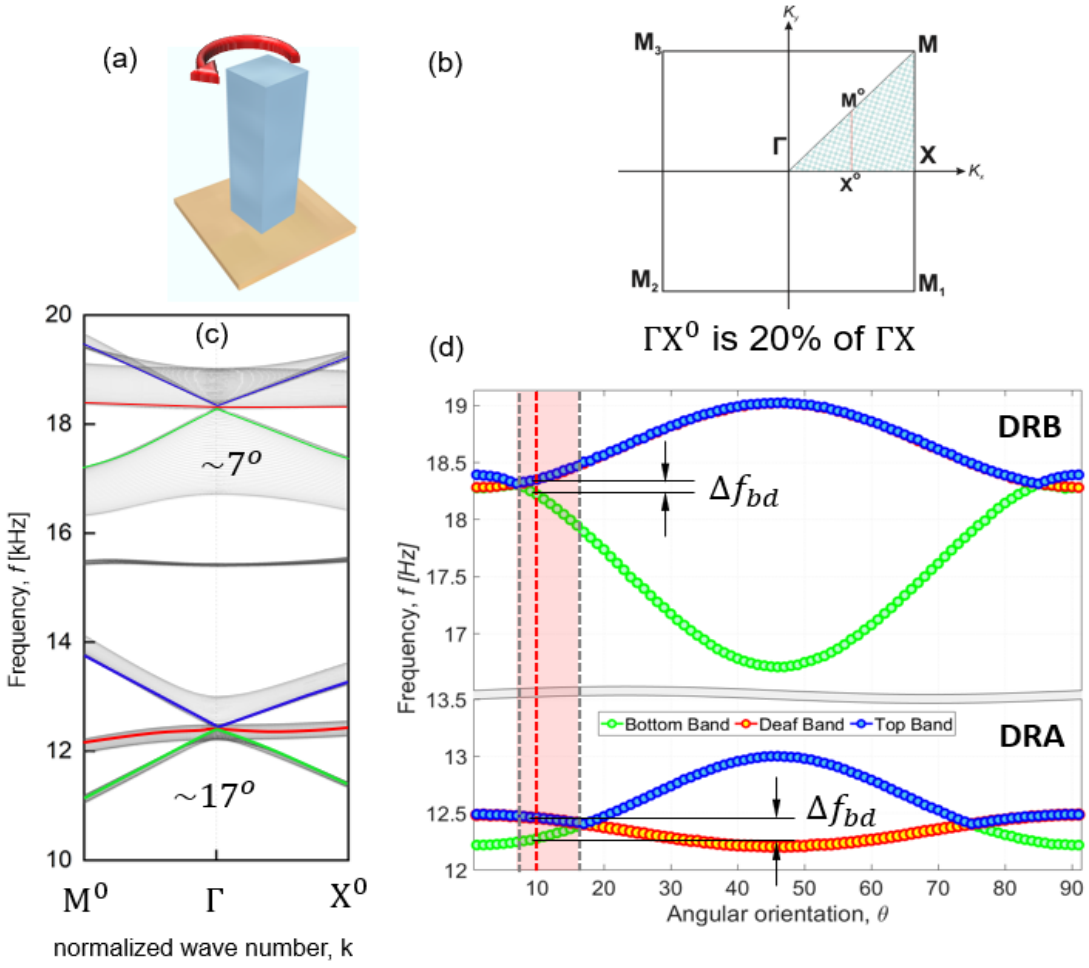

Figure 4.3: (a) Geometric representation of square rod PnCs embedded in the air matrix and rotated counterclockwise (CCW). This angular tuning was conducted at 1o intervals over a range of 0°-90°. (b) First Brillouin zone and normalized wave number segment used in (c), (c) Superposed band structure obtained from different CCW unit cells. The dispersion relationship shows that a Dirac cone is achieved at a ~7° rotation for DRB and at a ~17° rotation for DRA. (d) Modulation of the T, deaf, and B bands as a function of the rotational angle with different CCW unit cells. A red box is identified between ~7° and ~17° where the T and deaf bands are degenerated, but the B band is separated by a band gap Δf_{dh}. The angle of rotation is identified where Δf_{dh} is equal for DRA and DRB.

Figure 4.1b and 1c was used in this study. Using a hypothetical mechanism (shown in Appendix A), it is assumed that all of the square PVC rods in the periodic media can be

rotated at the same time. The first Brillouin zone (BZ), which is the region inside the red square in Figure 4. 1b, is reduced to a smaller region, ΓMX, called the irreducible BZ due to lattice symmetry [81]. The acoustic band structure shown in Figure 4. 1d is obtained inside the irreducible BZ with the wave propagation vector along (ΓX), (XM), and (MΓ), respectively. In the band structure at the Γ point, multiple regions are observed where a single mode and doubly degenerated modes prevail. Two regions are identified in the dispersion bands: (1) Dirac region A (DRA) and (2) Dirac region B (DRB) as shown in Figure 4. 1d. Both regions are identified for the occurrence of potential degeneration. DRB is already triply degenerated, while DRA has doubly degenerated bands and a single bottom band with a partial band gap between them. Multiple Dirac-like cones at the Γ point in a single lattice orientation have not been previously reported. By closely observing DRA and DRB and elucidating the geometric perturbations, it was found that tuning pivoting the deaf bands, they may create predictive degeneracy [82] at different frequencies.

As reported in condensed matter physics, the generation of a triply degenerated point at the center of a Brillouin zone (BZ) or Γ point is the result of accidental degeneracy [68, 83]. As this cannot be predicted in advance, converting this accidental degeneration into a deterministic degeneracy is challenging. We propose a tunable engineered PnCs system in which multiple Dirac-like points are generated at the Γ point by tuning the orientation of the solid resonator with respect to the BZ.

Infinite squared PVC rods arranged in squared arrays are used at an initial 0^{o} rotation (Figure 4.1a) with respect to the lattice orientation. By carefully tuning the structure i.e. by rotating the phononic crystals counterclockwise, the dispersion behavior may produce triply degenerated points at multiple frequency locations at the center of the

BZ (at Γ point). Close observation of both regions (DRA and DRB) indicates that the bands (red in Figure 4.2a) that are nearly flat or parallel to the wave vector axis are the deaf bands. We designate the T bands as the top bands and the B bands as the bottom bands. To prove the deaf bands' deafness, the acoustic pressure mode shapes and solid deformations of PVC rods for DRA are presented in Figure 4.2b (only DRA is shown). By investigating the acoustic pressure distribution in air (of DRA and DRB), it is apparent that the T and B bands with mutual orthogonal quadrupolar modes are properly symmetric with respect to the incident plane wave along the ΓX [100] and MΓ [010] directions. However, both deaf bands are anti-symmetric with respect to the incident wave direction, lacking group velocity. The transmission study validates the band deafness ΓX [100], demonstrating almost zero transmission near the deaf band (Figure 4.2c). Thus, the deaf band remains inert to any kind of normal-incident plane wave due to anti-symmetry. Pivoting these deaf bands to form Dirac-like cones is relatively new and is presented herein for a single lattice structure at multiple frequencies simultaneously.

The band structures at DRA and DRB are investigated with their respective T, deaf, and B bands. These three specific bands between ΓX^o and ΓM^o (Figure 4.3c) are obtained from separate eigen solutions when the unit cells are rotated about their respective central axes (Figure 4.3a). Solutions at every 1^o interval (from 0^o to 90^o) are superposed and summarized in Figure 4.3c. Under different angular rotation, the T, deaf, and B bands are moved/modified within ~1 kHz and ~3 kHz frequency ranges at the DRA and DRB locations, respectively. Eigen frequency solutions at the Γ point as a function of rotational angle θ when the unit cells are rotated are presented in Figure 4.3d. At DRA, an absolute Dirac cone was achieved when the rotational angle was ~17^o. Similarly, at DRB, an

absolute Dirac cone was achieved when the rotational angle was ~7°. As shown in Figure 4.3d, the eigen solutions are symmetric with respect to the rotation angle 45°. To simultaneously demonstrate the Dirac cone behavior at DRA and DRB, an important observation should to be made that will further guide the selection of a common frequency. At both Dirac cone locations, there is only a narrow window of θ where the T and deaf bands are doubly degenerated but the B band is separated by a small frequency band gap Δf_{db} between the B and deaf bands. This small window is highlighted with a red box in Figure 4.3d. In this window, the B band moves up in the frequency scale to triply degenerate and merge with the deaf band. As the unit cells rotate, a Dirac cone is generated at a specific angle of rotation. This does not happen anywhere else over the θ range. A mirror image of the same window occurs between ~73° and ~83°.

When the deaf and B bands are doubly degenerated, the T band is separated with a band gap between the T and deaf bands, and the Dirac cones experience significant alterations. Hence, the Dirac cones reported earlier are dominated only between the red window shown in Figure 4. 3d. This window may be located over a different range of θ axes depending on the filling fraction and a/b ratio. Although the specific Dirac cone is dominant at a specific angle of rotation called the Dirac rotation, the Dirac phenomena does not disappear as long as the doubly degenerated band is formed by the T and deaf bands. This happens only within the red box in Figure 4. 3d. However, when the B band is farther away from the doubly degenerated frequency point degenerated by the T and deaf bands, the Dirac cone behavior slowly diminishes. Although the Dirac cones dominated in the window at both DRA and DRB frequency ranges, they tend to diverge from a common angular rotation. When both DRA and DRB have equal Δf_{db} frequency gaps between the

doubly degenerated bands and B bands, the Dirac cone behavior prevails at DRA and DRB. A minute but equal Δf_{db}=~166 Hz was obtained at $\theta = \sim 9.7^{o}$ through non-linear interpolation within the red window in Figure 4. 3d. This angular rotation is unique and non-ambiguous for the predictive design of the Dirac cones at multiple frequencies simultaneously. All of the studies are presented at $\theta = 9.7^{o}$.

To establish if fully triply degenerated points are created at the center of the Brillouin zone, equifrequency contours are presented in Figure 4. 4. As described in the literature, quadro-degenerated points are reported where 4 bands intersect at a Dirac point, called a double Dirac-like cone [84, 85]. However, in this study, six bands simultaneously generate two Dirac cones at two distinct frequencies. Henceforth, we call our deaf band-based optimized formation of Dirac-like cones multifrequency Dirac cones (MDC). Figure 4. 4a and 4b denote the MDC Dirac cones (θ = 9.7^{o}) and present 3D equifrequency surfaces

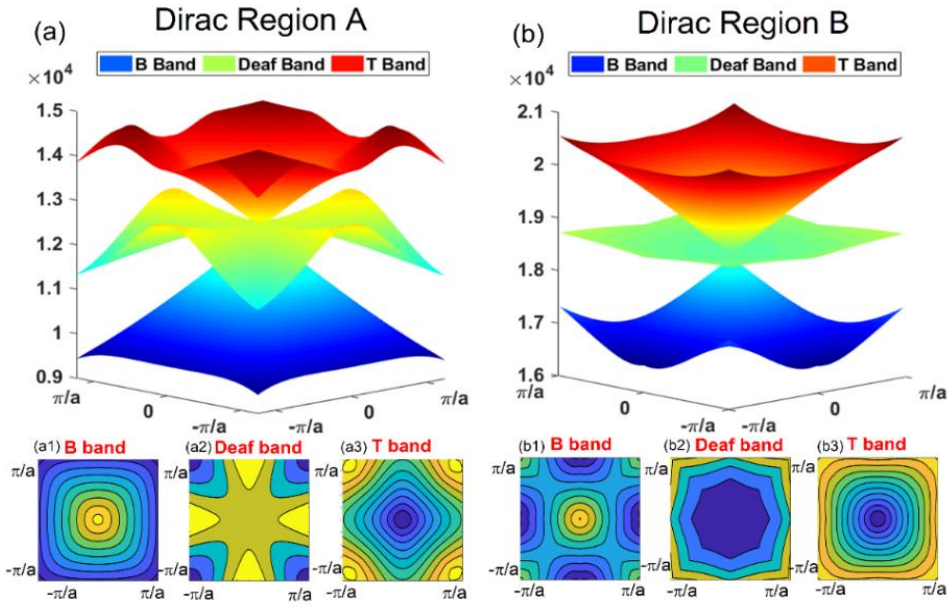

Figure 4.4: (a) and (b) The equifrequency contours (EFC) for DRA and DRB when the bands are triply degenerated at Θ = 9.7o showing nearly triple degeneracy or Dirac cones at Γ of the BZ. The equifrequency surfaces (EFS) or contour maps of the acoustic band frequencies of the bands (T, deaf, and B bands, respectively) for both regions displayed in the whole area of the first BZ are shown in the insets.

(EFS) for the B, deaf, and T bands, respectively (4a1-4a3 and 4b1-4b3). As frequency decreases the equifrequency contour gradually transforms from noncircular shapes to concentric circular shapes for a T band. This indicates gradual convergence to a point [68]. And such phenomenon is likely to generate threefold Bloch mode comprising Dirac-like cone. The validation of the presence of Dirac-like points is confirmed by numerical frequency-domain studies with a meta-structure produced with the θ = 9.7º rotated staggered square PnCs as shown in Figure 4. 5.

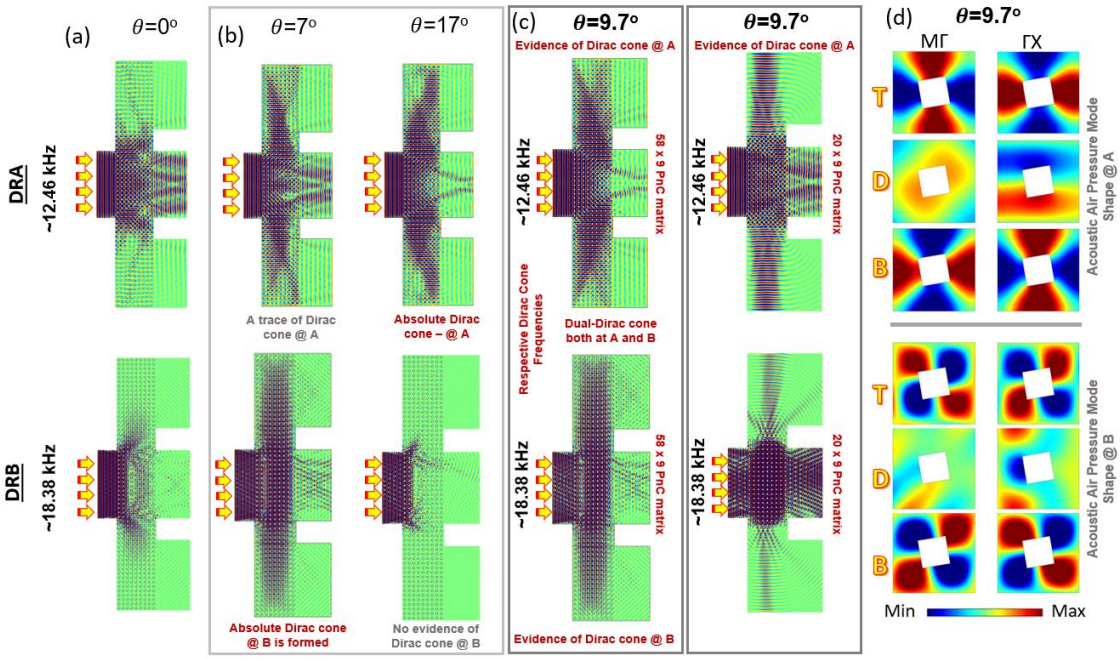

Figure 4.5: (a) Wave propagation and acoustic pressure distribution in a PnC guide with a 58 × 9 matrix of PVC/air media at DRA and DRB at excitation frequencies at the Dirac point f = ~12.46 kHz and f = ~18.374 kHz, respectively. The square PnCs are not rotated. (b) Wave propagation in the PnC guide at DRA and DRB at excitation frequencies at the Dirac points. The square PnCs are rotated at angles of 7o (left) and 17o (right). DRB demonstrates Dirac phenomena at 7o, and DRA demonstrates Dirac phenomena at 17o. (c) Wave propagation in the PnC guide at DRA and DRB at excitation frequencies at the Dirac points. In this arrangement, the square PnCs are rotated at a 9.7o angle. Wave propagation behavior for channels without the PnCs have also demonstrated the presence of the Dirac phenomena, where the PnC matrix have been reduced to 20 × 9. Both the cases for both the frequencies demonstrate perfect Dirac phenomena. (d) Absolute acoustic pressure mode shapes of the unit cells in the MΓ and ΓX directions for DRA and DRB, respectively, for the T, deaf, and B bands when the PnCs are rotated at a 9.7o angle.

To prove the presence of Dirac-like points, a periodic arrangement of 58×9 solid PVC square rods with filling fraction f = 0.1169 are placed in an air medium. Frequency domain numerical experiments are conducted using the finite element analysis-based commercially available COMSOL Multiphysics software package. The square PnCs are actuated by a guided plane wave source located ~110 mm away from the air-PVC interface. Absorbing boundary conditions are enforced around the boundary. The acoustic pressure field distribution at the DRA and DRB regions are shown in Figure 4. 5. Orthogonal wave transportation at Dirac-like frequencies, as reported earlier [68], are visualized using the arrangement shown in Figure 4. 5. The DRA and DRB regions demonstrate their own unique features that are explained by their respective wave-dispersion behavior.

The acoustic pressure distribution in the metastructure is shown in Figure 4. 5a, where the PnCs are not rotated and regular arrangement of the square matrix at $\theta = 0°$ is demonstrated. It shows no sign of Dirac phenomena in the grid. However, when the square PnCs in the grid are rotated together at an angle $\theta = 7°$, as predicted, DRB at frequency ~18.38 kHz demonstrates absolute Dirac phenomena. DRA at frequency ~12.46 kHz also shows a trace of Dirac cone behavior [50], but it is not fully developed. When the square PnCs in the grid are rotated together at an angle $\theta = 17°$, as predicted, DRA at frequency ~12.46 kHz demonstrates absolute Dirac phenomena. But the Dirac behavior at DRB is totally dispersed. This parity can be explained by Figure 4. 3d. As the angle of rotation increases, DRB experiences a large separation/band gap (Δf_{db}) between the B band and the doubly degenerated T and deaf bands. This is not the case for DRA when the rotational angle was $\theta = 7°$. At DRA, Δf_{db} slowly changes due to the relative curvature of the B and deaf bands as the angle of rotation changes between 7º and 17º. Guided by the Δf_{db} gap

between the B and deaf bands at DRA and DRB, an equal gap of ~166 Hz was identified at $\theta = \sim 9.7°$ where the Dirac phenomena predictively prevailed. To prove this, a numerical experiment was conducted at both Dirac frequencies. The acoustic pressure distribution in the grid at DRA and DRB is shown in Figure 4. 5c when the PnCs are rotated together at an angle $\theta = 9.7°$. The incident plane wave propagates in the actuation direction with no distortion at $f = 10\ kHz$ (not shown), but a drastic orthogonal bent line is demonstrated when the actuation frequency increases near the Dirac-like frequency for DRA (~= 12.46 kHz) and DRB (~= 18.38 kHz) as shown in Figure 4. 5c. Minimal acoustic energy transmits in the actuation direction, forming an apparent band gap. Keeping the phase shift nearly zero, the plane wave travels along the PnCs orthogonally with respect to the actuation direction (Figure 4. 5c). This establishes a prominent energy shift, producing a 45^o bifurcation pattern. The wave front bends another 90^o toward the original actuation direction (ΓX), keeping the plane wave front relatively intact. Due to its anti-symmetry, the deaf band exhibits strong spatial localization and allows the wave front to propagate orthogonally.

In the same Figure 4. 5c we present a different scenario when the spread of meta structure or the PnCs guide is reduced to the length of the acoustic source. In this case there are only 20×9 PnCs instead of 58×9 PnCs. At the DRA frequency orthogonal transport prevails in the air media beyond the PnCs, but the intensity of the normal transport is increased as well. This is because the meta structure guide does not have enough PnCs to carry the energy in the orthogonal direction. At mutually orthogonal directions, the intensity of the propagating waves is comparable when the length of the PnCs guide in the orthogonal direction is reduced. This phenomena at the Dirac cone provides opportunity to

exploit the pseudo diffusion, discussed later in this manuscript. Similar behavior is also evident at DRB frequency, but here the wave is more focused than flat crested wave fronts in DRA.

To further demonstrate the reason for the Dirac phenomena, the acoustic pressure mode shapes of the T, deaf, and B bands for wave propagation along the ΓX and MΓ directions at DRA and DRB frequencies are shown in Figure 4. 5d. In both the DRA and DRB cases, the T and B band mode shapes are symmetric quadrupolar mode shapes with opposite pressure distributions. When the mode shapes are superposed at the Dirac frequencies, the T and B mode shapes cancel each other, causing the deaf band mode shape to dominate. The local dispersion behavior of the T and B bands with degenerated acoustic pressure mode shapes are quadrupolar and mutually orthogonal; in contrast, the deaf band mode is dipolar (for ΓX) (Figure 4. 5d). Hence, at the Dirac frequency, both the T and B bands nullify each other, maintaining the dipolar deaf band mode dominance. A 45^{o} bent

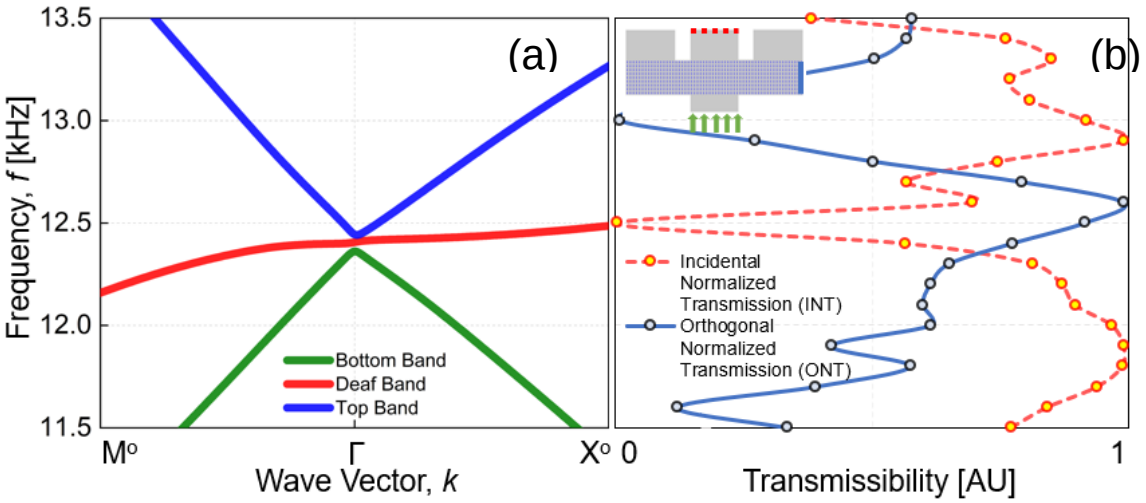

Figure 4.6: (a) A close-up view of the DRA dispersion relationship at Θ = 9.7o. (b) A comparison of the numerical results of the acoustic transmission (normalized) excited along the *ΓX* direction with the DRA frequencies. The peak transmission occurs at the Dirac-like frequency along the orthogonal direction (ONT: blue) shown in the PnC arrangement inset, while the transmission decreases along the actuation direction (INT: red) at the respective frequencies, validating the phenomenon demonstrated in Figure 4.5.

line helps the dipolar deaf mode carry the wave energy orthogonally like origami. The T and B bands' quadrupolar local dispersion modes rotated by 90° between the MΓ and ΓX directions of propagation at both DRA and DRB (Figure 4. 5d) frequencies. *To summarize, there are other scenarios where flat bands are achieved. They are due to the local resonance of the PnCs and yield zero-group velocity. Although Deaf band is almost flat, the phenomena inside the material is not due to the local resonance but due to antisymmetric mode shape at the triple degenerated state, as depicted in Figure 4. 5.*

The transmissibility study of DRA at $\theta = 9.7^{o}$ in Figure 4. 6 shows that the transmission decreases to approximately zero along the ΓX direction, while the

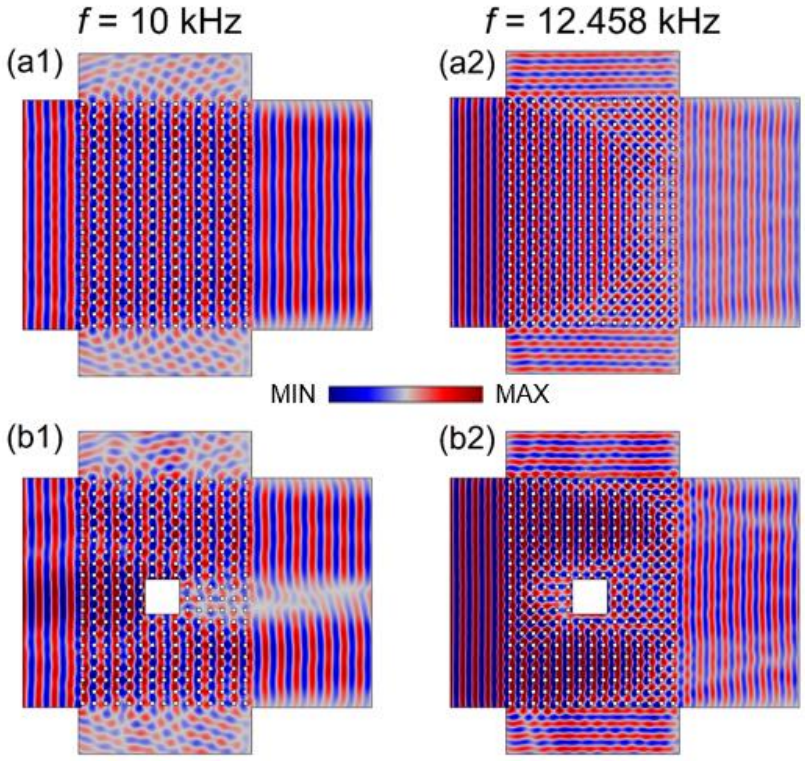

Figure 4.7: Numerical experiments showing the absolute pressure field distribution where the waves can pass through a waveguide with an embedded obstacle. (a1) and (a2) The case when no square steel rod is inserted into the middle of the PnC slab. The incident plane wave frequencies are 10kHz and 12.458 kHz, respectively. (b1) and (b2) The same case as shown in (a) except that we inserted a square steel block to be cloaked.

transmission remains maximum along the orthogonal PnCs (XM) only when the PnCs guide is at least three times larger compared to the acoustic source dimension.

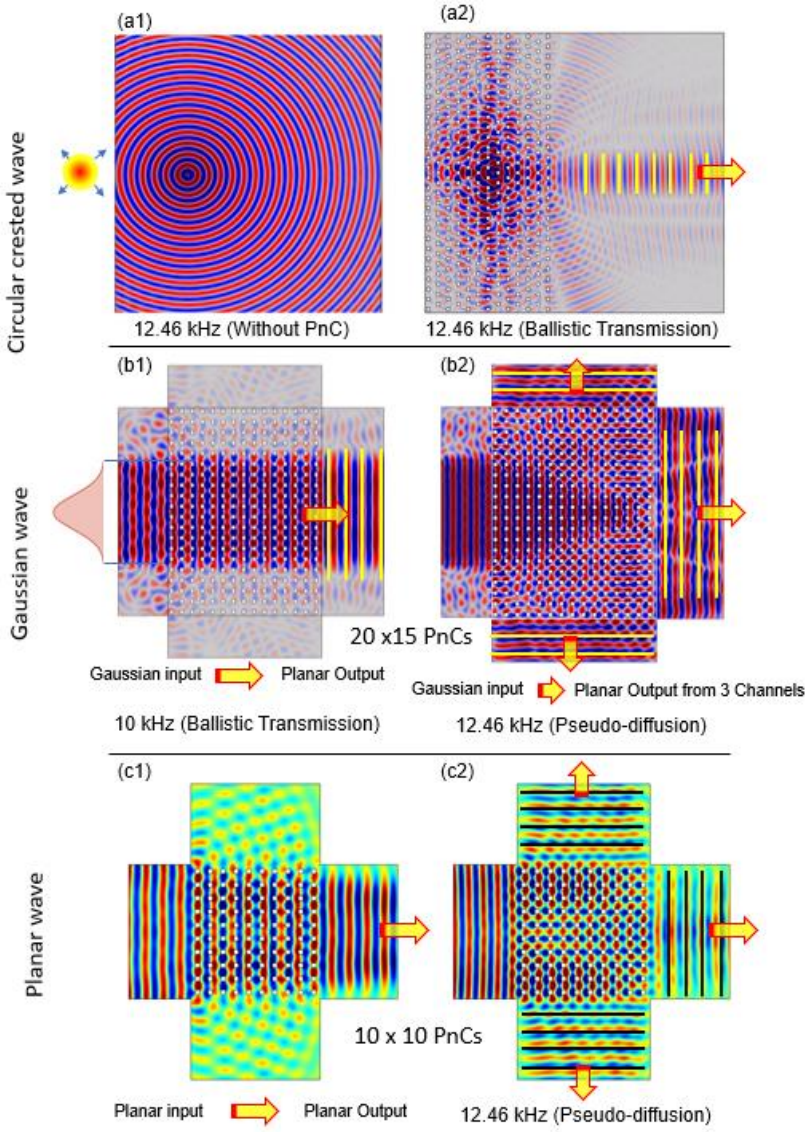

Figure 4.8: (a1) Pressure field distribution in air media when a circular crested wave front is excited by a pseudo-point source at the Dirac frequency with no PnC ribbon. (a2) A prominent ballistic transmission along the ΓX direction is evident when the square rod PnCs are introduced at f = ~12.46 kHz. A PnCs ribbon with a 20 x 15 matrix acting as a perfect acoustic collimator and diffuser. (b1) A Gaussian wave source is excited at frequencies below the Dirac frequency, output wave transmission is planar wave. (b2) A Gaussian wave source is excited at the Dirac frequency. Wave diffusion due to orthogonal transport is eminent. PnCs ribbon with 10x10 PnCs for experiments: c1) A planar wave source is excited at frequencies below the Dirac frequency, output wave transmission is planar wave. (b2) A planar wave source is excited at the Dirac frequency. Wave diffusion due to orthogonal transport is eminent.

Due to excitation of an accidental threefold degenerate Bloch mode, the spatial phase reconstruction is reported and discussed in phononics at the high symmetry Γ point . Utilizing this property, acoustic cloaking also develops with a nearly flat band (deaf band) around Γ point of the BZ. Acoustic cloaking has attracted significant attention over the past few years [86, 87].

As shown in Figure 4. 7, a 75 mm x 75 mm square steel (AISI 4340) block is embedded in the middle of the PnCs guide with 20 × 15 matrices arrayed in air media. The square steel block is the object to be cloaked. The plane wave source is placed approximately 127 mm away from the left interface of the air-PVC PnC ribbon. Two different combinations are used to prove the acoustic cloaking: the first has no square steel block (Figure 4. 7a1 and 7a2) and the second has a square steel block (Figure 4. 7b1 and 7b2). Both conFigure 4.urations experience the incident plane wave. These conFigure 4.urations are excited at two different frequencies, one at 10 kHz and the other at a DRA Dirac frequency of 12.46 kHz. As shown in Figure 4. 7a1 and 7a2, typical orthogonal wave transportation occurs with no cloaking object inside the PnCs. As shown in Figure 4. 7b2, it is evident that the acoustic wave can transmit through the PnCs as if the square steel block does not exist. Comparing Figure 4. 7a2 and 7b2, the transmitted acoustic wave's planar wave front remains undistorted inside and outside the PnCs. However, the planar wave severely distorts when excited at a frequency of 10 kHz as shown in Figure 4. 7b1.

Apart from acoustic cloaking, a spatial phase reconstruction along with wave front reshaping, pseudo-diffusion, and acoustic collimation are studied in past few years [88, 89]. Such phenomena are also present in our proposed deaf band based tuned angle of the PnCs. The absolute acoustic pressure field distributions are demonstrated with incident

Gaussian waves with planar wave fronts and incident circular waves with concentric wave fronts. We show the normalized pressure field inside the PnCs guide with circular crested wave fronts at the Dirac frequency. In the absence of PnCs, the circular wave front maintains its phases and wave shape with no distortion (Figure 4. 8a1) at the Dirac frequency ~12.46 kHz. However, once the PnCs are placed inside the air media, the propagation of the circular wave front from a source in the PnCs exhibits a different phenomenon. The transmitted circular acoustic wave transforms into a plane wave with a planar wave front after leaving the PnCs, indicating beam collimation and ballistic wave transmission (Figure 4. 8a2). The acoustic wave transmission inside a 20 x 15 PnCs guide arranged with Dirac rotation is studied when a Gaussian wave ($\mu = 0$ and $\sigma = 2.5e3$) is incident along the ΓX direction. The incident wave's amplitude across the actuator's width varies using a Gaussian function. The Gaussian wave input transforms into a planar wave output with equal amplitudes along the planar wave front due to the presence of the PnCs. However, when the actuation frequency increases to 12.46 kHz, wave diffusion occurs, creating planar wave fronts through all three outlets as shown in Figure 4. 8b2. Surprisingly when the smaller number of PnCs are used in the guide, wave diffusion not only happens along the incident direction but also wave also diffuses with planar wave front in the orthogonal direction. Orthogonal transport prevails even above 12.46 kHz up to ~13kHz. This is in contrast to the Figure 4. 6 obtained from a matrix of 40x7 elements. Hence, the presence of the PnCs plays a vital role in reconstructing the phase to form collimated plane waves and wave diffusion, which may have practical applications in engineering and biomedical science when waves are required to predictively guide in fluid and solid media. Similar scenario with planar wave incident is shown in Figure 4. 8c1 and Figure 4. 8c2 on

a comparatively smaller setup with 10 x 10 PnCs, suitable for performing laboratory experiment discussed in the following section.

4.4 EXPERIMENTAL STUDY

Fabrication of PnCs and creating an experimental set up with high numbers of element used in the numerical experiments shown in Figure 4. 5 is challenging and thus the phenomena are demonstrated on a comparatively smaller setup with 10x10 PnCs as shown in Figure 4. 9. We will demonstrate the scenario presented in Figure 4. 8c1 and 8c2 experimentally. To experimentally validate the numerical results, the incident wave transport, IT and orthogonal wave transport, OT in Figure 4. 8c1 and 8c2 were investigated over a range of frequencies from 10 kHz – 14 kHz, which includes the 'DRA' Dirac-like frequency at ~12.46 kHz. The coefficients of transmissibility along IT and OT were obtained from numerical experiments over the same frequency range. Transmission energy measured in decibels (dB) obtained from the experiments are mapped between zero to one, where, one being the maximum transmission and zero being the minimum transmission. Please note that when PnCs guide is smaller wave output from IT and OT will be comparable and closer to each other through the mechanism of pseudo diffusion.

First, 100 commercially available extruded PVC cylinders of b = 0.348a = ~8.84 mm (the lattice constant a = 25.4 mm) were arranged in a 10 × 10 matrix as shown in Figure 4. 9. The PVC cylinders were cut to 4" length elements and machined to have a smooth surface to minimize the experimental error. Acoustic pressure was created (Figure 4. 9a-e) using a speaker (Pyle Gear (PLG 3.2) 3.5" 2-way coaxial, 120-watt, 4-ohm impedance) capable of generating frequencies up to 18 kHz. To absorb the acoustic energy and to avoid reflection from the boundary of the experimental setup, acoustic dampers (0.5-inch-thick

foam sheets) were used at the boundaries (Figure 4. 9d & 9e). To simulate the absorbing boundary conditions, a channel made of foam was designed to guide the incident acoustic wave. A condenser pressure microphone (Sterling S30 Class-A FET 30 Hz –18 kHz) was used to detect the acoustic transmission (Figure 4. 9a, 9d & 9e), placed at incident (for IT) and orthogonal (for OT) directions. The microphone was connected to a PreSonus AudioBox 44VSL signal conditioner and then the conditioner was connected to a computer with a USB connector where an audio signal analysis software (Studio One3 x64) was used to record the signals (Figure 4. 9a). Finally, the spectral analyses were performed automatically using the software where, amplitude of the transmitted wave at frequencies 10 kHz – 14 kHz at 100 Hz interval were collected. The output was recorded in a csv data file for further plotting using Matlab. Twenty-seven date sets were collected for each IT and OT experiments at each frequency. The microphones were placed at nine different

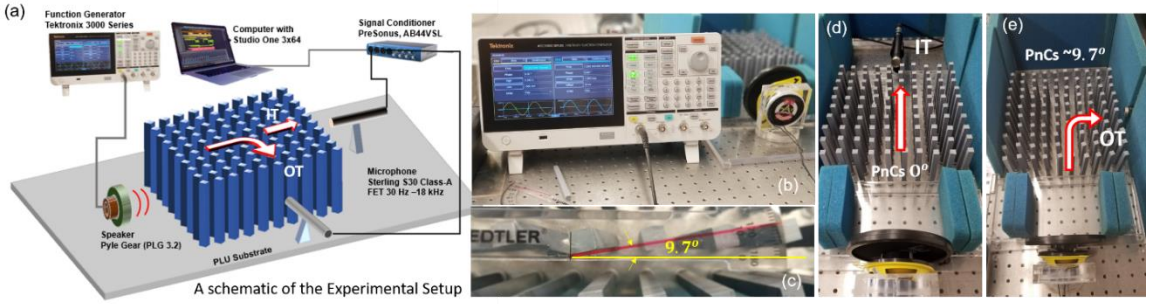

Figure 4.9: (a) A schematics of a generalized experimental setup showing Orthognal Transport (OT) experiment and Incident Transport (IT) experiments, where PnCS rotation can be manually controlled (b) Setup showing excitation of the speaker with a Function Generator generating continuous sine wave. c) Rotation of the PnCs by $\sim 9.7^{o}$. (d) IT experimental setup with PnCs rotation 0^{o}(results not shown) e) OT experimental setup with PnCs rotation $\sim 9.7^{o}$(results shown in Figure 4. 10)

locations and three sets of data were collected from each location. With 10 PnCs in this setup, there were 9 air outlets between the two consecutive PnCs. These 9 locations were used to probe the microphone. The recording channel was open for 10 seconds for every

experiment. First, the data were collected for IT and then for OT, when the PnCs were placed without any rotation ($\theta = 0^o$ Figure 4. 9d). Next the data were collected for IT and OT, when PnCs were rotated by $\sim 9.7^o$ (Figure 4. 9c and 9e).

Results obtained from the experiment described above is summarized in Figure 4. 10. Figure 4. 10a shows the results on transmission coefficients obtained from the numerical simulation setup (with $\theta = \sim 9.7^o$) shown in Figure 4. 8c1 and 8c2. Both IT (Figure 4. 8c1) and OT (Figure 4. 8c2) coefficients as functions of frequency between 10 kHz and 14 kHz is presented at an interval of 1 Hz. A red zone between 12 kHz and 13 kHz is identified when the DRA frequency is approximately ~12.46 kHz. It can be seen that the IT coefficient is close to one till the frequency ~11.5 kHz and close to ~0.6 near the DRA frequency. As indicated by the pseudo diffusion, similar to the IT transmission, the OT coefficients are close to zero till the frequency ~11 kHz, but gradually increases after ~11.5 kHz, and get closer to the ~0.6 at the DRA frequency. Although the experimental results did not confirm the exact values obtained from the numerical results at respective frequencies, certainly the Dirac phenomena is apparent and dominant in the experiments, qualitatively. Figure 4. 10b shows the boxplot created from the twenty-seven experimental transmission coefficients obtained at each frequency step (at 100 Hz interval). The data shows the change in both the IT and OT coefficients obtained experimentally as a function of frequency between 10 kHz – 14 kHz at an interval of 100 Hz. Figure 4. 10c shows only the boxplot of the experimental OT coefficients as a function of frequency for better clarity. From the experimental results it can be seen that the medians of the OT coefficients are significantly lower compared to the median of the IT coefficients below 11 kHz. These two states are easily distinguishable and mutually exclusive. Near the DRA

frequency medians of the OT coefficients are consistently higher than the IT coefficients between the range 12 kHz to 13 kHz. This indicates that the orthogonal propagation tends to dominate near the Dirac frequency. However, near the Dirac frequency ~12.3 and ~12.4 kHz, the boxplots (blue boxes for IT and red boxes for OT) are approximately overlapped each other's with very close median values. When, near the Dirac frequency, the numerical result indicates almost equal IT and OT coefficients, the experimental results indicate higher median of the OT coefficients than the IT coefficients. This small discrepancy might

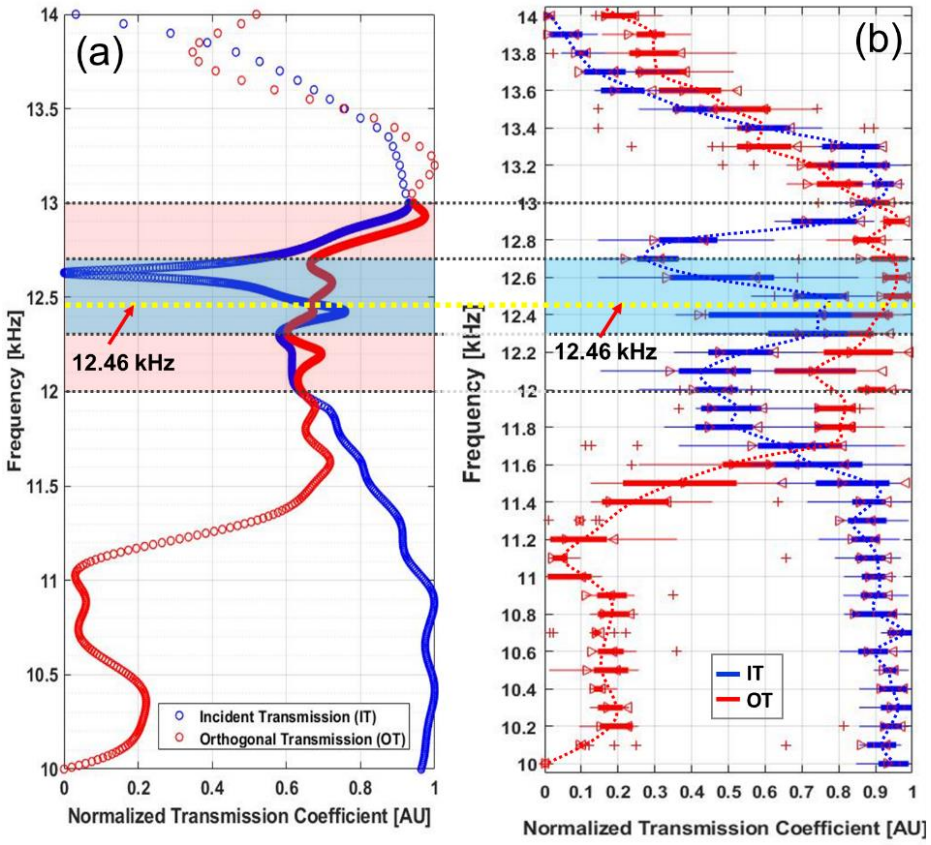

Figure 4.10: PnCs with ~9.7^{o} rotation (a) Simulation: Transmission coefficients mapped between 0-1, obtained from numerical simulation, IT indicates, incident transmission and OT indicate orthogonal transmission as shown in Figure 4. 9a. b) Experiment: Median, box with whiskers shows the variation of the transmission coefficients due to IT and OT over the frequency range 10-kHz -14 kHz.

be due to the fabrication and placement of the PnCs and also the discretization of the frequency scale, which was 1 Hz in numerical simulation, and was 100 Hz in the experiments. Nonetheless, the OT of acoustic wave at Dirac frequency is validated.

4.5 CHAPTER SUMMARY

This study proposed deaf band-based angular tuning to generate multiple triple degeneracies (Dirac cones) called multi-Dirac cones at the center of the BZ. The predictive optimization process discussed in this article demonstrated the dual Dirac cone. Dirac cones were achieved near the region where near zero-group velocity flat or deaf bands exists. By maintaining the same filling fraction and without replacing the crystal, deaf band-based angular tuning was accomplished, yielding multiple degenerated regions. The rotation effects of high-density inserts in low-density hosts were also investigated. The widening of the dispersion bands was maximized or minimized, modulating the deaf band, demonstrating the dual Dirac phenomenon. An analytical approach to solving the eigenvalue problem of a square rod in a fluid media was presented. The wave transmission behavior through square PnCs wave guides were studied by calculating the absolute acoustic pressure using finite element analysis-based software. Mode identification, the relationship between the mode shapes, and their role in deaf band-based angular tuning were analyzed and discussed in depth. Different acoustic application-based phenomena that occurred at Dirac-like points, such as acoustic orthogonal transportation, acoustic phase reconstruction, and acoustic collimation including ballistic transmission and pseudo-diffusion were also studied and realized using the proposed numerical model. The correlated acoustic cloaking and wave front reshaping effects were also demonstrated. Further acoustic pseudo diffusion was experimentally validated to demonstrate and realize

the physical nature of the Dirac cone phenomena. These PnCs provide an intriguing platform to explore condensed matter physics regarding Dirac-like cones at Γ point in acoustic wave systems. In conclusion, the dual Dirac cone dispersion method proposed herein increases the possibilities of exploiting numerous Dirac point behaviors at different frequencies in a single lattice structure, providing greater design flexibility for practical wave manipulation. We anticipate that this study will encourage further numerical and experimental investigations into band degeneracies for extensive acoustic device applications.

CHAPTER 5

ACOUSTIC COMPUTATION USING ACOUSTIC LOGIC GATES

5.1 INTRODUCTION

Hermitian Dirac-like cones are proposed for creating acoustic logic gates herein. The predictive phenomenon of creating Dirac-like cones near a bipolar antisymmetric deaf band was found to be useful for acoustic computing of Boolean algebra. Unlike previous approaches Dirac-like cone creates exclusive opportunity to perform all possible Boolean algebra computation with valid inputs. The phenomenon is demonstrated in two-dimensional Phononic Crystals (PnCs) consisting of tunable square columns in air media. By predictive tuning of the deaf bands, we report to form a triply to doubly degenerated Dirac-like cone, particularly useful for acoustic computing. It is only possible when a bottom band has a negative curvature. But that is lifted from a nearby doubly degenerated band with positive curvature, which is again degenerated with a deaf band. On the contrary similar computing possibilities are difficult when the bottom band degenerates with the deaf band, and the top band is lifted. Utilizing these phenomena, acoustic logic gates are designed to perform Boolean algebra through AND, NAND, OR and NOR gate operations. A simple one degree of freedom and a complex six degrees of freedom systems are proposed and demonstrated, where simple rotation of the PnCs activates a specific gate.

Wave propagation in Phononic crystals (PnCs) is studied for the past two decades with numerous potential applications [21, 61, 90, 91]. Prohibition of elastic/acoustic wave

transmission to design complete acoustic band gaps is one of the major applications of the PnCs, which ultimately helped understand the Anderson localization [92]. Exploiting these phenomena, the design of acoustic/elastic isolators, noise filter/control, and design of innovative transducers, and waveguides have potential engineering and biomedical applications. Only recently applications of acoustic computing using metamaterial design and PnCs are being proposed [93-96]. In this article deaf band-based acoustic computing near Dirac-like cone methodology is proposed and demonstrated.

Although the quest for Dirac-like cones was only noticed in the past few years [40], researchers have been reporting the periodic materials for complete acoustic band gaps in air media for the past two decades. Previously, numerous approaches are described to control the width of the band gaps by placing inclusions at well-defined places. It was reported that complete acoustic band gaps can be artificially increased by removing the band degeneracies. It was achieved by manipulating doubly or triply degenerated bands and maneuvering the spectral responses [97-99]. A tuning process was adopted to lift or move certain bands to enhance the band gaps [95, 96]. By tuning the PnCs various geometrical shapes with different lattice structures were proposed[40, 97, 98, 100]. Square PnCs made of polyvinyl chloride (PVC) in air matrix were tuned to widen the band gaps extensively [21]. Using the same process, however, achieving Dirac-like cones is not obvious, not only rare but extremely difficult. A deaf band-based predictive model is recently proposed to control Dirac cones [50, 51], where the diameter of circular PnCs was changed to achieve the Dirac-like cone.

Although the orthogonal wave transport, a key ingredient for acoustic computing is prominent in circular PnCs, we realized that the circular setup was not suitable for acoustic

computing applications. To achieve a Hermitian Dirac-like cone using circular PnCs required total replacement/reinstallation of the PnCs. Thus, the system of PnCs must be static, and no dynamic control would be possible. In this article, however, by breaking the symmetry using tunable square PnCs, a similar approach was explored. The square PnCs were rotated about their central axis. While exploiting the geometric tuning of square PnCs in air media, we observed that the spatial symmetry is broken and a triply degenerated point, a Hermitian Dirac-like cone is created near 12.5 kHz. The Dirac-like cone creates the opportunity to build a simple but robust acoustic computing structure. Here changing the entire geometry of the PnCs is not necessary unlike it is required in the previous studies [30, 101, 102]. Defying the conventional methods, deaf band-based tuning is demonstrated in this article to obtain multiple Dirac-like points at two different energy states. Conventionally, a Dirac-like cone must have a linear dispersion at the Γ point Figure 5. 1(a). However, close to this state, there are other unique states around the same deaf band frequency. When the PnCs are tuned, the bands tend to separate in two possible ways. In one case where the bottom band is separated but the top band degenerates with the deaf band. Another case is where the top band is separated but the bottom band degenerates with the deaf band. Irrespective of these cases, when the bands are separated, they no longer follow the exact linear dispersion. Although very low, the bands demonstrate some level curvatures. For the schematic purpose, the curvatures are exaggerated. These are two doubly degenerated states, as shown in Figure 5. 1(b) and (c). One state has a bottom band with negative curvature but is lifted from a nearby doubly degenerated band formed by a band with positive curvature degenerated with a deaf band. *This state is extremely valuable for acoustic computing.* Another state which has similar potential to form a Dirac-like cone

has the bottom band degenerated with the deaf band, and the top band is lifted. Similar computing possibilities are difficult for the second energy state where the deaf-band mode shape is not exactly dipolar. The physics of the deaf band is briefly described below.

Dirac-like cones that occur at the center of the BZ (Γ point) contain a doubly degenerate state with two intersecting linear dispersion bands and an additional single flat band (Figure 5. 1(a)). Together they form a three-fold degeneracy with linear dispersion at

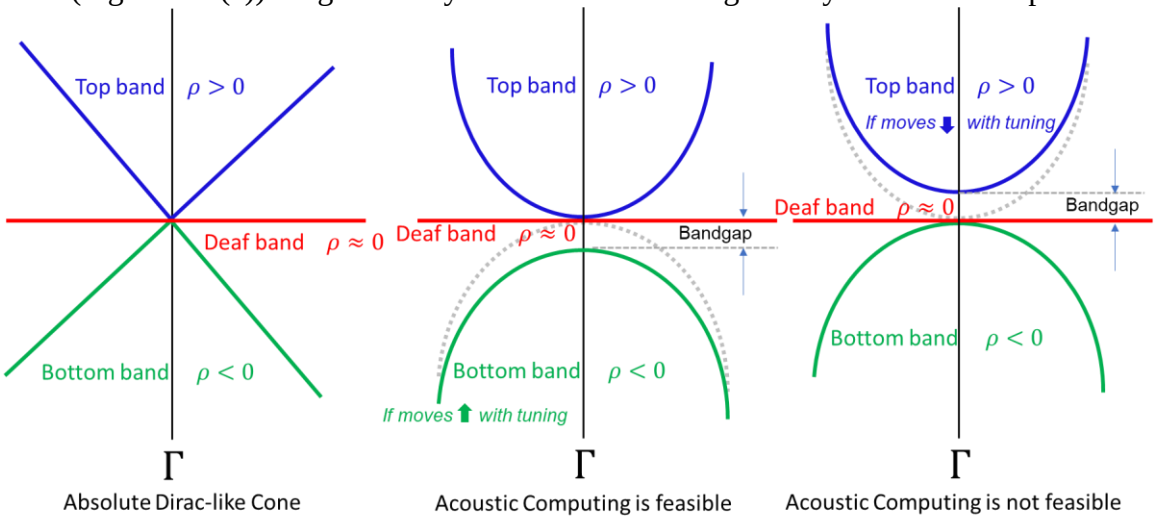

Figure 5.1: (a) Schematic representation of a configuration of top, deaf and bottom bands in absolute Dirac-like cone configuration (a) Schematic representation of a configuration of top, deaf and bottom bands where bottom band can move upward in frequency to form a Dirac-like cone at Γ point. This state is later demonstrated suitable for acoustic computing. (b) Schematic representation of a configuration of top, deaf and bottom bands where top band can move downward in frequency to form a Dirac-like cone at Γ point. This state was found to be insufficient for acoustic computing.

$\vec{k} = 0$. The flat band that passes through the degenerated point has inherently an antisymmetric mode shape and zero or minimal group velocity in the vicinity of the Dirac cone frequency. Because it is nearly flat and has no group velocity with an antisymmetric dipolar mode shape, it exhibits spatial localization allowing minimum acoustic energy to transport through PnCs (along the direction of incidence). Bands exhibiting this non-transporting acoustical deafness are called deaf bands. Deaf bands play a major role in

increasing or decreasing the bandgap above or below the respective bands. It also helps the degeneration of the bands from non-degenerate modes [51]. It means that by closing the bandgap (Figure 5. 1), the Deaf band helps to form the Dirac-like cones. Due to an anti-symmetric acoustic mode shape of the deaf band which is orthogonal to the direction of the incident plane wave, it can only be excited by an incident non-zero k-parallel components [34, 59]. If the PnCs are rightly tuned by breaking the special symmetry, and the wave is excited at a deaf-band frequency, the incident wave will take a 90^{o} bent and will propagate along the orthogonal direction. The other two modes of the top and bottom band at the Dirac-like cone must have self-canceling dipolar or quadrupolar wave modes with orthogonal phases. When the gap (Δf) between the bands is not too high, the influence of modal self-canceling is still evident and is demonstrated in section B Figure 5. 4. Withing a limited band gap the self-cancellation is only possible when the deaf band is antisymmetric with dipolar mode shape. When the deaf band is not dipolar, effective self-cancellation with distinct orthogonal wave transport is not possible [50, 51]. This distinct orthogonal wave transport is possible when the situation is replicated in Figure 5. 1(b) situation.

This scenario helps create the opportunity for acoustic computing, where a mechanism of rotating the PnCs together helps create AND, OR NAND, and NOR gates. The tuning techniques for acoustic computing previously proposed by researchers required total replacement of the PnCs due to the required changes in their geometrical dimensions [30, 103-105]. In this article, we exploited the deaf band-based predictive tuning avoiding the shape optimization process, in which replacement of the inclusions is not necessary.

Although not relevant for this study, a similar approach using a rotational tuning of different PnCs was demonstrated to obtain Quantum Spin Hall Effect (QSHE) [106].

This article describes the tunable dependency between acoustic deaf band modes and the rotation of a solid square rod with respect to the lattice orientation. First, to confirm the emergence of Dirac-like cones at the center of the BZ, we observe the orthogonal guidance of elastic waves through PnCs near multiple Dirac frequencies. Next, to explore if the design of the meta structure, such as length and width has any role on the wave behavior at the Dirac cone, different modes of orthogonal and longitudinal transports are investigated. Further, orthogonal wave transport, a key ingredient for acoustic computing using deaf bands is fully validated through experimental study. After validation, based on the understanding from the study, two different acoustic computing structure is formulated. A single matrix of PnCs with one degree of freedom for the rotational mechanism and another six arrays of PnCs with six degrees of freedom are designed to demonstrate the possibility of acoustic computing. One degree of freedom system creates a single opportunity to perform Boolean algebra through AND, OR, NAND, and NOR gates. Across four gates there is a total of twelve operations. Out of twelve operations, ten operations could be achieved using passive gates (like static gate configuration in electronics). Two operations require active tuning to fulfill the desired outcome. Further using passive modes, a six degrees of freedom system demonstrates more complex computing opportunities.

The method of finding the band structure for composite media with air and PVC square PnCS is briefly reported in Section II. The numerical results are discussed in Section

III. Experimental validation is presented in Section IV. Acoustic computing structures are presented in Section V.

5.2 NUMERICAL AND ANALYTICAL MODEL

Inhomogeneous elastic constants and coupling of transverse and longitudinal modes are inevitable in solid/fluid mixed media. Partial decoupling can occur in 2D PnCs, showing that the incidental wave is normal with respect to the normal direction to the periodic plane. Hence, pure transverse modes along the Z-axis are completely independent of the coupled modes (longitudinal) propagating through PnCs along the periodic plane [107]. In this solid/fluid mixed media system, plane wave expansion (PWE) is fully approximated [65, 108]. The governing wave motion equation in solid-fluid media is expressed as:

$$\sigma_{ij,j}(x_k) + f_i = \rho(x_k)\ddot{u}_i \quad ; \quad \left(C_{ijkl}(x_m)u_{k,l}\right)_{,j} + f_i = \rho(x_m)\ddot{u}_i \qquad (1)$$

where i, j, k, l and m are the index notation with values 1 and 2 considering the 2D cross-sectional plane of PnCs, $\sigma_{ij,j}(x_k)$ is the derivative of the stresses at the location x_k with respect to the jth direction, f_i is the body force in the ith direction, $\rho(x_k)$ is the density at the location x_k in the material, and $\ddot{u}_i$ is the acceleration in the ith direction.

The Bloch-Floquet periodic boundary conditions [68] in the reciprocal wave number space are then applied. $g_1 = 2\pi p/P_1$ and $g_2 = 2\pi q/P_2$ are real values of the periodic wave numbers or Bloch wave numbers (where $p = -\infty\ to + \infty$ and $q = -\infty\ to + \infty$ using only integers) are summed with the Eigen wave number to obtain the Bloch-Floquet displacement function. P_i is the periodicity of the media in the ith direction. If the wave number $\mathbf{k}$ is the solution of the system at a frequency ω, then $\mathbf{k} + \mathbf{g}$ is also a solution

of the system at that same frequency. Hence, the Bloch-Floquet displacement function is expressed as

$$u_1(x_k,t) = \sum_p \sum_q \Phi_{pq} e^{i\mathbf{k}.\mathbf{x}} e^{i\mathbf{g}.\mathbf{x}} e^{-i\omega t} \qquad (2)$$

$$u_2(x_k,t) = \sum_p \sum_q \Psi_{pq} e^{i\mathbf{k}.\mathbf{x}} e^{i\mathbf{g}.\mathbf{x}} e^{-i\omega t}, \qquad (3)$$

Where, $\mathbf{g} = g_i \hat{e}_i$ and $\hat{e}_i$ are the Cartesian basis vectors and $\mathbf{g}.\mathbf{x} = g_k x_k$ is the dot product between the reciprocal Bloch wave number and position vector. Differentiating the displacement function twice, with respect to time, the acceleration can be written as

$$\ddot{u}_1(x_k,t) = -\omega^2 \sum_p \sum_q \Phi_{pq} e^{i(\mathbf{k}+\mathbf{g}).\mathbf{x}} e^{-i\omega t} \qquad (4)$$

$$\ddot{u}_2(x_k,t) = -\omega^2 \sum_p \sum_q \Psi_{pq} e^{i(\mathbf{k}+\mathbf{g}).\mathbf{x}} e^{-i\omega t} \qquad (5)$$

The expressions in Eqs. (2) to (5) signify the summations over a range of integer values of p and q. Stresses in Eq. (1) are further expressed as a product of the constitutive properties of the medium ($C_{ijkl}(x_m)$) and strain (ε_{kl}). The strains can be further derived from the derivative of the displacement functions (Eqs. (2) and (3)) with respect to the spatial variable x_k like it is expressed in Eq. (1). For 2D PnCs and applying symmetries eighty-one coefficients of C_{ijkl} tensor can be reduced to nine coefficients tensor C_{ij}. Within an array of PnCs, the constitutive matrix can be assumed to be the periodic function of space and is expressed using Fourier coefficients in the periodic medium. Hence, applying the Fourier transform constitutive function $C_{ij}(x_m)$ in terms of the Fourier coefficients C_{ij}^{pq} can be expressed as

$$C_{ij}(x_m) = \sum_{p=-\infty}^{\infty} \sum_{q=-\infty}^{\infty} C_{ij}^{pq} e^{i\left({}^{2\pi p}/_{P_1} x_1 + {}^{2\pi q}/_{P_2} x_2\right)} = \sum \sum C_{ij}^{pq} e^{i\mathbf{g}.\mathbf{x}} \qquad (6)$$

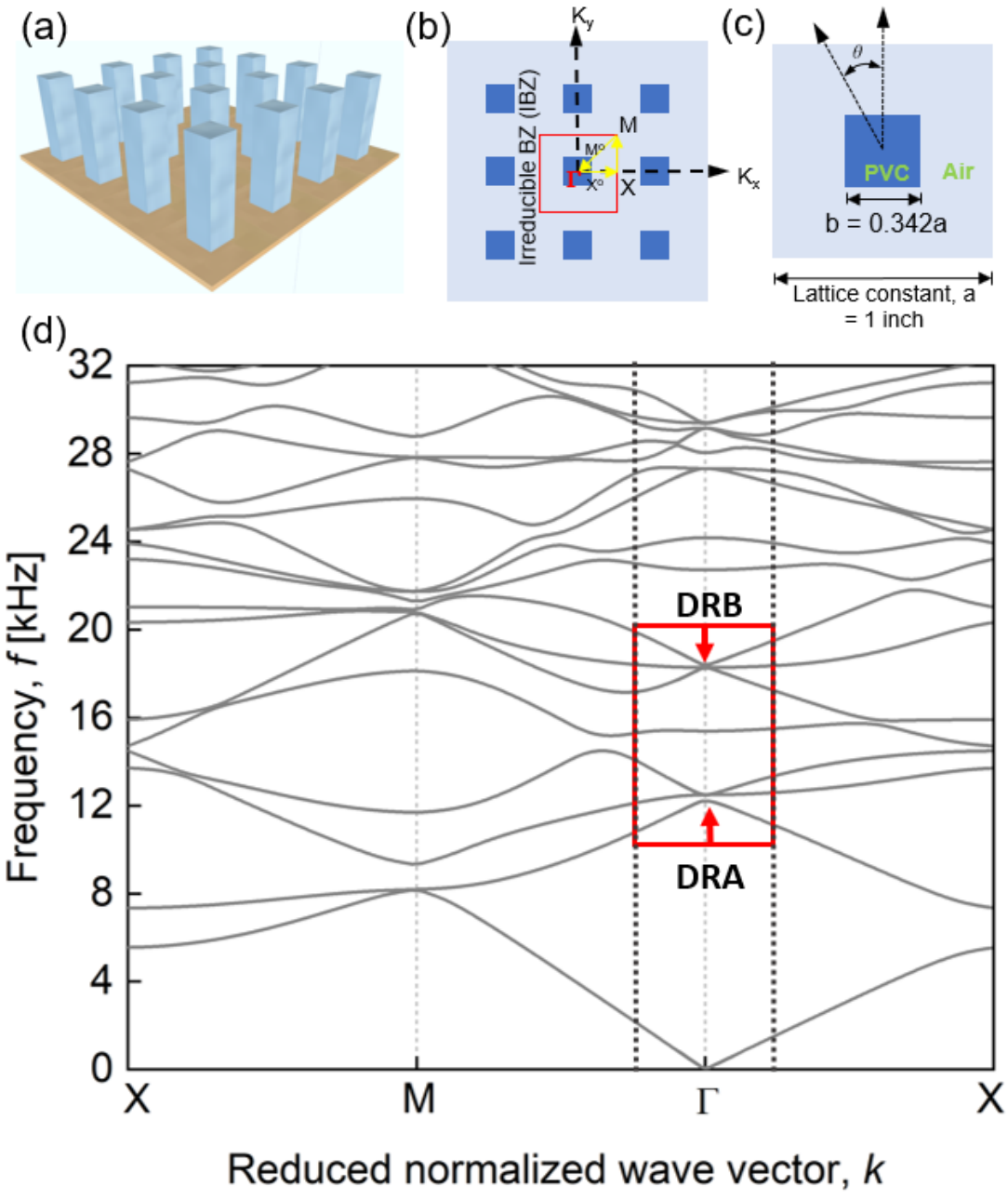

Figure 5.2: (a) Schematic representation of the 2-dimensional periodic systems of hard square rods in a square lattice. The filling fraction is 0.1169 and the square array has the same orientation as the lattice. (b) Transverse cross-section of 2D square lattice in a 3 x 3 supercell with 9 squares of b=0.342a (where a=lattice constant) hosted in air media, depicting the irreducible BZ with wave-vector directions (ΓX-XM-MΓ). (c) Schematic view of a single PnC inside irreducible BZ composed of PVC, where the two constituents are denoted by white and blue as air and PVC rods, respectively. (d) Acoustic band structure of PVC square rods with filling fractions F = 0.1169 embedded in an air host. The rotational angle is $\Theta = 0^{o}$. The colored blocked regions around the Γ point denote probable Dirac region A (bottom) and Dirac region B (top).

The Fourier coefficients of constitutive parameters can be expressed using inverse

Fourier transform as

$$C_{ij}^{pq} = \frac{1}{A_c} \int C_{ij}(x_m)\ e^{-i\mathbf{g}.\mathbf{x}} d\mathbf{x} \qquad (7)$$

Similarly, the Fourier coefficients of density $\rho(x_m)$ of the media can also be expressed as

$$\rho^{pq} = \frac{1}{A_c} \int \rho(x_m)\ e^{-i\mathbf{g}.\mathbf{x}} d\mathbf{x} \qquad (8)$$

A generalized expression for the modulus or density is thus expressed as

$$\alpha^{pq} = \frac{1}{A_c} \int \alpha(x_m)\ e^{-i\mathbf{g}.\mathbf{x}} d\mathbf{x} \qquad (9)$$

where $\alpha(x_m)$ is equivalent to $C_{ij}(x_m)$ or $\rho(x_m)$

Substituting the Eqs in Eq. (1) we obtain two governing equations in a generalized form as follows

$$\begin{aligned}\sum_m \sum_n \sum_p \sum_q \Big[& \Phi_{mn} C_{11}^{pq} e^{i(\mathbf{k}+\mathbf{g_{pq}}+\mathbf{g_{mn}}).\mathbf{x}} (k_1 + g_1^m)\left[-k_1 - (g_1^m + g_1^p)\right] \\ & + \frac{1}{2}\Phi_{mn} C_{66}^{pq} e^{i(\mathbf{k}+\mathbf{g_{pq}}+\mathbf{g_{mn}}).\mathbf{x}} (k_2 + g_2^n)\left[-k_2 - (g_2^n + g_2^q)\right] \\ & + \Psi_{mn} C_{12}^{pq} e^{i(\mathbf{k}+\mathbf{g_{pq}}+\mathbf{g_{mn}}).\mathbf{x}} (k_2 + g_2^n)\left[-k_1 - (g_1^m + g_1^p)\right] \\ & + \frac{1}{2}\Psi_{mn} C_{66}^{pq} e^{i(\mathbf{k}+\mathbf{g_{pq}}+\mathbf{g_{mn}}).\mathbf{x}} (k_1 + g_1^m)\left[-k_2 - (g_2^n + g_2^q)\right] \Big] \\ & = -\omega^2 \sum_m \sum_n \sum_p \sum_q \Phi_{mn} \rho^{pq} e^{i(\mathbf{k}+\mathbf{g_{pq}}+\mathbf{g_{mn}}).\mathbf{x}} \qquad (10)\end{aligned}$$

$$\sum_m \sum_n \sum_p \sum_q \Big[\Phi_{mn} C_{21}^{pq} e^{i(\mathbf{k}+\mathbf{g_{pq}}+\mathbf{g_{mn}}).\mathbf{x}} (k_1 + g_1^m)\big[-k_2 - (g_2^n + g_2^q)\big]$$

$$+ \frac{1}{2}\Phi_{mn} C_{66}^{pq} e^{i(\mathbf{k}+\mathbf{g_{pq}}+\mathbf{g_{mn}}).\mathbf{x}} (k_2 + g_2^n)\big[-k_1 - (g_1^m + g_1^p)\big]$$

$$+ \Psi_{mn} C_{22}^{pq} e^{i(\mathbf{k}+\mathbf{g_{pq}}+\mathbf{g_{mn}}).\mathbf{x}} (k_2 + g_2^n)\big[-k_2 - (g_2^n + g_2^q)\big]$$

$$+ \frac{1}{2}\Psi_{mn} C_{66}^{pq} e^{i(\mathbf{k}+\mathbf{g_{pq}}+\mathbf{g_{mn}}).\mathbf{x}} (k_1 + g_1^m)\big[-k_1 - (g_1^m + g_1^p)\big]\Big]$$

$$= -\omega^2 \sum_m \sum_n \sum_p \sum_q \Psi_{mn} \rho^{pq} e^{i(\mathbf{k}+\mathbf{g_{pq}}+\mathbf{g_{mn}}).\mathbf{x}}, \qquad (11)$$

where $\mathbf{k} = k_1\hat{e}_1 + k_2\hat{e}_2$, $\mathbf{x} = x_1\hat{e}_1 + x_2\hat{e}_2$ $\mathbf{g_{pq}} = \frac{2\pi p}{P_1}\hat{e}_1 + \frac{2\pi q}{P_2}\hat{e}_2$, and $\mathbf{g_{mn}} = \frac{2\pi m}{P_1}\hat{e}_1 + \frac{2\pi n}{P_2}\hat{e}_2$.

$$g_1^p = \frac{2\pi p}{P_1} \;;\; g_1^m = \frac{2\pi m}{P_1} \quad ; \quad g_2^q = \frac{2\pi q}{P_2} \;;\; g_2^n = \frac{2\pi n}{P_2}$$

For square PnCs with dimension b in an air matrix with equal periodicity $P_1 = P_2 = a$ in both directions, the Fourier coefficients are expressed as

$$\alpha^{mn} = \frac{4\alpha_{sq}}{a^2 g_1 g_2} \sin\left(\frac{g_1 b}{2}\right) \sin\left(\frac{g_2 b}{2}\right), \qquad (12)$$

where α_{sq} is the numerical value of the respective property of a square PnC. Eq. (13) is obtained from a generalized equation derived in Appendix A. After rotating the square rod at an angle θ (please see Appendix A), the reciprocal lattice vectors following Eq. (A.14), $g_{1'}$ and $g_{2'}$ can be written as

$$g_{1'} = \frac{2\pi}{a}(p.cos\theta + q.sin\theta) \qquad g_{2'} = \frac{2\pi}{a}(-p.sin\theta + q.cos\theta), \qquad (13)$$

where p and q are the integers defined earlier and a is the lattice constant defined in the Appendix. Hence, both $\mathbf{g_{pq}}'$ and $\mathbf{g_{mn}}'$ are transformed due to the rotation of the square PnCs with their respective integers. They are substituted in Eqs. (10) and (11). Eqs. (10)

and (11) together create an eigenvalue problem, where wave number **k** solves the system of equations at a given frequency ω. The solution in $k-\omega$ plane is the dispersion solution. To obtain the converged dispersion relationship using the PWE on the periodic media, the eigenanalysis was conducted with 625 reciprocal vectors, which was adequate when p and q were -12 to 12 [23].

5.3 RESULTS AND DISCUSSION

First, square PVC rods are arranged in a periodic fashion and assumed to be attached to a mechanism where all the rods can be rotated together to achieve the tunability of the system (**Figure 5. 2**). PVC rods with dimension b = 0.342a and filling fraction = 0.1169, are placed in air media, where a = lattice constant, is approximately 25.4 mm, shown in **Figure 5. 2b** and **2c**. The first Brillouin zone (BZ), a region inside the red square (**Figure 5. 2c**), is reduced to a smaller region, ΓMX, called the irreducible BZ due to lattice symmetry [109]. The acoustic band structure shown in **Figure 5. 2d** is obtained inside the irreducible BZ with the wave propagation vector along (ΓX), (XM), and (MΓ), respectively when the PVC rods are not rotated, i.e. $\theta = 0^o$. At the Γ point, multiple regions are observed where a single-mode and doubly degenerated modes exist as presented in Figure 5. **1**. Two regions are identified in the dispersion bands: (1) Dirac region A (DRA) and (2) Dirac region B (DRB) as shown in **Figure 5. 2d**. Both regions are identified for the occurrence of potential triple degeneration. Both DRA and DRB are doubly degenerated. However, they have a characteristic difference at $\theta = 0^o$. At DRA, the top band which has positive curvature degenerates with the deaf-band, and the bottom band with negative curvature is lifted leaving a small bandgap. However, at the DRB scenario, it is the opposite. Here, the top band with positive curvature is lifted from the doubly degenerated

deaf-band, and a bottom band with negative curvature. By closely observing DRA and DRB and elucidating the geometric perturbations, it was found that geometric tuning pivoting the deaf bands, may create predictive triple degeneracy [51] forming Dirac-like cones at different frequencies.

As reported in condensed matter physics, the generation of a triply degenerated point at the center of a Brillouin zone (BZ) is the result of accidental degeneracy [68, 83]. Although based on physics the Dirac-like cones are accidental, earlier, author showed [50, 51] that identifying a prevalent deaf-band and tuning about the frequency to modulate the

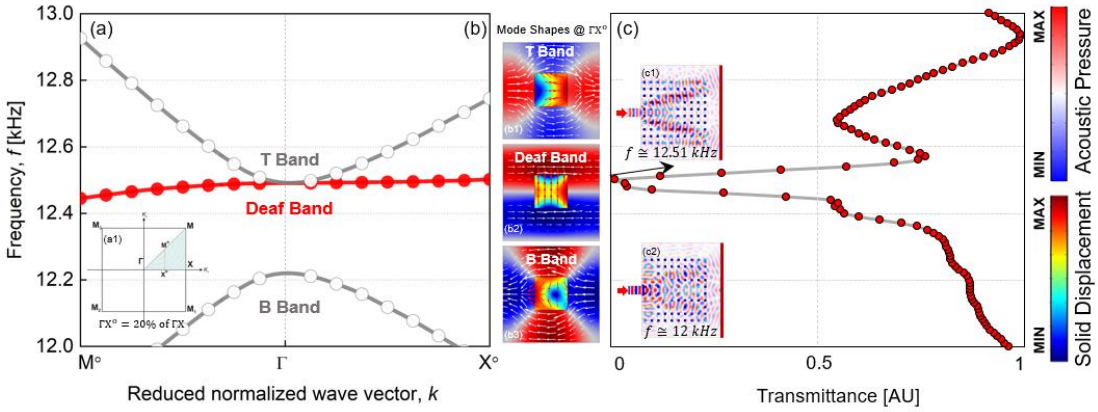

Figure 5.3: (a) Dispersion diagram for the DRA location, showing a small band gap between doubly degenerated ‘T band’ and ‘Deaf band’ and a ‘B band’, the irreducible BZ is demonstrated on the inset as (a1). (b) Respective mode shapes of a unit lattice of ‘T band’, ‘Deaf band’ and ‘B band’ along ΓX normalized wave vector direction. Both the absolute acoustic pressure distribution field and the solid displacement field are shown in two different colormaps, with their respective displacement vectors (white arrowed vectors depicts absolute acoustic pressure and red arrows inside the square PnC depicts solid displacement, c) The wave transmission decreases to zero near the deaf band if transmitted along ΓX [100] (top). The numerically calculated acoustic pressure field and solid displacement fields are shown for a 10×10 PnC matrix, excited at ‘Deaf band’ frequency and another arbitrary frequency for B band.

Dirac-like cone is very predictable from an engineering perspective. Similarly, here it is shown that by identifying the deaf band and by tuning the orientation of the solid resonator, multiple Dirac-like points can be created at the Γ point. Both Dirac-like cones are suitable

for exploiting acoustic computing as long as the condition presented in Figure 5. 1 is satisfied.

Close observation of regions DRA and DRB indicates that the bands (e.g. red flat band in **Figure 5. 3a**) which are nearly flat or parallel to the wave vector axis are the deaf bands. We designate the top bands as T bands and the bottom bands as B bands. To verify the deafness of the deaf bands' acoustic pressure mode shapes and solid deformations of PVC rods are presented in **Figure 5. 3b** (only DRA is shown herein). The numerical simulation is performed in COMSOL Multiphysics 4.3. By investigating the acoustic pressure distribution in air, it is apparent that the T and B bands with mutual orthogonal quadrupolar modes are symmetric with respect to the incident plane wave along the ΓX [100] and XM [010] directions. However, deaf band is anti-symmetric with respect to the incident wave direction, lacking group velocity. The transmission study demonstrates close to zero transmission near the deaf band (**Figure 5. 3c**), which verifies the deafness of the band along ΓX [100] direction. Thus, the deaf band remains inert to any kind of normal-incident plane wave due to the anti-symmetric mode shape. Although not shown, DRB has a similar antisymmetric but a hexapolar mode shape. The respective T and B bands at DRB are also hexapolar with no phase shifts. If the PVC rods are rotated and tuned it is possible to achieve a Dirac-like cone at both DRA and DRB but at different angles of rotation.

Further, to analyze the characteristics suitable for acoustic computing, the band structures at DRA and DRB are investigated with their respective T, deaf, and B bands. These three specific bands between ΓX^o and ΓM^o are obtained from separate Eigen solutions when the unit cells are rotated about their respective central axes (**Figure 5. 4a & 4b**). Solutions at every 1^o interval (from 0^o to 90^o) are summarized in **Figure 5. 4c**.

Please note that the target would be to achieve the condition laid out in **Figure 5. 1a**. After rotating the unit cells, eigenfrequency solutions at the Γ point as a function of rotational angle θ are presented in **Figure 5. 4d**. At DRA, an absolute Dirac-like cone was achieved

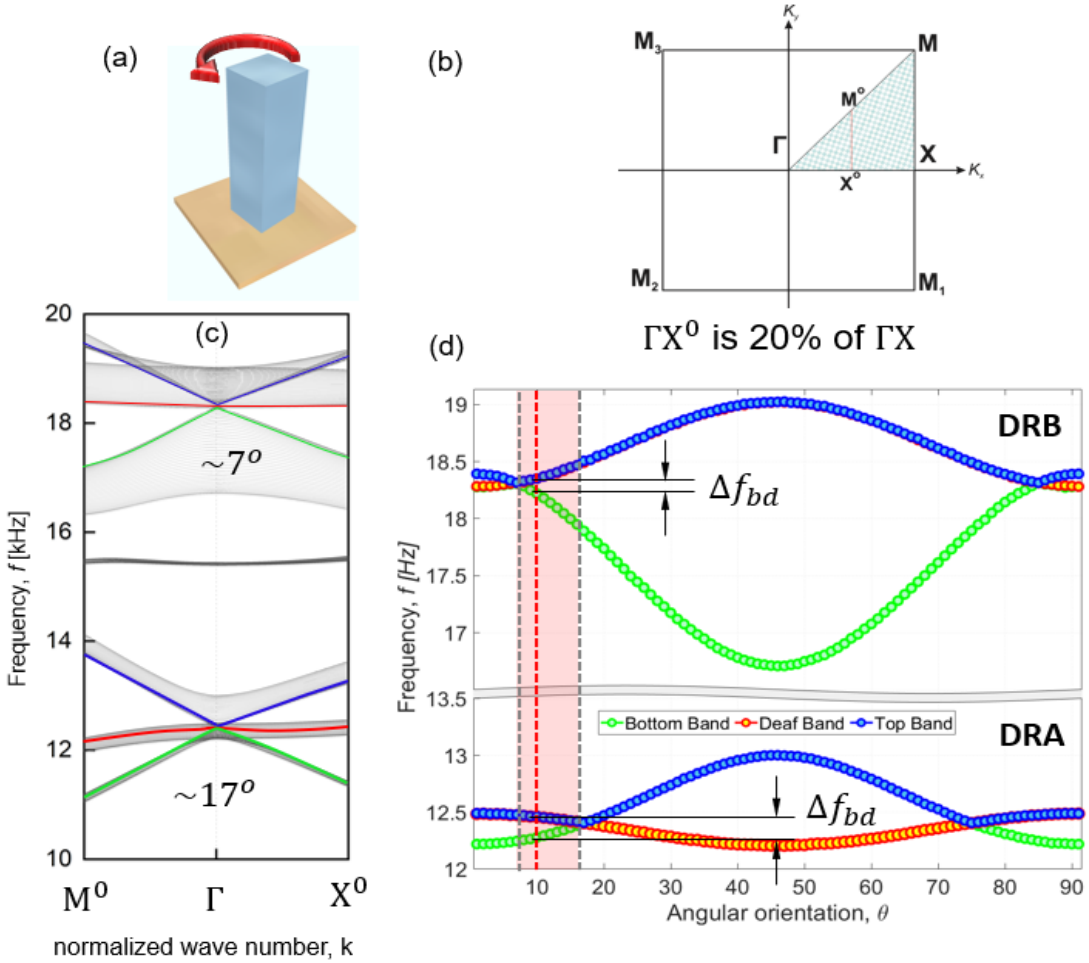

Figure 5.4: (a) Geometric representation of square rod PnCs embedded in the air matrix and rotated counterclockwise (CCW). This angular tuning was conducted at 1° intervals over a range of 0°-90°. (b) First Brillouin zone and normalized wave number segment used in (c), (c) Superposed band structure obtained from different CCW unit cells. The dispersion relationship shows that a Dirac cone is achieved at a ~7° rotation for DRB and at a ~17° rotation for DRA. (d) Modulation of the T, deaf, and B bands as a function of the rotational angle with different CCW unit cells. A red box is identified between ~7° and ~17° where the T and deaf bands are degenerated, but the B band is separated by a band gap Δf_{db}. The angle of rotation is identified where Δf_{db} is equal for DRA and DRB.

when the rotational angle was ~17°. Similarly, at DRB, an absolute Dirac cone was achieved when the rotational angle was ~7°. As shown in **Figure 5. 4d**, the Eigen solutions

are symmetric with respect to the rotation angle 45^o where the bandgap is maximum. To test if both DRA and DRB can generate Dirac cone behavior aligned with the condition presented in **Figure 5. 1a**, a narrow window of θ is investigated, where the T and deaf bands are doubly degenerated, but the B band is separated by a small frequency bandgap Δf_{db} (e.g. case in Figure 5. **1a**) at both frequency ranges of DRA and DRB. This small window is marked with a red box in **Figure 5. 4d**. In this window, the B band moves up in the frequency scale to triply degenerate and merge with the deaf band. A mirror image of the same window occurs between ~73^o and ~83^o.

When the deaf and B bands are doubly degenerated, the T band is separated with a bandgap between the T and deaf bands (e.g case **Figure 5. 1b**), and Dirac cones experience a significant alteration in their behavior. Hence, the Dirac-like cone dominated only between the red window shown in **Figure 5. 4d**. This window may be located over a different range of θ axes depending on the filling fraction and a/b ratio. It was found that when both DRA and DRB have equal Δf_{db} frequency gaps between the doubly degenerated bands and B bands, the Dirac cone behavior prevails at DRA and DRB and acoustic computing can be exploited. A minute but equal Δf_{db}=~166 Hz was obtained at $\theta = \sim 9.7^o$ through non-linear interpolation within the red window (**Figure 5. 4d).**

To explore which Dirac frequency creates prominent orthogonal transport a periodic arrangement of 58 x 9 solid PVC square rods with filling fraction f = 0.1169 are placed in an air medium. Frequency domain numerical experiments are conducted. The square PnCs are actuated by a guided plane wave source located ~110 mm away from the air-PVC interface. Absorbing boundary conditions are enforced around the boundaries. The acoustic pressure field distributions at the DRA and DRB regions are shown in **Figure**

5. 5. Orthogonal wave transportation at Dirac-like frequencies [68], is visualized in **Figure 5. 5**. The DRA and DRB regions demonstrate their own unique features that are explained by their respective wave-dispersion behavior.

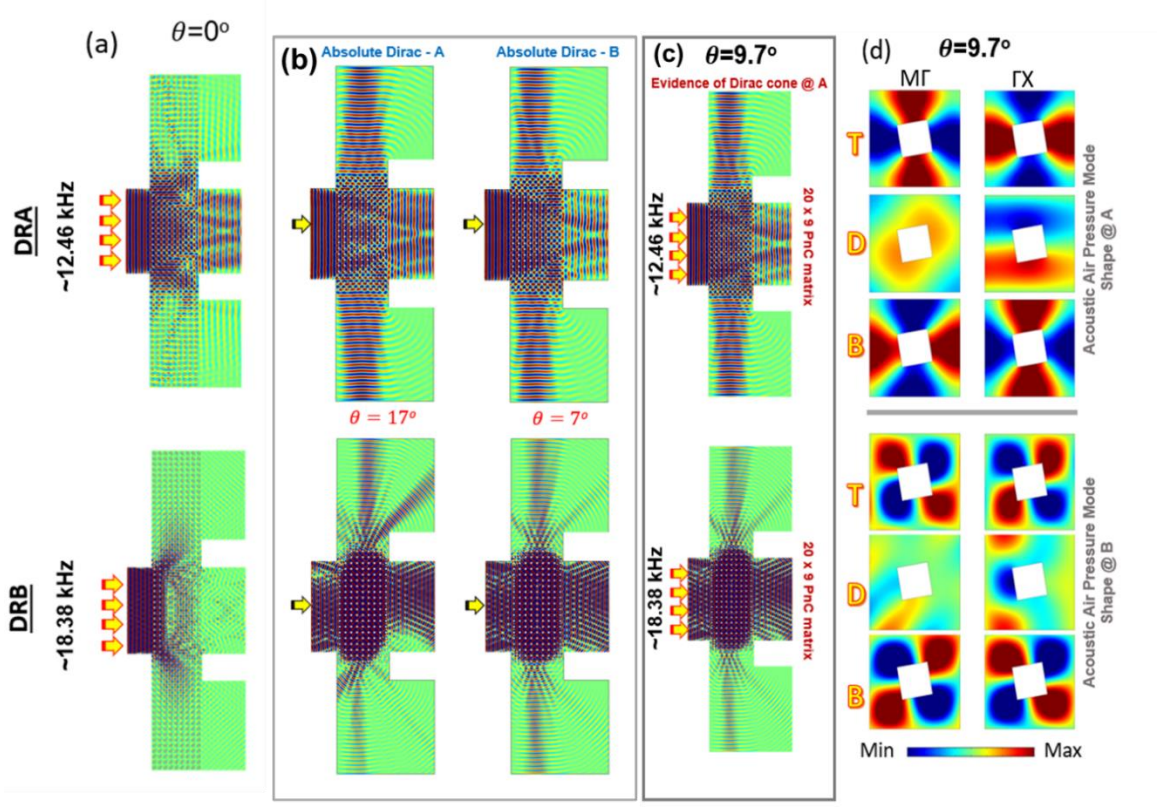

Figure 5.5: (a) Wave propagation and acoustic pressure distribution in a PnCs wave guide with a 58×9 matrix of PVC/air media at DRA and DRB at excitation frequencies at the Dirac point f = ~12.46 kHz and f = ~18.374 kHz, respectively. The square PnCs are not rotated in this Figure 5. 5. and thus orthogonal transport is not feasible. (b) Wave propagation in the PnCs guide with a 20×9 matrix is investigated at DRA and DRB at excitation frequencies at the Dirac points. The square PnCs are rotated at angles of 17° (left) and 7° (right). DRA demonstrates Dirac phenomena at 17° & DRB demonstrates Dirac phenomena at 7°. c) To explore the situation presented in Figure 5. 1 the PnCs are rotated at 9.7° considering the Figure 5. 4. The orthogonal wave transport prevails in both DRA and DRB at their respective Dirac frequencies. (d) Absolute acoustic pressure mode shapes of the unit cells in the MΓ and ΓX directions for DRA and DRB, respectively, for the T, deaf, and B bands when the PnCs are rotated at a 9.7° angle.

The acoustic pressure distribution is shown in **Figure 5. 5a**, where the PnCs are not rotated and the regular arrangement of the square matrix at $\theta = 0°$ is demonstrated. It

shows no sign of Dirac phenomena in the grid. Next, a smaller periodic arrangement of 20 x 9 solid PVC square rods is studied. When the square PnCs are rotated together at an angle $\theta = 7°$, as predicted, orthogonal wave transport at frequency ~18.38 kHz, that demonstrates a Dirac phenomenon (DRB). When the square PnCs in the grid are rotated together at an angle $\theta = 17°$, as predicted, orthogonal wave transport is prominent at frequency ~12.46 kHz which demonstrates the Dirac phenomena (DRA). The intensity of the normal transport is also increased as the pseudo-diffusion prevails as another prominent Dirac behavior [88, 89]. The Δf_{ab} gap between the B and deaf bands at DRA and DRB are equal (~166 Hz) at $\theta = \sim 9.7°$ where the Dirac phenomena prevail for both DRA and DRB. **Figure 5. 5c** shows the Dirac behavior at 9.7°, at DRA (~= 12.46 kHz), and DRB (~= 18.38 kHz). Please note that at both DRA and DRB, the system will result in a bandgap when rotated at $\sim 45°$ clockwise or counterclockwise.

At the DRA frequency, orthogonal transport prevails in the air media beyond the PnCs, but the intensity of the normal transport is increased as well because of the pseudo diffusion [110]. This is because the meta structure guide does not have enough PnCs to carry the energy in the orthogonal direction.

To further demonstrate the reason for the Dirac phenomena, the acoustic pressure mode shapes of the T, deaf (D), and B bands for wave propagation along with the ΓX and MΓ directions at DRA and DRB frequencies are shown in **Figure 5. 5d**. In both the DRA and DRB cases, the T and B band mode shapes are symmetric, quadrupolar mode shapes with opposite pressure distributions. When the mode shapes are superposed at the Dirac frequencies, the T and B mode shapes cancel each other, causing the deaf band mode shape to dominate. The local dispersion behavior of the T and B bands with degenerated acoustic

pressure mode shapes are quadrupolar and mutually orthogonal; in contrast, the deaf band mode is dipolar (for ΓX) (**Figure 5. 5d**). Hence, at the Dirac frequency, both the T and B bands nullify each other, maintaining the dipolar deaf band mode dominance. A 45^{o} bent line helps the dipolar deaf mode carry the wave energy orthogonally like an origami fold. The quadrupolar local dispersion modes are rotated by 90^{o} of T and B bands' between the MΓ and ΓX directions of propagation at both DRA and DRB (**Figure 5. 5d**) frequencies. Although the Deaf band is almost flat, the phenomenon inside the material is not due to the local resonance but due to the antisymmetric mode shape at the triple degenerated state, as depicted in **Figure 5. 5**.

5.4 EXPERIMENTAL EVIDENCE OF ORTHOGONAL TRANSPORT

Fabrication of PnCs and creating an experimental setup with high numbers of elements used in the numerical experiments shown in **Figure 5. 5** is challenging and thus the phenomena are demonstrated on a comparatively smaller setup with 10x10 PnCs as shown in **Figure 5. 6.** To experimentally demonstrate the feasibility of harnessing orthogonal transport, the incident wave transport, IT and orthogonal wave transport, OT

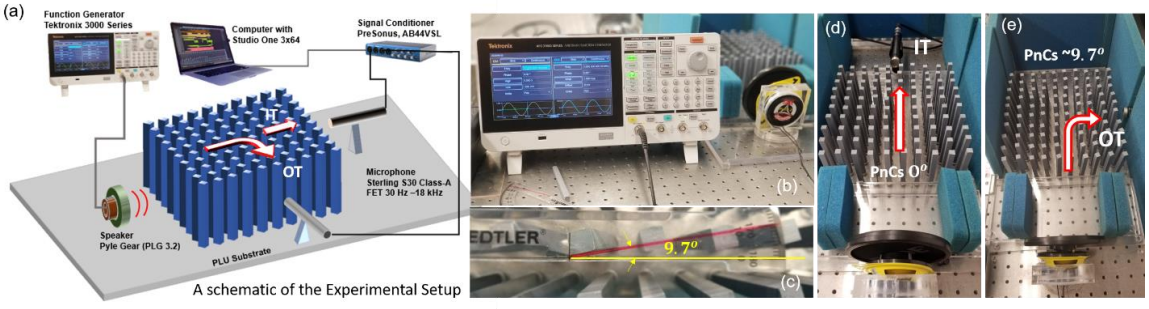

Figure 5.6: (a) A schematics of a generalized experimental setup showing Orthognal Transport (OT) experiment and Incident Transport (IT) experiments, where PnCS rotation can be manually controlled (b) Setup showing excitation of the speaker with a Function Generator generating continuous sine wave. c) Rotation of the PnCs by $\sim 9.7^{o}$. (d) IT experimental setup with PnCs rotation 0^{o}(results not shown) e) OT experimental setup with PnCs rotation $\sim 9.7^{o}$(results shown in Figure 5. 10)

was investigated over a range of frequencies from 10 kHz – 14 kHz, which includes the 'DRA' Dirac-like frequency at ~12.46 kHz. The coefficients of transmissibility along IT and OT were obtained from numerical experiments over the same frequency range. Transmission energy measured in decibels (dB) obtained from the experiments are mapped between zero to one, where, one being the maximum transmission and zero being the minimum transmission. Please note that when PnCs guide is smaller wave output from IT and OT will be comparable and closer to each other through the mechanism of pseudo diffusion.

First, 100 commercially available extruded PVC cylinders of b = 0.348a = ~8.84 mm (the lattice constant a = 25.4 mm) were arranged in a 10 × 10 matrix as shown in **Figure 5. 6**. The PVC cylinders were cut to 8" length elements and machined to have a smooth surface to minimize the experimental error. Acoustic pressure was created (Figure 5. **6a-e**) using a speaker (Pyle Gear (PLG 3.2) 3.5" 2-way coaxial, 120-watt, 4-ohm impedance) capable of generating frequencies up to 18 kHz. To absorb the acoustic energy and to avoid reflection from the boundary of the experimental setup, acoustic dampers (0.5-inch-thick foam sheets) were used at the boundaries (**Figure 5. 6d & 6e).** To simulate the absorbing boundary conditions, a channel made of foam was designed to guide the incident acoustic wave. A condenser pressure microphone (Sterling S30 Class-A FET 30 Hz –18 kHz) was used to detect the acoustic transmission (**Figure 5. 6a, 6d** & **6e**), placed at the incident (for IT) and the orthogonal (for OT) directions. The microphone was connected to a PreSonus AudioBox 44VSL signal conditioner and then the conditioner was connected to a computer with a USB connector where an audio signal analysis software (Studio One3 x64) was used to record the signals (**Figure 5. 6a**). Finally, the spectral analyses were

performed automatically using the software where the amplitude of the transmitted wave at frequencies 10 kHz – 14 kHz at 100 Hz intervals were collected. The output was recorded in a CSV data file for further plotting using Matlab. Twenty-seven data sets were collected for each IT and OT experiment at each frequency. The microphones were placed at nine

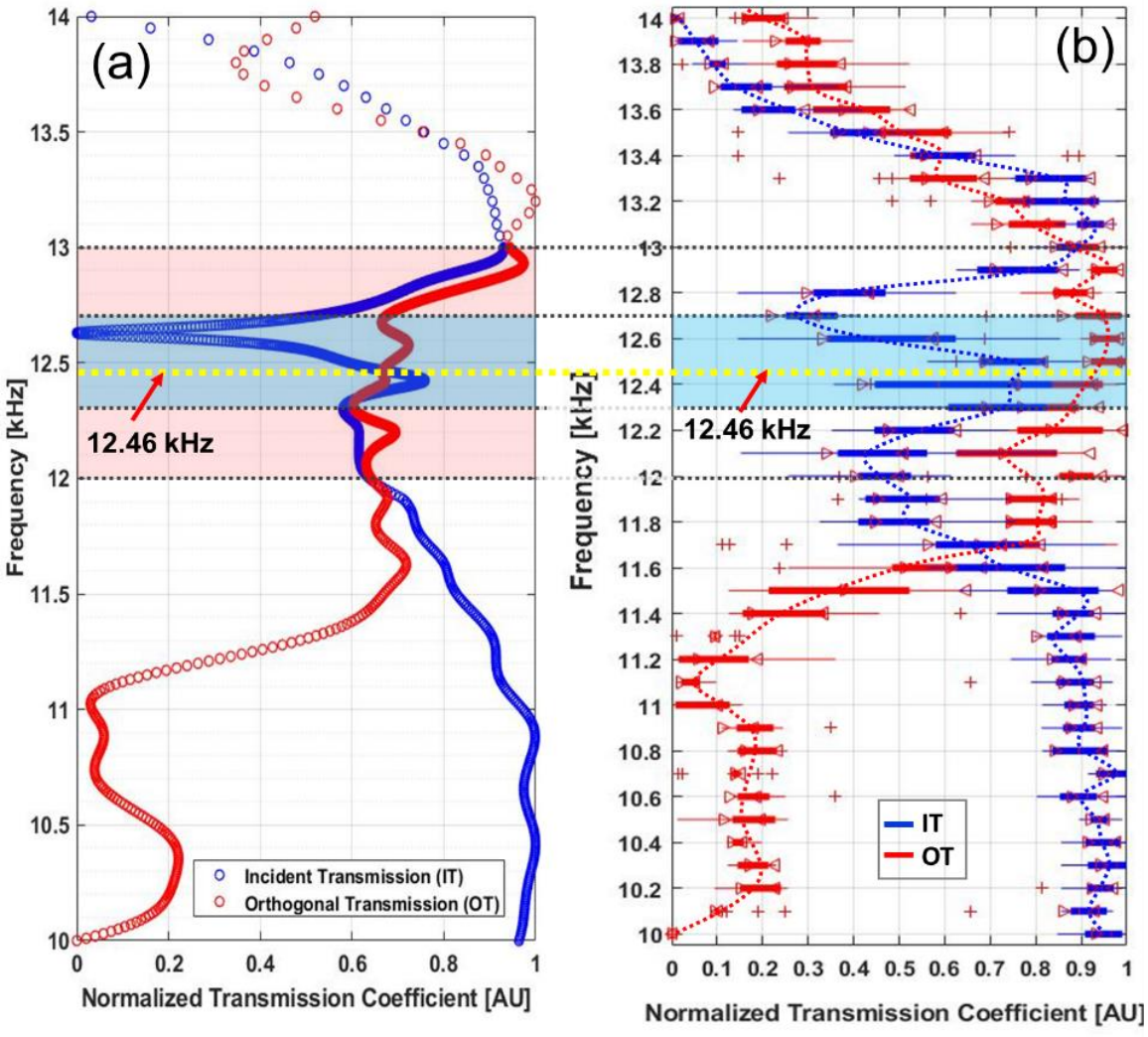

Figure 5.7: PnCs with ~9.7^{o} rotation (a) Simulation: Transmission coefficients mapped between 0-1, obtained from numerical simulation, IT indicates, incident transmission and OT indicate orthogonal transmission as shown in Figure 5. 6 b) Experiment: Median, box with whiskers shows the variation of the transmission coefficients due to IT and OT over the frequency range 10-kHz -14 kHz. The dotted line is drawn to show the trend line from the experimental data for both IT and OT.

different locations and three sets of data were collected from each location. With 10 PnCs in this setup, there were 9 air outlets between the two consecutive PnCs. These 9 locations were used to probe the microphone. The recording channel was open for 10 seconds for every experiment. First, the data were collected for IT and then for OT, when the PnCs were placed without any rotation ($\theta = 0^o$ **Figure 5. 6d**). Next, the data were collected for IT and OT, when PnCs were rotated by $\sim 9.7^o$ (**Figure 5. 6c** and **6e**).

Results obtained from the experiment described above are summarized in **Figure 5. 7**. **Figure 5. 7** shows the boxplot created from the twenty-seven experimental transmission coefficients obtained at each frequency step (at 100 Hz intervals). The data shows the change in both the IT and OT coefficients obtained experimentally as a function of frequency between 10 kHz – 14 kHz at an interval of 100 Hz. From the experimental results, it can be seen that the medians of the OT coefficients are significantly lower compared to the median of the IT coefficients below 11 kHz. These two states are easily distinguishable and mutually exclusive. Near the DRA frequency medians of the OT coefficients are consistently higher than the IT coefficients between the range 12 kHz to 13 kHz. This indicates that the orthogonal propagation tends to dominate near the Dirac frequency. However, near the Dirac frequency ~12.3 and ~12.4 kHz, the boxplots (blue boxes for IT and red boxes for OT) are approximately overlapped each other with very close median values. Additional plus marks are showing a few outlier data at each frequency where experiments were conducted.

5.5 ACOUSTIC COMPUTING

Exploiting the behavior presented above several acoustic computing units are devised and functionality is demonstrated through virtual experiments. First, a single block

of 35x35 elements is composed in a matrix. Two input terminals, A and B are defined on either side of the matrix. Simultaneously, the other two orthogonal directions are considered output with Q as shown in Figure 5. **8. Figure 5. 8** also shows the typical inputs and output schedule for AND, OR, NAND, and NOR gates. All inputs, if not zero, are wave excitation input from the respective terminals. Frequency of excitation to be kept near the Dirac frequencies, e.g. ~12.46 kHz, or ~18.38 kHz. Here acoustic computing of Boolean algebra is demonstrated at ~18.38 kHz. However, similar phenomena persist at ~12.46 kHz (not shown).

Please note that 9.7^{o} rotation of the square PnCs results in a Dirac cone behavior while a 45^{o} rotation results in a bandgap (refer **Figure 5. 4**). Exploiting these facts, a single degree of freedom system of the acoustic computing logic gate is devised (Figure 5. **8**). Every input is considered 1 if the wave is excited at the frequency ~18.38 kHz at the respective terminals A or B. From the output terminals Q, if the transmission coefficient is above 0.75 then the terminal output is considered 1, else the output is considered 0. The

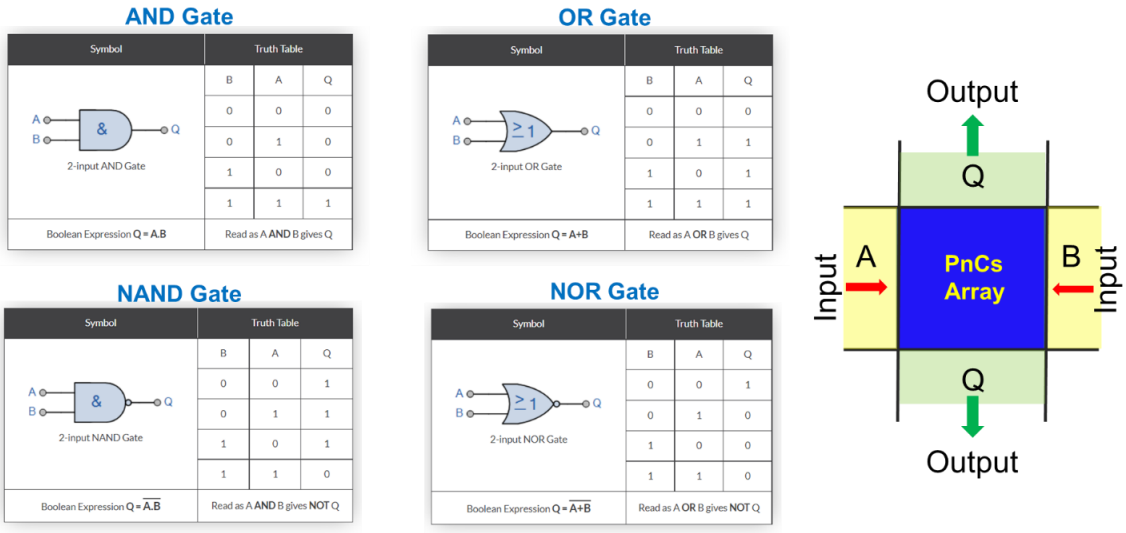

Figure 5.8: Left: Schedule input/output for different gates, Right: PnCs structure to test the computing logics.

following logics are created to perform all the tasks that are necessary to perform by each 'gate' as depicted in Figure 5. **8**.

AND Gate: Unless both A and B are 'on' with positive input of wave, i.e. 1, the PnCs orientation will be fixed to 45^{o} rotation. Hence, when A and B are excited independently, i.e. A=1, B=0, or A=0, B=1, the output terminal will read 0, resulting in, A AND B operation. However, when both A and B are 'on' the PnCS automatically rotate to 9.7^{o} creating the opportunity for orthogonal transport. In such a scenario output terminal will read 1.

OR Gate: This gate is fixed at a fixed rotation of 9.7^{o} of the PnCs. When A=1, B=0, it will result in transmission through the output terminal result output 1. This will be the same for B=1, and A=0. When both A and B are on, i.e., A=1, B=1, the output will still read 1 due to the orthogonal transport at the Dirac cone. From the output amplitude at the Q terminals, the input status of the A and B terminals can be deduced.

NAND Gate: In this gate, the PnCs orientation will be 9.7^{o} unless both A and B are 'on' with positive input of wave i.e. 1. When A=1, B=0, this gate will result in output Q=1 and vice versa. However, when both A and B terminals excite the wave with input 1 then the system would rotate to 45^{o}. This will result in output Q=0. In acoustic wave, zero inputs can not be functionalized, and hence, A=0, B=0, and Q=1 can not be achieved.

NOR Gate: This gate is fixed at a fixed rotation of 45^{o} of the PnCs. When A=1, B=0, it will prohibit transmission through the output terminal, which will result in output Q=0. This will be the same for B=1, and A=0. When both A and B are on, i.e., A=1, B=1, the output will still read 0 due to the bandgap. In acoustic wave, zero inputs cannot be functionalized, and hence, A=0, B=0, and Q=1 cannot be achieved.

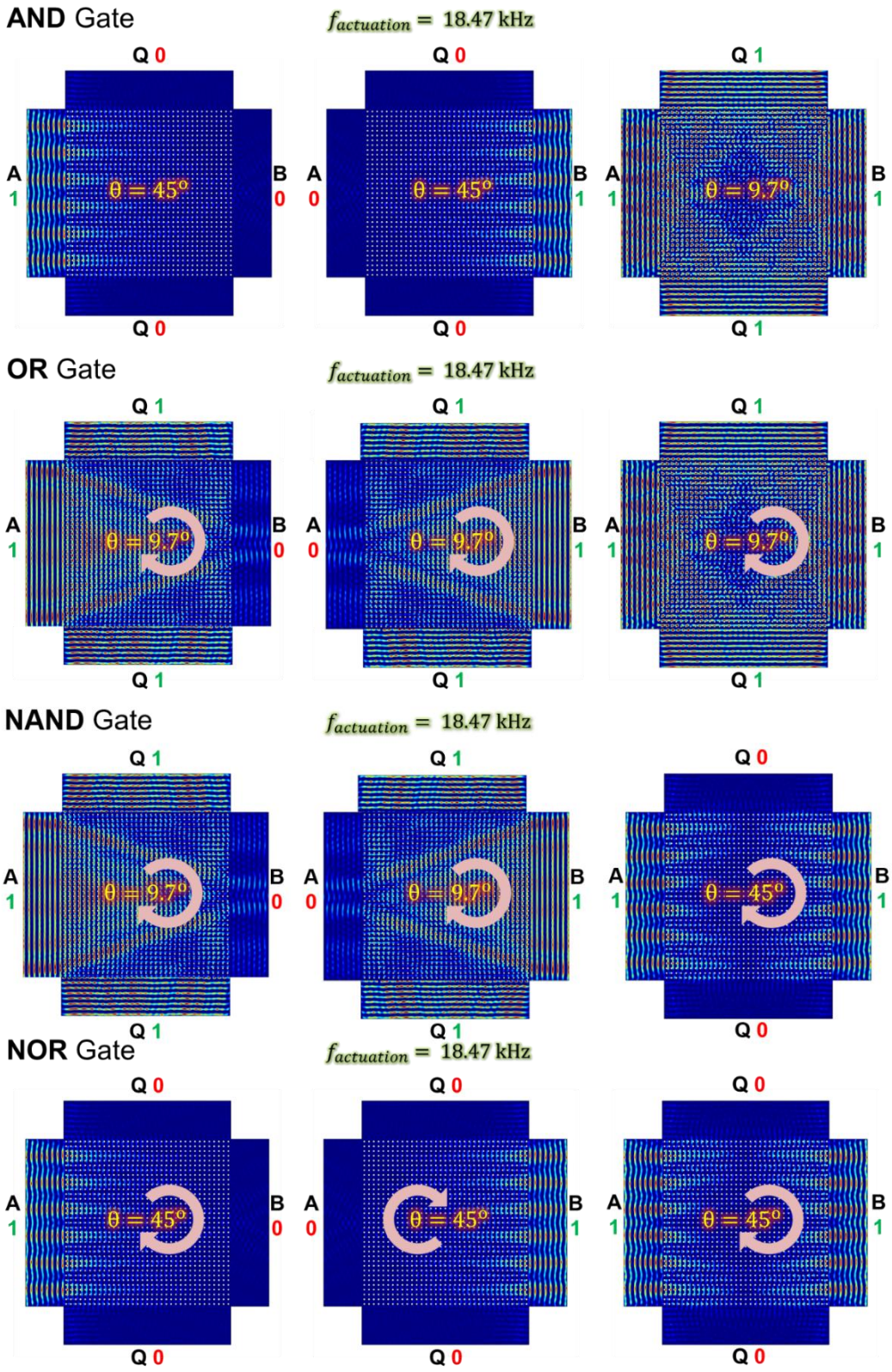

Figure 5.9: Functionality of AND, OR, NAND and NOR gates.

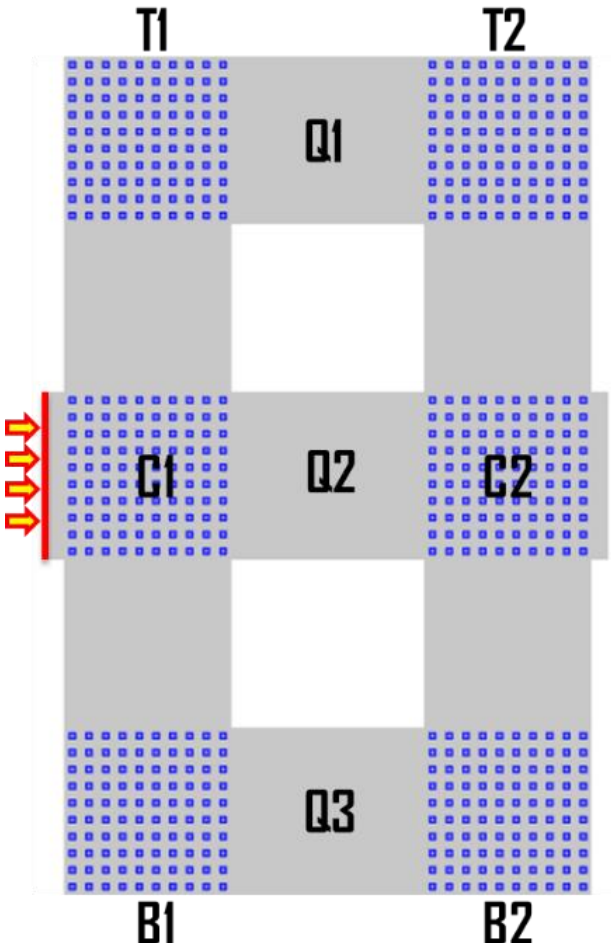

Figure 5.10: A six degrees of freedom system for Acoustic Computing.

Further, based on this concept, a six degrees of freedom system is created to perform more complex computing tasks where every single component is utilized to perform Boolean algebra. A conceptual design is presented in **Figure 5. 10**. Six square PnCs matrices (T1, T2, C1, C2, B1, and B2) are created. Each matrix will have its own control of rotation. This control will help them to rotate to a specific angle of 45^{o} or 9.7^{o} as needed to perform the Gate operation presented in **Figure 5. 9.** Although multiple input terminals could be created, only one input terminal at C1 is considered for a simple

demonstration. This demonstration is simulated at ~12.46 kHz at DRA, however, a similar could be achieved at DRB, as demonstrated in **Figure 5. 9**.

Keeping a constant input of wave excitation at terminal C1, outputs through the horizontal gray channels (Q1, Q2, and Q3) are investigated. Terminals are rotated independently to achieve certain output. **Figure 5. 11** shows a few such scenarios (cases).

Case 1: C1 is excited and kept a 0^o rotation, while all the other matrix terminals are rotated to 45^o. This situation shows no transport and no output through Q1, and Q3 but Q2 has an output, i.e. Q2=1. If C1 was also rotated to 45^o, all outputs would be 0.

Case 2: C1 is excited while all the matrix terminals (C1, C2, T1, T2, B1, and B2) are rotated at 9.7^o. This situation shows full orthogonal transport and outputs through Q1, Q2, and Q3 are all equal to 1.

Case 3: C1 is excited. C1, C2, T1, and T2 are rotated at 9.7^o while B1 and B2 are rotated at 45^o. This situation resulted in Q1=1, Q2=1, and Q3=0.

Case 4: Vice versa, C1 is excited. But C1, C2, B1, and B2 are rotated at 9.7^o. T1 and T2 are rotated at 45^o. This situation resulted in Q1=0, Q2=0, and Q3=1.

Following the above rules, many more situations could be created using the proposed structure. Other output terminals that are vertical channels in **Figure 5. 10** (gray

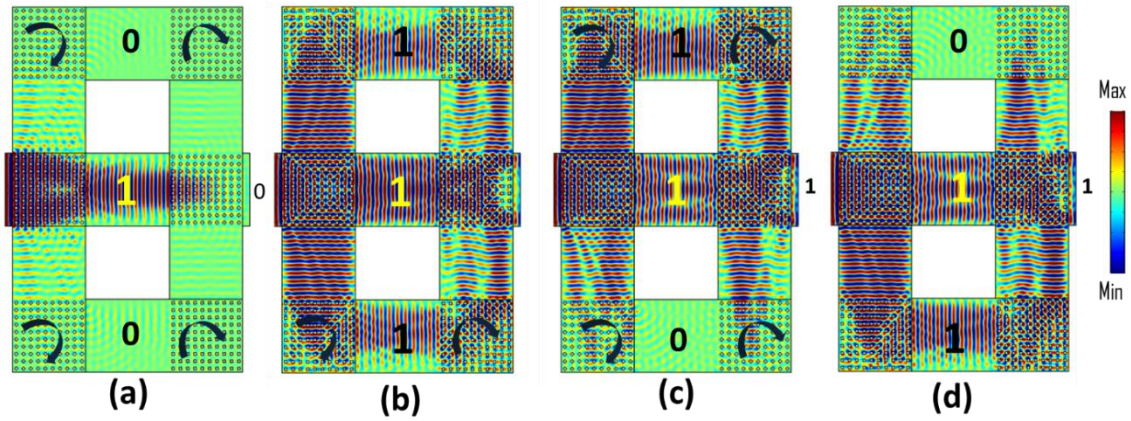

Figure 5.11: Acoustic computing using a multi-degree of freedom system to exploit multi-channel input and multi-channel output. a) Case 1, b) Case 2, c) Case 3, d) Case 4

channels) could be added as additional outputs to investigate (not shown) more complex scenarios.

5.6 CHAPTER SUMMARY

Acoustic computing of Boolean algebra using the deaf band-based angular tuning of Dirac-like cones at the center of the BZ is presented herein. The predictive optimization process demonstrated the dual Dirac-like cone. Orthogonal transport near Dirac-like cone with triple degeneracy has been demonstrated elsewhere. However, here in this article, a double degeneracy state near Dirac-like point was found to be extremely valuable for acoustic computing. A state described to have a bottom band with negative curvature but lifted from a nearby doubly degenerated Dirac-like point, formed by a band with positive curvature degenerated with a deaf band is identified for this purpose. This state is specifically valuable due to the retention of the antisymmetric wave mode shape of the deaf-band. Followed by theoretical description of the state, first a block of 35x35 PnCs elements is composed in a matrix with two input terminals defined on either side of the

matrix. Simultaneously, the other two orthogonal directions are considered output. Next few designs are created to perform AND, OR, NAD, and NOR operations by tuning the PnCS to a specific angle when the above-mentioned state is activated. Additionally, a six degrees of freedom system is created to perform more complex computing tasks where every single component is designed to perform specific Boolean algebra. Although only four different cases are demonstrated, multiple different combinations could be explored to perform more complex computing performance. Dirac-like cones dispersion at a specific state mentioned above increases the possibility of exploiting numerous computing opportunities at different frequencies in a single lattice structure. This will provide greater design flexibility with acoustic computing for practical wave manipulation. We anticipate that this study will encourage further numerical and experimental investigations into band degeneracies for extensive acoustic device applications.

CHAPTER 6

TOPOLOGICAL BLACKHOLE: A NEW SECTOR IN THE FIELD OF TOPOLOGY

6.1 BACKGROUND:

Incorporation of periodic crystals, both in electronic and classical wave systems, started a new path of research, yielding exotic phenomena related to topological phases. In traditional band theory, topology has not yet been extensively utilized in mass scale. Topology defines the global properties of a wavefunction over an entire band. It preserves certain symmetries by keeping the robustness against local perturbations. Topology has mitigated the ambiguity of not solving and understanding certain acoustic and mechanical systems through Newtonian or Lagrangian equations for years. It reflects new paradigms for designing devices with enhanced functionalities, fueling interest in the emerging fields of topological acoustics and topological mechanics.

In the previous chapters, tailoring of acoustic waves exploiting Dirac-like points in the periodic crystals has been demonstrated. In this chapter, a topological phenomenon in acoustics is attained and discussed in detail. Here, a bulk topological phenomenon exploiting dispersive band degeneracy in **K**-space is discussed. The intrinsic spin dependence of wave propagation behavior yielding a specific topological state in acoustics is demonstrated. A short explanation of how topological physics has emerged over the last couple of decades has also been discussed here.

6.2 TOPOLOGY:

Mathematically, topology relates to the global properties of space, preserved under continuous deformation. The word, topology means the study of position or location. It studies their shapes including their properties, applied deformations, mapping and configurations composed of them. In topology, distances and angles are apparently irrelevant. It is often described as rubber-sheet geometry. Objects in traditional geometries such as, triangles, circles, planes and polyhedral are considered rigid with well-defined distances and angles between points and edges/surfaces respectively. But in topology, objects are allowed to be molded to change shape without ripping apart. That's why a torus and a sphere is said to be topologically distinct as they cannot be molded or shaped to one

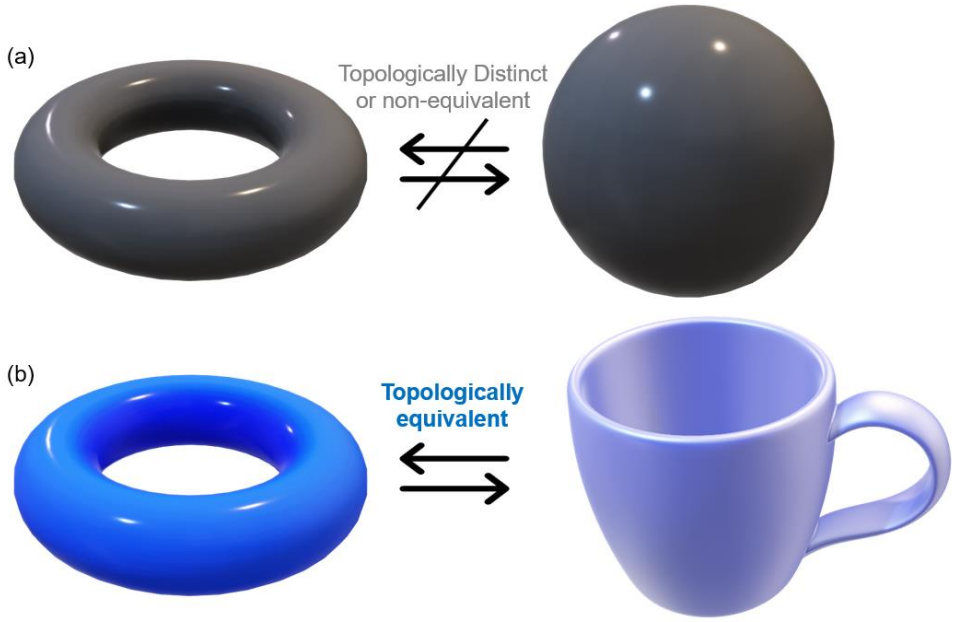

Figure 6.1: (a) The torus and the sphere are not topologically equivalent, (b) but the torus is topologically equivalent to the coffee mug.

another due to having the hole for the torus. While such torus can be molded to coffee mug, which is why they can be termed as topologically equivalent. Figure 6. 1 illustrates two different states of topology and their topological equivalence respectively.

6.2.1 Topology in crystals and Quantum Hall Effect (QHE):

In the early 1900s, Landau helped characterizing the stable phases of matter by a local order parameter which vanishes in the disordered phases and is nonzero in the ordered phase [111]. This symmetry breaking theory categorized the phases with non-zero order parameter by the way they transform under symmetry operation. It remained accepted and unchallenged by the greater scientific community believing that this theory is capable of describing all possible phases of matters as well as possible continuous phase transitions. But the discovery of the Berezinskii-Kosterlitz-Thouless (BKT) transition changed the plot by explaining the phase transition in a two-dimensional model which cannot be explained by symmetry breaking theory [112, 113]. With this, the integer Quantum Hall effect emerged [114]. The Quantum Hall Effect (QHE) is observed in 2D electron system with low temperatures and strong magnetic field. Here, the bulk state behaves as a featureless insulator, which cannot be characterized by local order parameters. But, a robust edge-state in the boundary under external deformation exists. Such behavior intuitively contradicts

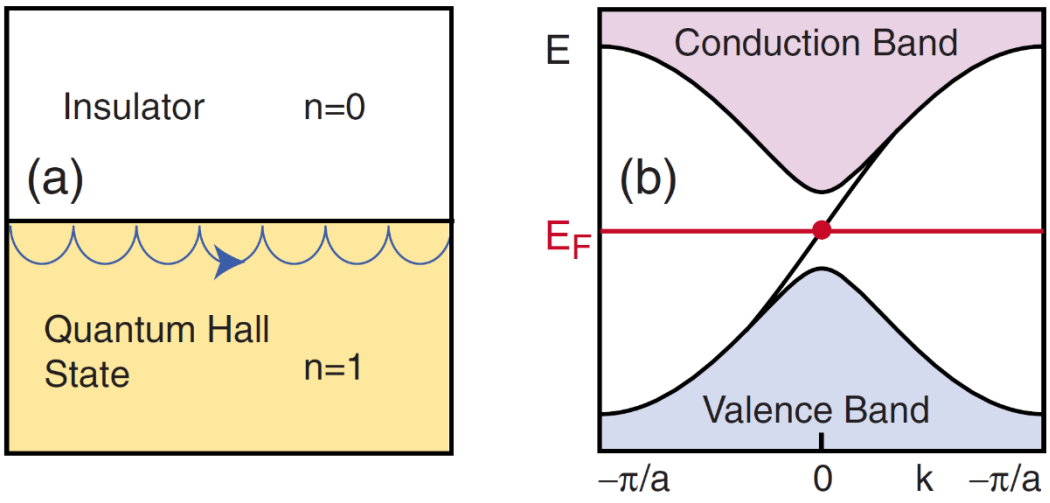

Figure 6.2: (a) the chiral edge state in the interface between a quantum Hall insulator and a conventional insulator. (b) The band structure of the structure, with a single edge state connecting the valence band to the conduction band is shown. The Figure 6.s are adapted from ref [119]

our understanding of Anderson Localization where the edge state is supposed to be affected by impurities. Thus, the existence of truly distinct phases of matter is established by QHE. Here, the bulk is characterized by a topologically invariant as the bulk order parameters fails to describe the new phase. The quantized hall conductance is an invariant which does not change with the arbitrary phase appearing in the eigenfunctions.

An analytic derivation of the quantized Hall conductivity in periodic crystals was given by Thouless, Kohomoto, Nightingale and den Nijs (TKNN) in 1982 [115]. They considered a 2D electronic gas under a uniform perpendicular magnetic field and an arbitrary lattice potential described by a single particle Hamiltonian. The conductivity was expressed utilizing the Kubo formula of linear response as an integral involving valence band state.

$$\sigma_{xy} = \nu \frac{e^2}{h}$$

$$\nu = \frac{i}{2\pi} \int_{BZ} d^2k \sum_{E_m < E_f} 2iIm \left\langle \frac{\partial}{\partial k_x} u_m(k) \middle| \frac{\partial}{\partial k_y} u_m(k) \right\rangle = \frac{i}{2\pi} \int_{BZ} Tr(\mathcal{F}) \in \mathbb{Z}$$

Here, the summation is taken over the occupied periodic crystal and the integral is over the magnetic Brillouin Zone [116], $\mathcal{F}$ is the Berry curvature [117]. The topology of the occupied band is characterized by the TKNN integer, ν, also known as the first Chern number. E_m and E_f indicates all the branches below a particular band gap, describing the topological properties of that band gap. For non-zero Chern number, the band gap is called a topologically non-trivial band gap and for $\nu = 0$, it is called a topologically trivial band gap [115]. A gap with a certain topological invariant cannot be smoothly transformed into another gap associated with a different topological invariant. The topological difference of the band gap distinguishes the QH insulators from conventional insulator and gives rise to

the bulk-edge correspondence [118]. The topological invariant represents the number of the chiral edge-state, ensuring conduction on the surface without dissipation or back-scattering, even in the presence of large impurities. Figure 6. 2 illustrates chiral edge states in interface between a quantum Hall insulator and a conventional insulator [119].

However, realizing such topological behaviors poses great challenges, difficult to overcome in the electronics system, which is why researchers have extended this study mostly to photonics and phononic systems. Fabrication and control over the system gets

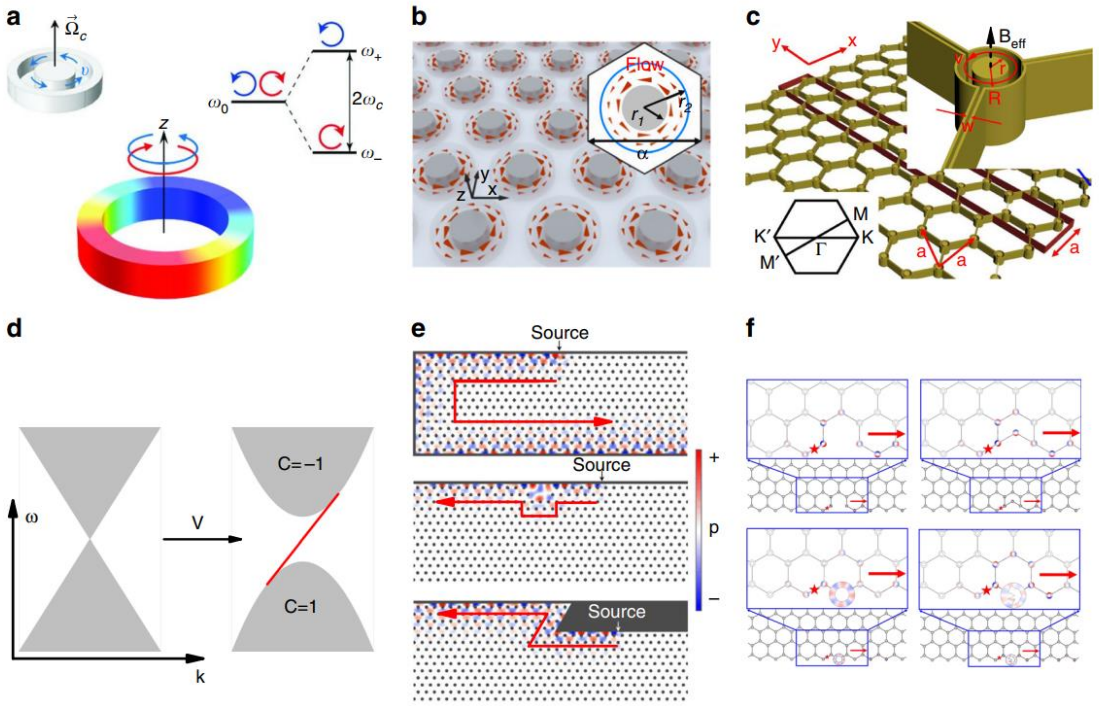

Figure 6.3: Quantum Hall effect in phononic crystals. (a) The airflow-induced acoustic nonreciprocity, (b) and (c) two acoustic quantum Hall lattices incorporated with circulating airflow are presented, (d) Illustration of the band gap opening induced by the airflow, associated with a one-way edge state that spans the bulk gap region, (e) and (f) The robust edge state propagation against various defects. The Figure 6.s are adapted from: ref [120-123].

easier in the case of photonics and phononics. Moreover, multi-regional wide spectrum can be covered by photonic/phononics system, not limiting to Fermi levels only. However, photons/phonons do not possess any half integer spin to interact with the applied magnetic

field. Breaking the time-reversal symmetry poses greater challenge in such cases. Especially, phononic systems in acoustics lacks transverse polarization degree of freedom that can be used to construct pseudospins to mimic the spin up and spin down in electronic system. The first analogue QHE in photonics was proposed and demonstrated in 2008 by Haldane [52]. A gyromagnetic material subjected to a magnetic field was used to break the time-reversal symmetry for a 2D photonic crystal. But breaking time-reversal symmetry in the case of acoustics using phononic crystal is more challenging. Utilizing dynamic fluid flow in phononic crystals can break the time-reversal symmetry. Here, the imparted fluid-flow takes the role of magnetic bias by splitting the degeneracy of two counter-propagating

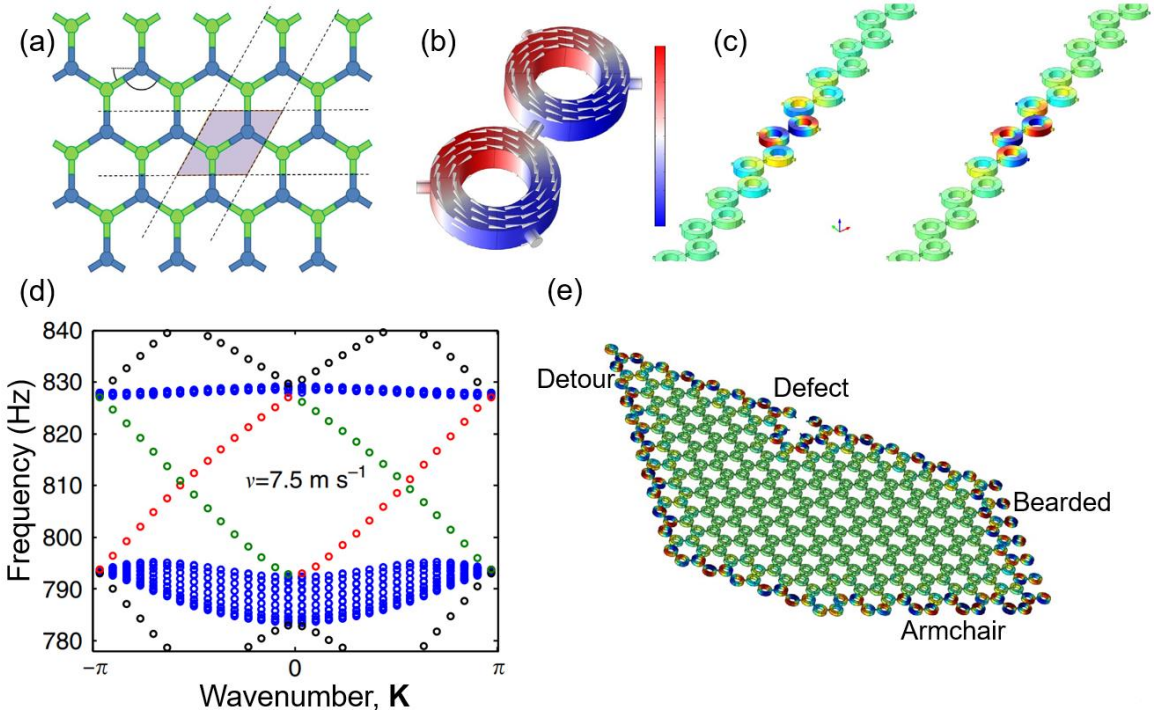

Figure 6.4: (a) Diatomic lattice forming an acoustic analog of graphene, (b) Unit cell of lattice with acoustic pressure distribution and direction of airflow, (c) Acoustic pressure profiles of one-way edge mode localized at the bottom and top of supercell, (d) Acoustic band structure with bulk modes shown in blue and edge modes in black, green and red, (e) One way edge propagation along different cuts including bends, defects, detour, bearded and armchair. The Figure 6.s are adapted from ref [124].

azimuthal resonant modes inside PnCs (Figure 6. 3a) [120-123]. The wave equation for sound propagating in a circulating airflow with velocity **V** would be,

$$[(\nabla - i\mathbf{A}_{eff})^2 + \omega^2/c^2 + (\nabla\rho/2\rho) - \nabla^2\rho/(2\rho)]\phi = 0$$

Where, ϕ is the velocity potential, ω is the angular frequency, c is the sound speed and ρ is the mass density of air. For non-zero **V**, the term $\mathbf{A}_{eff} = -\omega\mathbf{V}/c^2$ creates an effective vector potential, generating an effective magnetic field,

$$\mathbf{B}_{eff} = \nabla \times \mathbf{A}_{eff}$$

This $\mathbf{B}_{eff}$ helps breaking time-reversal symmetry. Figure 6. 3 also shows hexagonal lattice and honeycomb lattice respectively, used in obtaining QHE analogue in acoustics. A pair of Dirac-like degeneracies emerge due to intrinsic lattice symmetry at the BZ boundary for **V** = 0. After introducing the fluid flow, the degeneracy lefts due to broken time0reversal symmetry by opening a bandgap. According to the bulk-edge correspondence principle, one-way edge states prevail with such signature topologically nontrivial system, shown in Figure 6. 3e. Here, acoustic wave propagation exhibits unidirectional behaviors, which hare topologically protected and robust against various defects and sharp bends.

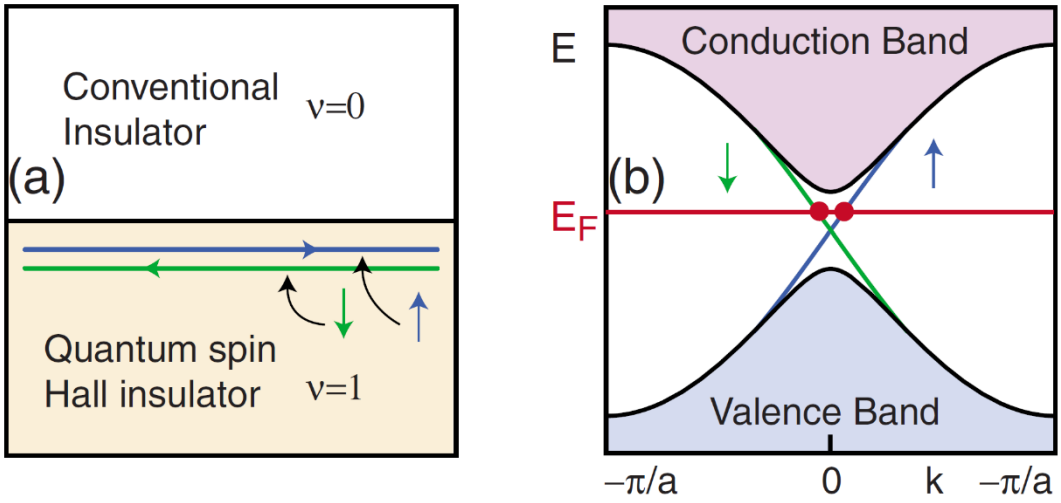

Figure 6.5: (a) The helical edge states in the interface between a quantum spin Hall insulator and conventional insulator. (b) The band structure of the corresponding structures. Pairs of helical edge state connects the valence band to the conduction band. The Figure 6.s are adapted from ref [119]

A graphene like resonator lattice is also reported to allow one way edge state with circular airflow around the resonator. Figure 6. 4 illustrates the lattice along with the unit cell to allow the circular motion [124]. Unlike a nontopological guided edge mode, this system shows strong robustness against structural defects and irregularities like sharp corners, defects, detour, armchair and many more (Figure 6. 4e). This edge state allows idea reflection-les routing along arbitrarily defined pathways, reconfigurable in real time, by creating line boundaries within lattice with opposite applied angular momenta on two sides.

However, Haldane also introduced periodic magnetic flux substituting external applied field to concur the time-reversal symmetry breaking [119]. Such effect, named as Quantum Anomalous Hall effect (QAHE) is similar to QHE in expressing in terms of the same topological invariant. Later, studies have been extended to replace the periodic magnetic flux by a ferromagnetic insulator with strong spin-orbit coupling [125-127]. This discovery leads to one of the most groundbreaking phenomenon in the field of condensed

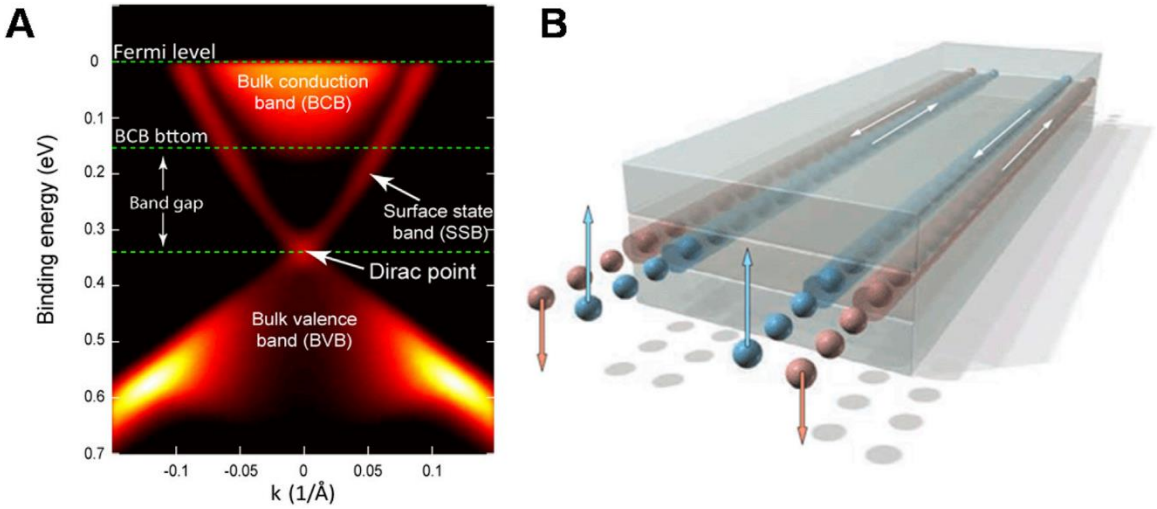

Figure 6.6: Topological Insulators and the spin-momentum locking mechanism, (a) energy band structure of Bi2Se3, (b) illustration of spin-polarized helical edge channel in a TI material. The Figure 6.s are adapted from ref [132]

matter

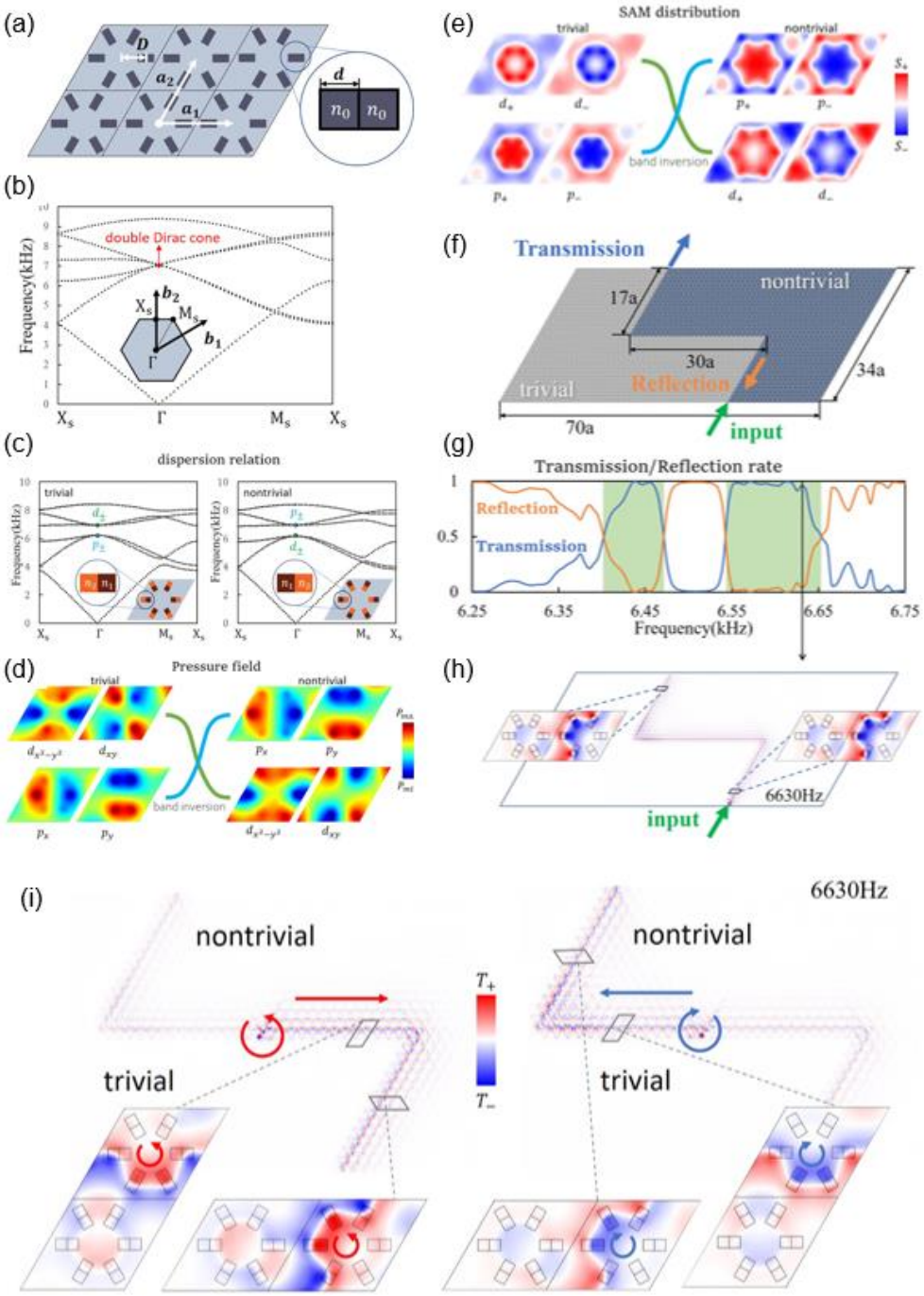

Figure 6.7: (a) Schematic of phononic crystal with double square unit, (b) the dispersion relation of the lattice, (c) The dispersion relation of trivial and nontrivial unit cells, (d) Topological phase transition from trivial to nontrivial units depicting acoustic pressure field distribution with dipole and quadrupole modes, (e) Spin angular momentum distribution of p and d modes in trivial and nontrivial unit cells, (f) The schematic of test setup with Z-shape edge, (g) The transmission/reflection rate of Z-shape edge wave guide, (h) Spin angular momentum distribution on the Z-shape edge for 6.63 kHz, (i) topological one-way edge wave guide mode on Z-shape edge with CW and CCW spin denoting source mode. The Figure 6.s are adapted from ref [146].

Effect (QSHE) [128-132].

6.2.2 Quantum Spin Hall Effect and Topological Insulators:

Instead of breaking the time-reversal symmetry, topological states can still exist with preserving the time-reversal symmetry intact. This new state exhibits robust edge state without breaking the time-reversal symmetry. Here, two states with opposite spin polarization counterpropagating at a given edge resembles as two copies of QHE. The spin is correlated to the direction of motion.

Although the electrons propagate both forward and backward on the same edge, the nonmagnetic impurity leads to a destructive interference of backscattering, which contributes to a perfect transmission of the edge state. When time-reversal symmetry breaks, the backscattering remains no longer destructive. But, since the TR symmetry is preserved, the Chern number is zero and the total Hall conductance vanishes due to opposite spins that counter-propagate and contribute to opposite quantized Hall conductivities.

Kane and Mele first proposed the QSHE to exist in graphene with spin-orbit coupling, shown in Figure 6. 5 [119, 133]. But due to having extremely small gap induced by the spin-orbit coupling, searching for a better alternative continued and ultimately obtained in HgTe quantum wells in 2007, leading to the discovery of topological insulators [134]. Such HgTe-based quantum well heterostructure can host pair of counter-propagating edge states which are related to each other through time-reversal symmetry. From there, the name, topological insulator emerged as such material has a bulk insulating gap while exhibiting topologically protected metallic states at the boundary. The band structure of one topological insulator material is given in Fig 6 [135-137]. Here, a gapless surface state

with a single Dirac cone with a linear *E-k* relation is observed. The surface electrons behave as massless Dirac fermions with ultra-high mobility. The most essential feature which distinguishes topological insulators from traditional insulators is the surface spin-momentum locking mechanism. This mechanism dictates the spin orbit coupling resulting the spin polarization of the surface electrons to be locked to its momentum direction. Hence, with applied external current, electrons with opposite spins separates along the edges, causing such topologically insulating phenomenon, as illustrated in Fig 6 [135-137]. Due to the time-reversal symmetry being protected, back-scattering by the non-magnetic impurities are forbidden during the electron transport, leading to the QSHE. Hence, topological insulators are widely known as QSH insulators as well [138-142].

Due to space symmetry, the wave equation is diverse in different continuous limits for periodic potential modulation. Studying the behavior of relativistic particles can be approached by reproducing the Dirac equation under the frame of band theory [143, 144]. But, topology, being a global property of the band in the Brillouin zone, cannot be confined in the continuous limit. An unconfined lattice model in the high symmetry point is more appropriate. However, a lattice model can indeed be mapped near the critical point of topological quantum phase transition. The topology of the lattice remains unchanged when energy band gap persists without closing. Then the Hamiltonian of a 2D lattice model as an electron in an effective magnetic field would be, $H = \boldsymbol{d}(\boldsymbol{k}) \cdot \sigma$, whose dispersion relations are,

$$E_{k,\pm} = \pm|\boldsymbol{d}(\boldsymbol{k})|.$$

For 2×2 modified Dirac models with time-reversal symmetry preserved, with time-reversal operator, $\Theta = i\sigma_y K$, where K is the conjugate.

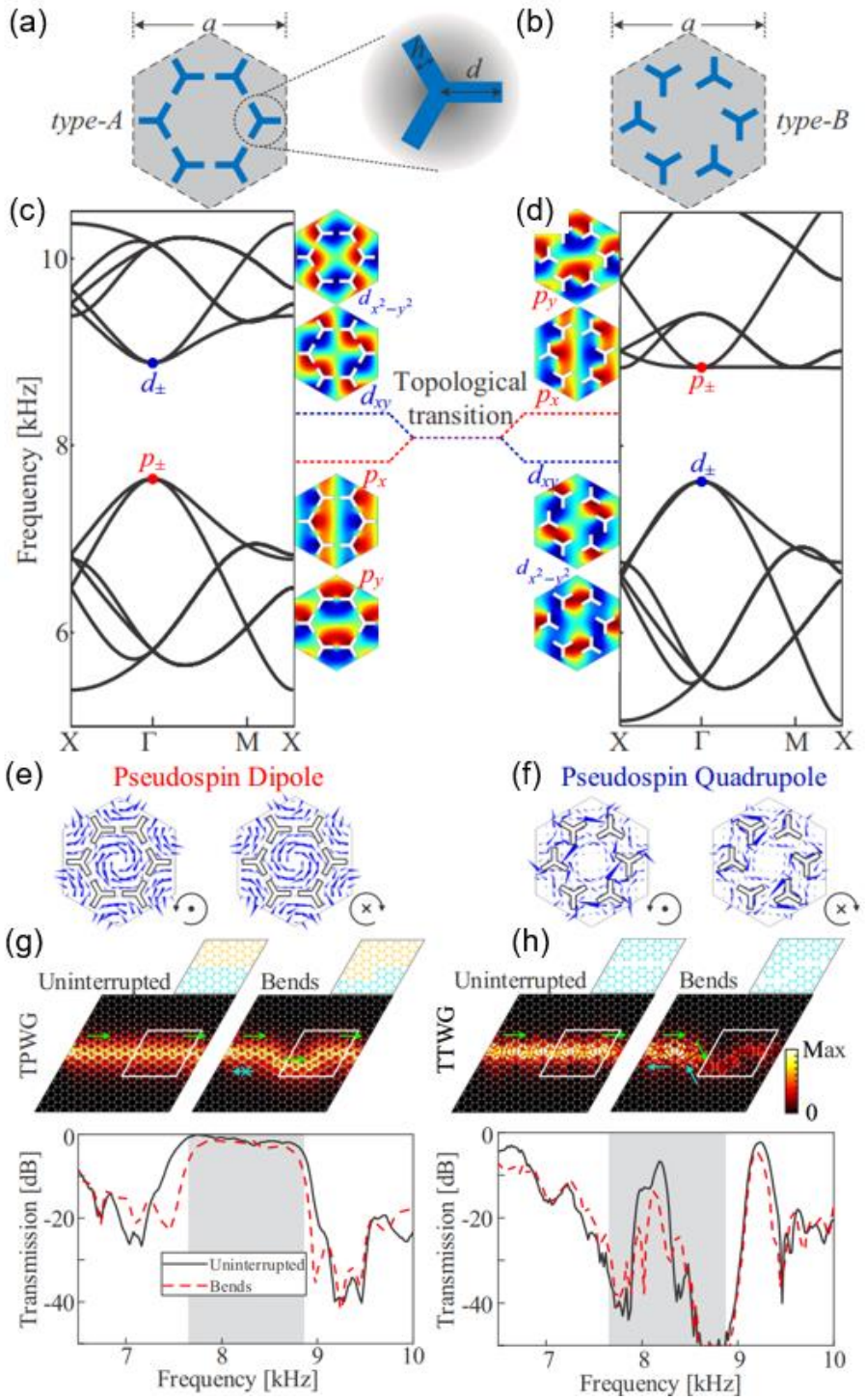

Figure 6.8: (a) and (b) Schematics of two snowflakes like metamolecules, Type A and type B, (c) and (d) Corresponding dispersion of the topologically trivial and nontrivial structure, (e) and (f) Sound intensity for pseudospin-down and pseudospin-up modes at Γ point for trivial and nontrivial regimes, (g) and (h) Simulated pressure filed distribution along with transmission spectra showing the stronger robustness for topologically protected waveguide. The Figure 6.s are adapted from ref [147].

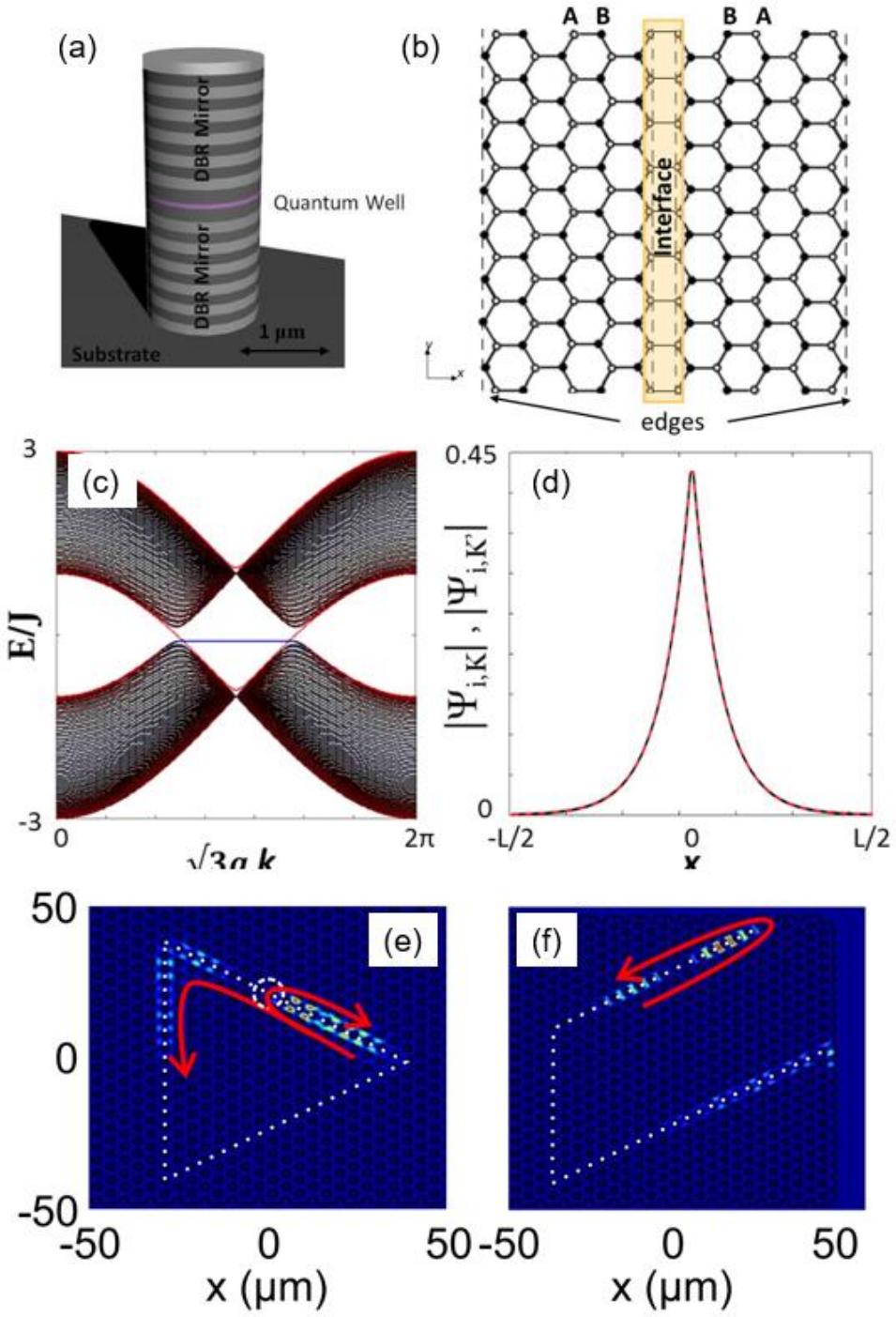

Figure 6.9: (a) Cavity micropillar (artificial atom) scheme. (b) Zigzag interface between two lattices with opposite organization giving rise to zero lines modes and quantum valley Hall effect with a proper choice of parameters, (c) Ribbon dispersion (d) Corresponding in-gap interface wave-function absolute values projection on the transverse (x) direction for K (solid black) and K' (dashed red) valleys, (e) and (f) QVHE edge state propagation with little backscattering perturbation on a localized defect and at the boundary respectively. The Figure 6.s are adapted from ref [154].

Where, $\mathbf{d}(\mathbf{k}) \cdot \sigma$ is the spin up component and $-\mathbf{d}(-\mathbf{k}) \cdot \sigma$ is the spin down

component. Thus, the effective Hamiltonian for a simple QSHE can be obtained:

$$H_{QSHE} = \begin{pmatrix} \mathbf{d}(\mathbf{k}) \cdot \sigma & 0 \\ 0 & -\mathbf{d}(-\mathbf{k}) \cdot \sigma \end{pmatrix}$$

This a simpler version of QSHE where further spin-orbit coupling, Rashba spin-orbit coupling and Zeeman splitting can be added and expanded more [145].

In the field of acoustics, the waveguide modes in acoustic QSHE are traditionally described with spin-like modes rather than real spin angular momentum due its longitudinal curl-free nature. The equivalence between acoustic pseudospin and real spin angular momentum is absent in this case. However, an intrinsic acoustic spin angular momentum of an acoustic field is obtainable by a velocity field with rotational polarized properties despite it being curl-free. The spin angular momentum in acoustic wave can be expressed as:

$$s = \frac{\rho}{2\omega} Im[v^* \times v]$$

where ρ is the mass density, ω is the frequency, v is the particle vibration velocity and v* is the conjugate of v. So, by absorbing the acoustic spin angular momentum, a small particle will receive a torque proportional to 's'. Figure 6. 7 illustrates a phononic crystal unit cell with the dispersion relation of the lattice showing a double Dirac cone at the Γ point [146]. The spin angular momentum mode is introduced by the circular polarization of the velocity field. The dispersion relation for both the trivial and non-trivial cases are given in Figure 6. 7c. Topological phase transition occurs between trivial case to non-trivial case. Px and Py – two dipole modes in trivial case undergoes band inversion in the non-trivial state (Figure 6. 7d). Spin angular momentum distribution also affirms the band inversion occurrence. In band inversion, p-states get exchanged with d states by transitioning topological phase. To illustrate the mechanism of topological phase transition,

k.p perturbation theory is used to derive the effective Hamiltonian and calculate Chern numbers. The acoustic eigenequation can be written as

$$-\nabla \cdot [\rho^{-1}(\boldsymbol{r})]\nabla\phi_{n,\boldsymbol{k}}(\boldsymbol{r}) = \omega_{n,\boldsymbol{k}}^2(\rho(\boldsymbol{r})c^2)^{-1}(\boldsymbol{r})\phi_{n,\boldsymbol{k}}(\boldsymbol{r})$$

Where, $\phi_{n,\boldsymbol{k}}(\boldsymbol{r})$ is the wavefunction of the pressure field and $\omega_{n,\boldsymbol{k}}$ is the eigenfrequency of the acoustic Bloch state with wavevector **k** in the nth band. $\rho(\boldsymbol{r})$ is the mass density and c being the acoustic velocity. The wavefunction around Γ point can be expressed as summation of Bloch wavefunctions and $\boldsymbol{k}$ is perturbation so that the Hamiltonian can be expanded as Taylor expansion of $\boldsymbol{k}$ with *k.p* form,

$$H_{nn'} = \omega_{n,\Gamma}^2\delta_{nn'} + k \cdot P_{nn'} + k \cdot M_{nn'} + \cdots$$

The effective Hamiltonian near Γ point on the basis $(p_+, d_+, p_-, d_-)^T$ is,

$$H_{eff}(k) = \begin{pmatrix} -D - Bk^2 & Ak_+ & 0 & 0 \\ A^*k_+^* & D + Bk^2 & 0 & 0 \\ 0 & 0 & -D - Bk^2 & Ak_- \\ 0 & 0 & A^*k_-^* & D + Bk^2 \end{pmatrix}$$

Where, $k_\pm = k_x \pm ik_y$ and $D = \frac{\varepsilon_d - \varepsilon_p}{2}$ are the frequency difference between the d state and p state, which is the positive in the trivial state and negative in the nontrivial state due to band inversion. A is determined by the off diagonal elements of the first order perturbation term of effective Hamiltonian and B is the diagonal elements of the second order perturbation term of Hamiltonian. k^2 for p and d orbitals are opposite, which are related to the curvature of dispersion relation near Γ point.

The spin orbit momentum distribution from Figure 6. 7d shows a strong correlation with the pseudospin. This spin orbit momentum is neither pure positive nor a negative value, but a spatial distribution. The topological edge waveguide in a finite structure with a Z-shaped edge is shown in Figure 6. 7f. A plane wave is generated from the input point

and the transmission spectra are plotted in Figure 6. 7g. The green region highlights the robust edge modes. The spin angular momentum distribution on the Z-edge for 6.63 kHz is given in Figure 6. 7h. The acoustic spin angular momentum when absorbed by an object to produce torque, having positive spin excitation inducing a positive torque. This chiral spin excitation creates a topologically robust mode that will cross the sharp corner of the Z-shape edge without apparent back scattering (Figure 6. 7i). That is how an analogue QSHE in acoustics are demonstrated exploiting acoustic intrinsic spin angular momentum.

Another example of QSHE analogue in acoustics is shown in Figure 6. 8 [147]. Here, a snowflake-like metamolecule unit of phononic triangular lattice is studied to achieve one-way edge state. Pseudospin states are transitioned by topological mode inversion method. Topological transition between trivial and non-trivial structure is shown in Figure 6. 8c. Topological mode inversion between the pseudospin states are illustrated. Sound intensity $\boldsymbol{I}$ associated with pseudospin-down and pseudospin-up modes at the Γ point for both trivial and nontrivial regimes are given in Figure 6. 8e and 8f. Numerical simulations of absolute pressure fields at the frequency 8.2 kHz for both topologically protected waveguide (TPWG) and topologically trivial waveguide (TTWG) are shown in Figure 6. 8g and 8h. Experimental transmission spectra illustrates TPWG sustaining stronger robustness than TTWG. TTWG transmission weakens through the waveguide due to lack of topological protection. Now let's look at the another phenomenon called QVHE.

6.2.3 Quantum Valley Hall Effect:

To achieve nonreciprocal edge states propagating unidirectionally, complexity of fabrication to break time-reversal symmetry made them less viable for practical applications. Hence, obtaining unperturbed edge states keeping the time-reversal symmetry

protected has been a quest for researchers for the last decade. Several studies have investigated topological materials based on broken space-inversion symmetry, instead of time-reversal symmetry. The effect of the asymmetry opens a topological bandgap at a Dirac cone associated with the K and K' symmetry points, hence creating the conditions

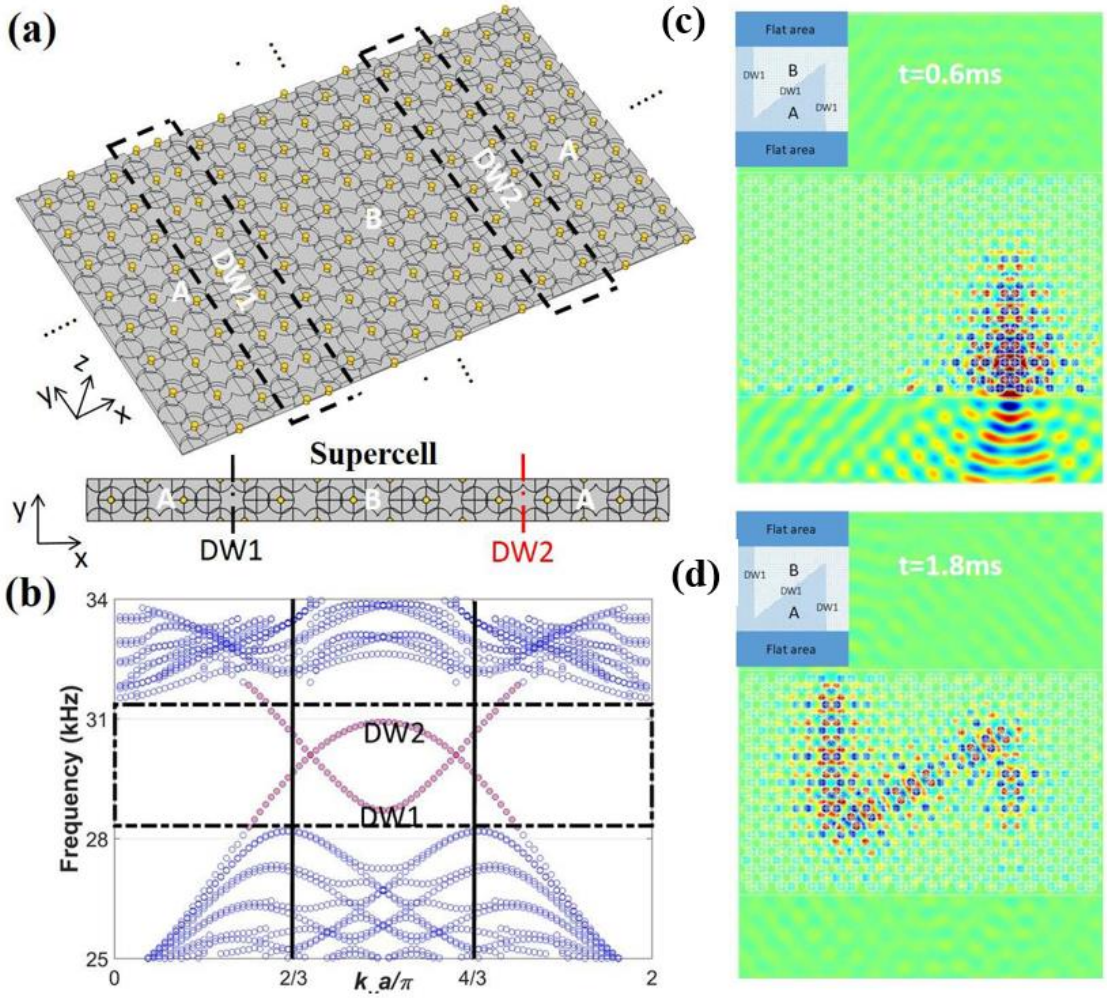

Figure 6.10: (a) Schematics of an elastic waveguide having A- and B-state lattices connected along their zigzag edges. This configuration gives rise to two different domain walls DW1 and DW2, as marked by the dashed black boxes. The primitive supercell of such waveguide is also shown. (b) The dispersion relations of the waveguide clearly show the existence of edge states in the topological band. For clarity, only the flexural modes are drawn in the dispersion plot. (c) Plots of the eigenstates of the edge modes supported at the domain walls DW1 and DW2. The plots illustrate different symmetry patterns (either symmetric or antisymmetric) taking place with respect to the interface plane (marked by dashed lines). The Figure 6.s are adapted from ref [144].

for the existence of edge states. These edge states cannot be explained in the context of

either QHE or QSHE. Although the lattice still possesses a trivial topology within the context of QHE as the time-reversal symmetry is intact. And it also possesses a trivial topology from QSHE perspective as it lacks the spin degree of freedom. However, due to the large separation in k-space of the two valleys (K and K' symmetry points), valley-dependent topological invariants can be defined and used to classify the topological states of the different lattices. This approach is called as the Quantum Valley Hall Effect (QVHE) [52, 148-151]. The QVHE exploits valley states instead of spin states, with the advantage that each lattice site needs to have only on degree of freedom. This concept helps obtaining the configuration of reduced geometrical complexity. Valley degrees of freedom arise naturally in systems with time reversal symmetry and have been predicted theoretically in graphene, where wavefunctions at opposite valleys demonstrates opposite polarizations and thus emulate spin orbit interaction [149, 150, 152, 153]. For practical implantation, QVHE is less complicated than QHE and QSHE but on the other hand, it results in a less robust (weak) topological effect.

Figure 6. 9 portrays an example of QVHE in a photonic system using a honeycomb lattice of coupled micropillars with a tunable energy detuning between A and B pillars [154]. Pillar diameters tunes the gap size given in Figure 6. 9c. A perfect valley filter is shown here using a domain wall between QAH and QVH phases using mixed light-matter excitation-polariton quasiparticles. The QAH phase for polaritons has been predicted to occur in different kind of polariton lattices under Zeeman field. A zigzag interface between two state lattices with opposite organization is given in Figure 6. 9b. The dispersion and corresponding in-gap interface wave-function absolute values for K and K' valleys are given in Figure 6. 9c and 9d. As mentioned, above, QVHE states implicate poor robustness

while propagating along edge state. Figure 6. 9e and 9f shows two distinct situations demonstrating localized defects leading to backscattering while maintaining the edge propagation somewhat intact.

However, the acoustic and elastic analogue of QVHE is referred as acoustic valley hall effect (AVHE). AVHE does not exhibit any actual quantum mechanical behavior. Here, edge state supporting along domain wall (DW) phenomenon is given in Figure 6. 10 [151]. DW are those interfaces between two adjacent phases. Schematic view of the fundamental lattice structure is given here. This analysis contains two different state lattices with a broken space inversion symmetry. Two different DW are formed in the elastic waveguide at the interface between the two states (DW1 and DW2). The supercell is also given in the Fig 10, which helps to obtain the dispersion properties of the composite waveguide. Periodic boundary conditions are applied on all the sides of the supercell before solving the dispersion relations in a frequency range around the topological bandgap. The edge states at DW1 and DW2 are given in Fig 10 where the edge modes are in red. This edge states are almost immune to backscattering due to large separation in momentum space between forward and backward traveling modes. Full field transient simulation demonstrates the propagation of wave bursts at two successive time instants. The energy is capable of traveling along sharp bends with very minimal backscattering.

6.3 KEY POINTS FROM QUANTUM TRIO:

As discussed above, QHE, QSHE and QVHE, commonly referred as ‘Quantum Trio’, all belong to the quantized edge transport phenomena, though their intrinsic mechanisms are quite distinct. The major characteristics of these three phenomena are:

QHE is realized in a Chern insulator, insulating the bulk because of discrete Landau levels, with conduction channel existing only at the edges. The applied external magnetic field performs as a gauge field coupling with the momentum of the electron, resulting cyclotron motions in real space. Time reversal symmetry is not preserved here.

QSHE is realized with no externally applied magnetic field, preserving the time-reversal symmetry intact. The strong spin-orbit coupling leads to the band inversion at the

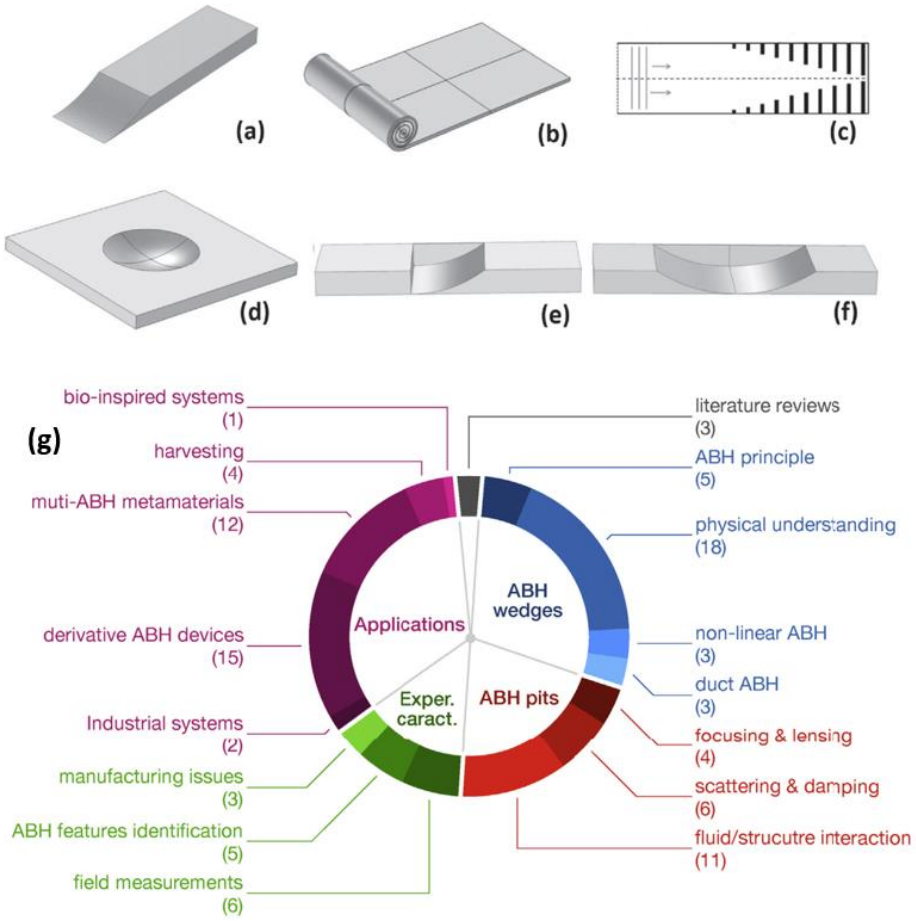

Figure 6.11: Examples of, so-called, retarding structures based on the concept of power-law taper, (a) tapered wedge, (b) Spiral ABH, (c) Acoustic tube with axially varying impedance made with a collection of branch discs of increasing diameters, (d) two-dimensional circular acoustic black hole, (e) one-sided, and (f) two-sided ABH slots. (g) Summary of the available literature related to the Acoustic Black Hole effect. The Figure 6.s are adapted from ref [156].

center of the Brillouin zone. The resulting quantum edge states are helical instead of chiral due to the spin-orbit interaction.

QVHE is realized by breaking the space-inversion symmetry in a lattice possessing Dirac dispersion at the high symmetry points, keeping the time-reversal symmetry intact. Opening a topological bandgap between the Dirac cone associated with the **K** and **K'** symmetry points (at the boundary of the Brillouin zone) results the valley dependent edge state propagation.

6.4 AN APPROACH TO EXPLORE TOPOLOGICAL BLACKHOLE (TBH):

Edge state conduction, modulation and controlling has been widely studied for the past decade under the concept of Hall conductance in the fields of electromagnetism and acoustics. Although advancement in the field of acoustic is minor compared to the other fields, due to the complexity of practical implementation. That is why, a deaf band based new physics of a topological phenomenon in acoustics has been discussed in detail in this chapter. A spin controlled bulk conduction waveguide, keeping the edge state insulated, is proposed in this chapter. Such topological bulk containment of energy in the field of

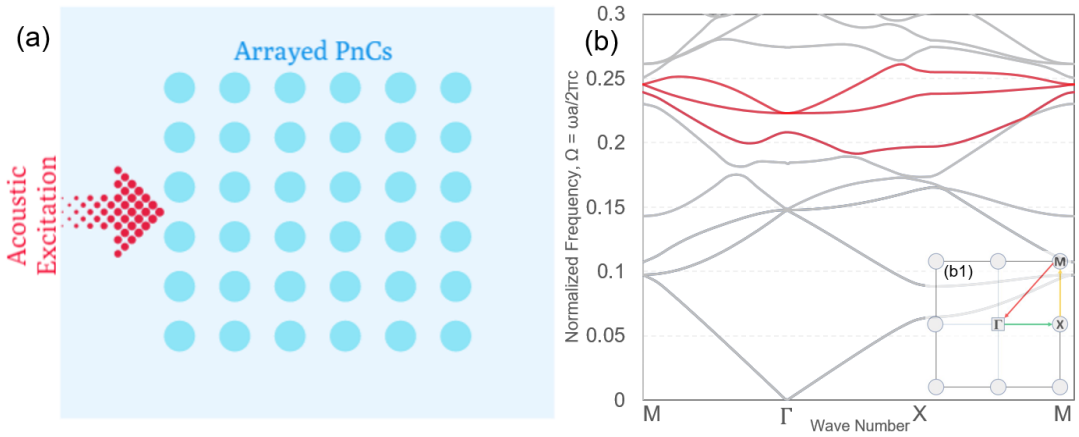

Figure 6.12: Experimental setup for frequency domain analysis, where the left-most edge/boundary (Red marked) has been excited with prescribed displacement. The band diagram for the cylindrical unit cell.

acoustics has never been reported in the literature. Periodic crystals, termed as PnCs, are utilized in this acoustic design setup. Encouraged from the deaf band-based energy modulation discussed in the earlier chapters, such topological bulk conduction is achieved with negligible leakage. This is why, this phenomenon has been termed as 'Topological Blackhole' (TBH). Earlier, very few researches have been conducted identifying acoustic blackhole (ABH), which helps trapping flexural waves based on local heterogeneities [155, 156]. However, ABH has mostly been exploited to achieve efficient passive structural vibration control [157-161]. The velocity of the incoming flexural wave has been reduced to zero, resulting a non-reflecting or a fully absorbing termination with the help of a wedge having a power-law decreasing thickness profile. This concept has always been confined to the wave reflectivity using ABH indentation, in the forms of wedges, pits, spiral meta-structure and acoustic tubes, showed in Figure 6. 11 [162-164].

However, Dirac cone based robust topological energy containment has yet to be discussed in the literature. A doubly-degeneration formed at the Γ point causing TBH to be implemented can be utilized in the broader spectrum of acoustical physics society. The proposed TBH possesses a unique bulk-boundary distinction, resulting an acoustic energy sink inside the periodic meta-structures. This behavior functions as a counterpart of the topological acoustic insulator. Polarization of two energy modes, degenerated at the Γ point, has to be orthogonal to each other to acquire TBH. Such mismatched polarity results an ambiguity within the energy propagating through the PnCs, resulting alternate spinning to allow the energy to be trapped within. Changing the waveguide media shape made of PnCs does not interrupt the occurrence of the TBH, confirming high robustness of the system. Regardless of any defects inside the PnCs array, the topological behavior persists

when excited at the doubly degenerated frequency. Hence, the energy trapping is independent of the impurities within the arrayed PnCs.

6.5 METHODOLOGY

Topological insulator helps to conduct electrons along the boundary of the material, where the rest of the material acts as an insulator, prohibiting bulk media conduction. Similarly, there might be a phenomenon where the bulk media acts as a conductor, keeping

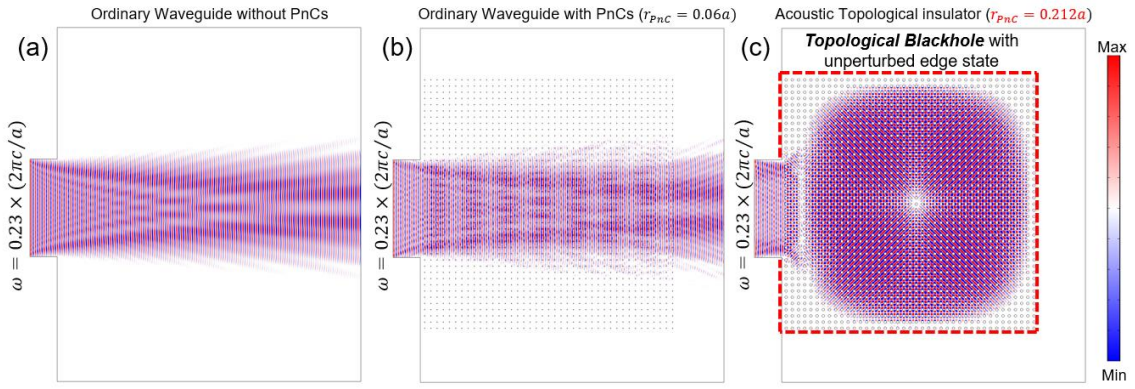

Figure 6.13: Formation of topological conduction phenomenon, using proposed PnC techniques. The plane wave generated from the left terminal of the model propagates linearly through the air media for no PnCs and with PnCs for r=0.06a. When the parameter r is changed to 0.212a, energy content tends to accumulate inside the PnC matrix, without interfering the edge states at all. This counterpart of Topological insulation is being stated as “Acoustic Topological Blackhole”.

the edge protected from the conduction. Here, the boundary exhibits insulating phenomena, keeping transportation away from the edge. We have developed an acoustic model where this phenomenon has been observed. As mentioned earlier, the counter phenomenon of topological insulator made us name it a topological blackhole (TBH). If an arrayed PnCs set is excited from one end at a certain frequency, the meta-structure behaves like a TBH, keeping the edge state unperturbed.

A sample schematic of obtaining the desired TBH is given in Figure 6. 12a. Acoustic energy excited at a specific frequency generates the TBH. A plane wave excited from the left boundary, shown in Figure 6. 12a, impinges on the periodic PnCs array. The

excitation frequency is swept for a wide range, where the normalized frequency, $\omega = 0.231 \cdot (2\pi c/a)$ generates the bulk propagation of the acoustic energy. The normalized frequency is calculated by

$$\Omega = \frac{\omega a}{2\pi c}$$

Where, Ω is the normalized frequency, ω is the real actuation frequency, a is the lattice constant and c is the wave speed in the travelling medium; air in this case. This frequency, which can be termed as TBH frequency, is the frequency very close to a doubly degenerated state of two modes at Γ point of the BZ, shown in Figure 6. 12b. As discussed in the earlier chapters, deaf band-based modulation can be executed in this region to convert this double degeneracy into a triply degenerated Dirac-like point. However, in the current state, a directional bandgap (from $\omega = 0.208 \cdot (2\pi c/a)$ to $\omega = 0.231 \cdot (2\pi c/a)$) exists

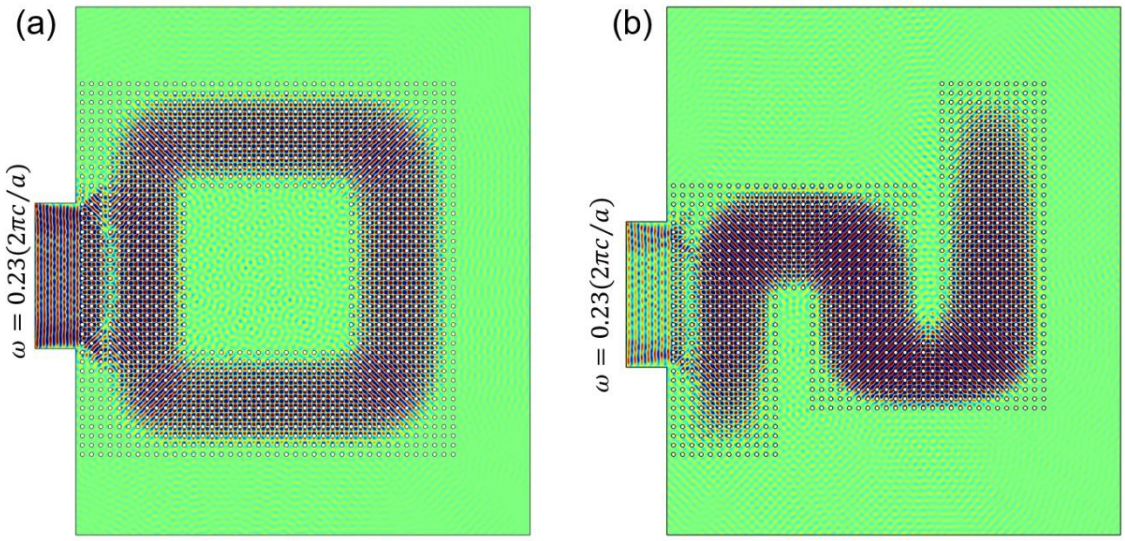

Figure 6.14: (a) Wave propagating inside S shaped PnC arrayed matrix, validating the robustness of the proposed TBH and conductor in the field of acoustics, (b) TBH through a O-shaped PnC array, (c) and (d) depicts asymmetric T-shaped cylindrical matrices preserving the topological feature but not breaking edge-state.

between the doubly degenerated point and a single mode below the bandgap. As the

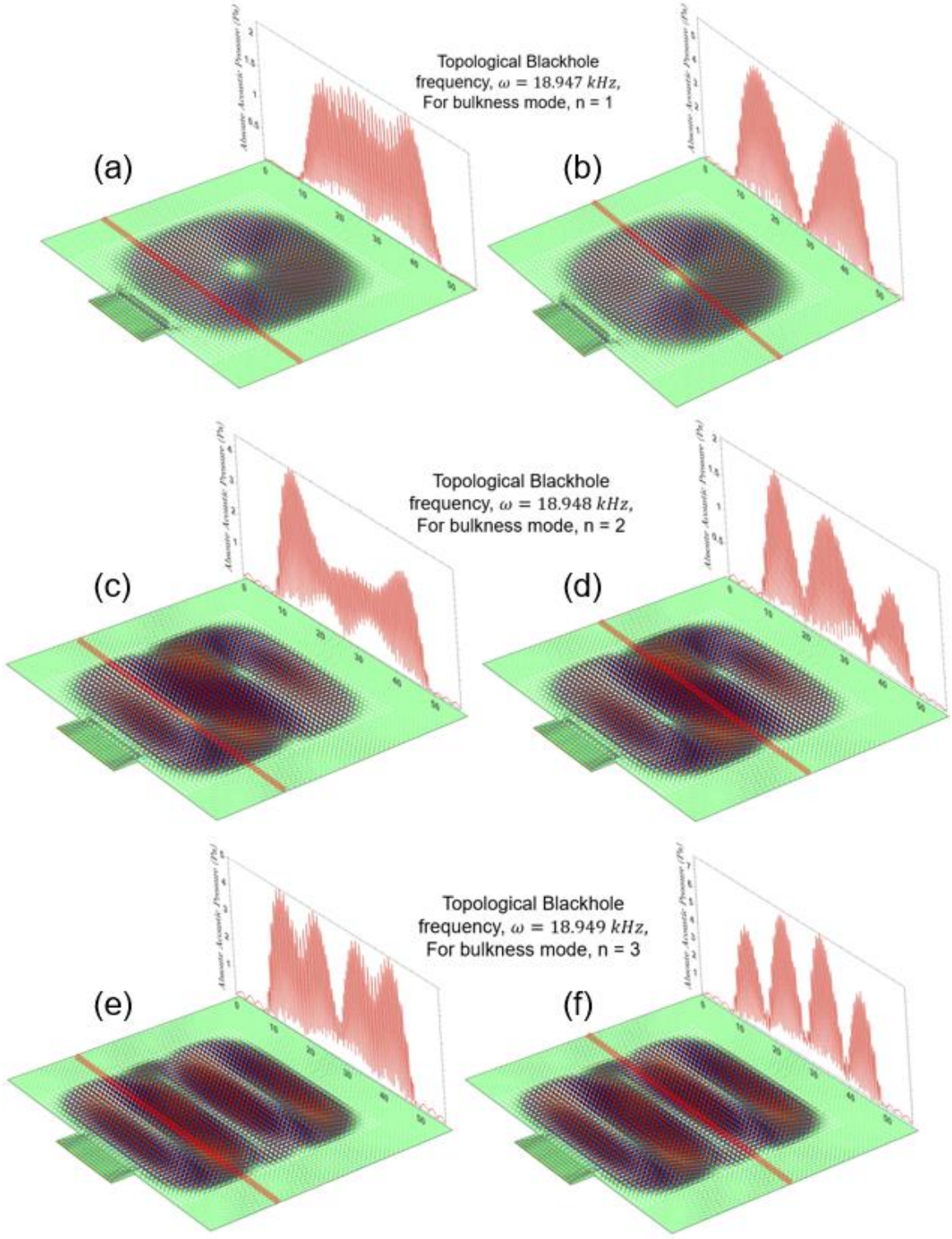

Figure 6.15: Absolute acoustic pressure distribution with pressure plots across 2D cut-lines through a side and the center of the PnC arrayed matrix, for frequency (a) and (b) $\omega = 18.947\ kHz$, (c) and (d) $\omega = 18.948\ kHz$, (e) and (f) $\omega = 18.949\ kHz$,

directional bandgap is along ΓX direction of the BZ, and the degenerated point is also at the Γ point, exciting plane wave along ΓX results the TBH inside the arrayed PnCs bulk.

For initial numerical study, an array of 41×41 PnCs have been arranged in square lattice formation. An excitor is placed at a distance of $\approx 115\, mm$ from the first unit cell of PnCs. A normal pressure excitation is generated from the excitor along the ΓX direction towards the arrayed PnC matrix. All the other boundaries have been assumed to be non-reflective by implementing plane wave radiation boundary condition, to avoid unwanted reflective wave. The PnCs are assumed to have free boundary condition. The lattice constant, taken to be $a = 25.4\, mm$, defines the Brillouin Zone, where only one PnC insertion have been placed at the center. The plane wave generated by the excitation edge at the TBH frequency propagates with minimum interactions inside an ordinary waveguide without installed PnCs (Figure 6. 13a). The wave propagates maintaining almost the similar pattern keeping the wavefronts intact after placing 41×41 PnCs with radius, r = 0.06a, where a is the lattice constant. However, changing the radii of the PnCs from r = 0.06a to r = 0.212a, the propagating energy gets trapped as a bulk inside the PnCs array, with no or negligible leakage out of the array (Figure 6. 13b). Figure 6. 8c portrays the stagnant acoustic energy contained inside the PnC array, keeping the edge state unperturbed. Almost 99% of the energy excited by the excitor is been confined inside array. Such unique phenomenon of bulk energy containment using periodic insertions in air has been termed as ‘topological blackhole (TBH)’. This arrangement allows robust propagation and acts as topologically protected system, as bulk containment is not affected by edge deformation of the array. PnC matrix size and shape has been changed afterwards to observe the

topological property of this topological conductor, and regardless of any shape and size, this topological property remain unharmed and the PnCs remain topologically protected.

Figure 6. 14 demonstrates two different cases of TBH generation, where in the first case (Figure 6. 14a), a portion of PnCs insertion from the arrayed matrix are taken off, creating a closed loop waveguide. A proper formation of bulk containment inside the PnC waveguide is observed when excited at the TBH frequency. However, offsetting the source and changing the waveguide shape does not interrupt the TBH properties, as shown in Figure 6. 14b. Hence, the robustness of this system can be stated to be stronger than a usual valley-Hall conduction. Although, it is found that, decreasing the width of the waveguide weakens the TBH propagation and containment (not shown here), TBH characteristics remain still persevered. Tuning the TBH frequency yields mode harmonics with incremental frequency change. Figure 6. 15 shows multiple mode harmonics generating

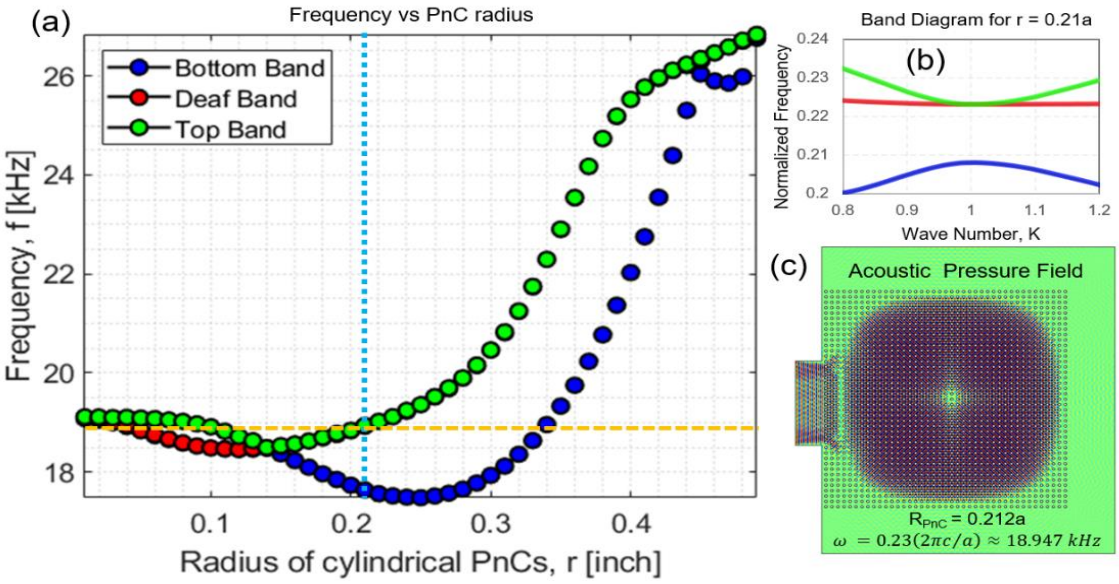

Figure 6.16: (a) The band diagram of PnC for DRB. (b) T band, Deaf band and B band frequencies for varied PnC radius has been plotted. Here, the formation of Dirac-like cone is evident for r=0.21a. (c) The expected wave dissipation through PnCs with forming an edge-state.

inside the bulk pf PnC array matrix, keeping the topology protected. As discussed above,

for the current model, the first bulkness mode is achieved at the frequency, $\omega = 18.947\ kHz$. The wave contained within the bulk forms a single mode with a single central lobe at the center. The energy is distributed around the central lobe, similar to a whirling pattern. The absolute acoustic pressure distribution plotted for cut-lines taken along a side (Figure 6. 15a) and along the center (Figure 6. 15b) depicts the bulk-stagnation of the energy excited at the TBH frequency. The pressure along the side is almost uniform across the PnC arrays, while the pressure dips down to almost zero at the center of the PnC arrays.

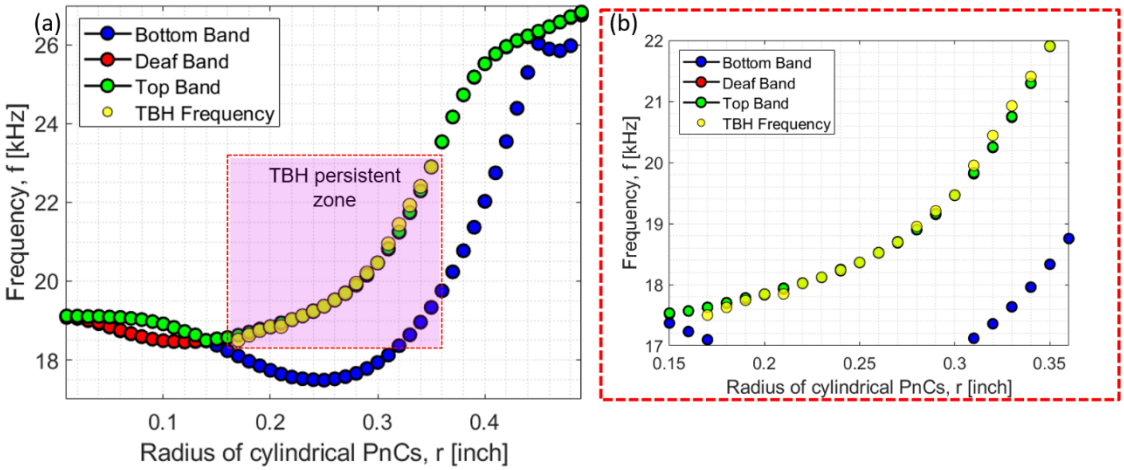

Figure 6.17: (a) The frequency at which TBH exists for different radius of PnCs. It is to be noted that, the trend of TBH formation merges and aligns with deaf band frequencies band. Hence, impact of deaf band on TBH formation is present. (b) closer look at the TBH frequency slope with respect to Deaf band frequency slope for varied r.

With increasing the frequency to $\omega = 18.948\ kHz$, second harmonic bulkiness mode is observed. The pressure plots across a side and at the center is given in Figure 6. 15c and 15d. Changing the mode harmonic yields more central lobe at the bulk. Figure 6. 15e and 15f demonstrates 3rd harmonic mode generated inside the PnC bulk. The pressure distribution across cut lines shows the formation of TBH keeping the topology preserved.

6.6 BAND MODULATIONS AND TBH GENERALIZATION

Upon adopting the blackhole formation for a fixed geometry, further band modulations-based investigation is conducted to determine the robustness of the formed

TBH. Similar to earlier chapters, the bands below and around the TBH frequency have been named as Bottom band, Deaf band and Top Band respectively. With changing the physical parameters of the PnC inclusion, radius in the case of circular PnCs (2D approximation for cylindrical PnCs), the frequency curve is plotted in Figure 6. 16a. From the Figure 6., we spot the radius ($r = 0.212a$) and the frequency ($\omega = 18.947\ kHz$) of the current obtained TBH. Now, will this behavior persist if the PnCs unit cell is altered? With this question, investigation on obtaining more robust TBH phenomena with changed PnCs parameters initiated. Altering the geometrical parameter of the PnC unit cell, the TBH phenomena is achieved with a significant wide range of actuation frequency. Keeping

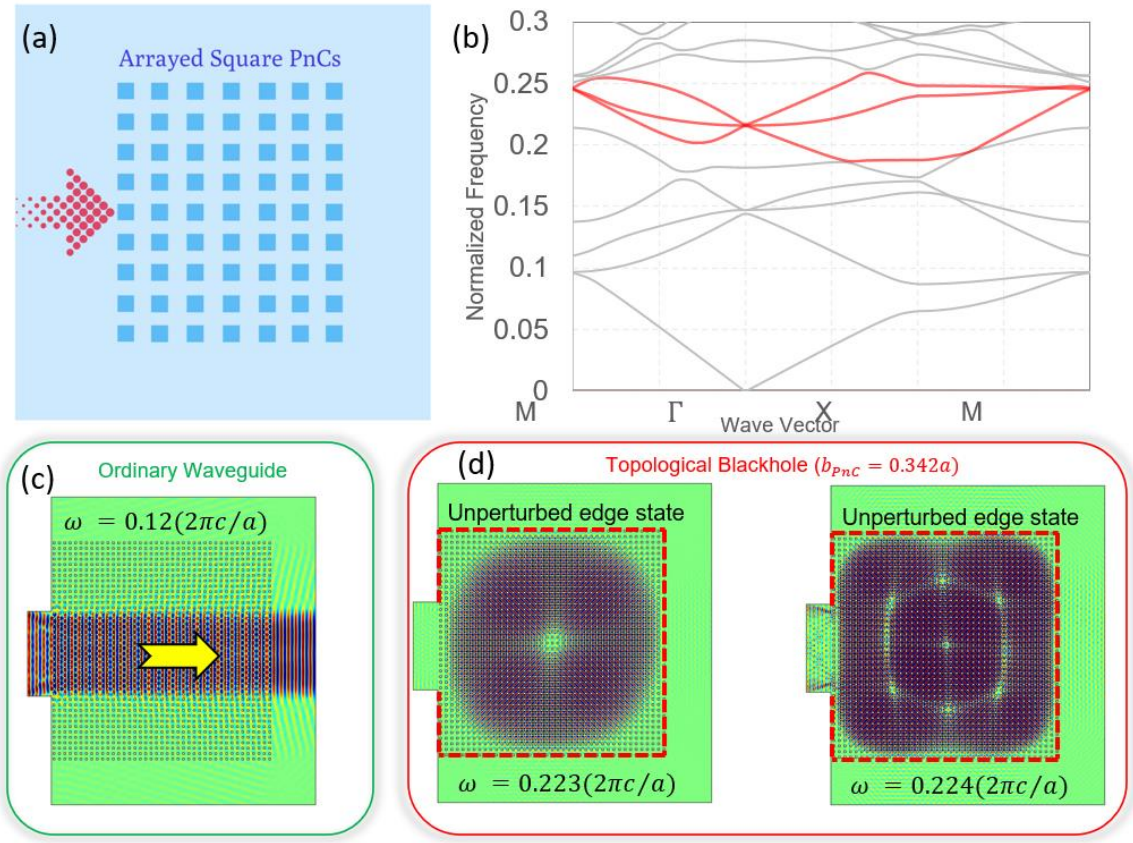

Figure 6.18: TBH and conduction for square resonator of b=0.342a. (a) is the band diagram with the frequencies of actuation for (b). It is intriguing to see the formation of single mode TBH lobe for f = 18.48 kHz (c). While for f=10kHz propagates the wave in a planar manner (d).

the radius of the PnC from 0.17a to 0.35a ensures the generation of the TBH. Hence, such TBH is consistently present for a wide range of filling fraction, regardless of any lattice size for a cylindrical PnC. The red square region in Figure 6. 17a shows the TBH persistent zone. When cropped in, TBH frequency is seen to be very close to the degenerated frequency of deaf band and the top band. The frequency – radius slope is also almost equal for both the degenerated curve and TBH frequency curve. This strengthens the proposal of not only generation of such unique topological transportation, but also acquiring higher robustness preserving the edge state.

6.7 TBH WITH SQUARE PNCS

Instead of cylindrical or circular PnCs, some other shaped PnCs are also investigated in finding the generation of TBH. Numerical formulation verifies the existence of TBH for a different unit cell, i.e., a unit cell identical to the one we discussed in Chapter 4. A square PVC rod of b=0.342a, while a = 1 inch, is the lattice constant. The square PnC are placed with no angular orientation with respect to the incident wave direction, shown in Figure 6. 18a. The region of interest of obtaining possible TBH in **K** space are plotted in red in the band structure given in Figure 6. 18b. For a normalized frequency of $\omega = 0.12(2\pi c/a)$, the plane wave propagates through the PnCs keeping planar wavefront unperturbed by the PnCs, shown in Figure 6. 18c. However, the generated plane wave at a different frequency, $\omega = 0.223(2\pi c/a)$, a frequency almost equal to the deaf band frequency, administers the black-hole pattern inside the 41 x 41 PnC matrix. Figure 6. 18d demonstrates successful generation of bulk wave containment which we call TBH. Hence, alike the previous case with cylindrical PnCs, square shaped rod PnCs also possesses such unique characteristics. The edge state is unperturbed and almost 99% of the energy excited

from the left excitor end is conserved inside the bulk PnC array. Regardless to say, Figure 6. 18d shows the first harmonic bulkiness mode. Increasing the excitation frequency reveals more mode harmonics inside the bulk, preserving the edge state. A sample higher harmonic mode is shown in Figure 6. 18e with a little increase of excitation frequency of $\omega = 0.224(2\pi c/a)$. In this case, TBH frequency is almost similar to the degenerated frequency of the deaf band and another coupled band. A thorough investigation on the formation of the TBH with different modifications of PnCs are being carried over.

Now, alike the previous chapter, tuning technique used for acoustic computing is also implemented in this case. Acquiring the maximum robustness in TBH is the goal here. Rotating the square PnC rods clockwise and counterclockwise with angle θ (with respect to the wave incident direction, ΓX), the wave behavior inside the PnC bulk is monitored. Although such tuning technique alters the dispersion modes in **K** space, surprisingly does

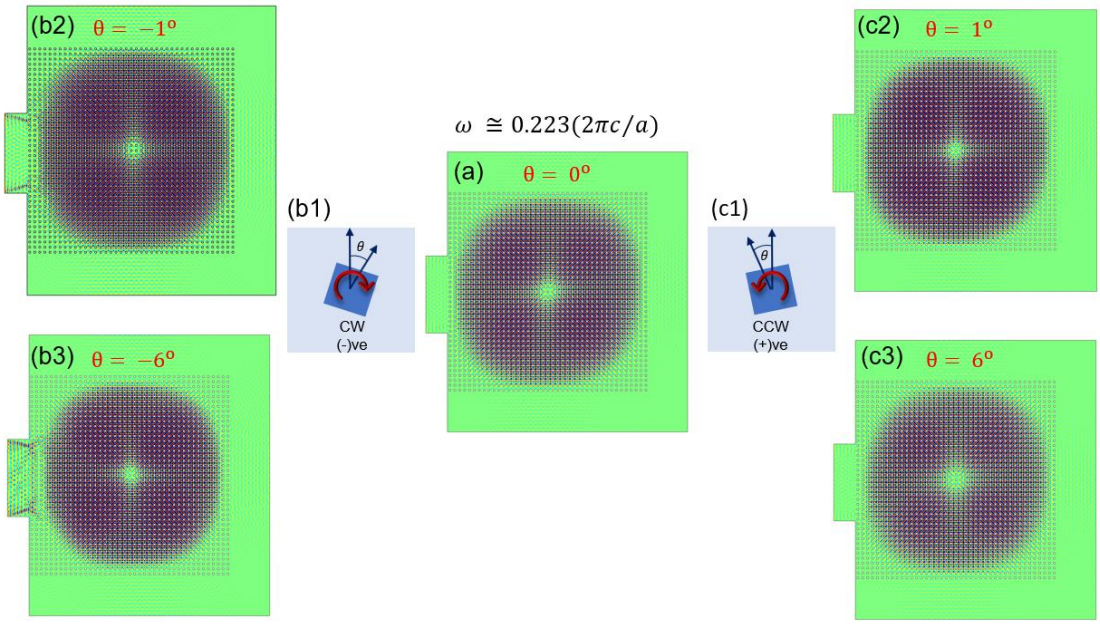

Figure 6.19: (a) Persistence of TBH development for changing the incidence angle or the PnC angles with respect to the incident plane wave from left terminal. Almost identical TBH is formed for both (a) $\theta = -1^o, 0^o \; and \; 1^o$, And (b) $\theta = -6^o, 0^o \; and \; 6^o$.

not hamper the robustness of the TBH formation. That means, the robustness of the system remains preserved, with negligible edge leakage of energy, keeping the rest within the PnC array. Figure 6. 19 shows the pressure field distribution with different PnC arrangement in terms of angular orientation. For square PnC orientation angle, $\theta = 0^o$, the first harmonic bulkiness mode is shown in Figure 6. 19a. With counterclockwise rotation of $\theta = 1^o$ and $\theta = 6^o$, the TBH remains preserved, shown in Figure 6. 19c1 and 19c2 respectively. Similarly, rotating the PnC other way i.e. clockwise with angles of $\theta = -1^o$ and $\theta = -6^o$, TBH also persists as shown in Figure 6. 19b1 and 19b2 respectively. Such behavior persists till $\theta \approx 15^o$, in either directions. The system starts losing the bulk containment characteristics when the PnCs are rotated for more than $\theta \approx 15^o$.

Figure 6. 20 shows the results of the parametric sweep for the angular orientation of PnCs for all possible angles with an increment of 1^o. In this case, the deaf band remains degenerated with bottom band when $-6^o < \theta < 6^o$. Triple degeneracy occurs for $\theta \cong 6.2^o$, after that the deaf band keeps merging with the top band, generating direction bandgap with the bottom band. However, as the TBH generation exists for the range of

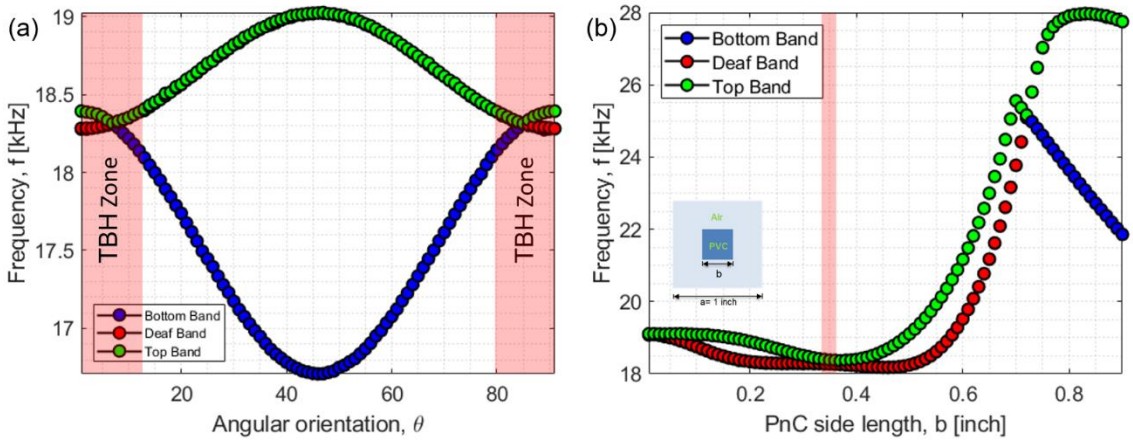

Figure 6.20: (a) The range of angles for PnCs with respect to incidence wave, from 0° to almost 14° and from 76° to 90°.

$-15^o < \theta < 15^o$, the involvement of deaf band for such phenomenon is evident. According to this Figure 6., 6.1^o and 9.7^o produces stronger blackhole effects as the earlier is the closest Dirac-like point and the later angle is the angle that we have found to be effective in chapter 4. However, the attachment of T Band and Deaf band for a certain period of time match up with TBH formation. Hence, the role of such negative radii of curvature may have an impact on the blackhole formation too.

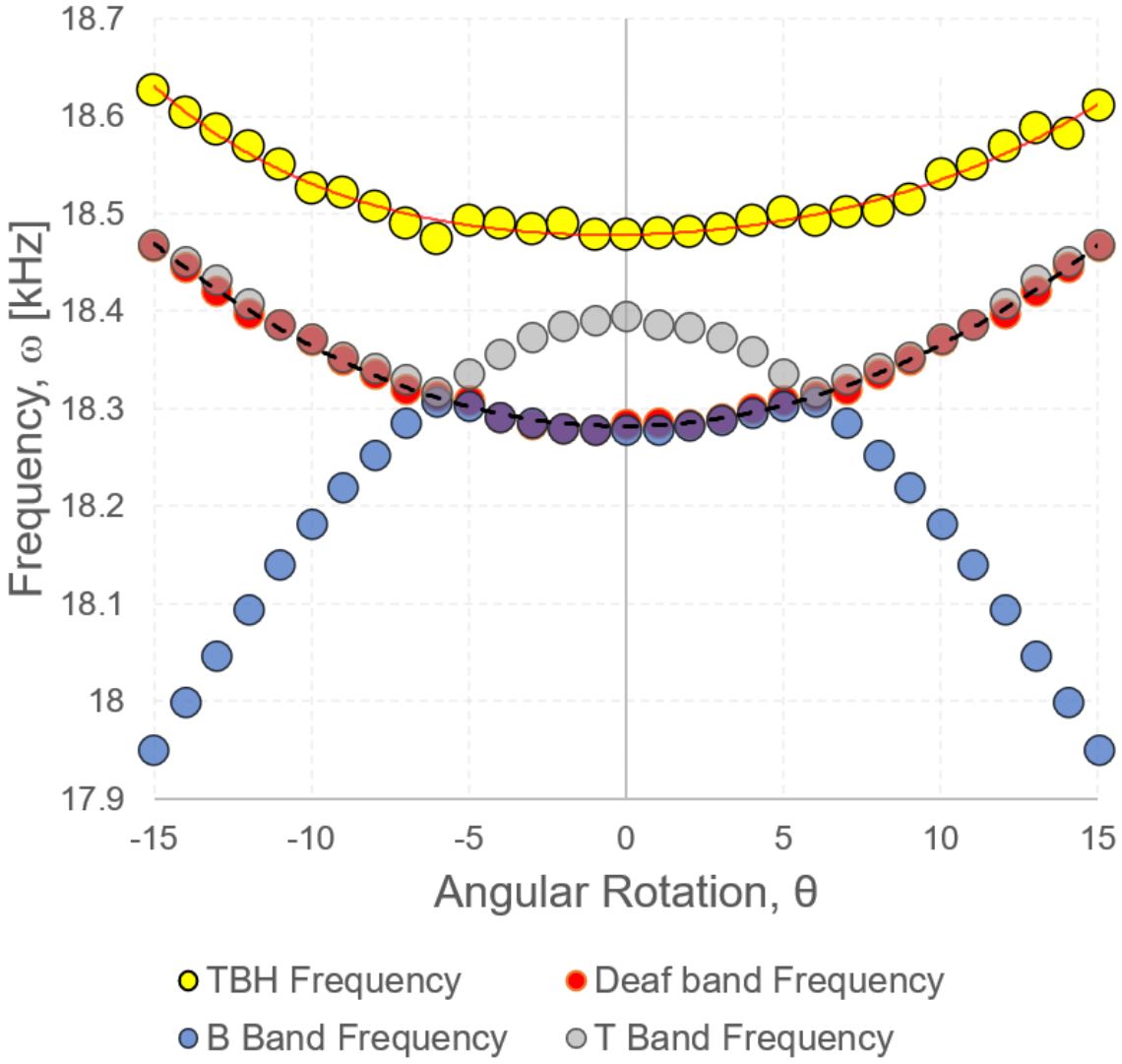

Figure 6.21: Co-ordinance of TBH frequency with the deaf band frequencies for PnC angles starting from-15^o to 15^o

Apart from PnC rotation, studies have also been conducted with changing the size of the PnCs square rods. Although changing the filling fraction by enlarging or minimizing PnC size affects the TBH phenomenon. Only a small window of filling fraction (ff), $0.13 <$

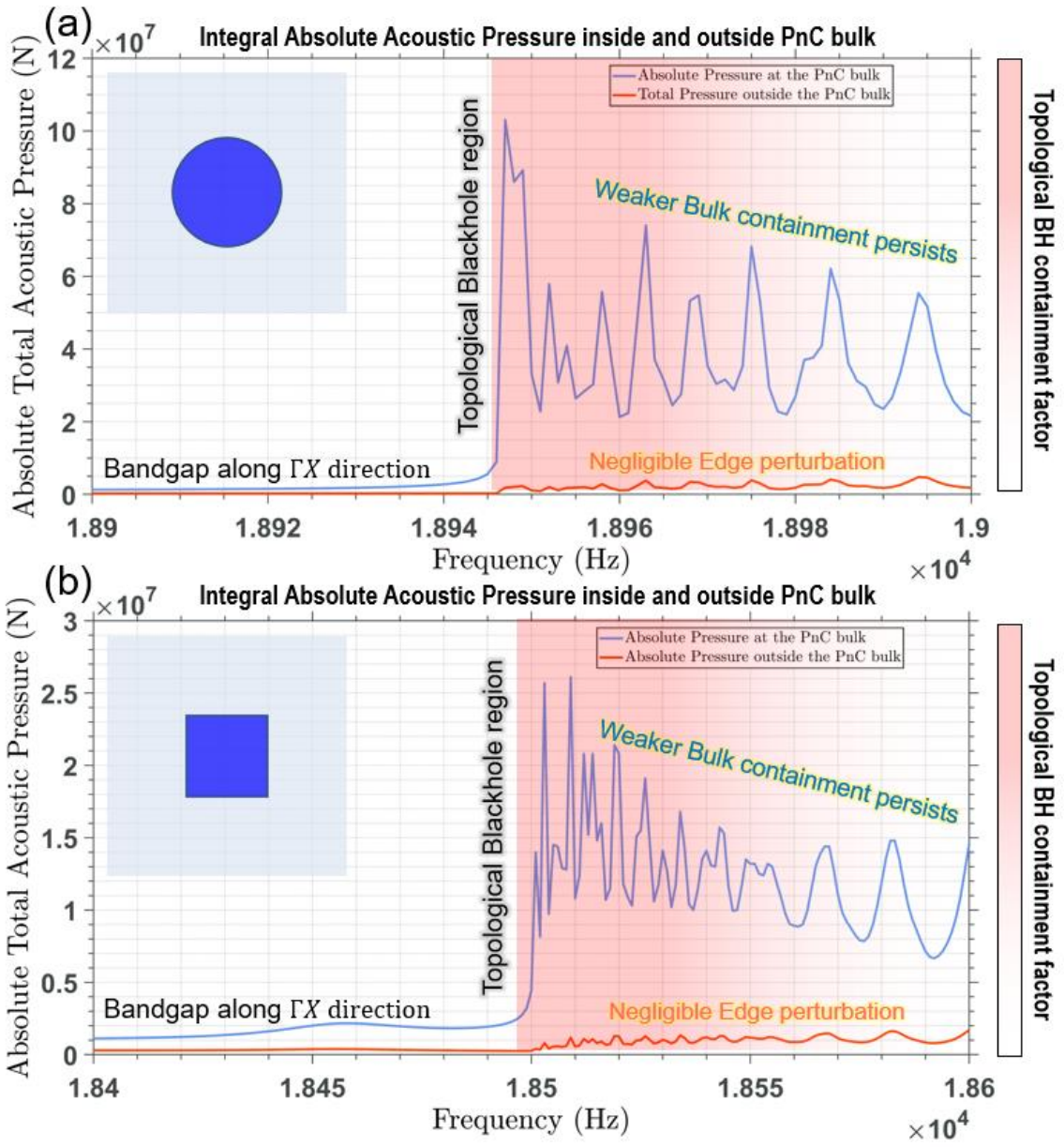

Figure 6.22: Surface integral of absolute acoustic pressure inside and outside of PnC arrayed matrix. Comparison shows the full containment of wave energy trapped inside the TBH, leaking no or negligible energy out of the system for (a) circular PnC, (b) Square PnC.

$ff < 0.109$, allows the TBH in this case. Figure 6. 20b shows three of the bands' energy with changing the PnC size. A small slit of region is where the TBH exists in this case.

Nevertheless, the deaf band frequency mode with changing PnC orientation, θ, matches the curvature of the TBH frequency mode. Figure 6. 21 shows the TBH frequencies for each of the PnC orientation, along with the dispersion relation of top band, deaf band and bottom band. This proves the generation of TBH is not accidental, rather controlled and tunable for varieties of PnCs with different orientations and filling fractions. Absolute acoustic pressure in air inside and outside of the PnC array are calculated and plotted in Figure 6. 22. The absolute pressure has been integrated over the 2D surface and plotted against a range of excitation frequency for both cylindrical and square PnCs. Figure 6. 22a shows the pressure amplitude to be minimal till the TBH frequency as direction bandgap persists in that frequency region. At the degeneracy point of deaf band and top band, the TBH originates, with maximum containment of the wave with sudden spike of

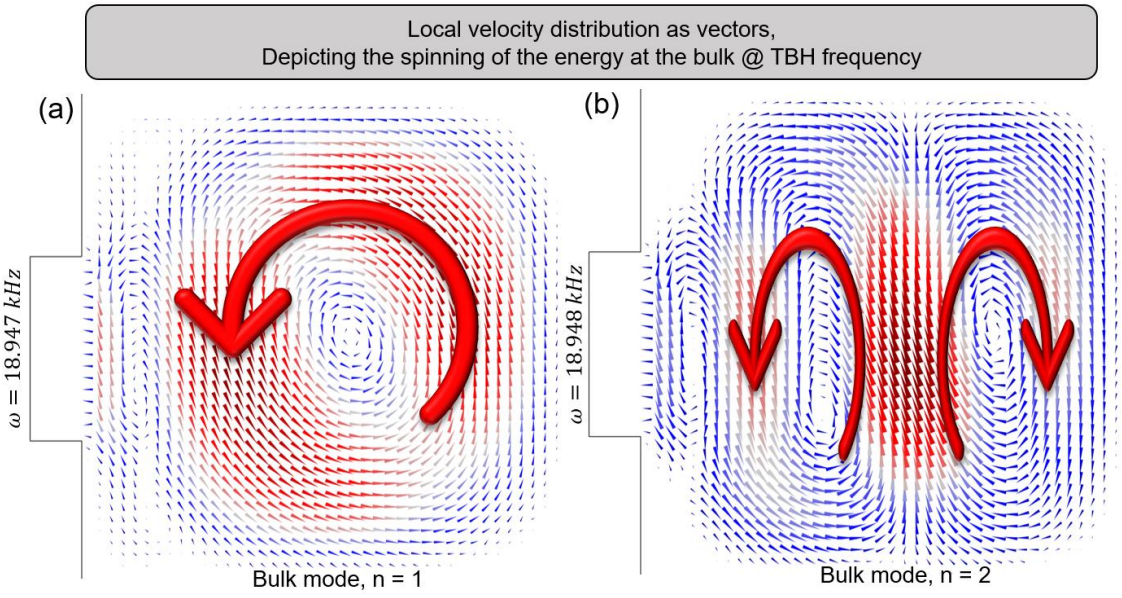

Figure 6.23: Local velocity vectors distributed spatially obtained from frequency dependent study. The spin generated vortex is evident for both the harmonic bulk modes, (a) for 1st bulk mode with frequency of 18.947 kHz, (b) for 2nd bulk mode with frequency of 18.948 kHz.

the pressure plot (plotted in blue). Total pressure plot outside the bulk PnCs (plotted in red) is negligible at and after the TBH frequency. Similar pattern is observed for the case of square PnC rods (Figure 6. 22b). However, TBH effect starts weakening with the increasing frequency, as portrayed in Figure 6. 22.

6.8 POLARIZATION ANOMALY: REASONS BEHIND TBH

Wave polarization characteristics of elastic waves are distinct. Spin is associated with circular polarization of waves and is characterized by the local rotation of the vector field. Although acoustics are spin-0 in nature, locally rotation velocity vector field **v** is found very recently, which is called as acoustic spin. However, the spatial integration of the acoustic spin density for a localized wave must be zero in agreement with its spin-0 nature. And the Spin-orbit interaction (SOI) generated by the coupling of spin and Orbital angular Momentum (OAM) are absent for longitudinal waves in acoustics. Hence, acoustic

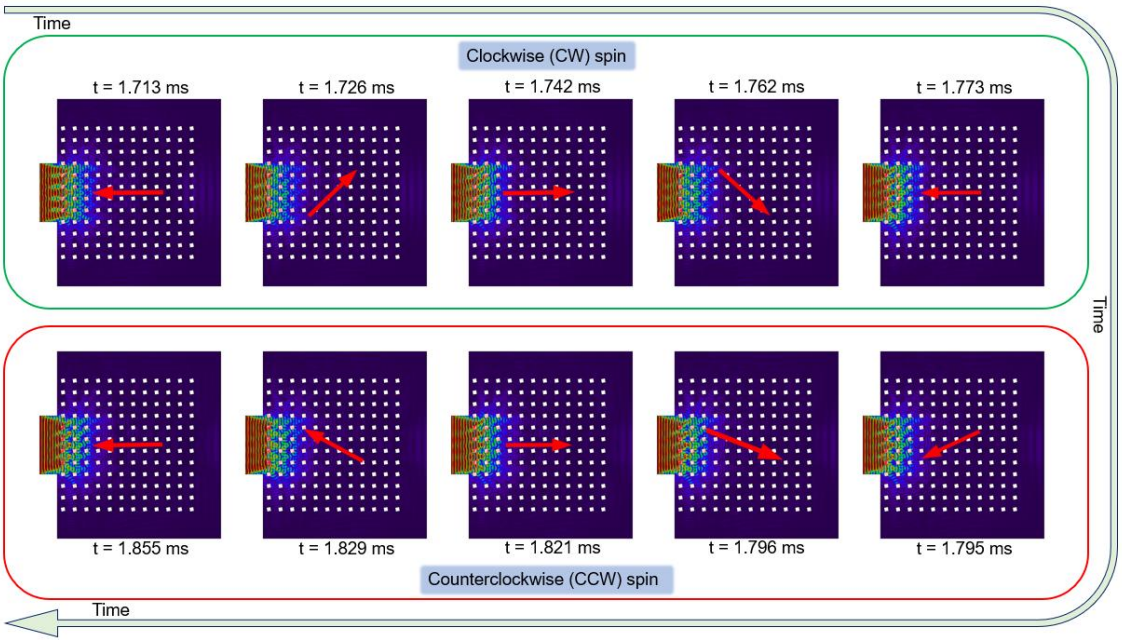

Figure 6.24: Instantaneous local acoustic velocity field with the calculated instantaneous field polarity. Starting from 1.713 msec, the polarity encounters a CW rotation of 2π at t = 1.773 msec, and then reverse the rotation in CCW by 2π at t = 1.855 msec.

energy with non-zero acoustic spin density spatially has to behave like a transverse wave

with well defined polarization. Transverse sound is spin-1 in nature and possesses elastic wave properties. It can be assumed to be the analog of chirality in electromagnetism. And the polarization anomaly occurs when the wavevector move along a certain Equi-frequency

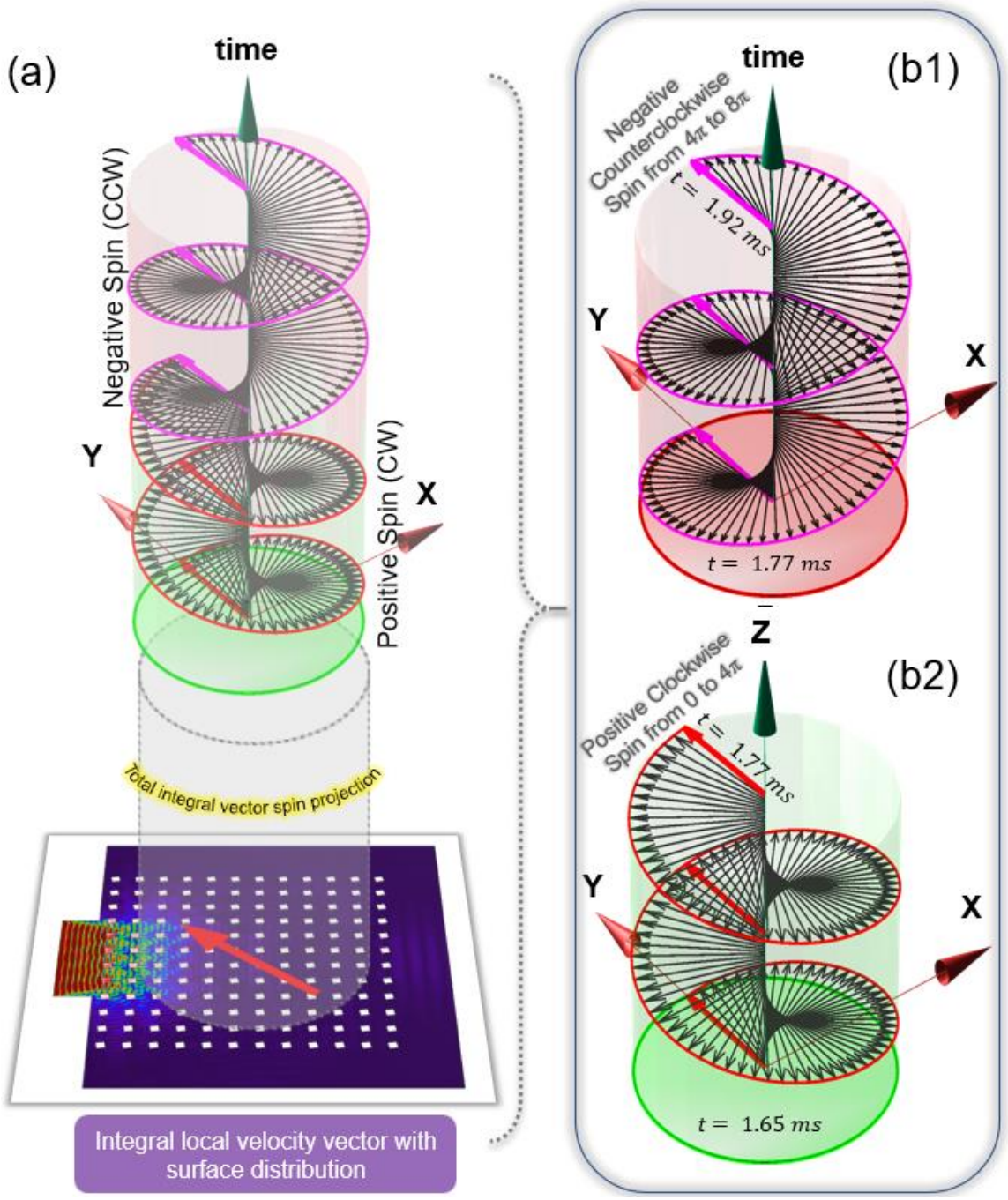

Figure 6.25: (a) TBH yielding polarity phase shit from 0 to 4π with CW spin, and 4π to 8π with CCW spin obtained from time dependent study, (b1) and (b2) illustrates positive CW spin and negative CCW spin respectively.

contour branch with a transition of modes. And due to the anomaly, spin dependent wave vortex develops causing the wave to be trapped within the artificial meta-structures.

Existence of such spin dependent vortex is evident in our case, shown in Figure 6. 23. TBH frequency induces the wave to be contained within the bulk, with local rotations/spins. With phase shifts, the energy spins clockwise and counterclockwise alternately. Upon observing the time-domain analysis results for the square PnCs, of b=0.342a with $\theta = 9.7^{o}$, an interesting generation of acoustic vortex or well is observed. After entering the PnC arrayed matrix the micro-spins initiates forming wave sinks, where the wave tends to die down like a well or a blackhole. This is the reason we have termed this phenomenon as TBH, as the absorption of energy inside the PnC arrays is evident by forming constructive and destructive blackholes. Fig 24 portrays the formation the acoustic TBH for the time, t = 2.1058 msec.

Instead of analyzing local spin, taking integration over the instantaneous surface acoustic velocity field results the instantaneous polarity. Such chiral property changes with incremental time. Time dependent study results demonstrate the polarized energy spinning clockwise (CW) and counterclockwise (CCW) within the periodic media. The direction ambiguity due to positive (CW) and negative (CCW) spin results the bulk propagation phenomenon i.e. the TBH effect. Figure 6. 25 shows the instantaneous polarity for different incremental time steps. For t = 1.713 msec, the polarity is towards the excitor. But with time, the CW spinning shifts the polarity by π radian at t = 1.742. The polarity returns to the initial state after a rotation of 2 π at t = 1.773 msec. Instead of continuing the CW spin, the polarity switches by initiating CCW rotation. With a 2 π rotation CCW, the polarity reaches to the initial state. This polarization is widely known as circular polarization.

Hence, the spin generates positive OAM, resulting shifting the geometric phase from 0 to 2π for each full CW rotation and similarly generates negative OAM to shifting the phase from 2π to 0. This unique SOI with zero resultant phase change results in containment of the wave energy within the periodic bulk media. And that is how, Topological Blackhole terminology emerged.

We have, local instantaneous velocity components, $v_x(t)$ and $v_y(t)$. The resultant local instantaneous velocity would be

$$\mathbf{v}\,(x, y, t) \;=\; \sqrt{v_x^2 + v_y^2}$$

with an orientation of an angle, $\theta_l(t) = \; tan^{-1}\left(\frac{v_y}{v_x}\right)$.

Integrating the local velocity over the entire bulk surface of air inside the arrayed PnCs results an integrated velocity vector with a certain polarity. With a transient study, the polarity is observed to be changing with time. Then the surface integral to achieve the integrated net velocity would be,

$$\mathbf{V_g}(t) = \iint_S \mathbf{v}(x, y, t)dxdy,$$

with a global component of V_x and V_y. Here, S indicates the surface integral over the entire domain of simulation. The global polarity for that instant would be,

$$\theta_g(t) = \; tan^{-1}\left(\frac{V_y}{V_x}\right)$$

Which determines the polarity direction for that instant time step, t. For each time step, the global velocity vector, $\mathbf{V_g}(t)$ and the orientation polarity, $\theta_g(t)$ changes. It was found that the $\theta_g(t)$ is continually changing from $-\pi$ and $+\pi$ and then again from $+\pi$ and $-\pi$, continually oscillating as shown in Figure 6. 25 With this we conclude that the energy is

trapped inside the Bulk. Reason for this spin mediation is explained below using the modal polarity of the deaf band and the top band.

Figure 6. 26 shows this entire SOI graphically. A time axis placing on top of the TBH system with velocity polarity helps understanding the polarization phase change over time. The circular polarization is projected to an extent for better understanding the polarity shift over the time in CW direction with a total phase shift of 4π. The initial time is 1.65 msec, and after the phase change by 4π, the time changes to 1.77 msec. Phase start shifting

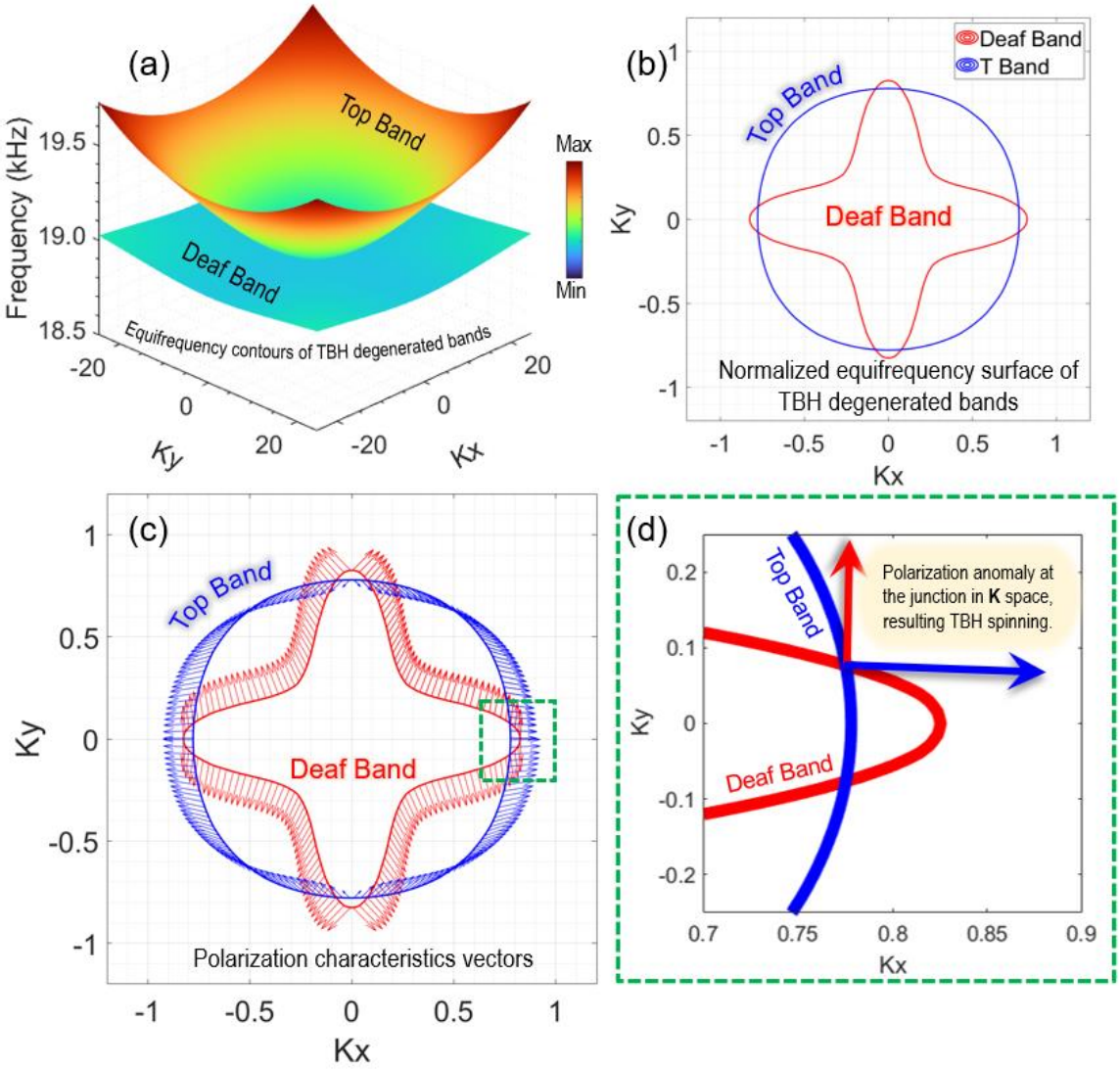

Figure 6.26: (a) Equifrequency contour of Deaf band and Top band for cylindrical PnCs, (b) Normalized equifrequency surface for deaf and top band, (c) polarization characteristics vectors in wavenumber space, (d) polarization anomaly at the intercepted junction of two EFS modes, indicating the origin of the TBH bulkness mode.

backwards by rotating CCW from t = 1.77 msec with a total phase change of 4π again, reaching at t = 1.92 msec. The resultant polarity shifting path takes 2 spiral shapes rotating CW and CCW connected to each other at the phase of 4π. That is how, the wave energy forms a localized energy sink/well, keeping the edge preserved.

As discussed earlier, the TBH frequency is very close to the degenerated frequency of deaf band and the top band, for the case of cylindrical PnCs. As degenerated at Γ point of the BZ, the equifrequency contour (EFC) of both the bands are shown in Figure 6. 27a. The normalized equifrequency surface (EFS) for TBH frequency is plotted in Figure 6. 27b. The red EFS belongs to the deaf band and the blue EFS belongs to the top band from

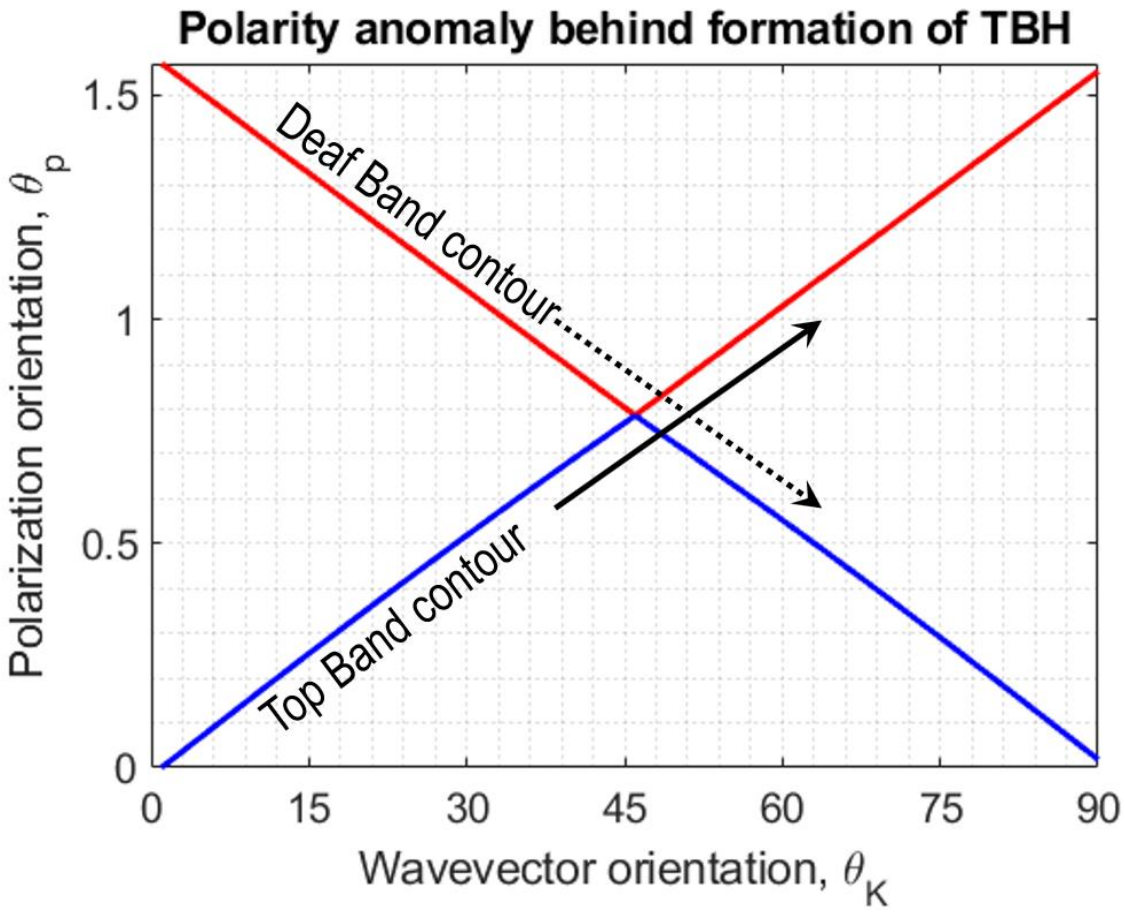

Figure 6.27: Anomalous polarity from the polarization orientation plot with respect to the wavenumber orientation plot.

the band structure. As both the surface are intercepted at multiple points, the intercepted points depicts the equal wavenumber for that energy in **K** space. Hence, the polarity for that specific intercepted point has to align for a trivial case. The polarization characteristics of the PnCs are evaluated by θ_P, which denotes the angle of the polarization orientation. The polarization vectors are illustrated with arrows at the wavevectors with an interval of $\theta_K = 1^o$ is plotted in the EFS in Figure 6. 27c. The local polarity for each particular orientation can be similar or different. But, two different polarities for a specific wavenumber is not practically possible. This is where the polarity anomaly occurs. Figure 6. 27d portrays the polarity ambiguity for deaf band and top band, having orthogonal polarities at the junction of interception. This is where the wave gets trapped and starts spinning ambiguously and develop TBH. Figure 6. 28 illustrates the polarization orientation, θ_P to be merging for both bands for $\theta_K = 45^o$. Such merging of θ_P with θ_K validates the anomalous polarization. Thus, the generation of this unique TBH is materialized and can be utilized widely in the field of acoustics.

6.9 CHAPTER SUMMARY

In this chapter, a new patterned wave manipulation can be utilized in wide spectrum of fields of acoustics and elastic waves. By altering geometry and other material properties of the inclusion materials, the topological frequency can be shifted to any frequency depending on the applications. A unique acoustic phenomenon, termed as topological blackhole, is proposed. The ability of gathering all generated pressure wave energy inside periodic materials makes TBH unique. The containment of energy in the bulk of the PnCs without any leakage through the edge state makes it a counter phenomenon of topological insulators. That is how, the term topological blackhole emerged, as it works as an energy

well or an energy sink. Regardless of deformation on the PnC arrays, the topology is preserved, keeping the bulk contained. Such methodology working for acoustics is the first to be observed here. No phenomenon similar to this physics has been reported in the literature before.

This TBH is a dispersion band dependent phenomenon, where the band related here, known as deaf band, regulates the TBH behavior. Tailoring the PnC unit cell and resonator size and shape does not tend to affect the generation of the bulk harmonic modes of energy. Both frequency dependent and time dependent numerical studies have been performed. Spin dependent topology is found from the time dependent results where the anomalous polarity resulting the TBH phenomenon has been observed. Due to having local spin inside the PnC arrays, the polarity phase shifts from 0 to 2π and returns to 0 again with counter rotation. This alternate phase shift causes the energy to be stagnant in the core of the PnCs, keeping the edge states undisturbed, and practically acquiring an outstandingly new phenomena in the field of acoustics.

CHAPTER 7

CONCLUSION

In present state-of-the-art technologies, acoustic sensors and logic gates are widely employed in industrial applications for selecting user defined frequencies. We have demonstrated the utilization of Dirac-cone like behaviors in acoustics in multiple intriguing applications including acoustic logic gates or diodes, and topologically protected sensors. Here, we have analytically solved the dispersion behavior of PVC PnCs in air media, having multiple probable triple degeneracy at the Dirac-like point at $\vec{k} = 0$. We pivoted our study on two 'deaf bands' that are identified as probable governor of the Dirac–like cones. There we selected two frequency regions, to study further if the accidental degeneracies occur by modulating the physical parameter of the resonators.

A predictive optimization process discussed in this article leads us to find the region of the Dirac-like cone based on the zero-group velocity flat bands, or the 'Deaf bands'. With this unique phenomenon depending on the deaf band, we fabricated two numerical experiments to determine the behaviors of the Dirac-like points, to test if the regions identified are actually the Dirac-like points. After test, we demonstrated that the orthogonal wave guidance at the Dirac points are evident in Region A and Region B. However, only the Region A Dirac point behaviors are discussed with several other phenomena like, orthogonal wave transport, channeling plane waves along the offset axes, acoustic No Zone, acoustic clocking, acoustic vortex or self-looping leaving imaginary acoustic sources at offset locations. Mode identification, relation between the mode shapes and their role in

the above-mentioned unique wave propagation behavior are logically analyzed and discussed in this article. This this study, it will help us in the future to further find the intriguing wave guiding properties of Dirac cone in acoustic metamaterials.

Exploiting the Dirac-like cone characteristics on periodic meta-materials, a setup of acoustic computing has been generated. Acoustic diode gates can be formulated using the proposed technique. Analytical formulations on determining the Fourier coefficients for periodic PnCs are given here. AND, OR, NAND and NOR operation are performed by this acoustic computing setup. A six-degree of freedom complex acoustic diode has also been proposed with the Boolean principle. Greater design flexibility can be implemented by exploiting this technique in waveguide computation in acoustics.

And finally, the proposal of a spin-based topological phenomenon, named as topological blackhole is discussed in detail. The mechanics of the bulk wave containment in acoustic microarchitecture metamaterials has been explained. It possesses a unique bulk-boundary distinction, alike topological insulators. An acoustic energy sink originates within the periodic microarchitectures, PnCs in this case, by exploiting deaf band degeneracy with SOC. SOC allow the acoustic energy to be coupled with the spin momentum, resulting energy sink or a blackhole, where no energy diverge from the PnCs arrays. Playing with the geometric phase, energy containment can be made robust by changing unit cell geometric parameters. Regardless of changing the geometric parameters, the TBH persist for wide range of discrepancies. Such blackhole can serve the field of acoustics in a immense way.

REFERENCES

[1] X. Zhang and Z. Liu, "Extremal Transmission and Beating Effect of Acoustic Waves in Two-Dimensional Sonic Crystals," *Physical Review Letters,* vol. 101, no. 26, p. 264303, 12/30/ 2008. [Online]. Available: https://link.aps.org/doi/10.1103/PhysRevLett.101.264303.

[2] F. Liu, Y. Lai, X. Huang, and C. T. Chan, "Dirac cones at $\stackrel{P\vec}{k}=0$ in phononic crystals," *Physical Review B,* vol. 84, no. 22, p. 224113, 12/22/ 2011. [Online]. Available: https://link.aps.org/doi/10.1103/PhysRevB.84.224113.

[3] F. Liu, X. Huang, and C. T. Chan, "Dirac cones at k→=0 in acoustic crystals and zero refractive index acoustic materials," *Applied Physics Letters,* vol. 100, no. 7, p. 071911, 2012, doi: 10.1063/1.3686907.

[4] J. Mei, Y. Wu, C. T. Chan, and Z.-Q. Zhang, "First-principles study of Dirac and Dirac-like cones in phononic and photonic crystals," *Physical Review B,* vol. 86, no. 3, 2012, doi: 10.1103/PhysRevB.86.035141.

[5] J. Lu, C. Qiu, S. Xu, Y. Ye, M. Ke, and Z. Liu, "Dirac cones in two-dimensional artificial crystals for classical waves," *Physical Review B,* vol. 89, no. 13, p. 134302, 04/04/ 2014. [Online]. Available: https://link.aps.org/doi/10.1103/PhysRevB.89.134302.

[6] X. Huang, Y. Lai, Z. H. Hang, H. Zheng, and C. T. Chan, "Dirac cones induced by accidental degeneracy in photonic crystals and zero-refractive-index materials," *Nat Mater,* vol. 10, no. 8, pp. 582-6, May 29 2011, doi: 10.1038/nmat3030.

[7] X. Zhang, "Observing Zitterbewegung for Photons near the Dirac Point of a Two-Dimensional Photonic Crystal," *Physical Review Letters,* vol. 100, no. 11, p. 113903, 03/21/ 2008. [Online]. Available: https://link.aps.org/doi/10.1103/PhysRevLett.100.113903.

[8] V. P. Gusynin and S. G. Sharapov, "Unconventional Integer Quantum Hall Effect in Graphene," *Physical Review Letters,* vol. 95, no. 14, p. 146801, 09/28/ 2005. [Online]. Available: https://link.aps.org/doi/10.1103/PhysRevLett.95.146801.

[9] D. Torrent and J. Sanchez-Dehesa, "Acoustic analogue of graphene: observation of Dirac cones in acoustic surface waves," *Phys Rev Lett,* vol. 108, no. 17, p. 174301, Apr 27 2012, doi: 10.1103/PhysRevLett.108.174301.

[10] T. Ochiai and M. Onoda, "Photonic analog of graphene model and its extension: Dirac cone, symmetry, and edge states," *Physical Review B,* vol. 80, no. 15, p. 155103, 10/02/ 2009. [Online]. Available: https://link.aps.org/doi/10.1103/PhysRevB.80.155103.

[11] D. Malko, C. Neiss, F. Viñes, and A. Görling, "Competition for Graphene: Graphynes with Direction-Dependent Dirac Cones," *Physical Review Letters,* vol. 108, no. 8, p. 086804, 02/24/ 2012. [Online]. Available: https://link.aps.org/doi/10.1103/PhysRevLett.108.086804.

[12] Y. Zhang, Y.-W. Tan, H. L. Stormer, and P. Kim, "Experimental observation of the quantum Hall effect and Berry's phase in graphene," *Nature,* vol. 438, p. 201, 11/10/online 2005, doi: 10.1038/nature04235

https://www.nature.com/articles/nature04235#supplementary-information.

[13] R. W. Ziolkowski, "Propagation in and scattering from a matched metamaterial having a zero index of refraction," *Physical Review E,* vol. 70, no. 4, p. 046608, 10/21/ 2004. [Online]. Available: https://link.aps.org/doi/10.1103/PhysRevE.70.046608.

[14] Z. Liang and J. Li, "Extreme Acoustic Metamaterial by Coiling Up Space," *Physical Review Letters,* vol. 108, no. 11, p. 114301, 03/16/ 2012. [Online]. Available: https://link.aps.org/doi/10.1103/PhysRevLett.108.114301.

[15] Y. Cheng, C. Zhou, B. G. Yuan, D. J. Wu, Q. Wei, and X. J. Liu, "Ultra-sparse metasurface for high reflection of low-frequency sound based on artificial Mie resonances," *Nature Materials,* Article vol. 14, p. 1013, 08/31/online 2015, doi: 10.1038/nmat4393

https://www.nature.com/articles/nmat4393#supplementary-information.

[16] B.-I. Popa, L. Zigoneanu, and S. A. Cummer, "Experimental Acoustic Ground Cloak in Air," *Physical Review Letters,* vol. 106, no. 25, p. 253901, 06/22/ 2011. [Online]. Available: https://link.aps.org/doi/10.1103/PhysRevLett.106.253901.

[17] X. Zhu, B. Liang, W. Kan, X. Zou, and J. Cheng, "Acoustic Cloaking by a Superlens with Single-Negative Materials," *Physical Review Letters,* vol. 106, no. 1, p. 014301, 01/04/ 2011. [Online]. Available: https://link.aps.org/doi/10.1103/PhysRevLett.106.014301.

[18] S. Zhang, L. Yin, and N. Fang, "Focusing Ultrasound with an Acoustic Metamaterial Network," *Physical Review Letters,* vol. 102, no. 19, p. 194301, 05/15/ 2009. [Online]. Available: https://link.aps.org/doi/10.1103/PhysRevLett.102.194301.

[19] A. Sukhovich *et al.*, "Experimental and Theoretical Evidence for Subwavelength Imaging in Phononic Crystals," *Physical Review Letters,* vol. 102, no. 15, p. 154301, 04/17/ 2009. [Online]. Available: https://link.aps.org/doi/10.1103/PhysRevLett.102.154301.

[20] J. Zhu *et al.*, "A holey-structured metamaterial for acoustic deep-subwavelength imaging," *Nature Physics,* vol. 7, p. 52, 11/07/online 2010, doi: 10.1038/nphys1804

https://www.nature.com/articles/nphys1804#supplementary-information.

[21] M. S. Kushwaha, P. Halevi, L. Dobrzynski, and B. Djafari-Rouhani, "Acoustic band structure of periodic elastic composites," *Physical Review Letters,* vol. 71, no. 13, pp. 2022-2025, 09/27/ 1993. [Online]. Available: https://link.aps.org/doi/10.1103/PhysRevLett.71.2022.

[22] Z. Liu *et al.*, "Locally Resonant Sonic Materials," *Science,* vol. 289, no. 5485, pp. 1734-1736, 2000, doi: 10.1126/science.289.5485.1734.

[23] W. Fugen, L. Zhengyou, and L. Youyan, "Acoustic band gaps in 2D liquid phononic crystals of rectangular structure," *Journal of Physics D: Applied Physics,* vol. 35, no. 2, p. 162, 2002. [Online]. Available: http://stacks.iop.org/0022-3727/35/i=2/a=309.

[24] Y. Yao, F. Wu, X. Zhang, and Z. Hou, "Thermal tuning of Lamb wave band structure in a two-dimensional phononic crystal plate," *Journal of Applied Physics,* vol. 110, no. 12, p. 123503, 2011, doi: 10.1063/1.3669391.

[25] Y. Li, Y. Wu, and J. Mei, "Double Dirac cones in phononic crystals," *Applied Physics Letters*, vol. 105, no. 1, p. 014107, 2014, doi: 10.1063/1.4890304.
[26] H. Ahmed, R. Ahmed, M. M. Indaleeb, and S. Banerjee, "Multifunction acoustic modulation by a multi-mode acoustic metamaterial architecture," *Journal of Physics Communications*, vol. 2, no. 11, p. 115001, 2018.
[27] "The quantum theory of the electron," *Proceedings of the Royal Society of London. Series A*, vol. 117, no. 778, pp. 610-624, 1928, doi: 10.1098/rspa.1928.0023.
[28] M. C. Rechtsman *et al.*, "Photonic Floquet topological insulators," *Nature*, vol. 496, p. 196, 04/10/online 2013, doi: 10.1038/nature12066

https://www.nature.com/articles/nature12066#supplementary-information.
[29] A. Khelif and A. Adibi, *Phononic Crystals*. Springer, 2015.
[30] Z.-G. Chen and Y. Wu, "Tunable Topological Phononic Crystals," *Physical Review Applied*, vol. 5, no. 5, 2016, doi: 10.1103/PhysRevApplied.5.054021.
[31] A. Shelke, Banerjee, S., Habib, A., Rahani, E. K., Ahmed, R., Kundu, T., , "Wave Guiding and Wave Modulation using Phononic Crystal Defects," *Journal of Intelligent Materials Systems and Structures*, vol. 25, no. 13, pp. 1541-1552, 2013, doi: 10.1177/1045389X13507344.
[32] I. Psarobas, A. Modinos, R. Sainidou, and N. Stefanou, "Acoustic properties of colloidal crystals," *Physical Review B*, vol. 65, no. 6, p. 064307, 2002.
[33] J. Li and C. T. Chan, "Double-negative acoustic metamaterial," *Physical Review E*, vol. 70, no. 5, p. 055602, 2004.
[34] W. Robertson, G. Arjavalingam, R. Meade, K. Brommer, A. M. Rappe, and J. Joannopoulos, "Measurement of photonic band structure in a two-dimensional periodic dielectric array," *Physical review letters*, vol. 68, no. 13, p. 2023, 1992.
[35] A. I. Islam, "Monitoring Wear in Sliding Surfaces by Using Acoustic Emission Signals," North Carolina Agricultural and Technical State University, 2013.
[36] A. Hossain, A. Riaz, I. Mustahseen Mobashwer, and B. Sourav, "Multifunction acoustic modulation by a multi-mode acoustic metamaterial architecture," *Journal of Physics Communications*, vol. 2, no. 11, p. 115001, 2018. [Online]. Available: http://stacks.iop.org/2399-6528/2/i=11/a=115001.
[37] M. Indaleeb, H. Ahmed, and S. Banerjee, "Investigation on multi-occurrence of Dirac cone and exceptional ring (Conference Presentation)," in *SPIE Smart Structures and Materials + Nondestructive Evaluation and Health Monitoring*, 2018, vol. 10600: SPIE.
[38] Y. Li, Y. Wu, X. Chen, and J. Mei, "Selection rule for Dirac-like points in two-dimensional dielectric photonic crystals," *Opt. Express*, vol. 21, no. 6, pp. 7699-7711, 2013/03/25 2013, doi: 10.1364/OE.21.007699.
[39] M. M. Indaleeb, S. Banerjee, H. Ahmed, M. Saadatzi, and R. Ahmed, "Deaf band based engineered Dirac cone in a periodic acoustic metamaterial: A numerical and experimental study," *Physical Review B*, vol. 99, no. 2, p. 024311, 01/31/ 2019, doi: 10.1103/PhysRevB.99.024311.
[40] F. Liu, Y. Lai, X. Huang, and C. Chan, "Dirac cones at $\vec{k}=0$ in phononic crystals," *Physical Review B*, vol. 84, no. 22, p. 224113, 2011.
[41] C. M. Anderson and K. P. J. P. r. l. Giapis, "Larger two-dimensional photonic band gaps," vol. 77, no. 14, p. 2949, 1996.

[42] D. Caballero *et al.*, "Large two-dimensional sonic band gaps," vol. 60, no. 6, p. R6316, 1999.
[43] N. J. J. o. a. p. Susa, "Large absolute and polarization-independent photonic band gaps for various lattice structures and rod shapes," vol. 91, no. 6, pp. 3501-3510, 2002.
[44] F. Wu, Z. Liu, and Y. J. P. R. E. Liu, "Splitting and tuning characteristics of the point defect modes in two-dimensional phononic crystals," vol. 69, no. 6, p. 066609, 2004.
[45] C. Goffaux and J. J. P. R. B. Vigneron, "Theoretical study of a tunable phononic band gap system," vol. 64, no. 7, p. 075118, 2001.
[46] X. Li, F. Wu, H. Hu, S. Zhong, and Y. J. J. o. P. D. A. P. Liu, "Large acoustic band gaps created by rotating square rods in two-dimensional periodic composites," vol. 36, no. 1, p. L15, 2002.
[47] L. Zhong, F. Wu, X. Zhang, H. Zhong, and S. J. P. L. A. Zhong, "Effects of orientation and symmetry of rods on the complete acoustic band gap in two-dimensional periodic solid/gas systems," vol. 339, no. 1-2, pp. 164-170, 2005.
[48] A. Song, X. Wang, T. Chen, and L. J. I. J. o. M. P. B. Wan, "Band structures in a two-dimensional phononic crystal with rotational multiple scatterers," vol. 31, no. 6, p. 1750038, 2017.
[49] J. Hyun, W. Choi, S. Wang, C.-s. Park, and M. J. S. r. Kim, "Systematic realization of double-zero-index phononic crystals with hard inclusions," vol. 8, no. 1, p. 7288, 2018.
[50] M. M. Indaleeb, H. Ahmed, M. Saadatzi, and S. Banerjee, "Deaf band-based prediction of Dirac cone in acoustic metamaterials," *Journal of Applied Physics*, vol. 127, no. 6, p. 064903, 2020, doi: 10.1063/1.5122297.
[51] M. Indaleeb, Banerjee, S., Ahmed, H., Saadatzi, M., Ahmed, R., "Deaf band based engineered Dirac cone in a periodic acoustic metamaterial: A numerical and experimental study," *Phys. Rev. B*, vol. 99, no. 2, p. 024311, 2019, doi: https://doi.org/10.1103/PhysRevB.99.024311.
[52] S. Raghu and F. D. M. J. P. R. A. Haldane, "Analogs of quantum-Hall-effect edge states in photonic crystals," vol. 78, no. 3, p. 033834, 2008.
[53] F. G. Zhaoju Yang, Xihang Shi, Xiao Lin, Zhen Gao, Yidong Chong, and Baile Zhang, "Topological Acoustics," *Phys. Rev. Lett.*, vol. 114, no. 11, p. 114301, 2015.
[54] X. N. Cheng He, Hao Ge, Xiao-Chen Sun, Yan-Bin Chen, Ming-Hui Lu, Xiao-Ping Liu, Yan-Feng Chen "Acoustic topological insulator and robust one-way sound transport," *Nature Physics*, vol. 12, pp. 1124-1129, 2016.
[55] X. Zhang *et al.*, "Enlarging a photonic band gap by using insertion," vol. 61, no. 3, p. 1892, 2000.
[56] M. Yang, X.-J. Ran, Y. Cui, and R.-Q. Wang, "Quantum Hall-like effect in gated four-terminal graphene devices without magnetic field," vol. 99, no. 22, p. 222101, 2011, doi: 10.1063/1.3663625.
[57] L.-H. Wu and X. Hu, "Scheme for Achieving a Topological Photonic Crystal by Using Dielectric Material," *Physical Review Letters*, vol. 114, no. 22, p. 223901, 06/03/ 2015, doi: 10.1103/PhysRevLett.114.223901.
[58] H.-W. Dong *et al.*, "Customizing acoustic dirac cones and topological insulators in square lattices by topology optimization," vol. 493, p. 115687, 2021.

[59] F.-L. Hsiao, A. Khelif, H. Moubchir, A. Choujaa, C.-C. Chen, and V. Laude, "Complete band gaps and deaf bands of triangular and honeycomb water-steel phononic crystals," *Journal of applied physics,* vol. 101, no. 4, p. 044903, 2007.
[60] M. Kafesaki, R. Penciu, and E. Economou, "Air bubbles in water: a strongly multiple scattering medium for acoustic waves," *Physical review letters,* vol. 84, no. 26, p. 6050, 2000.
[61] Z. Liu, C. T. Chan, P. Sheng, A. L. Goertzen, and J. H. Page, "Elastic wave scattering by periodic structures of spherical objects: Theory and experiment," *Physical Review B,* vol. 62, no. 4, p. 2446, 2000.
[62] I. Psarobas, N. Stefanou, and A. Modinos, "Scattering of elastic waves by periodic arrays of spherical bodies," *Physical Review B,* vol. 62, no. 1, p. 278, 2000.
[63] I. Psarobas, N. Stefanou, and A. Modinos, "Phononic crystals with planar defects," *Physical Review B,* vol. 62, no. 9, p. 5536, 2000.
[64] P. Deymier, "Acoustic Metamaterial and Phononic Crystals," *Springer series in solid state sciences,* vol. 173, 2013.
[65] Y. Tanaka, Y. Tomoyasu, and S.-i. Tamura, "Band structure of acoustic waves in phononic lattices: Two-dimensional composites with large acoustic mismatch," *Physical Review B,* vol. 62, no. 11, p. 7387, 2000.
[66] J. Bucay *et al.*, "Positive, negative, zero refraction, and beam splitting in a solid/air phononic crystal: Theoretical and experimental study," *Physical Review B,* vol. 79, no. 21, p. 214305, 2009.
[67] Y. Pennec, J. O. Vasseur, B. Djafari-Rouhani, L. Dobrzyński, and P. A. Deymier, "Two-dimensional phononic crystals: Examples and applications," *Surface Science Reports,* vol. 65, no. 8, pp. 229-291, 2010.
[68] Z.-G. Chen *et al.*, "Accidental degeneracy of double Dirac cones in a phononic crystal," *Scientific reports,* vol. 4, p. 4613, 2014.
[69] J. Bucay, et al., , "Positive, negative, zero refraction, and beam splitting in a solid/air phononic crystal: Theoretical and experimental study," *Physical Review B,* vol. 79, pp. 214305-1-7, 2009, doi: 10.1103/PhysRevB.79.214305.
[70] M. I. Hussein, "Reduced Bloch mode expansion for periodic media band structure calculations," *Proceedings of the Royal Society A: Mathematical, Physical and Engineering Science,* vol. 465, no. 2109, pp. 2825-2848, September 8, 2009 2009, doi: 10.1098/rspa.2008.0471.
[71] M. S. Kushwaha, P. Halevi, L. Dobrzynski, and B. Djafari-Rouhani, "Acoustic band structure of periodic elastic composites," *Physical review letters,* vol. 71, no. 13, p. 2022, 1993.
[72] C. Goffaux and J. Vigneron, "Theoretical study of a tunable phononic band gap system," *Physical Review B,* vol. 64, no. 7, p. 075118, 2001.
[73] J. Vasseur, P. A. Deymier, B. Chenni, B. Djafari-Rouhani, L. Dobrzynski, and D. Prevost, "Experimental and theoretical evidence for the existence of absolute acoustic band gaps in two-dimensional solid phononic crystals," *Physical Review Letters,* vol. 86, no. 14, p. 3012, 2001.
[74] V. Laude, M. Wilm, S. Benchabane, and A. Khelif, "Full band gap for surface acoustic waves in a piezoelectric phononic crystal," *Physical Review E,* vol. 71, no. 3, p. 036607, 2005.

[75] A. Khelif, B. Aoubiza, S. Mohammadi, A. Adibi, and V. Laude, "Complete band gaps in two-dimensional phononic crystal slabs," *Physical Review E*, vol. 74, no. 4, p. 046610, 2006.
[76] S. Mohammadi, A. A. Eftekhar, A. Khelif, W. D. Hunt, and A. Adibi, "Evidence of large high frequency complete phononic band gaps in silicon phononic crystal plates," *Applied Physics Letters*, vol. 92, no. 22, p. 221905, 2008.
[77] J. V. Sánchez-Pérez *et al.*, "Sound attenuation by a two-dimensional array of rigid cylinders," *Physical Review Letters*, vol. 80, no. 24, p. 5325, 1998.
[78] T.-T. Wu, Y.-T. Chen, J.-H. Sun, S.-C. S. Lin, and T. J. Huang, "Focusing of the lowest antisymmetric Lamb wave in a gradient-index phononic crystal plate," *Applied Physics Letters*, vol. 98, no. 17, p. 171911, 2011, doi: 10.1063/1.3583660.
[79] M. Sigalas and E. N. J. S. s. c. Economou, "Band structure of elastic waves in two dimensional systems," vol. 86, no. 3, pp. 141-143, 1993.
[80] A. Shelke, S. Banerjee, A. Habib, E. K. Rahani, R. Ahmed, and T. Kundu, "Wave guiding and wave modulation using phononic crystal defects," vol. 25, no. 13, pp. 1541-1552, 2014, doi: 10.1177/1045389x13507344.
[81] H. Dong, F. Wu, H. Zhong, X. Zhang, and Y. J. J. o. P. D. A. P. Yao, "Effects of asymmetrical rotated rectangular basis on the acoustic band gap in two-dimensional acoustic crystals: the bands are twisted," vol. 43, no. 10, p. 105404, 2010.
[82] M. M. Indaleeb, S. Banerjee, H. Ahmed, M. Saadatzi, and R. J. P. R. B. Ahmed, "Deaf band based engineered Dirac cone in a periodic acoustic metamaterial: A numerical and experimental study," vol. 99, no. 2, p. 024311, 2019.
[83] X. Huang, Y. Lai, Z. H. Hang, H. Zheng, and C. Chan, "Dirac cones induced by accidental degeneracy in photonic crystals and zero-refractive-index materials," *Nature materials*, vol. 10, no. 8, p. 582, 2011.
[84] Y. Li and J. Mei, "Double Dirac cones in two-dimensional dielectric photonic crystals," *Opt Express*, vol. 23, no. 9, pp. 12089-99, May 04 2015, doi: 10.1364/OE.23.012089.
[85] S.-H. Kim, S. Kim, and C.-S. Kee, "Photonic crystals composed of virtual pillars with magnetic walls: Photonic band gaps and double Dirac cones," *Physical Review B*, vol. 94, no. 8, p. 085118, 08/11/ 2016. [Online]. Available: https://link.aps.org/doi/10.1103/PhysRevB.94.085118.
[86] J. Hao, W. Yan, and M. Qiu, "Super-reflection and cloaking based on zero index metamaterial," *Applied Physics Letters*, vol. 96, no. 10, p. 101109, 2010, doi: 10.1063/1.3359428.
[87] L.-Y. Zheng, Y. Wu, X. Ni, Z.-G. Chen, M.-H. Lu, and Y.-F. Chen, "Acoustic cloaking by a near-zero-index phononic crystal," vol. 104, no. 16, p. 161904, 2014, doi: 10.1063/1.4873354.
[88] C. T. Chan, Z. H. Hang, and X. Huang, "Dirac Dispersion in Two-Dimensional Photonic Crystals," *Advances in OptoElectronics*, vol. 2012, p. 11, 2012, Art no. 313984, doi: 10.1155/2012/313984.
[89] S.-Y. Yu *et al.*, "Acoustic phase-reconstruction near the Dirac point of a triangular phononic crystal," vol. 106, no. 15, p. 151906, 2015.
[90] M. M. Sigalas and E. N. Economou, "Attenuation of multiple-scattered sound," *Europhysics Letters (EPL)*, vol. 36, no. 4, pp. 241-246, 1996/11/01 1996, doi: 10.1209/epl/i1996-00216-4.

[91] J. O. Vasseur, P. A. Deymier, G. Frantziskonis, G. Hong, B. Djafari-Rouhani, and L. Dobrzynski, "Experimental evidence for the existence of absolute acoustic band gaps in two-dimensional periodic composite media," *Journal of Physics: Condensed Matter*, vol. 10, no. 27, pp. 6051-6064, 1998/07/13 1998, doi: 10.1088/0953-8984/10/27/006.

[92] F. Wu, Z. Liu, and Y. Liu, "Acoustic band gaps created by rotating square rods in a two-dimensional lattice," *Physical Review E*, vol. 66, no. 4, p. 046628, 10/30/ 2002, doi: 10.1103/PhysRevE.66.046628.

[93] S. A. Cummer, J. Christensen, and A. Alù, "Controlling sound with acoustic metamaterials," *Nature Reviews Materials*, vol. 1, no. 3, pp. 1-13, 2016.

[94] D. Roca, D. Yago, J. Cante, O. Lloberas-Valls, and J. Oliver, "Computational design of locally resonant acoustic metamaterials," *Computer Methods in Applied Mechanics and Engineering*, vol. 345, pp. 161-182, 2019.

[95] Z. Lv, P. Liu, and Y. Pei, "Temporal acoustic wave computational metamaterials," *Applied Physics Letters*, vol. 117, no. 13, p. 131902, 2020.

[96] F. Zangeneh-Nejad, D. L. Sounas, A. Alù, and R. Fleury, "Analogue computing with metamaterials," *Nature Reviews Materials*, vol. 6, no. 3, pp. 207-225, 2021.

[97] Z. Zhang, X. Han, and G. Ji, "The bandgap controlling by geometrical symmetry design in hybrid phononic crystal," *International Journal of Modern Physics B*, vol. 32, no. 04, p. 1850034, 2018.

[98] F. Wu, Z. Liu, and Y. Liu, "Splitting and tuning characteristics of the point defect modes in two-dimensional phononic crystals," *Physical Review E*, vol. 69, no. 6, p. 066609, 06/11/ 2004, doi: 10.1103/PhysRevE.69.066609.

[99] F. Wu, H. Zhong, S. Zhong, Z. Liu, and Y. Liu, "Localized states of acoustic waves in three-dimensional periodic composites with point defects," *The European Physical Journal B - Condensed Matter and Complex Systems*, vol. 34, no. 3, pp. 265-268, 2003/08/01 2003, doi: 10.1140/epjb/e2003-00220-6.

[100] N. Susa, "Large absolute and polarization-independent photonic band gaps for various lattice structures and rod shapes," *Journal of Applied Physics*, vol. 91, no. 6, pp. 3501-3510, 2002.

[101] H. Dai, B. Xia, and D. Yu, "Dirac cones in two-dimensional acoustic metamaterials," *Journal of Applied Physics*, vol. 122, no. 6, p. 065103, 2017/08/14 2017, doi: 10.1063/1.4998438.

[102] M. M. Indaleeb and S. Banerjee, "Simultaneous Dirac-like Cones at Two Energy States in Tunable Phononic Crystals: An Analytical and Numerical Study," *Crystals*, vol. 11, no. 12, 2021, doi: 10.3390/cryst11121528.

[103] L. Xu, H.-X. Wang, Y.-D. Xu, H.-Y. Chen, and J.-H. Jiang, "Accidental degeneracy in photonic bands and topological phase transitions in two-dimensional core-shell dielectric photonic crystals," *Opt. Express*, vol. 24, no. 16, pp. 18059-18071, 2016.

[104] X.-P. Song, T.-N. Chen, C. Chen, and W. Ding, "Observation of frequency band-switchable topological edge modes using a 2 bit coding acoustic topological insulator," *Journal of Physics D: Applied Physics*, vol. 54, no. 25, p. 255302, 2021.

[105] Z. Zhang, Q. Wei, Y. Cheng, T. Zhang, D. Wu, and X. Liu, "Topological creation of acoustic pseudospin multipoles in a flow-free symmetry-broken metamaterial lattice," *Physical review letters*, vol. 118, no. 8, p. 084303, 2017.

[106] Z. Zhang, Y. Tian, Y. Cheng, X. Liu, and J. Christensen, "Experimental verification of acoustic pseudospin multipoles in a symmetry-broken snowflakelike topological insulator," *Physical Review B*, vol. 96, no. 24, p. 241306, 2017.
[107] M. Sigalas and E. N. Economou, "Band structure of elastic waves in two dimensional systems," *Solid State Communications*, vol. 86, no. 3, pp. 141-143, 1993/04/01/ 1993, doi: https://doi.org/10.1016/0038-1098(93)90888-T.
[108] A. Shelke, S. Banerjee, A. Habib, E. K. Rahani, R. Ahmed, and T. Kundu, "Wave guiding and wave modulation using phononic crystal defects," *Journal of Intelligent Material Systems and Structures*, vol. 25, no. 13, pp. 1541-1552, 2014/09/01 2013, doi: 10.1177/1045389X13507344.
[109] H. Dong, F. Wu, H. Zhong, X. Zhang, and Y. Yao, "Effects of asymmetrical rotated rectangular basis on the acoustic band gap in two-dimensional acoustic crystals: the bands are twisted," *Journal of Physics D: Applied Physics*, vol. 43, no. 10, p. 105404, 2010/02/25 2010, doi: 10.1088/0022-3727/43/10/105404.
[110] S.-Y. Yu *et al.*, "Acoustic phase-reconstruction near the Dirac point of a triangular phononic crystal," *Applied Physics Letters*, vol. 106, no. 15, p. 151906, 2015/04/13 2015, doi: 10.1063/1.4918651.
[111] H. T. Stoof, K. B. Gubbels, and D. Dickerscheid, *Ultracold quantum fields*. Springer, 2009.
[112] V. J. S. P. J. Berezinskii, "Destruction of long-range order in one-dimensional and two-dimensional systems having a continuous symmetry group I. Classical systems," vol. 32, no. 3, pp. 493-500, 1971.
[113] J. M. Kosterlitz and D. J. J. J. o. P. C. S. S. P. Thouless, "Ordering, metastability and phase transitions in two-dimensional systems," vol. 6, no. 7, p. 1181, 1973.
[114] K. v. Klitzing, G. Dorda, and M. J. P. r. l. Pepper, "New method for high-accuracy determination of the fine-structure constant based on quantized Hall resistance," vol. 45, no. 6, p. 494, 1980.
[115] D. J. Thouless, M. Kohmoto, M. P. Nightingale, and M. J. P. r. l. den Nijs, "Quantized Hall conductance in a two-dimensional periodic potential," vol. 49, no. 6, p. 405, 1982.
[116] J. J. P. R. Zak, "Magnetic translation group," vol. 134, no. 6A, p. A1602, 1964.
[117] M. V. J. P. o. t. R. S. o. L. A. M. Berry and P. Sciences, "Quantal phase factors accompanying adiabatic changes," vol. 392, no. 1802, pp. 45-57, 1984.
[118] G. M. Graf and M. J. C. i. M. P. Porta, "Bulk-edge correspondence for two-dimensional topological insulators," vol. 324, no. 3, pp. 851-895, 2013.
[119] M. Z. Hasan and C. L. J. R. o. m. p. Kane, "Colloquium: topological insulators," vol. 82, no. 4, p. 3045, 2010.
[120] X. Zhang, M. Xiao, Y. Cheng, M.-H. Lu, and J. J. C. P. Christensen, "Topological sound," vol. 1, no. 1, pp. 1-13, 2018.
[121] R. Fleury, D. L. Sounas, C. F. Sieck, M. R. Haberman, and A. J. S. Alù, "Sound isolation and giant linear nonreciprocity in a compact acoustic circulator," vol. 343, no. 6170, pp. 516-519, 2014.
[122] X. Ni *et al.*, "Topologically protected one-way edge mode in networks of acoustic resonators with circulating air flow," vol. 17, no. 5, p. 053016, 2015.
[123] Z. Yang *et al.*, "Topological acoustics," vol. 114, no. 11, p. 114301, 2015.

[124] A. B. Khanikaev, R. Fleury, S. H. Mousavi, and A. J. N. c. Alu, "Topologically robust sound propagation in an angular-momentum-biased graphene-like resonator lattice," vol. 6, no. 1, pp. 1-7, 2015.
[125] M. Onoda and N. J. P. r. l. Nagaosa, "Quantized anomalous Hall effect in two-dimensional ferromagnets: quantum Hall effect in metals," vol. 90, no. 20, p. 206601, 2003.
[126] C.-X. Liu, X.-L. Qi, X. Dai, Z. Fang, and S.-C. J. P. r. l. Zhang, "Quantum anomalous Hall effect in Hg 1− y Mn y Te quantum wells," vol. 101, no. 14, p. 146802, 2008.
[127] Z. Qiao *et al.*, "Quantum anomalous Hall effect in graphene from Rashba and exchange effects," vol. 82, no. 16, p. 161414, 2010.
[128] C. J. P. r. l. Wu, "Orbital analogue of the quantum anomalous Hall effect in p-band systems," vol. 101, no. 18, p. 186807, 2008.
[129] C.-Z. Chang *et al.*, "Experimental observation of the quantum anomalous Hall effect in a magnetic topological insulator," vol. 340, no. 6129, pp. 167-170, 2013.
[130] G. Jotzu *et al.*, "Experimental realization of the topological Haldane model with ultracold fermions," vol. 515, no. 7526, pp. 237-240, 2014.
[131] C. L. Kane and E. J. J. P. r. l. Mele, "Z 2 topological order and the quantum spin Hall effect," vol. 95, no. 14, p. 146802, 2005.
[132] B. A. Bernevig and S.-C. J. P. r. l. Zhang, "Quantum spin Hall effect," vol. 96, no. 10, p. 106802, 2006.
[133] C. L. Kane and E. J. J. P. r. l. Mele, "Quantum spin Hall effect in graphene," vol. 95, no. 22, p. 226801, 2005.
[134] M. Konig *et al.*, "Quantum spin Hall insulator state in HgTe quantum wells," vol. 318, no. 5851, pp. 766-770, 2007.
[135] Y. L. Chen *et al.*, "Massive Dirac Fermion on the Surface of a Magnetically Doped Topological Insulator," vol. 329, no. 5992, pp. 659-662, 2010, doi: doi:10.1126/science.1189924.
[136] M. König *et al.*, "Quantum Spin Hall Insulator State in HgTe Quantum Wells," vol. 318, no. 5851, pp. 766-770, 2007, doi: doi:10.1126/science.1148047.
[137] X. Kou, Y. Fan, K. L. J. J. o. P. Wang, and C. o. Solids, "Review of quantum Hall trio," vol. 128, pp. 2-23, 2019.
[138] H. Zhang, C.-X. Liu, X.-L. Qi, X. Dai, Z. Fang, and S.-C. J. N. p. Zhang, "Topological insulators in Bi2Se3, Bi2Te3 and Sb2Te3 with a single Dirac cone on the surface," vol. 5, no. 6, pp. 438-442, 2009.
[139] Y. Chen *et al.*, "Experimental realization of a three-dimensional topological insulator, Bi2Te3," vol. 325, no. 5937, pp. 178-181, 2009.
[140] L. J. P. R. L. Fu, "Topological crystalline insulators," vol. 106, no. 10, p. 106802, 2011.
[141] S.-Y. Xu *et al.*, "Observation of a topological crystalline insulator phase and topological phase transition in Pb1− xSnxTe," vol. 3, no. 1, pp. 1-11, 2012.
[142] Y. Okada *et al.*, "Observation of Dirac node formation and mass acquisition in a topological crystalline insulator," vol. 341, no. 6153, pp. 1496-1499, 2013.
[143] C. J. R. o. M. P. Beenakker, "Colloquium: Andreev reflection and Klein tunneling in graphene," vol. 80, no. 4, p. 1337, 2008.

[144] A. C. Neto, F. Guinea, N. M. Peres, K. S. Novoselov, and A. K. J. R. o. m. p. Geim, "The electronic properties of graphene," vol. 81, no. 1, p. 109, 2009.
[145] K.-I. Imura, A. Yamakage, S. Mao, A. Hotta, and Y. J. P. R. B. Kuramoto, "Zigzag edge modes in a Z 2 topological insulator: Reentrance and completely flat spectrum," vol. 82, no. 8, p. 085118, 2010.
[146] C. Yang, Y.-T. Tan, H. Chen, and J. J. J. o. A. P. Ren, "Real spin angular momentum and acoustic spin torque in a topological phononic crystal," vol. 129, no. 13, p. 135106, 2021.
[147] Z. Zhang, Y. Tian, Y. Cheng, X. Liu, and J. J. P. R. B. Christensen, "Experimental verification of acoustic pseudospin multipoles in a symmetry-broken snowflakelike topological insulator," vol. 96, no. 24, p. 241306, 2017.
[148] D. Xiao, W. Yao, and Q. J. P. r. l. Niu, "Valley-contrasting physics in graphene: magnetic moment and topological transport," vol. 99, no. 23, p. 236809, 2007.
[149] R. K. Pal and M. J. N. J. o. P. Ruzzene, "Edge waves in plates with resonators: an elastic analogue of the quantum valley Hall effect," vol. 19, no. 2, p. 025001, 2017.
[150] J. Vila, R. K. Pal, and M. J. P. R. B. Ruzzene, "Observation of topological valley modes in an elastic hexagonal lattice," vol. 96, no. 13, p. 134307, 2017.
[151] H. Zhu, T.-W. Liu, and F. J. P. R. B. Semperlotti, "Design and experimental observation of valley-Hall edge states in diatomic-graphene-like elastic waveguides," vol. 97, no. 17, p. 174301, 2018.
[152] T.-W. Liu and F. J. P. R. A. Semperlotti, "Tunable acoustic valley–hall edge states in reconfigurable phononic elastic waveguides," vol. 9, no. 1, p. 014001, 2018.
[153] J. Lu *et al.*, "Observation of topological valley transport of sound in sonic crystals," vol. 13, no. 4, pp. 369-374, 2017.
[154] O. Bleu, D. Solnyshkov, and G. J. P. R. B. Malpuech, "Quantum valley Hall effect and perfect valley filter based on photonic analogs of transitional metal dichalcogenides," vol. 95, no. 23, p. 235431, 2017.
[155] J. Y. Lee and W. J. T. J. o. t. A. S. o. A. Jeon, "Vibration damping using a spiral acoustic black hole," vol. 141, no. 3, pp. 1437-1445, 2017.
[156] S. S. Ganti, T.-W. Liu, F. J. J. o. S. Semperlotti, and Vibration, "Topological edge states in phononic plates with embedded acoustic black holes," vol. 466, p. 115060, 2020.
[157] P. Q. Romano, S. C. Conlon, and E. C. J. T. J. o. t. A. S. o. A. Smith, "Investigation of contact acoustic nonlinearities on metal and composite airframe structures via intensity based health monitoring," vol. 133, no. 1, pp. 186-200, 2013.
[158] V. V. Krylov, "Acoustic'black holes' for flexural waves and their potential applications," 2002.
[159] V. V. J. A. A. u. w. A. Krylov, "New type of vibration dampers utilising the effect of acoustic'black holes'," vol. 90, no. 5, pp. 830-837, 2004.
[160] V. V. Krylov, R. J. J. o. S. Winward, and Vibration, "Experimental investigation of the acoustic black hole effect for flexural waves in tapered plates," vol. 300, no. 1-2, pp. 43-49, 2007.
[161] E. Bowyer and V. V. J. C. S. Krylov, "Experimental investigation of damping flexural vibrations in glass fibre composite plates containing one-and two-dimensional acoustic black holes," vol. 107, pp. 406-415, 2014.

[162] J. Y. Lee and W. Jeon, "Vibration damping using a spiral acoustic black hole," vol. 141, no. 3, pp. 1437-1445, 2017, doi: 10.1121/1.4976687.
[163] O. Guasch, M. Arnela, and P. Sánchez-Martín, "Transfer matrices to characterize linear and quadratic acoustic black holes in duct terminations," *Journal of Sound and Vibration,* vol. 395, pp. 65-79, 2017/05/12/ 2017, doi: https://doi.org/10.1016/j.jsv.2017.02.007.
[164] A. Pelat, F. Gautier, S. C. Conlon, and F. Semperlotti, "The acoustic black hole: A review of theory and applications," *Journal of Sound and Vibration,* vol. 476, p. 115316, 2020/06/23/ 2020, doi: https://doi.org/10.1016/j.jsv.2020.115316.

APPENDIX A: ANALYTICAL FORMULATION OF SQUARE PNC

In this section, the mathematical derivation of the Fourier coefficients for periodic (a_1 and a_2) PnCs composed of rectangular solids (b_1 and b_2) in air media shown in **Fig. A.1** is presented in a step-by-step process.

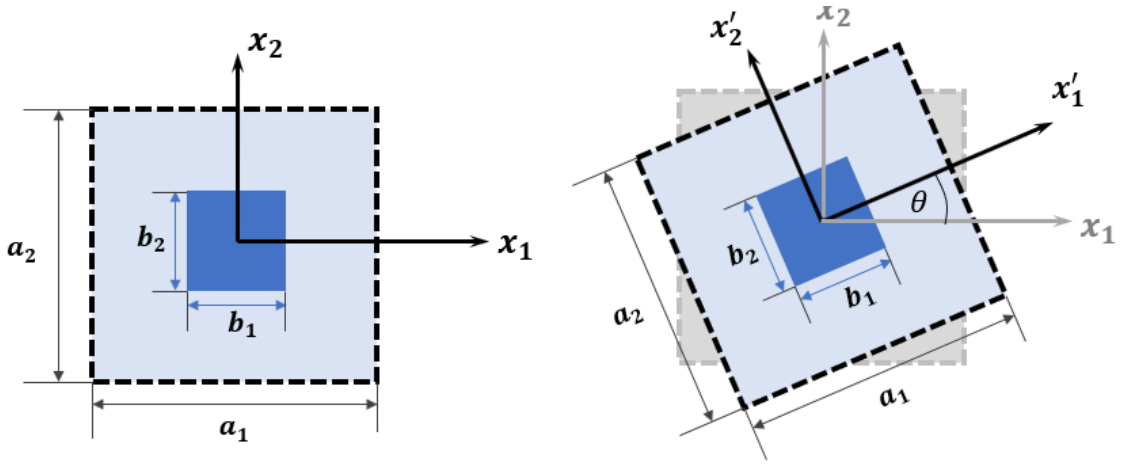

Figure A.1: (a) A typical periodic metamedia with square PVC PnCs in an air matrix. b) Periodic media with rotated square PnCs.

Applying the Heaviside step function, the $\alpha(x_k)$ function for the metamedia in Fig. A.1 is expressed as

$$\alpha(x_k) = \alpha_{sq} H(x_k), \tag{A.1}$$

where $H(x_k) = \mathbf{H}(x_1, x_2) = H(x_1).H(x_2)$

$$= \left[H\left(x_1 + \frac{b_1}{2}\right) - H\left(x_1 - \frac{b_1}{2}\right)\right]\left[H\left(x_2 + \frac{b_2}{2}\right) - H\left(x_2 - \frac{b_2}{2}\right)\right]$$

(A.2)

Following Eq. (6) and (10),

$$\alpha(x_k) = \sum_p \sum_q \alpha^{pq} e^{-i\mathbf{G_{pq}}.\mathbf{x}} = \sum_p \sum_q \alpha^{pq} e^{-i(G_1 x_1 + G_2 x_2)}, \tag{A.3}$$

where $\mathbf{G_{pq}} = \frac{2\pi p}{a_1}\hat{e}_1 + \frac{2\pi q}{a_2}\hat{e}_2$

Using the Fourier transform, the Fourier coefficients α^{pq} are expressed as

$$\alpha^{pq} = \frac{1}{a_1 a_2}\int_{-\frac{a_1}{2}}^{\frac{a_1}{2}}\int_{-\frac{a_2}{2}}^{\frac{a_2}{2}} \alpha_{sq}\cdot \mathbf{H}(x_1,x_2)e^{i(G_1x_1+G_2x_2)}\,dx_1dx_2 \qquad \text{(A.4)}$$

$$\alpha^{pq} = \frac{\alpha_{sq}}{a_1 a_2}\left[\int_{-\frac{a_2}{2}}^{\frac{a_2}{2}}\left[\int_{-\frac{a_1}{2}}^{\frac{a_1}{2}}\mathbf{H}(x_1)e^{i(G_1x_1)}dx_1\right]\mathbf{H}(x_2)e^{i(G_2x_2)}dx_2\right] \qquad \text{(A.5)}$$

Before conducting the integration, a few basic identities are important to note such as

$$\frac{dH(x)}{dx} = \delta(x)\ , \quad \int_{-\infty}^{\infty}\delta(x)\ dx = H(x) \quad , \quad \frac{de^{i(G_jx_j)}}{dx_j} = i\big(G_j\big)e^{i(G_jx_j)}\ ,$$

and $\int_{-\infty}^{\infty} e^{i(G_1x)}\delta(x-c)dx = e^{i(G_1c)}$.

Hence, Eq. (A.5) changes to

$$\alpha^{pq} = \frac{\alpha_{sq}}{a_1 a_2}\left[\frac{1}{iG_2}\int_{-\frac{a_2}{2}}^{\frac{a_2}{2}}\left[\frac{1}{iG_1}\int_{-\frac{a_1}{2}}^{\frac{a_1}{2}}\mathbf{H}(x_1)d\big(e^{i(G_1x_1)}\big)\right]\mathbf{H}(x_2)d\big(e^{i(G_2x_2)}\big)\right] \qquad \text{(A.6)}$$

Conducting the decoupled integration in parts separately for two orthogonal directions obtains

$$\int_{-\frac{a_1}{2}}^{\frac{a_1}{2}}\left[H\left(x_1+\frac{b_1}{2}\right)d\big(e^{i(G_1x_1)}\big)\right]dx_1$$

$$= \frac{1}{iG_1}\left[H\left(\frac{a_1+b_1}{2}\right)e^{i\left(G_1\frac{a_1}{2}\right)} - H\left(-\frac{a_1}{2}+\frac{b_1}{2}\right)e^{-i\left(G_1\frac{a_1}{2}\right)}\right] -$$

$$\int_{-\frac{a_1}{2}}^{\frac{a_1}{2}} e^{i(G_1x_1)}dH\left(x_1+\frac{b_1}{2}\right) \qquad \text{(A.7)}$$

Of note, $H\left(\frac{a_1+b_1}{2}\right) = 1$, $H\left(-\frac{a_1}{2}+\frac{b_1}{2}\right) = 0$, and

$$dH\left(x_1+\frac{b_1}{2}\right) = \delta\left(x_1+\frac{b_1}{2}\right)dx_1 \quad ; \quad \int_{-\frac{a_1}{2}}^{\frac{a_1}{2}} e^{i(G_1x_1)}\delta\left(x_1+\frac{b_1}{2}\right)dx_1 = e^{-i\left(G_1\frac{b_1}{2}\right)}$$

Substituting these formulas into Eq. (A.7) obtains

$$\int_{-\frac{a_1}{2}}^{\frac{a_1}{2}} \left[H\left(x_1 + \frac{b_1}{2}\right) d\left(e^{i(G_1 x_1)}\right) \right] dx_1 = \frac{1}{iG_1} \left[e^{i\left(G_1 \frac{a_1}{2}\right)} - e^{-i\left(G_1 \frac{b_1}{2}\right)} \right]$$

(A.8)

Similarly,

$$\int_{-\frac{a_1}{2}}^{\frac{a_1}{2}} \left[H\left(x_1 - \frac{b_1}{2}\right) d\left(e^{i(G_1 x_1)}\right) \right] dx_1 = \frac{1}{iG_1} \left[e^{i\left(G_1 \frac{a_1}{2}\right)} - e^{i\left(G_1 \frac{b_1}{2}\right)} \right]$$

(A.9)

Thus,

$$\left[\int_{-\frac{a_1}{2}}^{\frac{a_1}{2}} \mathbf{H}(x_1) e^{i(G_1 x_1)} dx_1 \right] = \frac{1}{iG_1} \left[e^{i\left(G_1 \frac{b_1}{2}\right)} - e^{-i\left(G_1 \frac{b_1}{2}\right)} \right]$$

(A.10)

Following similar integration steps,

$$\left[\int_{-\frac{a_2}{2}}^{\frac{a_2}{2}} \mathbf{H}(x_2) e^{i(G_2 x_2)} dx_2 \right] = \frac{1}{iG_2} \left[e^{i\left(G_2 \frac{b_2}{2}\right)} - e^{-i\left(G_2 \frac{b_2}{2}\right)} \right]$$

(A.11)

Substituting Eqs. (A.10) and (A.11) into Eq. (A.5) obtains

$$\alpha^{pq} = -\frac{\alpha_{sq}}{a_1 a_2 G_1 G_2} \left[e^{i\left(G_1 \frac{b_1}{2}\right)} - e^{-i\left(G_1 \frac{b_1}{2}\right)} \right] \left[e^{i\left(G_2 \frac{b_2}{2}\right)} - e^{-i\left(G_2 \frac{b_2}{2}\right)} \right]$$

(A.12)

Using the identity called Euler's formula $e^{i\Theta} = \cos\Theta + i \sin\Theta$ obtains

$$\alpha^{pq} = \frac{4\alpha_{sq}}{a_1 a_2 G_1 G_2} \left[\sin\left(G_1 \frac{b_1}{2}\right) \right] \left[\sin\left(G_2 \frac{b_2}{2}\right) \right] \quad \text{(A.13)}$$

When the square rods are rotated at an angle θ as shown in Fig. A.1, the reciprocal Bloch wave vector is transformed into

$$G_{1'} = (G_1 cos\theta + G_2 sin\theta) \qquad G_{2'} = (-G_1 sin\theta + G_2 cos\theta) \quad \text{(A.14)}$$